Study of pressurized membrane panels

Paul Lacorre

DOCTORAT BRETAGNE SCIENCES LOIRE POUR L'INGENIEUR

Nantes Université

THÈSE DE DOCTORAT DE

NANTES UNIVERSITÉ

ÉCOLE DOCTORALE N° 602
Sciences pour l'Ingénieur
Spécialité : Mécanique des Structures

Par
Paul LACORRE

Étude des panneaux membranaires pressurisés

Thèse présentée et soutenue à Nantes, le 22 décembre 2022
Unité de recherche : Institut de Recherche en Génie Civil et Mécanique (GeM), UMR CNRS 6183

Rapporteurs avant soutenance :

Kai-Uwe Bletzinger	Professeur, TUBVSTA Lehrstuhl für Statik, Munich, Allemagne
Olivier Millet	Professeur, LaSIE, Université de La Rochelle

Composition du Jury :

Président :	Olivier Millet	Professeur, LaSIE, Université de La Rochelle
Examinateurs :	Kai-Uwe Bletzinger	Professeur, TUBVSTA Lehrstuhl für Statik, Munich, Allemagne
	Mélina Skouras	Chargée de recherche, INRIA Grenoble - Rhône-Alpes
	Jean-Baptiste Casimir	Professeur, Institut Supérieur de Mécanique de Paris
Directeur de thèse :	Anh Le Van	Professeur, GeM, Nantes Université
Co-dir. de thèse :	Jean-Christophe Thomas	Maître de conférence, GeM, Nantes Université
Co-dir. de thèse :	Rabah Bouzidi	Maître de conférence, GeM, Nantes Université

Contents

Nomenclature

General quantities

Notation	Description	Unit
$\boldsymbol{A}_\alpha$, $\boldsymbol{A}^\alpha$	Tangent (resp. normal) base vector in the curvilinear system of coordinates ξ^α	?
$\boldsymbol{A}_3$	Initial director vector (orientation of the material segment in the reference configuration)	-
a, b	x, y dimension of a rectangular panel	m
D^*	Bending stiffness due to the panel's membranes resistance to traction $D^* = \frac{E\tilde{\tau}H^2}{2(1-\nu^2)}$	N.m
E	Young's modulus of the panel's isotropic membranes	Pa
E_y	Young's modulus of a single drop-stitch yarn	Pa
$\boldsymbol{E}$	Green-Lagrange strain tensor	-
$\boldsymbol{F}$	Deformation gradient tensor	-
H	Panel height (membranes thickness included) (typically around 15cm)	m
$H_\varnothing$	Natural panel height (before inflation)	m
$\tilde{H}$	Panel height between upper and lower membranes ($H - 2\tau$)	m
$\boldsymbol{I}^P$	Identity tensor restricted to plane $\boldsymbol{e}_1\boldsymbol{e}_2$ ($\boldsymbol{I}^P = \boldsymbol{e}_\alpha \otimes \boldsymbol{e}_\alpha$)	-
K	Total bending stiffness of inflatable panels $K = D^* + M_0^{(2)} = \frac{E\tilde{\tau}H^2}{2(1-\nu^2)} + \frac{pH^2\tilde{H}\tilde{\tau}}{4\tau}$	N.m
K_ν	Total bending stiffness coefficient used in Cartesian coordinates $K_\nu = D^*\frac{1-\nu}{2} + M_0^{(2)}$	N.m
K'	Bending stiffness coefficient for boundary conditions $K' = \nu D^* + \frac{p\tilde{H}^3}{12} = \nu\frac{E\tilde{\tau}H^2}{2(1-\nu^2)} + \frac{p\tilde{H}^3}{12}$	N.m
$M_0^{(2)}$	Second-order moment pre-tension $M_0^{(2)} = \frac{pH^2\tilde{H}\tilde{\tau}}{4\tau}$	N.m
$\boldsymbol{n}$	Normal vector to the upper / lower face	-
P	Point on the mid-surface in the current configuration	m
P_0	Point on the mid-surface in the reference configuration	m

Notation	Description	Unit
p	Internal pressure	N/m^2
$\mathbf{Q}$	Position in the plate in current configuration	m
$\mathbf{Q}_0$	Position in the plate in reference configuration	m
R	Radius of circular panel	m
$R_\varnothing$	Natural radius of circular panel (before inflation)	m
S_y	Cross section of a single drop-stitch yarn	m^2
t	Time	s
$\boldsymbol{U}$	Displacement vector	m
W	Vertical component of the deflection of the panel	m
λ	Coordinate along the edge of the panel	m
ν	Poisson's ratio of the panel's isotropic membranes	m^2/s
ξ	Curvilinear parameter	-
$\mathbf{\Pi}$	First Piola–Kirchhoff stress tensor	Pa
$\boldsymbol{\sigma}$	Cauchy stress tensor	Pa
$\mathbf{\Sigma}$	Second Piola–Kirchhoff stress tensor	Pa
τ	Panel membranes' thickness (typically below 1 mm)	m
$\tilde{\tau}$	Reduced thickness parameter (no physical significance) $\tilde{\tau} = \left(1 - \frac{2\tau}{H} + \frac{4\tau^2}{3H^2}\right)\tau$	m
$\boldsymbol{\psi}$	Fiber (or *material segment*) orientation vector field	-

Vibrations

Notation	Description	Unit
D_0	Frequency parameter $D_0^2 = \omega^2 \frac{2\tau\rho}{K}$	m^{-2}
D_c	Cut-off frequency parameter	m^{-2}
D_1, D_2, D_3	Square of the wavenumber corresponding to the potential W_i	m^{-2}
f_c	Cut-off frequency	Hz
f_{mn}	Natural frequency for the mode (m, n)	Hz
k_1, k_2	Coefficients that relate the amplitude of the shear eigenmodes to the bending eigenmodes	-

Notation	Description	Unit
V_s	Ratio of flexural stiffness over shear stiffness $V_s = \frac{K}{p\tilde{H}}$	m^2
V_i	Ratio of rotatory inertia and flexural inertia $V_i = \frac{\rho\tilde{\tau}H^2}{2} \times \frac{1}{2\tau\rho} = \frac{\tilde{\tau}H^2}{4\tau}$	m^2
W_1, W_2, W_3	Plate-displacement potentials for the eigenvalue problem	m
α, β	Wavenumbers for the rectangular panel	m^{-1}
$\delta_1, \delta_2, \delta_3$	Wavenumbers of the eigenmode potentials, equal to $\sqrt{\lvert\Omega_i\rvert}$	m^{-1}
λ	Eigenvalue of the generalized eigenvalue problem of inflatable panels $\lambda = \omega^2$	s^{-2}
σ_α	Coefficients that relate the amplitude of the shear eigenmodes to the bending eigenmodes	-
ω_c	Cut-off angular frequency	rad/s
ω_{mn}	Natural angular frequency for the mode (m, n)	rad/s
$\Omega_1, \Omega_2, \Omega_3$	Square of the wavenumber corresponding to the potential W_i	m^{-2}
$\boldsymbol{\Psi}$	Fiber orientation eigenmode	-

Résumé français

Les structures en textiles tendus sont en plein essor. L'écriture en cours d'un Eurocode appliqué aux structures membranaires et gonflables montre qu'elles occupent un rôle de plus en plus grand dans la construction : la membrane est en train d'être reconnue comme un élément architectural courant. Pour conférer aux membranes leur raideur, il est nécessaire d'assurer une prétension bi-axiale. Pour cela, deux techniques sont couramment employées. La première est la mise en tension par l'intermédiaire d'éléments mécaniques de type câble. C'est la grande majorité des structures tendues que l'on voit dans l'architecture. La seconde technique est l'utilisation d'un gaz sous pression, généralement de l'air, pour tendre la structure. C'est ce qui définit la famille des structures pneumatiques et c'est dans ce cadre que s'inscrit le travail présenté dans cette thèse.

Il existe de nombreuses structures mono-membranes de type bulle qui recouvrent des aires de sport telles que des courts de tennis ou des terrains de football de manière temporaire. Elles peuvent également être installées de façon pérennes, comme c'est le cas des coussins gonflables utilisés pour recouvrir des bâtiments tels que le stade de l'Allianz Arena à Munich (Fig. 1). De nombreuses structures pneumatiques temporaires tirent profit des qualités de ce type de structures : légères, faciles à transporter, faciles à monter et démonter, sans impact conséquent sur les sols.

Figure 1: L'Allianz Arena à Munich (Allemagne). (crédit photo : Wikimedia)

Les structures textiles tendues présentent généralement une double courbure opposées (en forme de selle de cheval, Fig. 2). Les structures gonflables, elles, sont naturellement bombées (comme dans le cas des coussins gonflables) ou encore avec une seule courbure non nulle (tubes gonflables). Il serait également très utile de disposer de surfaces sans courbures : c'est ce que permet la technologie de panneau gonflable qui allie la géométrie d'une plaque classique avec les qualités d'une structure membranaire, peu coûteuse et facilement transportable.

Un panneau gonflable est une structure membranaire étanche et remplie d'un gaz sous pression qui lui confère sa raideur et dont la forme une fois gonflée est maîtrisée par des fils qui relient les nappes supérieure et inférieure. Lorsque tous les fils ont la même longueur, le panneau a une épaisseur uniforme et peut être modélisé comme une plaque.

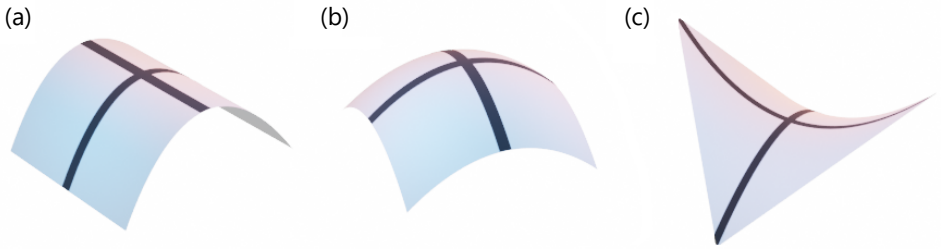

Figure 2: Surfaces monoclastique (a), synclastique (b) et anticlastique (c).

Du point de vue industriel, les premiers panneaux gonflables ont été proposés pour des applications liées à l'aviation ou à la conquête spatiale dans les années soixante. Ces projets sont restés à l'échelle de prototypes mais ont permis l'élaboration des techniques de fabrication, notamment du tissu double-paroi communément appelé « drop stitch ». De nos jours, les panneaux gonflables sont très utilisés dans le secteur des loisirs pour produire des paddles ou des pistes de gymnastique (Fig. 3). Dans le domaine de la construction, certaines structures sont déjà composées d'éléments assimilables à des poutres, tels que des tubes ou des arches, et l'apport d'éléments plans viendra naturellement combler un manque dans les outils de conception d'assemblages structurels. En effet, les théories classiques de la résistance des matériaux ne sont pas adaptées à l'étude des structures pressurisées puisqu'elles ignorent l'influence de la pression interne. En conséquent, des recherches ont été menées pour élaborer une nouvelle théorie adaptée à ces structures. Une fois les théories de poutres et de panneaux gonflables bien maîtrisées, il sera possible de dimensionner des structures porteuses de formes complexes entièrement gonflables.

(a) Piste de gymnastique gonflable (© Airtrack)

(b) Stand up paddle (© Décathlon)

Figure 3: Exemples d'application des panneaux gonflables dans les sports.

Poutres gonflables

Afin de montrer l'étendue des travaux réalisés dans le domaine des structures gonflables, nous commençons par un historique des recherches sur les poutres gonflables qui justifie les hypothèses adoptées pour la théorie des panneaux gonflables.

L'étude des tubes pressurisés commence en 1963 avec Comer et Levy [1] qui ont étudié une poutre console gonflable en se basant sur la théorie des poutres d'Euler-Bernoulli qui néglige le cisaillement. Les mêmes hypothèses sont reprises par Webber [2] qui a étudié des sollicitations combinées de flexion et torsion et réalisé des expériences avec des pressions de gonflage de l'ordre de 0,2 bar, ce qui est aujourd'hui consid-

éré comme étant faible. En 1995, Main et al. [3] mènent des expériences dans le but de valider l'hypothèse de cinématique d'Euler-Bernoulli pour les poutres gonflables. La gamme des pressions de gonflage considérée étant trop restreinte, la pression reste peu influente d'après leurs résultats et ils concluent que l'hypothèse de Comer et Levy doit être valable ; chose qui est réfutée de nos jours. En parallèle, d'autres auteurs avaient utilisé le théorème de l'énergie potentielle pour inclure la pression interne dans le modèle poutre. C'est le cas de Fichter [4], qui a introduit l'usage de la cinématique de Timoshenko pour les tubes gonflables, et de Steeves [5] qui a proposé des solutions sous la forme de fonctions de Green pour des poutres bi-appuyées ou bi-encastrées.

C'est à partir de 2002 avec les travaux et expériences de Wielgosz et Thomas [6] que des écarts importants à la théorie basée sur la cinématique d'Euler-Bernoulli sont observés pour des plages de pression étendues. Ils mettent en exergue l'effet du cisaillement et formulent un nouveau modèle avec une cinématique de Timoshenko. En 2005, Le Van et Wielgosz [7] montrent l'importance de distinguer la *configuration naturelle* (où la pression interne est nulle) et la *configuration de référence précontrainte*. Ils établissent la relation entre la charge de plissage et la pression de gonflage. Ils calculent également la charge de ruine. En 2013, Q. T. Nguyen [8] étend la théorie des poutres gonflables isotropes au cas orthotrope. Les propriétés matérielles de la membrane à l'état gonflé sont déterminées à partir de ses caractéristiques à l'état naturel.

Panneaux gonflables

La première étude des panneaux gonflables date de 1960 avec les travaux de R. W. Leonard et McComb [9, 10] pour le compte de la NASA. Ils développent une théorie linéaire des panneaux gonflables et concluent qu'il s'agit d'un cas particulier de théorie de plaque avec prise en compte du cisaillement. Bien que les fils dans le panneau soient généralement verticaux, ils montrent qu'avec des fils obliques (motif en « V ») on augmente la résistance au cisaillement au prix d'un gain de masse [11]. Leurs travaux sont suivis d'expériences menées par Stroud [12], toujours à la NASA, où ils mesurent le déplacement au centre d'un panneau rectangulaire chargé uniformément avec des bords appuyés ou encastrés. Ils mesurent également les premières fréquences propres en fonction de la pression de gonflage. Les modèles cités jusqu'à présent ne peuvent être appliqués qu'en coordonnées cartésiennes. En 1962, Haight [13] travaille sur les panneaux gonflables pour son mémoire de master et publie une solution non linéaire sous forme de série entière pour la déformée statique d'un panneau circulaire chargé uniformément [14]. Néanmoins, cette théorie néglige les moments de précontrainte d'ordre 2. D'autres variations autour des panneaux sont possibles : en espaçant davantage les fils dans une direction, on autorise une courbure périodique de la surface [15, 16].

Plus récemment, Wielgosz et Thomas [17] ont étudié le comportement de panneaux gonflables élancés pouvant être assimilés à des poutres. Cavallaro [18] a fait de même en réalisant une étude ciblée sur le matériau *drop-stitch*, à savoir le tissage 3D de deux membranes pour qu'elles restent à égale distance après gonflage. En 2021, Davids et al. [19] ont déterminé expérimentalement les propriétés d'un panneau gonflable (modules d'élasticité et de cisaillement en orthotropie). Ils présentent des simulations numériques non linéaires obtenues en adaptant leur modèle de poutre gonflable publié en 2008 [20]. Il s'agit encore une fois d'un modèle unidimensionnel.

Les recherches sur les éléments de construction gonflables ont été prolongées jusqu'à développer des modèles de coque gonflable, qui ont une surface moyenne courbée à l'état de référence, par exemple avec les travaux de J. W. Leonard et C. T. Li [21, 22, 23, 24, 25, 26].

Tout ceci montre que même s'il existe des théories de panneaux gonflables, elles sont anciennes et difficiles d'accès. Dans cette thèse, nous ne nous contentons pas de revisiter ces travaux et proposons une nouvelle théorie à partir du principe des puissances virtuelles en grandes transformations et en coordonnées

curvilignes. Les résultats de la littérature sont retrouvés avec un terme de raideur supplémentaire dû à la pression interne.

Vibrations des plaques de Reissner-Mindlin

En plus de la statique des panneaux gonflables, nous nous intéressons aux aspects dynamiques avec l'étude des vibrations par analyse modale à partir de la théorie linéarisée.

Bien qu'une théorie des plaques prenant en compte le cisaillement existe depuis les années cinquante, il reste difficile à ce jour de trouver des méthodes de résolution analytique dans la littérature. Cette théorie est souvent présentée comme une « simple extension » des plaques de Love–Kirchhoff et peu de résultats sont présentés. En réalité, l'étude des vibrations de telles plaques présente plusieurs difficultés supplémentaires : le couplage des modes de flexion et de cisaillement ainsi que l'existence de différents régimes de vibration (basse fréquence, haute fréquence). Le sujet est abordé pour la première fois en 1951 dans l'article fondateur de la théorie de Reissner–Mindlin [27] où l'auteur établit une théorie des plaques qui inclut l'inertie de rotation et la raideur en cisaillement. Il pose le problème aux valeurs propres et montre qu'il se réduit à des équations de Helmholtz mais ne les résout pas. Ensuite, de 1951 à 1956, Mindlin et Deresiewicz [28, 29, 30] consolident la théorie en résolvant ces équations pour des plaques rectangulaires et circulaires simplement appuyées. En 1980, Irie et al. [31] généralisent les solutions de Mindlin sur les vibrations de plaques circulaires à tous les types de conditions aux limites (bord encastré, appuyé ou libre). En 1993, Liew [32] approfondit l'étude des plaques de Reissner-Mindlin et publie un état de l'art où il introduit la distinction utile entre l'appui simple classique qu'il qualifie de « souple » et l'appui simple « dur » qui interdit les rotations dans le plan tangent au bord. En 2005, Hashemi et Arsanjani [33] synthétisent de nombreux travaux en donnant les équations caractéristiques pour toutes les plaques dont deux bords opposés sont appuyés.

Ces travaux portent sur les plaques classiques et devront donc être adaptés aux panneaux gonflables.

Théorie non linéaire des panneaux gonflables

Dans le cadre de cette thèse, nous avons développé un théorie des panneaux gonflables en grandes transformations. Il s'agit d'une approche moderne et unifiée qui permet de traiter les problèmes de statique, de dynamique et de flambement sans présupposer un système de coordonnées particulier. Nous prenons en compte les effets du cisaillement à travers la cinématique de Reissner-Mindlin et ceux de la pression qui est assimilée à un chargement suiveur extérieur. La prise en compte des fils se fait uniquement à travers l'hypothèse de non-élongation au cours de la phase de chargement, ce qui explique pourquoi la densité et les propriétés mécaniques des fils n'apparaissent pas explicitement dans les équations locales. La raideur des fils intervient uniquement pendant la phase de gonflage où le panneau atteint sa hauteur de référence, Fig. 4. Le principe des puissances virtuelles écrit en grandes transformations permet d'obtenir les équations locales non linéaires en coordonnées curvilignes. Ces équations contiennent les termes nécessaires à la bonne prise en compte de la pression de gonflage et ils contribuent effectivement à la raideur globale (en flexion et en cisaillement) de la structure.

Théorie linéarisée

Les équations non linéaires obtenues ont été linéarisées autour de la configuration gonflée, considérée comme configuration de référence. Cela permet d'étudier les petits mouvements du panneau au voisinage de cet

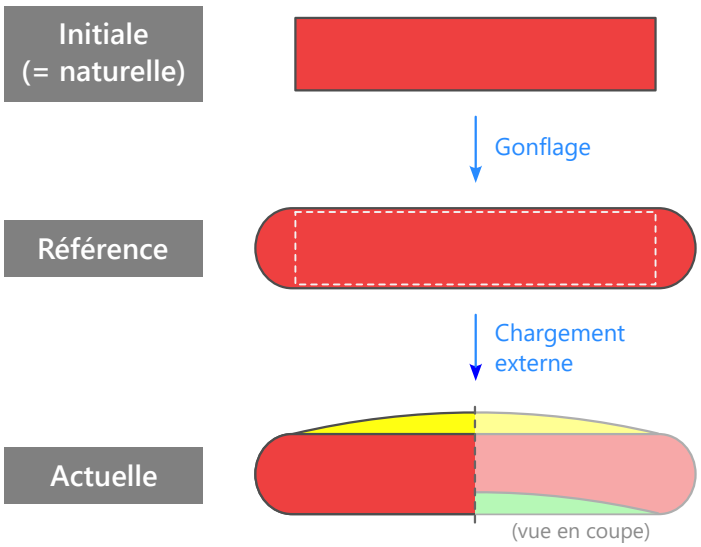

Figure 4: Vues de côté d'un panneau soumis à un chargement vertical dans les trois configurations d'intérêt.

état. Comme toutes les lois de comportement sont confondues avec la loi de Saint Venant–Kirchhoff sous l'hypothèse des petites déformations, il n'est pas nécessaire de prendre en compte une loi plus complexe lors de la linéarisation. On suppose de plus un état de contraintes planes dans les membranes. Les équations du mouvement ainsi obtenues sont semblables à celles de la théorie des plaques de Reissner-Mindlin. Néanmoins, elles comportent de nouveaux termes de raideur qui s'additionnent aux coefficients matériaux et qui dépendent de la pression. Nous montrons que la raideur en cisaillement du panneau provient entièrement de la précontrainte de gonflage et non plus de la raideur au cisaillement transverse des membranes qui a été négligée.

Solution statique : panneau circulaire simplement appuyé et chargé uniformément

Les équations locales ainsi linéarisées ont pu être résolues analytiquement pour le problème de flexion statique d'un panneau circulaire simplement appuyé sur son bord et soumis à un chargement vertical. La déformée obtenue est de forme parabolique et dépend de la pression interne, Fig. 5. Nous avons également pu déterminer la limite de validité de cette solution en précisant la charge de ruine au-delà de laquelle les contraintes s'annulent dans la membrane, causant une perte de raideur et la formation de plis.

Simulation numérique par éléments finis 3D

Nous avons réalisé des simulations à l'aide du programme éléments finis Evolver [34] qui permet de résoudre des problèmes statiques par minimisation de l'énergie potentielle. Ce programme prend en compte les grands déplacements, le chargement suiveur et le flambement local. Nous appliquons incrémentalement les chargements de gonflage puis le chargement extérieur. La méthode du gradient conjugué est utilisée pour minimiser l'énergie. Les fils qui relient la face supérieure et la face inférieure sont représentés par des éléments barre. La flèche du panneau obtenue numériquement est comparée aux résultats de la théorie linéarisée pour plusieurs géométries et pressions de gonflage. Un très bon accord a été obtenu entre les deux approches avec un écart

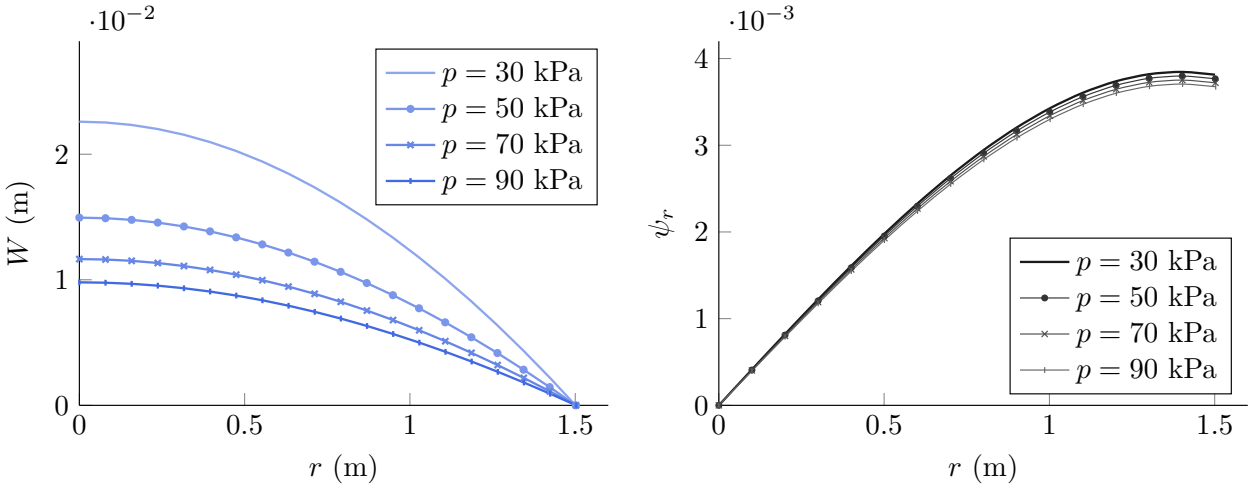

Figure 5: Déformée W et orientation des fibres ψ_r pour un panneau circulaire simplement appuyé et soumis à un chargement vertical de 100 Pa pour quatre pressions de gonflage p différentes. Avant d'être gonflé, le panneau a un rayon de 1,5 m et une épaisseur de 10 cm.

relatif moyen de 3 %. On observe une tendance : l'erreur relative sur la flèche augmente lorsque le panneau devient plus épais ou moins large, c'est-à-dire dans les cas où la non-linéarité de la raideur au cisaillement devient importante et met en défaut les hypothèses de petits déplacements. La non-linéarité de la simulation 3D est visible par l'aspect de la courbe effort–déplacement (Fig. 6), parfois même avant que la charge de plissage ne soit atteinte. Cependant, tant que les déplacements restent petits (de l'ordre de 3 % du rayon), la réponse est quasiment linéaire et en très bon accord avec la solution théorique linéarisée.

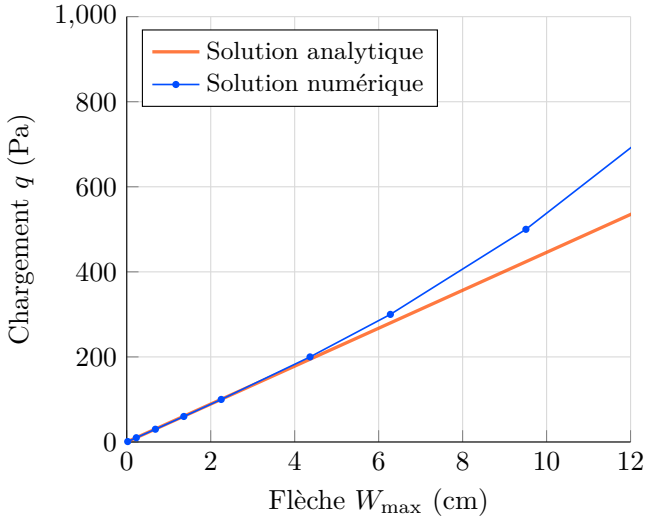

Figure 6: Courbes effort–déplacement issues de la simulation numérique et de la solution analytique pour un disque gonflable simplement appuyé et chargé verticalement. Le panneau fait 2 mètres de rayon et 10 centimètres d'épaisseur avant d'être gonflé à 90 kPa (0,9 bar).

Analyse modale

L'étude des vibrations des panneaux gonflables se fait également à partir de la théorie linéarisée. La démarche est la même que pour les vibrations de plaques de Reissner-Mindlin classiques. Le problème aux valeurs

propres est posé dans le formalisme tensoriel de façon intrinsèque. Il s'agit d'un système d'équations aux dérivées partielles qu'il faut découpler pour pouvoir résoudre. Après réécriture des équations, on parvient à exprimer le problème de flexion indépendamment des inconnues correspondant au cisaillement qui seront déterminées dans un second temps. On remarque que la forme des équations change en fonction de la fréquence à laquelle le système vibre, ce qui conduit à distinguer les modes de basses fréquences de ceux de hautes fréquences. En dernière analyse, la détermination des modes propres passe par la résolution de trois équations de Helmholtz découplées. Les conditions aux limites sont ensuite appliquées pour obtenir l'équation caractéristique. Les racines de cette équation permettent la détermination des fréquences propres et des longueurs d'onde du mode propre grâce aux relations de dispersion. La résolution est présentée pour des panneaux circulaires avec bords encastrés, simplement appuyés ou libres ainsi que pour des panneaux rectangulaires appuyés (Fig. 7). Les fréquences prédites sont comparées à celles d'un modèle simplifié. Nous avons également résolu le problème de vibrations axisymétriques par une méthode numérique pseudospectrale qui est présentée en annexe. Ces multiples validations nous permettent d'avoir confiance dans nos résultats théoriques mais ne dispensent pas de confronter le modèle à la réalité expérimentale.

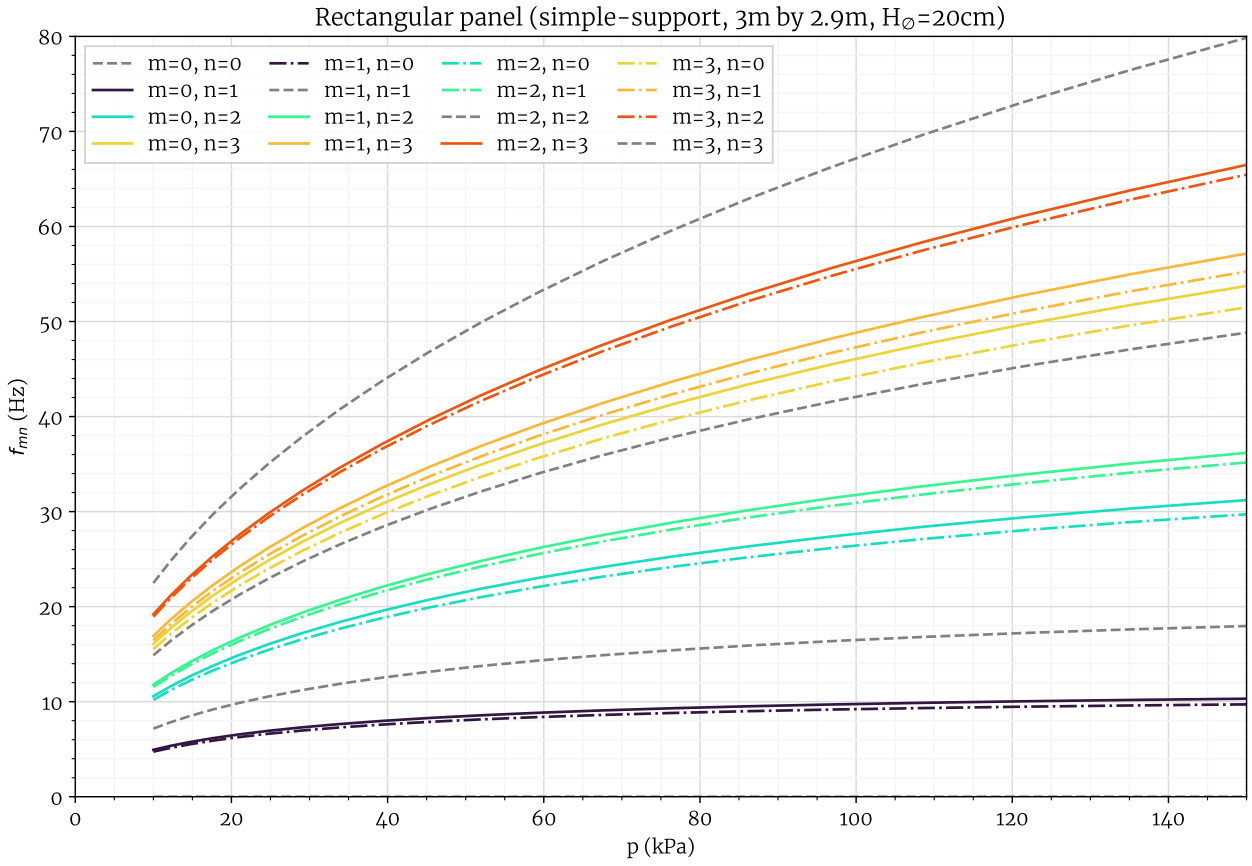

Figure 7: Fréquences propres d'un panneau rectangulaire simplement appuyé en fonction de la pression interne. Les entiers m et n indiquent le numéro du mode selon x et y. Dimensions initiales : 300 sur 290 sur 20 centimètres.

Expériences

Le problème du panneau circulaire en flexion sous chargement vertical a été étudié théoriquement et numériquement. Il convient à présent de confronter ces prédictions à la réalité physique. En amont des expériences, des

mesures de variations de géométrie des panneaux lors des phases de pressurisation ont permis d'identifier le module d'élasticité du matériau. Dans notre montage expérimental, une armature en métal permet de suspendre le panneau pour réaliser toutes sortes de conditions aux limites. Pour appliquer un chargement parfaitement uniforme sur toute la surface du panneau tout en maintenant le bord en appui simple, nous avons fabriqué une demi-sphère en tissu qui permet d'appliquer des chargements jusqu'à 200 Pa. Afin de supprimer l'influence du poids propre, le panneau a été maintenu à la verticale pendant toute la durée de l'expérience. La mesure a été faite à l'aide d'un capteur de déplacement placé sur un rail aligné avec un diamètre horizontal du panneau. Une attention particulière a été portée à la conservation de l'axisymétrie du problème et au parallélisme du panneau avec le rail de mesure sur lequel se déplaçait le capteur. L'objectif était de mesurer le profil de déplacement transverse du panneau sur un diamètre pour le comparer aux courbes théoriques de déplacement transverse. Les mesures présentées dans ce travail ont été faites pour plusieurs pressions internes et plusieurs chargement externes. Elles ont montré une comparaison théorie – expérience tout à fait satisfaisante, comme on peut le voir sur la Fig. 8. Une fois cette série de mesures terminée, des essais de vibrations ont été réalisés pour valider la théorie des vibrations. Ils ont été menés à l'aide d'un marteau d'impact pour générer le signal en entrée et la pose de quatre accéléromètres a permis de mesurer le mouvement en des points d'amplitude de vibration maximale. Les résultats de ces premières expériences montrent la possibilité d'identifier les fréquences de résonance mais des séries d'expériences complémentaires sont à prévoir pour parfaire la comparaison théorie – expérience, notamment par une estimation plus précise des propriétés matériaux.

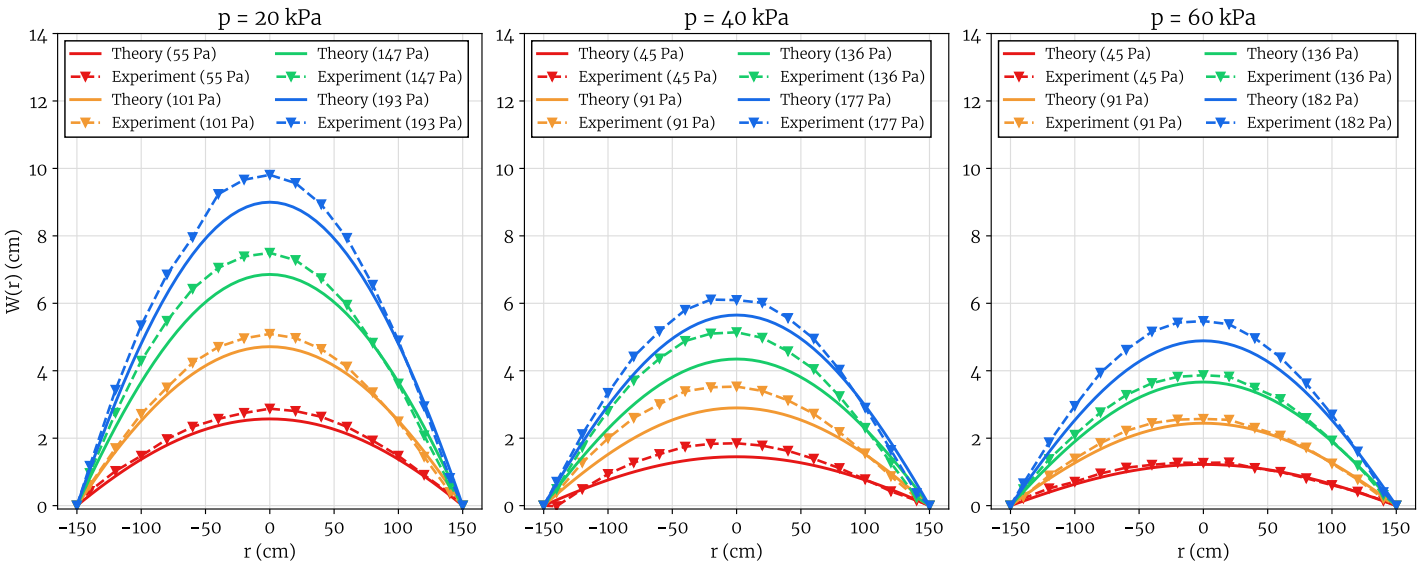

Figure 8: Comparaison des déplacements transverses expérimentaux et théoriques.

Conclusion

L'objectif de cette thèse était d'étudier les panneaux gonflables par trois approches complémentaires : analytique, numérique et expérimentale. Sur le volet analytique, un modèle de panneaux gonflables a été développé pour prendre en compte les effets de la pression interne et du cisaillement. Nous avons établi les équations non linéaires du mouvement à partir du principe des puissances virtuelles écrit en grandes transformations. Ces équations ont ensuite été linéarisées autour de la configuration de référence, ce qui a permis de résoudre le

problème de flexion d'un disque gonflable et de poser le problème aux valeurs propres pour l'étude des vibrations. Le système d'équations de Helmholtz a été résolu pour déterminer les modes et fréquences propres de panneaux circulaires (encastrés, appuyés ou libres) ou rectangulaires (simplement appuyés). Les fréquences propres ainsi déterminées sont très proches de celles obtenues par une méthode de résolution numérique approchée (pseudospectrale) et par des modèles physiques simplifiés. Dans le volet numérique, la méthode des éléments finis a été appliquée au panneau modélisé comme un assemblage de membranes et de fils en 3D afin d'obtenir une solution non linéaire du problème de flexion statique. Un très bon accord a été trouvé avec la solution linéaire. Enfin, dans le volet expérimental, nous avons réalisé une structure permettant de réaliser les conditions aux limites d'appui simple et d'appliquer un chargement uniforme afin de mesurer les déplacements transverses d'un panneau gonflable. Les résultats expérimentaux sont en accord avec la solution linéaire.

Perspectives

À l'issue de notre travail sur les panneaux gonflables, des pistes d'études restent à explorer pour maîtriser complètement la mécanique de ces structures très particulières. Les principales pistes sont :

- compléter les essais d'analyse modale réalisés dans cette étude en excitant la structure avec des signaux de type sinus balayé,
- prendre en compte l'orthotropie des membranes supérieure et inférieure,
- déterminer l'évolution des coefficients matériaux et du champ de déplacement lors du passage de la configuration naturelle (non gonflée) vers la configuration de référence, qui n'est actuellement décrite que par sa hauteur et ses dimensions caractéristiques (diamètre ou longueur des côtés),
- étudier le comportement post-plissage entre l'apparition du pli et la ruine globale de la structure par pliage,
- étudier l'influence des déformations différées dans le temps du fait du fluage et de la viscosité des membranes,
- création d'un élément fini plan de panneau gonflable pouvant être combiné avec l'élément tube gonflable pour le dimensionnement de structures porteuses entièrement gonflables.

Introduction

Generalities on pneumatic structures

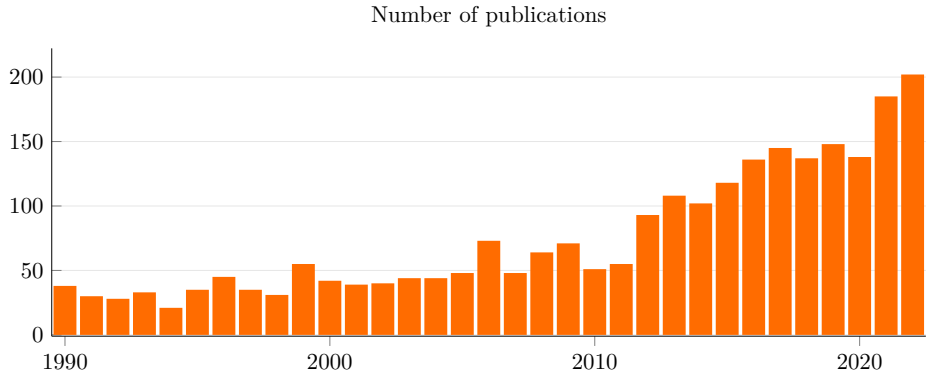

Figure 9: Interest in research on inflatable structures over the last decades shown by the number of publications in engineering containing the word "inflatable" (data from ScienceDirect).

Tensile membrane structures are in rapid development as evidenced by the efforts to guide the structural design of such structures in Europe [35]. The interest in pneumatic structures is growing over time, as illustrated by the number of papers and books published on this topic (Fig. 9). It is interesting not only for static inflatable buildings, but also to create mobile inflatable systems in the emerging field of soft robotics [36, 37].

The 60's and 70's were very prolific in terms of inflatable projects, culminating in the 1970 Osaka World Expo. On that occasion, several inflatable pavilions were proposed, including the American pavilion with an inflatable cover that later inspired many other stadiums and the well-known Fuji pavilion which is an impressive arch assembly (Fig. 10a). In parallel with the land-based inflatables, a number of applications were proposed for the conquest of space such as inflatable heat shields or reentry vehicles (Fig. 11a). Their main advantage is of course their light weight, which is vital for a structure that is launched into space using expensive rockets. In the 90's, due to the energy crisis, inflatable structures were less developed because large structures required a constant supply of air. More recent examples in aerospace applications include the deployable hangar that protects the Solar Impulse aircraft, Fig. 14 or the inflatable BEAM module that was installed on the International Space Station in 2016 (Fig. 11b). A more detailed history of the evolution of pneumatic structures can be found in the review of Chi and Pauletti [38].

The stiffness of a membrane structure is obtained by maintaining a bi-axial pre-tension state in the fabric. To this end, two techniques are commonly used. The first consists in stretching by means of mechanical elements such as cables and straps fixed to anchors. This is the vast majority of tension structures seen in architecture. The second technique is the use of a pressurized gas, generally air, to stretch the structure: this defines the family of *pneumatic structures* and it is the framework of this work. They have developed throughout the 20th century, especially with advances in materials such as the invention of nylon in 1938.

(a) Fuji Pavilion, Osaka 1970 World's fair.

(b) Medical tent for the International Committee of the Red Cross, supported by inflatable arches (© FlyPix)

Figure 10: Examples of inflatable buildings.

(a) Reentry vehicle.

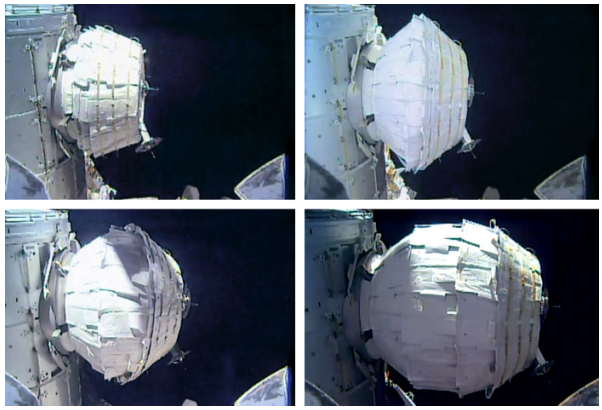

(b) Deployment of the BEAM inflatable module.

Figure 11: Inflatable structures for space exploration. (image credit: NASA)

Many different curved shapes can be obtained with inflatables. The family of pneumatic structures can be broken down into three subfamilies:

- single membrane structures, such as air halls or inflatable roofs,
- inflatable structures, such as inflatable beams, columns, cushions, panels or mattresses (Fig. 13a) and any assembly of these different structural elements,
- hybrid structures that combine different types of elements and are promising candidates for space exploration [39].

The most common structure is the mono-membrane cushion. They are made of plastic, generally ETFE (ethylene tetrafluoroethylene) or PTFE (polytetrafluoroethylene). Many temporary pneumatic structures take advantage of the qualities of this type of structure: light, easy to transport, easy to assemble and disassemble, with no significant impact on the ground. There are many single-membrane bubble structures that cover sports areas such as tennis courts or soccer fields on a temporary basis. They can also be installed permanently, as is the case with the inflatable cushions used to cover buildings such as the Allianz Arena in Munich (Fig. 12), the green house of the Aarhus Botanical Garden (Fig. 13b) or the Eden Project in England (Fig. 13c).

They are quite easy to manufacture nowadays thanks to the availability of laser cutting machines and pattern–making software that allow to preview the shapes after pressurization. More assembly techniques

Figure 12: Allianz Arena in Munich, Germany. (Wikimedia)

are now well mastered: the sewing of fabric strips, gluing, thermal welding or high frequency welding. With the first technique, a continuous air supply is required to compensate air leakage, which is not necessary when the structure is airtight. However, pressure regulation systems may be required in case of slight air leakage. With their minimal packed volume and their ease of repair, they can be reused a large number of times in a variety of environments and settings. They acquire load-bearing capacity from inflation alone, which makes them less material-consuming than standard tension structures that require external stiffeners. The inflation level may also be modified to achieve the desired stiffness, which is a rare property for a structure to have.

The main disadvantage of inflatable structures is the risk of deflation due to puncture or loss of airtightness, which can inspire distrust. The safety of pneumatic structures are addressed in current research, for instance the safe evacuation of collapsing inflatable buildings [40]. Nonetheless, even after failure, their integrity can be restored with simple and inexpensive repairs (patches), which considerably increases their durability. Also, the design of complex inflatable structures can be complicated: the shapes that compose the structure are cut from flat surfaces of fabric, which when inflated will acquire curvature. This poses several challenges that pave the way to active areas of research such as form-finding and optimization of the stretched structure or optimization of the cutting pattern and position of the seams to match a target shape [41].

Tensile fabric structures generally have opposing principal curvatures, and as such they belong to the *anticlastic* surfaces family (Fig. 15). On the other hand, inflatable structures naturally have *synclastic* curvature (principal curvatures of the same sign), as can be seen with airbags; or single curvature (*monoclastic*), which is the case of inflatable tubes. Ideally, one would want to have flat surfaces that also have the qualities of inflatable structures, i.e. being inexpensive and easily transportable: this is made possible by the inflatable panel technology.

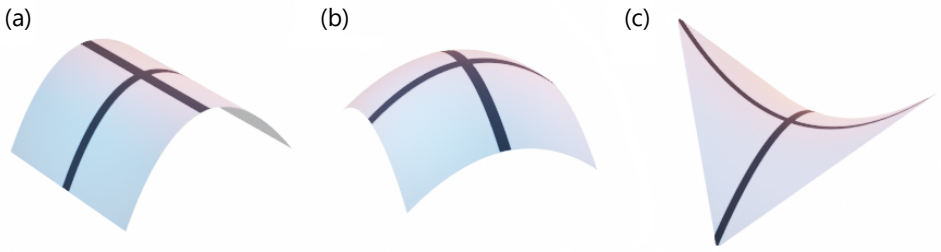

Figure 15: Monoclastic (a), synclastic (b) and anticlastic (c) surfaces.

(a) Inflatable building with mattress walls.

(b) Green house (Aarhus Botanical Garden, Danemark).

(c) Eden Project greenhouse complex in England (picture by Jürgen Matern).

Figure 13: Examples of temporary and permanent inflatable buildings.

Figure 14: Movable hangar for the Solar Impulse aircraft. (Wikimedia)

We have seen that pneumatic structures are in rapid expansion in architecture and other fields of engineering. Public and private research are motivated by the need to produce reusable, less material-intensive structures in keeping with ecological challenges of our century, as well as transporting and deploying structures that are required in remote locations for short periods of time (shelter, tent, hospital, bridge). At a larger scale, pneumatic structures are ideal candidates for space exploration: inflatable habitats have low mass-to-volume ratio which makes them competitively priced, since launching a kilogram into space still costs around $10,000 as of today.

Drop-stitch fabric

When a membrane is allowed to expand without constraints, the surface presents a familiar synclastic curvature. While this rounded aesthetic can be desirable, some applications require zero curvature inflatable elements, for instance to improve aerodynamic performance or to create usable storage surfaces. This is where inflatable panels come into play: the inflated thickness of drop-stitch panels is set by the length of the high-strength threads that connect the upper and lower membranes, and the panel is finally sealed by lateral walls to make it airtight. This type of structure is known as "drop-stitch", "double-wall fabric" or historically "Airmat" (for "air mattress"). The flexible fibers can be called "drop cords" or "drop yarns" and can be seen in Fig. 16. The fabric is usually coated with PVC, made flame retardant and resistant to UV. To this day,

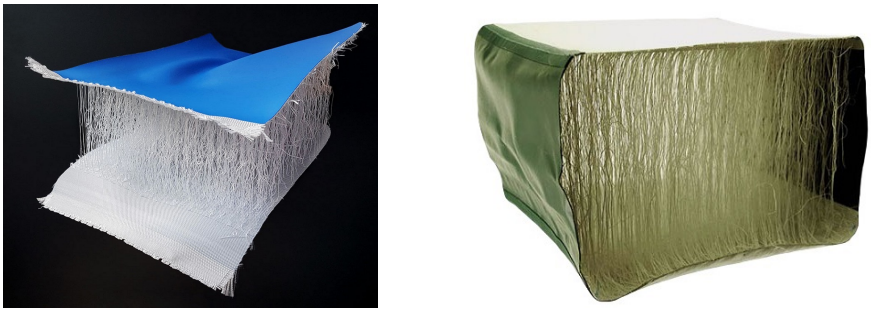

Figure 16: Cut-views of double-wall fabric with drop cords (drop-stitch).

the production of inflatable panels is partly directed towards leisure, with sports equipment such as inflatable gymnastics mats, stand up paddles (Fig. 17a), floating platforms for boat maintenance (Fig. 17b) and floating platforms to operate on water (Fig. 18). The US army experimented with air-supported tents [42] and a report of the Goodyear Aerospace Company from 1972 investigated the "technical feasibility of an expandable floating base" [43]. Other potential applications involve inflatable movie screens or inflatable plane wings. There are also patents for inflatable wings, antennas, dams and rescue boards [44].

(a) Stand up paddle (© Décathlon)

(b) Inflatable dock (© Solstice)

Figure 17: Floating platforms for leisure.

In the field of construction, some structures are already composed of inflatable elements similar to beams, such as tubes or arches (Fig. 10b), and a theory of inflatable panels will naturally find its place among the design tools available to engineers. Indeed, the classical theories of strength of materials are not suitable for the study of pressurized structures since they ignore the influence of the internal pressure. Therefore, research has been conducted to develop a new theory adapted to these structures. Once the theories of inflatable beams

Figure 18: Floating decontamination platform, an example of real-world application of the buoyancy of inflatable panels. (© Écocréation)

and panels are well mastered, it will be possible to design fully inflatable load-bearing structures of complex shapes.

Outline of this study

In this thesis, we study inflatable panels by analytical, numerical and experimental approaches. It is structured as follows:

- From a theoretical perspective, we develop an inflatable panel model that will incorporate the Mindlin–Reissner kinematics to allow shear deformation. As observed with inflatable beams, the internal pressure plays a critical role in the load-bearing capacity of the structure, which is why the mechanical response cannot be predicted correctly without incorporating pressure terms in the governing equations of inflatable panels. To take this fact into account, the formulation will be done in large deformations, large displacements and large rotations and we choose to derive the governing equations using the principle of virtual power, a simple and systematic method which yields a system of nonlinear equations containing all the pressure terms required for a theory of inflatable panels. All the equations will be given in the tensor form rather than in a particular coordinate system.
- Then, the usual case where the inflatable panel undergoes small displacements and rotations is addressed. The nonlinear equations are linearized around the inflated configuration, with special emphasis on the treatment of the terms relating to the inflating pressure and the other external loads.
- The linear solution to the static bending problem of a simply-supported inflatable disk with uniform vertical load is proposed along with its limit of validity due to the onset of wrinkling.
- In the numerical part, the finite element method is applied to an inflatable panel modeled as a 3D assembly of membranes and wires to obtain a nonlinear solution of the bending problem. These numerical results are compared to the analytical solution for a variety of geometries and inflation pressures.
- The dynamics of inflatable panels are also investigated through modal analysis. The eigenvalue problem is established from the linearized equations of motion and the partial differential equations describing the eigenmodes are derived in tensor form. The natural frequencies of rectangular and circular panels are determined analytically and confirmed both by approximate numerical solutions and simplified models.

- Finally, the above-found theoretical and numerical results are confronted to reality. An experimental setup is built to hold an inflatable disk of 3 meters in diameter on simple-support and apply a uniform load before measuring its transverse displacements. The analysis of vibrations is also explored using impact hammer tests to determine resonance frequencies.

Chapter 1

Bibliography

To understand the state of research in inflatable components, one needs to know the history of their development. We divide inflatable elements into three categories:

- one-dimensional, beam-like elements (tubes, columns, arches)
- two-dimensional, plate-like elements (mattresses, arrays of cylindrical tubes, panels)
- inflatable shells (whose mid-surface is not flat in the reference configuration)

This review of literature focuses on inflatable beams and panels, and shells will be mentioned as a perspective for future work. To set the context for the study of dynamics, some works on the vibrations of Mindlin–Reissner plates will also be presented.

1.1 Inflatable tubes and panels

1.1.1 Inflatable beams

One of the simplest pneumatic structures is the inflatable beam, which is a pressurized tubular membrane whose bearing capacity is entirely due to internal pressure. Whether they are a straight (column, mast) or curved (arch), they can be described using one-dimensional beam theories, while the geometry of membranes and panels require two dimensions and are therefore more complex.

To begin with, Wood [45] and Reissner [46] independently published in 1958 and 1959 two studies on the flexure of a cylindrical shell with internal pressure. However, they did not focus on fabric tubes specifically. The very first analytical work dedicated entirely to pressurized tubes made out of fabric was carried out by Comer and Levy [1] in 1963. They investigated the load-deflection relationship of a cantilever inflatable beam with tip load and determined the collapse load. Later, in 1982, Webber [2] extended Comer and Levy's theory by combining a torque and a vertical load at the end of the cantilever tube, inducing bending and twisting, and successfully determined the deflection, as well as the wrinkling and collapse loads. He also performed experiments with relatively low pressures by today's standards: less than 0.2 bar (20 kPa). Afterwards, Main et al. improved Comer and Levy's theory of pressurized membrane tubes by considering the orthotropic property of the fabric and the effect of the biaxial stress state on the wrinkling [3, 47]. It is one of the first works on this period to model the fabric as an orthotropic membrane. Experiments were conducted on pressurized tubes with circular cross-sections and the obtained results were compared with those of Comer and Levy's theory.

The theories mentioned so far share a common flaw: they adopted the Euler-Bernoulli kinematics, where the cross-sections remain perpendicular to the neutral axis, which makes it impossible for the inflation pressure to be correctly included in the equations since it is related to shear flexibility, which is ignored by this kinematics.

Other works, namely NASA technical reports, were based on the Timoshenko beam theory and accounted for the influence of pressurization on shear stiffness as early as 1966, with Fichter [4] and Steeves [5] (1975) who both used the principle of minimum potential energy principle to derive inflatable beam equations. In Fichter's analytical solutions, the pressure term is being added directly to the material stiffness term, thus increasing the overall resistance of the structure. Steeves proposed solutions using Green functions, performed bending and twisting experiments (Fig. 1.1), measured the wrinkling load [48] and also developed a finite element [49] and wrote a technical report on the optimal design of pressure stabilized beams [50].

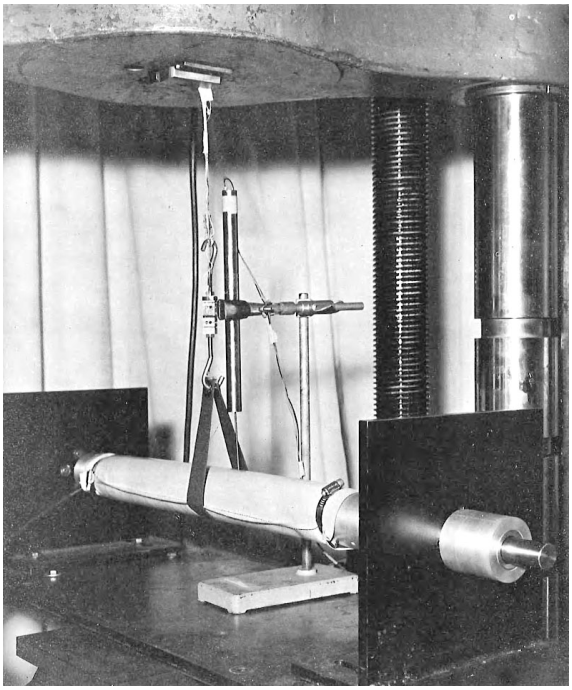

Figure 1.1: Bending testing apparatus used in Steeves' experiments [48].

At the beginning of the 21st century, Wielgosz and Thomas [17] derived equations for inflatable beams and drop-stitch panels seen as beams using Timoshenko's assumptions. Their analytical expressions and experimental results confirmed Fichter's findings (deflection and collapse load). They also proposed a finite element and performed experiments with inflation pressures as high as 300 kPa (3 bar), Fig. 1.2. One of their conclusions is that the overall deflection of an inflatable panel is the simple addition of the bending deflection caused by the membranes' compliance and the shear deflection permitted by the yarns. A finite element was also developed [51]. Soon after, in 2005, Le van and Wielgosz [7] improved Fichter's theory by using the virtual power principle in the context of the total Lagrangian formulation. They studied the wrinkling, buckling and collapse of inflatable beams. Suhey et al. [52] from the University of Florida carried out numerical computations on anisotropic pressurized membrane tubes by means of membrane finite elements and validated it by comparing their numerical results with the theoretical results of Main et al. [3, 47]. Their application system was an inflatable open-ocean aquaculture cage.

Up until now, the membranes had been assumed to have the elastic properties of an idealized isotropic material. Continuing the research at the university of Nantes, Z. Jiang incorporated orthotropic properties into the study of vibrations of inflatable tubes by performing experiments and developing a new finite element

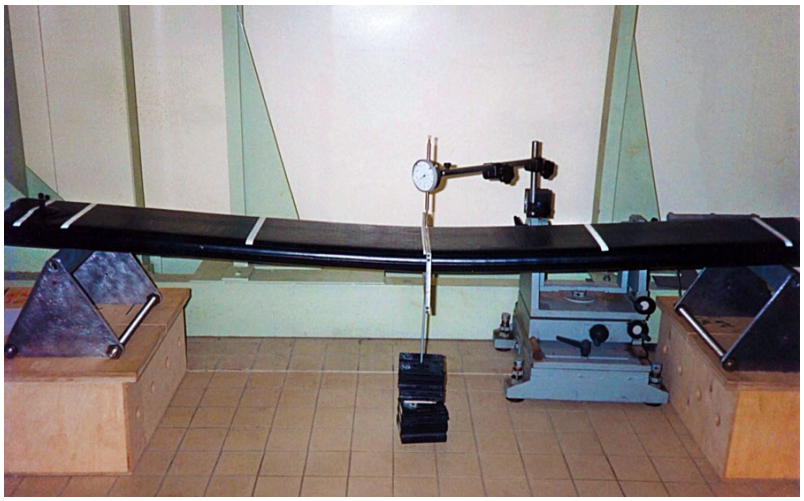

Figure 1.2: Three points bending tests on a slender inflatable panel performed by Wielgosz in 2005 at the University of Nantes (France).

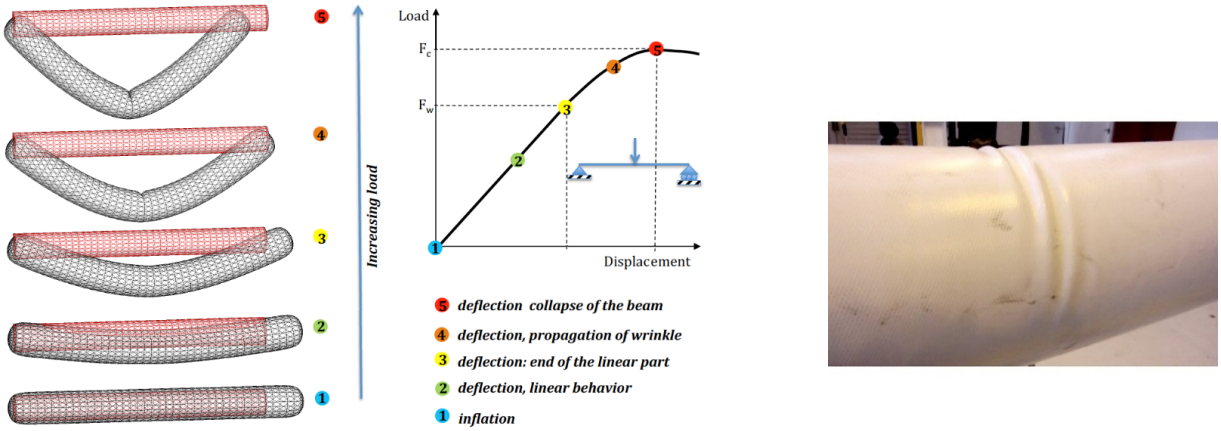

Figure 1.3: The five stages of behavior of inflatable beam from inflation to failure exemplified with three-point bending and picture of a wrinkled inflatable tube.

based on the recently enhanced theories with its stiffness and mass matrices [53, 54, 55]. Apedo extended these theories in his thesis [56] (2009) by adding orthotropy and buckling loads of beam-columns. At the same laboratory, the thesis that followed by T. T. Nguyen built upon Apedo's theory of pressurized membrane tubes with large displacements, small rotations and orthotropic directions of the material oriented along the axes of the tube [57, 58, 59]. Their initial formulation was three-dimensional but the equations were linearized in 2D to treat bending and buckling problems. In 2013, the important problem of accounting for the change in material properties between the natural and inflated configurations is addressed by solving the associated linear elasticity equations [60] and the analytical predictions are in very good accordance with finite element simulations. These results were included in Q. T. Nguyen's dissertation and second paper [8, 61] where he studied the inflation stage, bending and buckling and also perfected previous theories by taking into account the orthotropic nature of the fabric with arbitrarily oriented orthotropy basis [62]. Some works on the failure mechanisms and reliability of inflatable structures were undertaken around 2015 with A. Bloch's thesis [63] followed by a conference [64] on the limit states of an inflatable beam, Fig. 1.3. He also studied the post-wrinkling response of inflatable tubes and performed wind-tunnel experiments on inflatable beams and arches to measure drag. Two years later, Thomas and Schoefs [65] also presented a sensitivity analysis.

Now that inflatable beams theories are well-established, inflatable plate theory is the logical continuation

and thus worth investigating. While the technology of inflatable panels is not new, there are few studies dedicated to them and it is becoming an important issue to model them correctly.

1.1.2 Inflatable panels

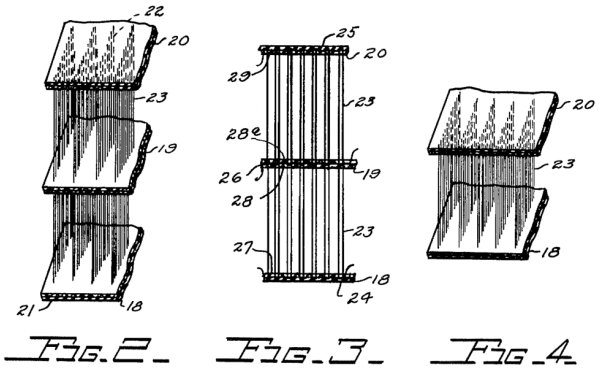

Figure 1.4: Drawings found in the first inflatable mattress patent [66].

If the pressurized membrane structure has two skins that are flat and parallel and one of the dimensions is small compared to the two others, then the pressurized structure can be considered as an inflatable plate. This is the case when the number of cords in the drop-stitch fabric becomes large enough to maintain the two connected membranes at a fixed distance determined by the length of the threads. It is a rare example of air-supported structure that does not involve a double curvature.

In the history of inflatable structures research, pressurized panels predated the study of tubes. After a promising start in the 1950s when the "Airmat" technology was introduced, the research on inflatable panels went through a period of decline in the 1970s only to be resumed at the beginning of the 20th century. In the mean time, the interest in inflatable beams research had remained constant, as their comprehension would help gain a better understanding of the fundamental principles that govern inflatable structures and thus represented the first step towards the greater scientific challenges associated with panel theories.

The first occurrence of inflatable panels as we know them today is a patent by E. D. Barker in 1951 [66]. It describes an "inflatable mattress especially adapted to military use, although capable of general employment". One of its original designs contained a rubberized inner sheet that materialized the middle surface of the panel.

In the 1950s, the Goodyear Aircraft Corporation developed a pressurized double-wall fabric with interconnected faces which they called *Airmat*; and in 1956, the first prototype of the Goodyear Inflatoplane was produced using this technology [67]. Although most panels applications require them to be airtight, the aircraft's inflatable parts received continuous pressure supply: the engineers used the air that came out of the motor to keep the structure inflated even in the event of holes or tears in the membranes. They stopped the production in 1962 after unsuccessful tests by the U.S. military.

Even though this attempt was short-lived, the technology was still of interest at NASA. Their potential use as reentry vehicles or heat shields lead them to write a first report in 1960, followed by technical reports and publications in 1961. An example of reentry vehicle made of inflatable tubes and panels is drawn in their paper and reproduced here in Fig. 1.5. The first paper, "Structural considerations of inflatable reentry vehicles" by Robert W. Leonard, Brooks and McComb [9], presented a small-deflection theory in Cartesian coordinates with elastic orthotropic membranes. The equations are derived from the principle of minimum potential energy. They already noticed that their equations were similar to the then recent Mindlin plate theory (1951), but

where the pressurization pre-stress replaces the transverse shear stiffness modulus of a classical plate. One year later, McComb [10] formulated a nonlinear theory with the principle of minimum potential energy and included the effects of a small linear taper. He found solutions in the form of Fourier series for the simply supported and clamped rectangular plates of constant thickness. This theory cannot be applied to circular panels and some terms are missing because of early linearization. These theories were simultaneously validated ex-

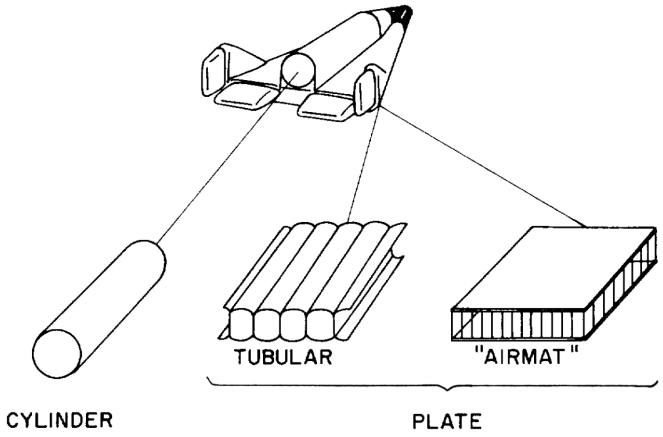

Figure 1.5: Inflatable component categories first defined by R. W. Leonard in 1960 [9].

perimentally by Stroud [12] (still at NASA). A square test specimen with sides 11 cm was made from two layers of woven nylons. The drop cords were also made out of nylon but they did not specify how closely spaced they were. The small panel was attached to the top of a loading tank to apply a uniform pressure loading. The simple-support is achieved by clamping a thin membrane connected to the boundary of the specimen. For clamped boundary-conditions, a wooden frame was used to immobilize the edge of the airmat. They tried to permit "a free buildup of inplane stresses" due to inflation, that is, they took care to allow the panel to expand from its natural shape to its inflated one without constraints. Nevertheless, given the small size of the panel, the boundary effects must have been important. The tank and the deflection measuring apparatus can be seen in Fig. 1.6. Even though the dimension of the valve was not negligible and the edges were very rounded, they managed to get concluding results. They showed that for high-frequency modes of vibrations, the shear deformation predominates.

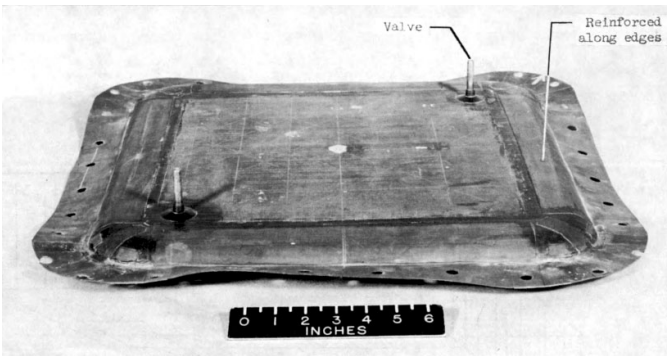

(a) Test specimen.

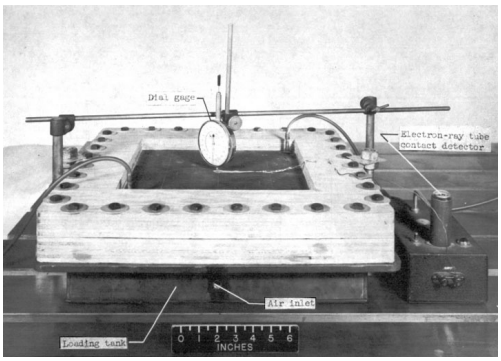

(b) Deflection-measuring apparatus.

Figure 1.6: Experimental setup of Stroud for measuring the static deflection of a small inflatable panel in clamped boundary conditions [12].

McComb and R. W. Leonard published a small article [11] where they explore the possibility of slanting the drop cords to increase the transverse shear stiffness. The cords run at an angle with the normal to the

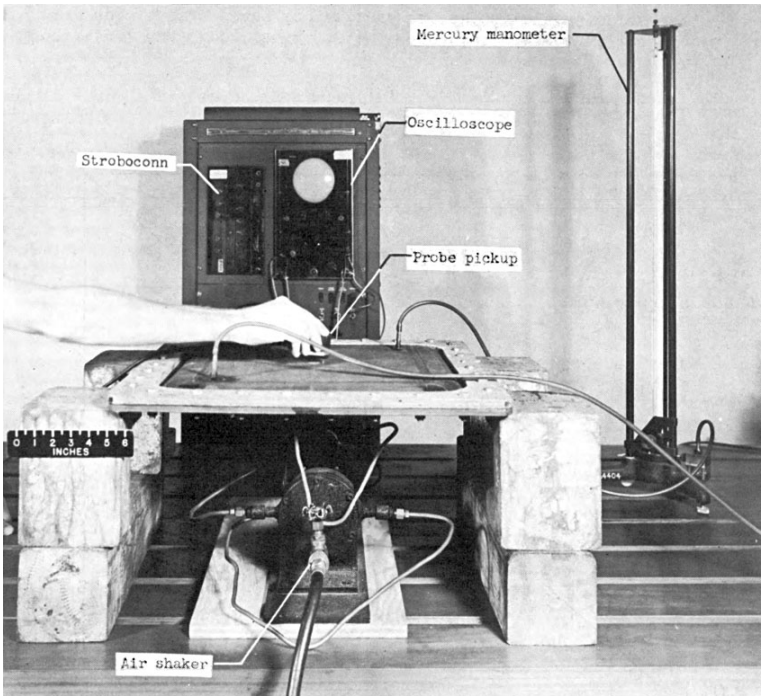

Figure 1.7: Experimental setup of Stroud to measure the natural frequencies of an Airmat sample in 1961 [12].

middle surface in the length direction. Two adjacent cords draw a "V" shape (⋁) that is complemented by a second set of threads on the opposite membrane, creating an "XX" pattern (⋁⋀) as can be seen in Fig. 1.8. As a rule of thumb, they advise to slant the cords by an angle θ such that the maximum shear force in the

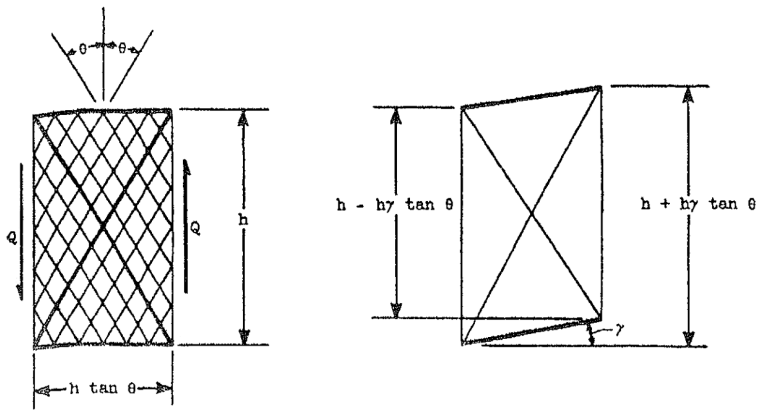

Figure 1.8: Slanted drop cords as drawn in McComb and R. W. Leonard's paper [11].

panel is always smaller than $pH \tan\theta$ where p denotes the inflation pressure and H the panel thickness. But one should also be careful not to make the angle too large or the bending moment may exceed the collapse moment $M_{\text{collapse}} = \frac{pH^2}{2}(1 - \tan^2\theta)$. This formula indicates that the collapse moment becomes negative for $\theta > 45°$, meaning that the pressurization alone would cause the collapse of the panel. Another factor to be considered is the increase of mass due to the longer and more numerous cords. The total weight of drop cords material increases by a factor $2/\cos^2\theta$, meaning that their mass will be 2 to 4 times larger than when they are not slanted, for a comparable increase in shearing stiffness. The additional weight can be easily compensated by reducing the width of the panel or removing stiffeners that are rendered useless by the increased stiffness.

In 1962, Haight wrote his Master's thesis [13]. His work is based on Leonard and McComb's findings. The deflection of a simply-supported rectangular panel is found in the form of Fourier series. He also approxi-

mated the non-linear solution in large displacements for a uniformly loaded circular panels as a power series. This result was published in 1969 but without the calculations presented in his thesis [14].

In the dissertation of D. D. Seath completed in 1963 [68], the author conducts an experimental investigation of the vibrations of an inflatable wing model constructed by the Goodyear Aircraft Corporation. He explains that the curved edges of the wing model are not accounted for in McComb's model [10], and thus the experimental natural frequencies may not be in good agreement with the theory, insofar as the total stiffness of the panel is underestimated at lower pressures. This document cites many relevant articles and proceedings that, unfortunately, could not be retrieved nowadays.

Kyser [15] analyzed the behavior of an inflatable cylindrical tube with two flat sides in an array of identical parallel tubes connected to each other, Fig. 1.9. Such structures are lighter and easier to fold than drop-stitch structures with closely-spaced drop cords. A review of other works published before 1965 can be found in Habip's 1965 literature survey [69]. Near the end of the 20th century, the research on drop-stitch panels was continued by Kawabata and Ishii [16]. Their paper discusses the effective stiffness of drop-stitch panels when the drop yarns density is low, allowing periodic bulges to form on the top and bottom surfaces (Fig. 1.9). The dissertation of Kawabata, "Study on Structural Characteristics of Double-Wall Air-Inflated Membrane Structures", also deals with form-finding and "air beams" (inflatable tubes). It is interesting to note that the tubular inflatable panel is currently a popular design choice for reentry vehicles [70, 71] in the space industry.

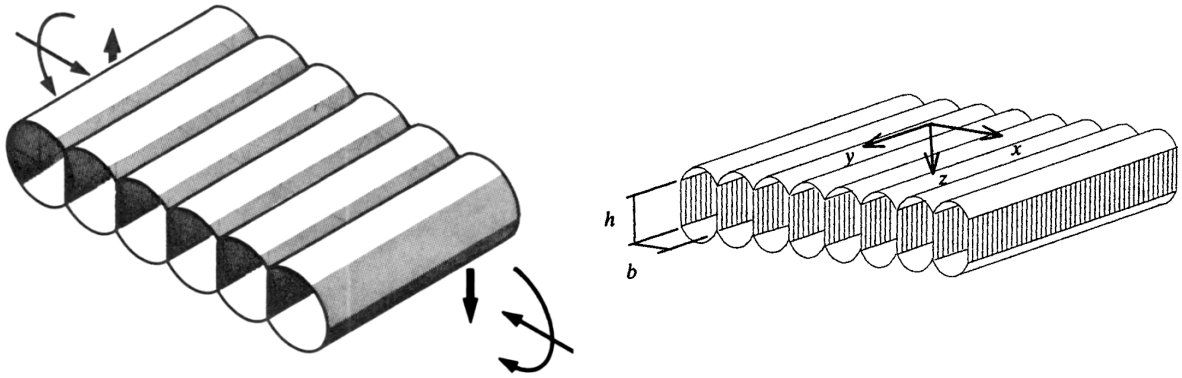

Figure 1.9: Tubular panel designs investigated by Kyser and Kawabata [15, 16].

In the 21st century, Wielgosz and Thomas [17] and Cavallaro [18] took another look at the deflection of inflatable panels by modelling them as inflatable beams. Wielgosz and Thomas [51] also built an inflatable finite element dedicated to inflatable panels, once again modeled using inflatable beam theory.

Since the beginning of our study (in 2019), several studies were conducted at the University of Rhode Island to experimentally determine material parameters and perform finite element simulations [72, 73, 74].

In 2008, Davids et al. [20] first proposed a nonlinear beam-type finite element and theorizes how to simulate post-wrinkling during isobaric transformations. Beyond wrinkling, they assumed that the bending neutral axis would move down when the curvature increases, and vice versa. All of these complex phenomena were implemented in their in-house Matlab code. In 2021, they continued to consider 1D models but for an inflatable panel with small width compared to its length [19] and conducted experimental and computational studies while including the orthotropic behavior of the membranes, the coupling between shear and moment and the presence of rounded panel edges for which they provide a mathematical parametrization. They simulated the nonlinear (softening / stiffening) post-wrinkling response numerically by adapting the code they had previously worked on.

1.1.3 Inflatable shells

Although shell theories are not discussed in this work, they are a logical continuation to plate theories. Hence, we will briefly summarize some works to help guiding future research on inflatable components.

John W. Leonard[1] wrote his thesis on inflatable shells of revolution [21] made of isotropic materials during their pressurization phase and in-service phase. Soon after, he published three articles concerning the pressurization phase [22] and the in-service phase [23], which were already addressed in his dissertation, and extends his results to nonsymmetric in-service loads [24]. For the first article on the inflation stage, he presents his general theory and solves the equations on the particular problem of a spherical membrane using perturbation theory. He finds that material non-linearities have a lesser effect than geometric non-linearities (large displacements). Later, in 1973, he co-authored an article with C. T. Li on the finite element analysis of inflatable shells [25], followed by a state of the art in inflatable shell research in 1974 [26].

1.2 Vibrations of Mindlin–Reissner plates

Since shear deformations are seen to be non-negligible from experiments on inflatable components, the load-deflection behavior of inflatable beams and panels can only be described accurately by theories where kinematics account for the existence of shear effects. When the first articles on inflatable panels were published, the Mindlin–Reissner theory of plates with transverse shear deformation had been worked out for only a decade: it was the state of the art and not the widely adopted theory that we know today. It will be seen in Chapter 3 that the eigenvalue problem of inflatable panels is identical to that of the theory of classical plates with transverse shear up to a change in the material coefficients, and so the methods to solve the vibration problem of inflatable panels are the same as for such plates.

While the theory of thin plates was established in 1888 by Love when he published "On the small free vibrations and deformations of elastic shells" based on the assumptions of Kirchhoff, it took another 60 years for the so-called "theory of thick plates" to emerge. Eric Reissner published two articles in 1945 and 1947 [75, 76] where he investigated the effects of transverse shear deformation on the bending of plates for the first time. In his time, researchers highlighted the appearance of a third boundary condition rather than the two of classical (thin) plate theory. A few years later, in 1951, driven by his research on piezoelectric plates at Columbia University, Raymond D. Mindlin built a theory upon Reissner's work [27]. In order to overcome the restrictions of the Love-Kirchhoff theory where the material segments always remain perpendicular to the mid-surface, which forbade the existence of shear, he introduced a compatibility equation that relates the vertical deflection gradient and the angles by which the fibers rotate. He compared the flexural and shear wave velocities predicted by the classical plate theory, an exact 3-dimensional solution and his plate theory with and without including the rotatory inertia correction or the shear correction. He also showed that the eigenvalue problem amounts to solve three Helmholtz equations, but does not proceed to solve them. While this article dealt exclusively with isotropic plates, another paper published the same year dealt with crystal plates where the elastic properties of the material had monoclinic symmetry [77]. In subsequent papers and technical reports, Mindlin and Deresiewicz addressed the vibrations of circular [28, 29] and rectangular plates [30].

Although it was not mentioned in the founding 1951 paper, Mindlin and Deresiewicz point out in their technical reports that two coefficients in the eigenvalue problem can either be real or imaginary depending on the frequency [28, 29]. Indeed, the natural shapes will change depending on whether the exciting frequency

[1] John W. Leonard (University of Illinois) should not be confused with the previously mentioned Robert W. Leonard who worked at the NASA Langley Research Center with McComb.

is below or above a given value named the *cutoff frequency* [2] which marks the transition for low-frequency vibrations to high-frequency vibrations, as is the case in Timoshenko beam theory [78]. It is undoubtedly related to the introduction of shear deformations into the model, given that the cutoff frequency is the lowest frequency of thickness-shear oscillations. If one were to try solving the Mindlin–Reissner's equations of plates at the cutoff frequency, it appears that the system of differential equations degenerates and further work is needed. This special case was addressed by Chao and Pao [79]. After deriving the governing equations for the flexural motions of plates at the cutoff frequency in Cartesian coordinates, they considered the reflection of flexural waves at the plate's edge with oblique or normal incidence, but did not calculate the natural bending mode shapes.

Irie et al. generalize the results of Mindlin and Deresiewicz on the vibrations of circular plates to the three commonly encountered boundary condition types: clamped, simply-supported and free [31].

At this point, a confusion persisted as to what the proper definition of the simple-support should be. Some authors claimed that the moment should vanish, while others cancelled the rotation of the material segment on the edge. After publishing a literature survey on thick plate vibrations in 1995 [32], Liew introduces the helpful distinction between the "soft type", which is the usual case where the border is free of loads, and the "hard type" simple-support which forbids rotations in the plane tangent to the edge [80]. The soft type states the moments should be zero at the edge, which is the first idea that comes to mind since no external forces are applied, while the hard type enforces the rotation to be zero. In some problems such as the vibrations of a rectangular panel, solutions exist with hard type simple support but not with the soft type.

In their 2005 article, Hashemi and Arsanjani [33] provide the exact characteristic equations and the eigenmodes shapes for all rectangular panels where two opposite sides are simply-supported in both low and high frequency domains.

1.3 Conclusion

Much research has been dedicated to inflatable tubes to the detriment of inflatable panels. For a long time their growth was limited due to insufficient material performances, which can now be overcome. To meet the currents needs of the industry, a modern and unified theory is required to synthesize previous works on inflatable panels. After the theory is established, we shall perform 3D nonlinear simulations of inflatable panels and conduct experiments to validate the analytical results, giving us a global understanding of this technology. Although the plate theory with shear effects is widely considered as a well-known and well-tried tool among models used in engineering, the resolution of the associated eigenvalue problem contains subtleties that deserve special attention and precautions. We will generalize the previous works to the tensor framework to carry out the modal analysis of rectangular and circular inflatable panels.

[2] Note that the so-called "cutoff frequency" in the context of the vibration of thick plates is unrelated to the frequency at which a reduction of amplitude is observed in filters or damped systems.

Chapter 2

Nonlinear theory of inflatable panels

2.1 Geometry and kinematics

Some essential definitions and properties of tensor vector calculus in curvilinear coordinates are recalled here. Let $(\boldsymbol{g}_1, \boldsymbol{g}_2, \boldsymbol{g}_3)$ be a basis of a three-dimensional Euclidean space, without any further assumptions. The *contravariant* components of a vector $\boldsymbol{u}$ in this basis, denoted u^i, are such that

$$\boldsymbol{u} = \sum_{i=1}^{3} u^i \boldsymbol{g}_i$$

which will be written using the Einstein summation convention over repeated indices to write $\boldsymbol{u} = u^i \boldsymbol{g}_i$. The *covariant* components u_i of a vector $\boldsymbol{u}$ are such that

$$u_i = \boldsymbol{u} \cdot \boldsymbol{g}_i$$

The coefficients $g_{ij} \equiv \boldsymbol{g}_i \cdot \boldsymbol{g}_j$ define a symmetric matrix $[g_{..}]$ which can be inverted to find another symmetric matrix $[g^{\cdot\cdot}]$ whose coefficients are denoted g^{ij}. The *dual basis* is defined by

$$\boldsymbol{g}^j = g^{ij} \boldsymbol{g}_i$$

A relationship exists between covariant and contravariant components:

$$u_i = u^j g_{ij} \quad \text{and} \quad u^i = u_j g^{ij}$$

which is a consequence of the above definitions:

$$u_i = \boldsymbol{u} \cdot \boldsymbol{g}_i = u^j \boldsymbol{g}_j \cdot \boldsymbol{g}_i = u^j g_{ji}$$

$$u^i = \boldsymbol{u} \cdot \boldsymbol{g}^i = u_j \boldsymbol{g}^j \cdot \boldsymbol{g}^i = u_j g^{ji}$$

The dot product of two vectors $\boldsymbol{u}$ and $\boldsymbol{v}$ can be computed using any of the following expressions:

$$\boldsymbol{u} \cdot \boldsymbol{v} = u^i v_i = u_i v^i = g_{ij} u^j v^i = g^{ij} u_j v_i$$

Note that, by construction, the vectors of the primal and dual bases are orthogonal:

$$\boldsymbol{g}_i \cdot \boldsymbol{g}^j = \delta_i^j$$

where $\delta_i^j = \delta_j^i = \delta_{ij}$ is the Kronecker symbol. It is often useful to decompose a vector $\boldsymbol{u}$ in the primal or dual basis: from the definitions of covariant and contravariant components,

$$\boldsymbol{u} = (\boldsymbol{u} \cdot \boldsymbol{g}^k)\boldsymbol{g}_k = u^k \boldsymbol{g}_k$$

and

$$\boldsymbol{u} = (\boldsymbol{u} \cdot \boldsymbol{g}_k)\boldsymbol{g}^k = u_k \boldsymbol{g}^k$$

These relations are presented graphically in Fig. 2.1.

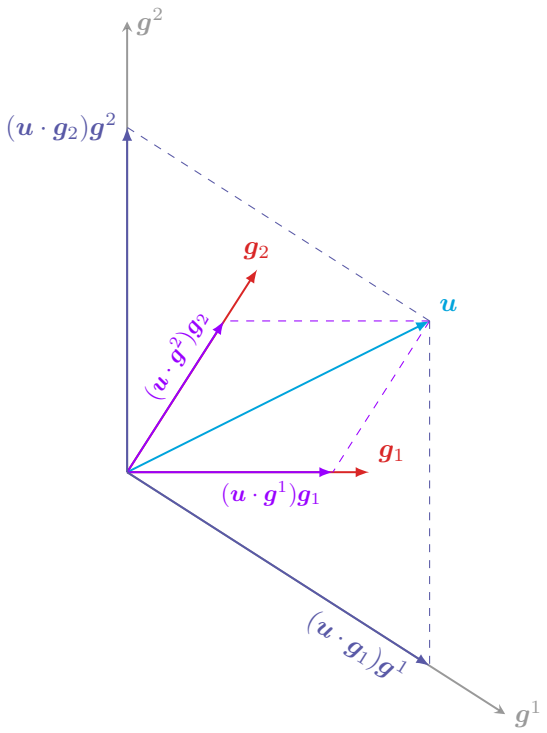

Figure 2.1: Components of a vector in primal and dual bases.

The cross product of two basis vectors is computed as follows:

$$\boldsymbol{g}_i \times \boldsymbol{g}_j = \sqrt{g}\epsilon_{ijk}\boldsymbol{g}^k$$

$$\boldsymbol{g}^i \times \boldsymbol{g}^j = \frac{\epsilon_{ijk}}{\sqrt{g}}\boldsymbol{g}_k$$

where g is the determinant of the matrix $[g_{..}]$ and ϵ_{ijk} is the Levi-Civita symbol.

2.1.1 Reference position of the plate

The kinematics of the panel is described in a three-dimensional Euclidean space endowed with an orthonormal coordinate system $(\mathrm{O}; \boldsymbol{e}_1, \boldsymbol{e}_2, \boldsymbol{e}_3)$. The *reference configuration* of the panel is the equilibrium *pre-stressed* position Ω_0 where the panel is subjected to the inflating pressure only. It is assumed that, in the reference configuration, the upper and lower membranes are parallel and at equal distance from the plane $(\mathrm{O}; \boldsymbol{e}_1, \boldsymbol{e}_2)$,

Fig. 2.2. The fibers (i.e. the drop-stitch yarns) are vertical, and their density is assumed to be high enough for the membranes to be flat in the reference configuration. The reader is referred to Kyser or Kawabata and Ishii's works [15, 16] for more details on the case when the drop yarns density is low, allowing periodic bulges to form on the top and bottom surfaces.

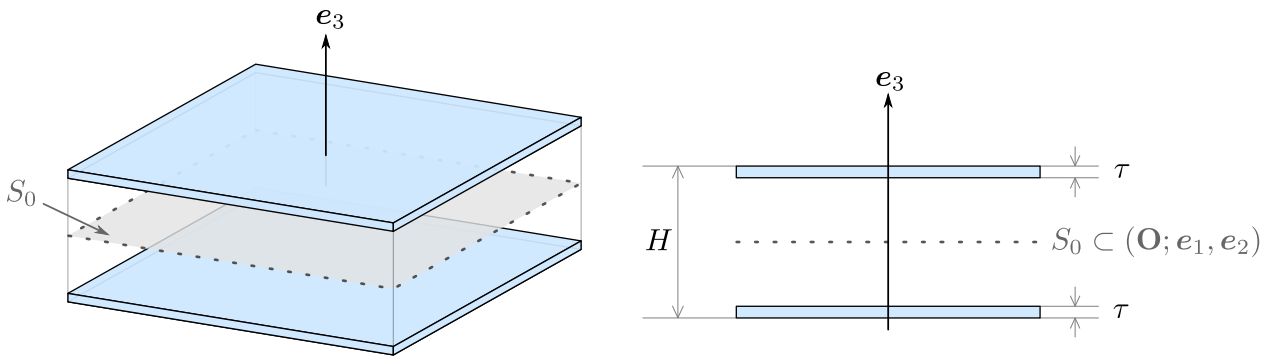

Figure 2.2: Reference configuration and cross-sectional view of the upper and lower membranes.

In the reference configuration, the mid-surface S_0 is a plane of symmetry of the panel and lies in the plane $(\mathbf{O}; \boldsymbol{e}_1, \boldsymbol{e}_2)$. Unlike a classical "full" plate, the mid-surface is not materialized, as there is only air and threads inside the membranes. Any point P_0 on S_0 corresponds to the unique curvilinear coordinates (ξ^1, ξ^2) that lie in a bounded subset of $\mathbb{R}^2$ called the *parameter space* S_ξ, Fig. 2.3. The local covariant basis vectors on the mid-surface are defined as

$$\forall \alpha \in \{1, 2\}, \quad \boldsymbol{A}_\alpha = \frac{\partial \mathrm{P}_0}{\partial \xi^\alpha}$$

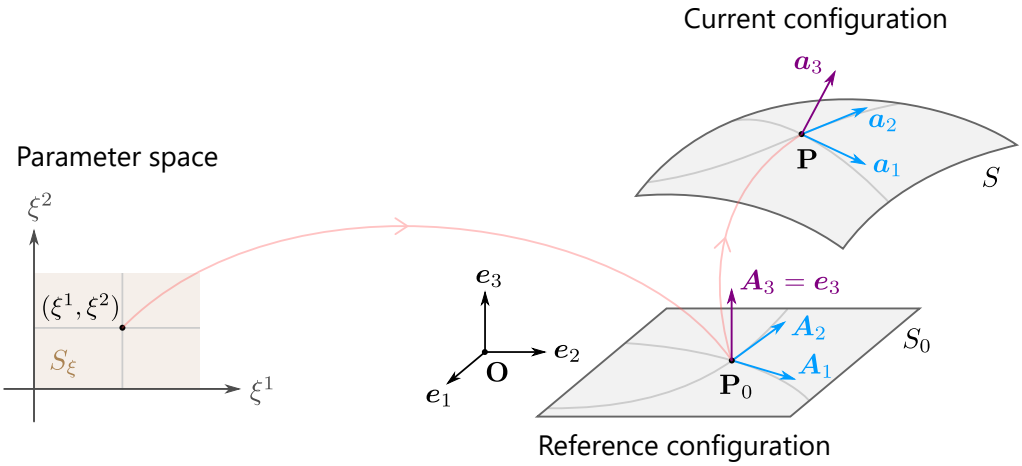

Figure 2.3: Mid-surface of the panel. The red lines represent the transformations from the parameter space to the reference configuration and from the reference configuration to the current one.

Let τ be the thickness of the membranes in the reference configuration, H the overall thickness of the panel, Fig. 2.2. The Cartesian coordinates of any point inside the region Ω_0, i.e. inside the membranes, are (X, Y, Z), where the coordinate Z belongs to the disconnected interval

$$T = \left[-\frac{H}{2}\,,\, -\frac{H}{2} + \tau\right] \cup \left[\frac{H}{2} - \tau\,,\, \frac{H}{2}\right] \tag{2.1}$$

The reference geometry of the panel can be described by a single equation that maps the parameter space

to the physical space. For a triplet of parameters $(\xi^1, \xi^2, \xi^3 \equiv Z) \in S_\xi \times T$, any point Q_0 in Ω_0 is such that $\mathrm{Q}_0 = \mathrm{P}_0(\xi^1, \xi^2) + Z\boldsymbol{e}_3$. The local basis vectors are also defined at any point $\mathrm{Q}_0 \in \Omega_0$:

$$\forall i \in \{1,2,3\}, \quad \boldsymbol{G}_i = \frac{\partial \mathrm{Q}_0}{\partial \xi^i} = \frac{\partial \mathrm{P}_0}{\partial \xi^i} + \frac{\partial Z}{\partial \xi^i}\boldsymbol{e}_3 = \boldsymbol{A}_i$$

2.1.2 Displacement field

The displacement of the panel at time t is defined by the displacement $\boldsymbol{U}(\mathrm{P}_0, t)$ of the mid-surface, which will be denoted $\boldsymbol{U}$ in the sequel, and the director vector $\boldsymbol{a}_3 \equiv \boldsymbol{a}_3(\mathrm{P}_0, t)$, which represents the drop-stitch yarns direction (not necessarily normal to the mid-surface):

$$\boldsymbol{U}(\mathrm{Q}_0, t) = \boldsymbol{U} + Z(\boldsymbol{a}_3 - \boldsymbol{e}_3) \tag{2.2}$$

The Mindlin–Reissner hypothesis states that the material segments may rotate but not stretch. As a consequence, the vector $\boldsymbol{A}_3 = \boldsymbol{e}_3$ is transformed into $\boldsymbol{a}_3$ by applying a time-dependent rotation:

$$\boldsymbol{a}_3 = \boldsymbol{R}(\xi^1, \xi^2, t) \cdot \boldsymbol{e}_3 \tag{2.3}$$

where $\boldsymbol{R}$ is the rotation tensor. The displacement field $\boldsymbol{U}$ and the director vector field $\boldsymbol{a}_3$ are the unknowns of the problem. The natural covariant basis vectors are expressed in terms of the unknowns of the problem $\boldsymbol{U}$ and $\boldsymbol{a}_3$: $\forall \alpha \in \{1,2\}$,

$$\forall \mathrm{P} \in S, \ \boldsymbol{a}_\alpha \equiv \frac{\partial \mathrm{P}}{\partial \xi^\alpha} = \boldsymbol{A}_\alpha + \boldsymbol{U}_{,\alpha} \qquad \forall \mathrm{Q} \in \Omega, \ \boldsymbol{g}_\alpha \equiv \frac{\partial \mathrm{Q}}{\partial \xi^\alpha} = \boldsymbol{a}_\alpha + Z\boldsymbol{a}_{3,\alpha} \tag{2.4}$$

Additionally, $\boldsymbol{g}_3 = \boldsymbol{a}_3$. The notations for all the natural bases vectors are summed up in Table 2.1. We also define the coefficients

$$\forall i,j \in \{1,2,3\}, \qquad a_{ij} = \boldsymbol{a}_i \cdot \boldsymbol{a}_j$$

	Initial (pressurized)	Deformed (pressurized and loaded)
Mid-surface ($Z = 0$)	$\boldsymbol{A}_\alpha = \dfrac{\partial \mathrm{P}_0}{\partial \xi^\alpha}$	$\boldsymbol{a}_\alpha = \dfrac{\partial \mathrm{P}}{\partial \xi^\alpha}$
For $Z \in \left[-\frac{H}{2}, \frac{H}{2}\right]$	$\boldsymbol{G}_\alpha = \dfrac{\partial \mathrm{Q}_0}{\partial \xi^\alpha} = \boldsymbol{A}_\alpha$	$\boldsymbol{g}_\alpha = \dfrac{\partial \mathrm{Q}}{\partial \xi^\alpha}$
Material segments	$\boldsymbol{A}_3 = \boldsymbol{G}_3 = \boldsymbol{e}_3$	$\boldsymbol{a}_3 = \boldsymbol{g}_3$

Table 2.1: Summary of the notations used for the natural covariant bases in inflatable panel theory.

Local kinematic of the membranes

Upon closer inspection of the upper and lower membranes, we observe that the kinematic field of Eq. (2.2) cannot apply inside the membranes ($Z \in T$). Indeed, given the very low bending stiffness and shear stiffness of the thin membranes, they cannot undergo shear deformation through their thickness: they bend according to Love–Kirchhoff kinematics, locally. As such, we should distinguish between the global kinematic of the

panel (described by Eq. (2.2)) and a local kinematic of the membranes (where $\boldsymbol{a}_3$ would be parallel to $\boldsymbol{a}_1 \times \boldsymbol{a}_2$, that is, to the normal vector of the surface), Fig. 2.4. In this manuscript, it is assumed that the distinct deformation of the membranes can be described by the global deformation of the panel, provided that the arising shear stresses in the membranes are *cancelled* by assuming plane stress inside the membranes (described in Section 3.2.3).

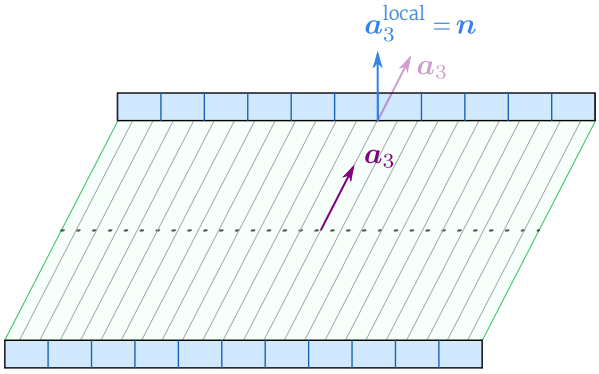

Figure 2.4: Global kinematic of the panel and local kinematic of the membranes shown in the case of pure shear deformation.

Justification of the Mindlin–Reissner kinematics in dynamics

When developing the theory of vibrations for inflatable panel, we had some concerns about whether or not the theoretical modeling of the panel would correspond to the real system. The Mindlin–Reissner kinematics binds together all the points along a material segment, which undergo rigid body motion. In an inflatable panel, this means that the movement of the upper membrane is unconditionally linked to the lower one. But the absence of solid matter between the membranes is unusual and raises some concerns. In a classical, "full" solid plate, a wave can travel through the thickness of the plate and bounce off the upper and lower faces. In a drop-stitch panel, neither the inertia of the drop cords nor that of the inflating gas is enough to efficiently carry the energy from top to bottom. Therefore, we must examine how an inflatable panel could behave as a Mindlin–Reissner plate even without a solid propagation medium: when one side of the panel is pulled, the drop cords will simply pull the opposite side, and when a side is pressed into the panel, the threads will shorten slightly, but not enough to loose pretension. The released tension allows the opposite side to be pushed by the pressurizing gas again, until the strain in the thread is uniform, in such a way that bending deformations work exactly the same as with a classical plate.

2.1.3 Green strain tensor

The displacement gradient is

$$\text{grad}_{\text{Q}_0} \boldsymbol{U}(\text{Q}_0, t) = \boldsymbol{U}_{,\alpha} \otimes \boldsymbol{A}^\alpha + (\boldsymbol{a}_3 - \boldsymbol{e}_3) \otimes \boldsymbol{e}_3 + Z \boldsymbol{a}_{3,\alpha} \otimes \boldsymbol{A}^\alpha \tag{2.5}$$

where $\boldsymbol{A}^\alpha = \boldsymbol{G}^\alpha$ is the dual vector of $\boldsymbol{A}_\alpha = \boldsymbol{G}_\alpha$ and Einstein summation convention is made from 1 to 2 on Greek indices. The material deformation gradient tensor can be defined from Eq. (2.5):

$$\boldsymbol{F}(\text{Q}_0, t) = \underbrace{\boldsymbol{I} + \text{grad}\, \boldsymbol{U}}_{\boldsymbol{F}} + (\boldsymbol{a}_3 - \boldsymbol{e}_3) \otimes \boldsymbol{e}_3 + Z \boldsymbol{a}_{3,\alpha} \otimes \boldsymbol{A}^\alpha \tag{2.6}$$

The Green strain tensor $\boldsymbol{E}$ is given by

$$\boldsymbol{E} = E_{ij}\boldsymbol{G}^i \otimes \boldsymbol{G}^j = \frac{1}{2}(g_{ij} - G_{ij})\boldsymbol{G}^i \otimes \boldsymbol{G}^j$$

where $g_{ij} \equiv \boldsymbol{g}_i \cdot \boldsymbol{g}_j$, $G_{ij} = A_{ij} \equiv \boldsymbol{A}_i \cdot \boldsymbol{A}_j$ and Einstein summation convention is made from 1 to 3 on Latin indices. It is found that $E_{\alpha\beta}$ may be written as a second-order polynomial in Z: $\forall \alpha, \beta \in \{1, 2\}$,

$$\begin{aligned} E_{\alpha\beta} &= E^{(0)}_{\alpha\beta} + ZE^{(1)}_{\alpha\beta} + Z^2E^{(2)}_{\alpha\beta} \\ E_{\alpha 3} &= \frac{1}{2}a_{\alpha 3} \\ E_{33} &= 0 \end{aligned} \tag{2.7}$$

where the components $E^{(0)}_{\alpha\beta}$, $E^{(1)}_{\alpha\beta}$, $E^{(2)}_{\alpha\beta}$ are, $\forall \alpha, \beta \in \{1, 2\}$,

$$\begin{aligned} E^{(0)}_{\alpha\beta} &= \frac{1}{2}\left(a_{\alpha\beta} - A_{\alpha\beta}\right) \\ E^{(1)}_{\alpha\beta} &= \frac{1}{2}\left(\boldsymbol{a}_\alpha \cdot \boldsymbol{a}_{3,\beta} + \boldsymbol{a}_{3,\alpha} \cdot \boldsymbol{a}_\beta\right) \\ E^{(2)}_{\alpha\beta} &= \frac{1}{2}\boldsymbol{a}_{3,\alpha} \cdot \boldsymbol{a}_{3,\beta} \end{aligned} \tag{2.8}$$

Remark 2.1. At this point of the demonstration, for classical solid plates, a shear correction factor commonly denoted k or κ^2 is introduced in Eq. (2.7). This is because the form of the displacement field causes the shear strain $E_{\alpha 3}$ to be constant through the thickness although it is known to be parabolic in reality. Therefore, a correction factor is applied so that the correct strain energy is predicted. For inflatable panels, since there is no solid matter between the membranes, having a uniform or parabolic shear strain profile across the thickness of the panel makes little difference in the overall strain energy and such a correction is not needed.

2.2 Equations of motion

2.2.1 Principle of virtual power

The equations of motion of the inflatable panel will next be obtained using the principle of virtual power, which states that, for any arbitrary virtual velocity field $\boldsymbol{U}^*(\mathrm{Q}_0)$ on the reference configuration (or $\boldsymbol{u}^*(\mathrm{Q}) = \boldsymbol{U}^*(\mathrm{Q}_0)$ on the current configuration), the sum of the virtual powers of internal forces $\mathcal{P}^*_{\text{int}}$ and external forces $\mathcal{P}^*_{\text{ext}}$ equals the virtual power of inertial quantities $\mathcal{P}^*_{\text{accel}}$:

$$\mathcal{P}^*_{\text{int}} + \underbrace{\mathcal{P}^*_p + \mathcal{P}^*_{\text{ext}\setminus p}}_{\mathcal{P}^*_{\text{ext}}} = \mathcal{P}^*_{\text{accel}} \tag{2.9}$$

In the above expression, $\mathcal{P}^*_{\text{ext}}$ is decomposed into two terms: the virtual power due to the inflation pressure $\mathcal{P}^*_p$ and the virtual power of other external loads $\mathcal{P}^*_{\text{ext}\setminus p}$.

2.2.2 Virtual velocity field

At any point Q_0 of the structure, the virtual velocity field is

$$\boldsymbol{U}^*(\mathrm{Q}_0) = \boldsymbol{U}^* + Z\boldsymbol{a}^*_3 \tag{2.10}$$

where $\boldsymbol{U}^* \equiv \boldsymbol{U}^*(\mathrm{P}_0)$ is the virtual velocity of the mid-surface and $\boldsymbol{a}_3^*$ the virtual director vector. According to the Mindlin–Reissner kinematics, the fibers do not stretch: they behave as rigid bodies, as shown by the relation $\dot{\boldsymbol{a}}_3 = \boldsymbol{\Omega} \times \boldsymbol{a}_3$ ($\boldsymbol{\Omega}$ is the axial vector of $\dot{\boldsymbol{R}}\boldsymbol{R}^{-1}$ with $\boldsymbol{R}$ the rotation tensor in Relation (2.3)). For this reason, the virtual director vector is taken of the same form:

$$\boldsymbol{a}_3^* = \boldsymbol{\omega}^* \times \boldsymbol{a}_3 \tag{2.11}$$

where the virtual rotation velocity vector $\boldsymbol{\omega}^*$ is arbitrary.

2.2.3 Virtual power of internal forces

The virtual power of internal forces $\mathcal{P}_{\text{int}}^*$ is defined as

$$\mathcal{P}_{\text{int}}^* = -\int_{\Omega_0} \boldsymbol{\Pi}^{\mathsf{T}} : \mathbf{grad}_{\mathrm{Q}_0} \boldsymbol{U}^*(\mathrm{Q}_0)\, \mathrm{d}\Omega_0 \tag{2.12}$$

where $\boldsymbol{A} : \boldsymbol{B} = \mathrm{Tr}(\boldsymbol{A}\boldsymbol{B})$ and $\boldsymbol{\Pi}$ is the first Piola-Kirchhoff stress tensor and the virtual velocity gradient is calculated using Relation (2.10):

$$\mathbf{grad}_{\mathrm{Q}_0} \boldsymbol{U}^*(\mathrm{Q}_0) = \boldsymbol{U}^*_{,\alpha} \otimes \boldsymbol{A}^\alpha + \boldsymbol{a}_3^* \otimes \boldsymbol{e}_3 + Z\boldsymbol{a}^*_{3,\alpha} \otimes \boldsymbol{A}^\alpha \tag{2.13}$$

In Relation (2.12), the integral over region Ω_0 of any scalar function $u(\mathrm{Q}_0, t)$ is rewritten using the following standard transformation

$$\int_{\Omega_0} u(\mathrm{Q}_0, t)\, \mathrm{d}\Omega_0 = \int_{S_\xi} \left(\int_T u(\mathrm{Q}_0, t)\, \mathrm{d}Z \right) \sqrt{A}\, \mathrm{d}\xi^1\, \mathrm{d}\xi^2 = \int_{S_0} \left(\int_T u(\mathrm{Q}_0, t)\, \mathrm{d}Z \right) \mathrm{d}S_0$$

in which A is the determinant of the metric tensor. Inserting the expression for the virtual velocity gradient (2.13) into Relation (2.12) leads to

$$\mathcal{P}_{\text{int}}^* = -\int_{S_0} \left(\int_T \boldsymbol{\Pi} \cdot \boldsymbol{A}^\alpha\, \mathrm{d}Z \cdot \boldsymbol{U}^*_{,\alpha} + \int_T Z\boldsymbol{\Pi} \cdot \boldsymbol{A}^\alpha\, \mathrm{d}Z \cdot \boldsymbol{a}^*_{3,\alpha} + \int_T \boldsymbol{\Pi} \cdot \boldsymbol{e}_3\, \mathrm{d}Z \cdot \boldsymbol{a}_3^* \right) \mathrm{d}S_0$$

Let us define the internal forces $\boldsymbol{R}^\alpha$, $\boldsymbol{S}$ and the internal moments $\boldsymbol{L}^\alpha$ as follows: $\forall \alpha \in \{1, 2\}$,

$$\begin{aligned} \boldsymbol{R}^\alpha &= \int_T \boldsymbol{\Pi} \cdot \boldsymbol{A}^\alpha\, \mathrm{d}Z \\ \boldsymbol{L}^\alpha &= \int_T Z\boldsymbol{\Pi} \cdot \boldsymbol{A}^\alpha\, \mathrm{d}Z \\ \boldsymbol{S} &= \int_T \boldsymbol{\Pi} \cdot \boldsymbol{e}_3\, \mathrm{d}Z \end{aligned}$$

Then, after integration by parts:

$$\boxed{\begin{aligned} \mathcal{P}_{\text{int}}^* = &\int_{S_0} \left(\frac{1}{\sqrt{A}} \left(\sqrt{A}\boldsymbol{R}^\alpha \right)_{,\alpha} \cdot \boldsymbol{U}^* + \left(\boldsymbol{a}_3 \times \frac{1}{\sqrt{A}} \left(\sqrt{A}\boldsymbol{L}^\alpha \right)_{,\alpha} - \boldsymbol{a}_3 \times \boldsymbol{S} \right) \cdot \boldsymbol{\omega}^* \right) \mathrm{d}S_0 \\ &- \int_{\partial S_0} \left(\boldsymbol{R}^\alpha \cdot \boldsymbol{U}^* \nu_{0\alpha} + \left(\boldsymbol{a}_3 \times \boldsymbol{L}^\alpha \right) \cdot \boldsymbol{\omega}^* \nu_{0\alpha} \right) \mathrm{d}s_0 \end{aligned}} \tag{2.14}$$

where $\forall \alpha \in \{1, 2\}$, $\nu_{0\alpha} = \boldsymbol{\nu}_0 \cdot \boldsymbol{A}_\alpha$, the vector $\boldsymbol{\nu}_0$ being the outward normal to the edge of the mid-surface ∂S_0. As can be seen later, it is more convenient to work with the so-called stress resultants $N^{\alpha\beta}$, $M^{\alpha\beta}$, $M^{(2)\alpha\beta}$, Q^β,

$Q^{(1)\beta}$ defined as: $\forall \alpha, \beta \in \{1,2\}$,

$$\begin{aligned} N^{\alpha\beta} &= \int_T \Sigma^{\alpha\beta}\,\mathrm{d}Z \\ M^{\alpha\beta} &= \int_T Z\Sigma^{\alpha\beta}\,\mathrm{d}Z \qquad & M^{(2)\alpha\beta} &= \int_T Z^2\Sigma^{\alpha\beta}\,\mathrm{d}Z \\ Q^{\beta} &= \int_T \Sigma^{3\beta}\,\mathrm{d}Z \qquad & Q^{(1)\beta} &= \int_T Z\Sigma^{3\beta}\,\mathrm{d}Z \end{aligned} \tag{2.15}$$

where the components Σ^{ij}, $\forall i,j \in \{1,2,3\}$, of the second Piola-Kirchhoff stress tensor $\boldsymbol{\Sigma} = \Sigma^{ij}\boldsymbol{A}_i \otimes \boldsymbol{A}_j$ are related to those of the first Piola-Kirchhoff stress tensor $\boldsymbol{\Pi}$ by $\Sigma^{ij}\boldsymbol{g}_i = \Pi^{ij}\boldsymbol{G}_i$. The stress resultants $N^{\alpha\beta}$ are called the membrane forces, $M^{\alpha\beta}$ the bending moments, $M^{(2)\alpha\beta}$ the bending moments of order 2, Q^{β} the shear forces and $Q^{(1)\beta}$ the shear forces of order 1. Using also Eq. (2.4), the internal forces $\boldsymbol{R}^{\alpha}$, $\boldsymbol{L}^{\alpha}$ and $\boldsymbol{S}$ can be written as: $\forall \beta \in \{1,2\}$,

$$\begin{aligned} \boldsymbol{R}^{\beta} &= N^{\alpha\beta}\boldsymbol{a}_{\alpha} + Q^{\beta}\boldsymbol{a}_3 + M^{\alpha\beta}\boldsymbol{a}_{3,\alpha} \\ \boldsymbol{L}^{\beta} &= M^{\alpha\beta}\boldsymbol{a}_{\alpha} + Q^{(1)\beta}\boldsymbol{a}_3 + M^{(2)\alpha\beta}\boldsymbol{a}_{3,\alpha} \\ \boldsymbol{S} &= Q^{\alpha}\boldsymbol{a}_{\alpha} + Q^{(1)\alpha}\boldsymbol{a}_{3,\alpha} + \int_T \Sigma^{33}\,\mathrm{d}Z\boldsymbol{a}_3 \end{aligned} \tag{2.16}$$

Remark 2.2. The calculations were done considering only the top and bottom layers, not the lateral wall. This allowed the virtual power of the internal forces to be expressed first as an integral over the surface S_0, then transformed by integration by parts to arrive at the expression (2.14). Discarding the lateral membrane is equivalent to neglecting the strain energy of the lateral membrane compared to that of the upper and lower layers.

2.2.4 Virtual power of external forces other than the inflating pressure

Apart from the inflating pressure, the inflatable panel is also subject to external loads in its current configuration:

- a body force $\rho\boldsymbol{f}$ applied at every points of the membranes,
- surface forces in the current configuration named $\boldsymbol{t}^{\text{sup}}$ on the upper membrane S^{sup}, $\boldsymbol{t}^{\text{inf}}$ on the lower membrane S^{inf} and $\boldsymbol{t}^{\text{edge}}$ on the lateral wall S^{edge} (the surfaces are shown in Fig. 2.5 and the loads are shown in Fig. 2.6).

The integrals over the current surfaces S^{sup}, S^{inf} and S^{edge} can be transposed to integrals over the reference surfaces S_0^{sup}, S_0^{inf} and S_0^{edge} respectively (Fig. 2.5). The virtual power of these force densities is

$$\mathcal{P}^*_{\text{ext}\setminus p} = \int_{\Omega} \rho\boldsymbol{f}\cdot\boldsymbol{u}^*(\mathrm{Q})\,\mathrm{d}\Omega + \int_{S^{\text{sup}}} \boldsymbol{t}^{\text{sup}}\cdot\boldsymbol{u}^*(\mathrm{Q})\,\mathrm{d}A + \int_{S^{\text{inf}}} \boldsymbol{t}^{\text{inf}}\cdot\boldsymbol{u}^*(\mathrm{Q})\,\mathrm{d}A + \int_{S^{\text{edge}}} \boldsymbol{t}^{\text{edge}}\cdot\boldsymbol{u}^*(\mathrm{Q})\,\mathrm{d}A$$

where $\mathrm{d}A$ is an infinitesimal surface element of $\partial\Omega$, which is different from an infinitesimal surface element $\mathrm{d}S$ on the mid-surface S. Let us now examine how each of these terms can be transposed to the reference configuration, which is the goal of this total Lagrangian approach.

External body forces

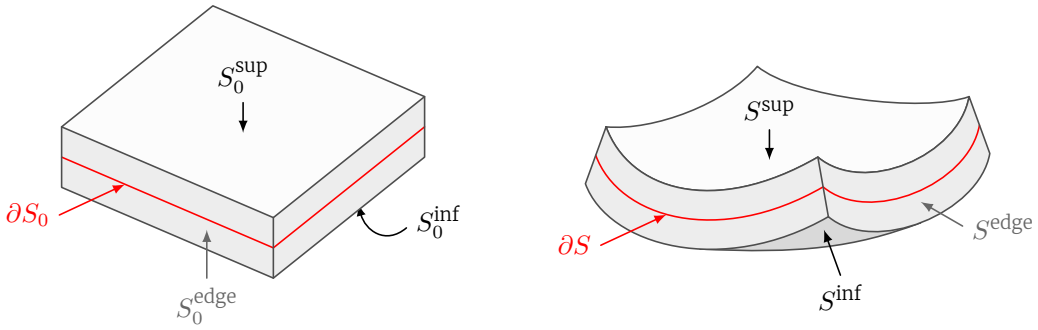

Figure 2.5: Decomposition of the plate into several surfaces in reference and deformed configurations.

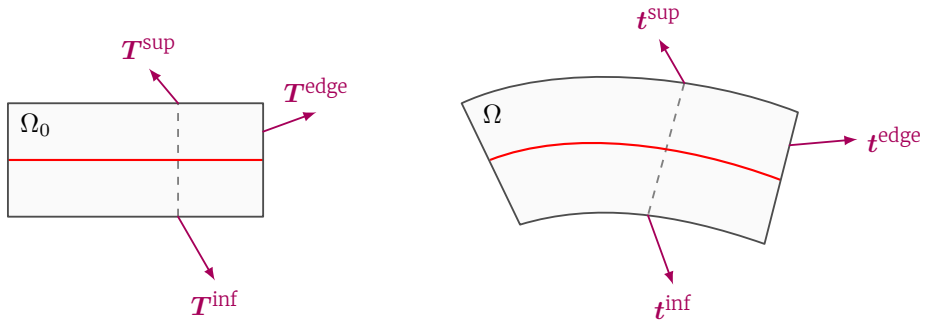

Figure 2.6: Cross-sectional view of the panel with surface loads vectors in reference and current configurations.

Using the conservation of mass $\rho_0 \,\mathrm{d}\Omega_0 = \rho \,\mathrm{d}\Omega$,

$$\begin{aligned}
\int_\Omega \rho \boldsymbol{f} \cdot \boldsymbol{u}^*(\mathrm{Q}) \,\mathrm{d}\Omega &= \int_{\Omega_0} \rho_0 \boldsymbol{f} \cdot \boldsymbol{U}^*(\mathrm{Q}_0) \,\mathrm{d}\Omega_0 \\
&= \int_{S_0} \int_T \rho_0 \boldsymbol{f} \cdot \boldsymbol{U}^*(\mathrm{Q}_0) \,\mathrm{d}Z \,\mathrm{d}S_0 \\
&= \int_{S_0} \underbrace{\left(\int_T \rho_0 \boldsymbol{f} \,\mathrm{d}Z \right)}_{\boldsymbol{q}_{\text{vol}}} \cdot \boldsymbol{U}^* \,\mathrm{d}S_0 + \int_{S_0} \underbrace{\left(\int_T Z \rho_0 \boldsymbol{f} \,\mathrm{d}Z \right)}_{\boldsymbol{c}_{\text{vol}}} \cdot \boldsymbol{a}_3^* \,\mathrm{d}S_0 \\
&= \int_{S_0} \boldsymbol{q}_{\text{vol}} \cdot \boldsymbol{U}^* \,\mathrm{d}S_0 + \int_{S_0} \boldsymbol{c}_{\text{vol}} \cdot \boldsymbol{a}_3^* \,\mathrm{d}S_0
\end{aligned} \tag{2.17}$$

In practice, the membranes are thin and their change of volume can be neglected, letting us write $\rho \approx \rho_0$.

External forces on the upper and lower faces

Let us focus on the integrals over the upper and lower membranes:

$$\int_{S^{\text{sup}} \cup S^{\text{inf}}} \boldsymbol{t} \cdot \boldsymbol{u}^*(\mathrm{Q}) \,\mathrm{d}A = \int_{S^{\text{sup}}} \boldsymbol{t}^{\text{sup}} \cdot \boldsymbol{u}^*(\mathrm{Q}) \,\mathrm{d}A + \int_{S^{\text{inf}}} \boldsymbol{t}^{\text{inf}} \cdot \boldsymbol{u}^*(\mathrm{Q}) \,\mathrm{d}A$$

First, starting with the upper surface:

$$\begin{aligned}
\int_{S^{\text{sup}}} \boldsymbol{t}^{\text{sup}} \cdot \boldsymbol{u}^*(\mathrm{Q}) \,\mathrm{d}A &= \int_{S_0} \boldsymbol{T}^{\text{sup}} \cdot \boldsymbol{U}^*(\mathrm{Q}_0) \,\mathrm{d}A_0 \\
&= \int_{S_0} \boldsymbol{T}^{\text{sup}} \cdot \boldsymbol{U}^* \,\mathrm{d}S_0 + \int_{S_0} \frac{H}{2} \boldsymbol{T}^{\text{sup}} \cdot \boldsymbol{a}_3^* \,\mathrm{d}S_0
\end{aligned}$$

where use was made of the property $\mathrm{d}A_0 = \sqrt{G|_{Z=\pm H/2}} \,\mathrm{d}\xi^1 \,\mathrm{d}\xi^2 = \sqrt{A} \,\mathrm{d}\xi^1 \,\mathrm{d}\xi^2 = \mathrm{d}S_0$. Then, the same treat-

ment is applied to the lower surface where $Z = -\frac{H}{2}$. Taking into account both expressions:

$$\begin{aligned}\int_{S^{\text{sup}}\cup S^{\text{inf}}} \boldsymbol{t}\cdot\boldsymbol{u}^*(\mathrm{Q})\,\mathrm{d}A &= \int_{S_0} \underbrace{\left(\boldsymbol{T}^{\text{sup}}+\boldsymbol{T}^{\text{inf}}\right)}_{\boldsymbol{q}_{\text{area}}}\cdot\boldsymbol{U}^*\,\mathrm{d}S_0 + \int_{S_0}\underbrace{\frac{H}{2}\left(\boldsymbol{T}^{\text{sup}}-\boldsymbol{T}^{\text{inf}}\right)}_{\boldsymbol{c}_{\text{area}}}\cdot\boldsymbol{a}_3^*\,\mathrm{d}S_0 \\ &= \int_{S_0}\left(\boldsymbol{q}_{\text{area}}\cdot\boldsymbol{U}^*+\boldsymbol{c}_{\text{area}}\cdot\boldsymbol{a}_3^*\right)\,\mathrm{d}S_0\end{aligned} \tag{2.18}$$

External forces on the edge

$$\begin{aligned}\int_{S^{\text{edge}}}\boldsymbol{t}^{\text{edge}}\cdot\boldsymbol{u}^*(\mathrm{Q})\,\mathrm{d}A &= \int_{S_0^{\text{edge}}}\boldsymbol{T}^{\text{edge}}\cdot\boldsymbol{U}^*(\mathrm{Q}_0)\,\mathrm{d}A_0 \\ &= \int_{S_0^{\text{edge}}}(\boldsymbol{T}^{\text{edge}}\cdot\boldsymbol{U}^*+Z\boldsymbol{T}^{\text{edge}}\cdot\boldsymbol{a}_3^*)\,\mathrm{d}A_0 \\ &= \int_{\partial S_0}\underbrace{\int_T\boldsymbol{T}^{\text{edge}}\,\mathrm{d}Z}_{\boldsymbol{q}'}\cdot\boldsymbol{U}^*\,\mathrm{d}s_0+\int_{\partial S_0}\underbrace{\int_T Z\boldsymbol{T}^{\text{edge}}\,\mathrm{d}Z}_{\boldsymbol{C}}\cdot\boldsymbol{a}_3^*\,\mathrm{d}s_0 \\ &= \int_{\partial S_0}(\boldsymbol{q}'\cdot\boldsymbol{U}^*+\boldsymbol{C}\cdot\boldsymbol{a}_3^*)\,\mathrm{d}s_0\end{aligned} \tag{2.19}$$

Virtual power of external forces other than the inflating pressure

Combining Relations (2.17), (2.18) and (2.19):

$$\mathcal{P}^*_{\text{ext}\setminus p} = \int_{S_0}\left((\boldsymbol{q}_{\text{vol}}+\boldsymbol{q}_{\text{area}})\cdot\boldsymbol{U}^*+(\boldsymbol{c}_{\text{vol}}+\boldsymbol{c}_{\text{area}})\cdot\boldsymbol{a}_3^*\right)\mathrm{d}S_0+\int_{\partial S_0}(\boldsymbol{q}'\cdot\boldsymbol{U}^*+\boldsymbol{C}\cdot\boldsymbol{a}_3^*)\,\mathrm{d}s_0 \tag{2.20}$$

One can define $\boldsymbol{q}\equiv\boldsymbol{q}_{\text{vol}}+\boldsymbol{q}_{\text{area}}$ and $\boldsymbol{c}\equiv\boldsymbol{c}_{\text{vol}}+\boldsymbol{c}_{\text{area}}$. Additionally, from $\boldsymbol{a}_3^*=\boldsymbol{\omega}^*\times\boldsymbol{a}_3$ (Relation (2.11)):

$$\begin{aligned}\mathcal{P}^*_{\text{ext}\setminus p} &= \int_{S_0}\left(\boldsymbol{q}\cdot\boldsymbol{U}^*+\boldsymbol{c}\cdot(\boldsymbol{\omega}^*\times\boldsymbol{a}_3)\right)\mathrm{d}S_0+\int_{\partial S_0}\left(\boldsymbol{q}'\cdot\boldsymbol{U}^*+\boldsymbol{C}\cdot(\boldsymbol{\omega}^*\times\boldsymbol{a}_3)\right)\mathrm{d}s_0 \\ &= \int_{S_0}\left(\boldsymbol{q}\cdot\boldsymbol{U}^*+\boldsymbol{\omega}^*\cdot(\boldsymbol{a}_3\times\boldsymbol{c})\right)\mathrm{d}S_0+\int_{\partial S_0}\left(\boldsymbol{q}'\cdot\boldsymbol{U}^*+\boldsymbol{\omega}^*\cdot(\boldsymbol{a}_3\times\boldsymbol{C})\right)\mathrm{d}s_0\end{aligned} \tag{2.21}$$

This last expression shows that the components of $\boldsymbol{c}$ and $\boldsymbol{C}$ along $\boldsymbol{a}_3$ are bound to disappear when calculating the cross product: they are not meaningful within the context of the Mindlin–Reissner kinematics. As a result, the notations $\boldsymbol{\mu}\equiv\boldsymbol{a}_3\times\boldsymbol{c}$ and $\boldsymbol{\Gamma}\equiv\boldsymbol{a}_3\times\boldsymbol{C}$ are introduced: they contain only information relevant to the components of $\boldsymbol{c}$ and $\boldsymbol{C}$ tangent to S. The surface force $\boldsymbol{q}$ and the surface couple $\boldsymbol{\mu}$ distributed over S_0, as well as the line force $\boldsymbol{q}'$ and the line torque $\boldsymbol{\Gamma}$ on the edge ∂S_0, are shown in Fig. 2.7. Finally, the virtual power of external forces other than the inflating pressure is

$$\boxed{\mathcal{P}^*_{\text{ext}\setminus p} = \int_{S_0}\left[\boldsymbol{q}\cdot\boldsymbol{U}^*+\boldsymbol{\mu}\cdot\boldsymbol{\omega}^*\right]\mathrm{d}S_0+\int_{\partial S_0}\left[\boldsymbol{q}'\cdot\boldsymbol{U}^*+\boldsymbol{\Gamma}\cdot\boldsymbol{\omega}^*\right]\mathrm{d}s_0} \tag{2.22}$$

In what follows, the surface couple $\boldsymbol{\mu}$ is discarded as it is rarely found in practice.

Remark 2.3. It will turn out to be more practical to deal with the components of the torque $\boldsymbol{\Gamma}$ in a local basis at a point P of the edge ∂S. By introducing the outward normal vector to the edge $\boldsymbol{n}$ and the tangent vector to the edge $\boldsymbol{s}=\dfrac{\boldsymbol{a}^3}{\|\boldsymbol{a}^3\|}\times\boldsymbol{\nu}$, the torque density is decomposed into $\boldsymbol{\Gamma}=\Gamma^\nu\boldsymbol{\nu}+\Gamma^s\boldsymbol{s}+\Gamma_3\boldsymbol{a}^3$. In fact, Γ_3 will never appear in the local equations and is therefore inaccessible. When projecting onto the unit normal and longitudinal

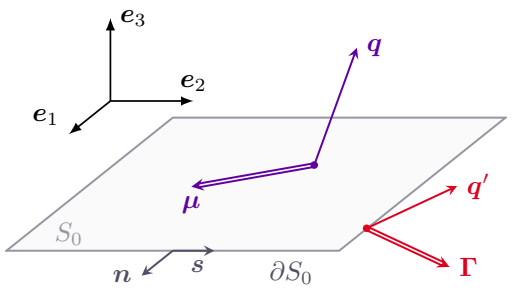

Figure 2.7: External forces and couples acting on the mid-surface of the panel.

vectors $\boldsymbol{n}$ and $\boldsymbol{s}$, the expressions below will come in handy. Since all calculations are done on the mid-surface where $Z = 0$, Eq. (2.6) yields

$$\boldsymbol{F}(\mathrm{Q}_0, t)_{|\mathrm{Q}_0=\mathrm{P}_0} = \boldsymbol{F} + (\boldsymbol{a}_3 - \boldsymbol{e}_3) \otimes \boldsymbol{e}_3$$

where $\boldsymbol{F} = \boldsymbol{I} + \operatorname{grad} \boldsymbol{U}$.

1. Let us compute $\boldsymbol{s} \cdot \boldsymbol{a}^\alpha$.

$$\boldsymbol{s} \cdot \boldsymbol{a}^\alpha = \boldsymbol{s} \cdot \boldsymbol{F}(\mathrm{Q}_0, t)^{-T}_{|\mathrm{Q}_0=\mathrm{P}_0} \cdot \boldsymbol{A}^\alpha = \left(\boldsymbol{F}^{-1}(\mathrm{Q}_0, t)_{|\mathrm{Q}_0=\mathrm{P}_0} \cdot \boldsymbol{s}\right) \cdot \boldsymbol{A}^\alpha$$

Since $\boldsymbol{A}^\alpha \cdot \boldsymbol{e}_3 = 0$,

$$\boldsymbol{s} \cdot \boldsymbol{a}^\alpha = \boldsymbol{s} \cdot \boldsymbol{F}^{-T} \cdot \boldsymbol{A}^\alpha = \left(\boldsymbol{F}^{-1} \cdot \boldsymbol{s}\right) \cdot \boldsymbol{A}^\alpha$$

The current tangent vector $\boldsymbol{s}$ is related to the tangent vector to the reference mid-plane $\boldsymbol{s}_0$. The relationship between the two is found by considering a small segment $\mathrm{d}\boldsymbol{X}$ from ∂S_0 transformed into

$$\mathrm{d}\boldsymbol{x} = \boldsymbol{F}(\mathrm{Q}_0, t)_{|\mathrm{Q}_0=\mathrm{P}_0} \, \mathrm{d}\boldsymbol{X} \underset{\mathrm{d}\boldsymbol{X}\cdot\boldsymbol{e}_3=0}{=} \boldsymbol{F} \, \mathrm{d}\boldsymbol{X}$$

However, nothing guarantees that the norm of this vector is 1. Therefore, it must be normalized:

$$\boldsymbol{s} = \frac{\mathrm{d}\boldsymbol{x}}{\| \mathrm{d}\boldsymbol{x}\|} = \frac{\boldsymbol{F} \cdot \mathrm{d}\boldsymbol{X}}{\sqrt{\mathrm{d}\boldsymbol{X} \cdot \boldsymbol{F}^T \cdot \boldsymbol{F} \cdot \mathrm{d}\boldsymbol{X}}} = \frac{\boldsymbol{F} \cdot \boldsymbol{s}_0}{\sqrt{\boldsymbol{s}_0 \cdot \boldsymbol{F}^T \cdot \boldsymbol{F} \cdot \boldsymbol{s}_0}} = \frac{\boldsymbol{F} \cdot \boldsymbol{s}_0}{\sqrt{1 + 2E_{ss}}}$$

hence

$$\boldsymbol{s} = \frac{1}{\lambda_s} \boldsymbol{F} \boldsymbol{s}_0$$

where $\lambda_s \equiv \sqrt{1 + 2E_{ss}}$. One concludes that

$$\boldsymbol{s} \cdot \boldsymbol{a}^\alpha \nu_{0\alpha} = \frac{1}{\lambda_s} \boldsymbol{s}_0 \cdot \boldsymbol{A}^\alpha \nu_{0\alpha} = \frac{1}{\lambda_s} \boldsymbol{s}_0 \cdot \boldsymbol{\nu}_0 = 0 \tag{2.23}$$

$$\boldsymbol{s} \cdot \boldsymbol{a}^\alpha s_{0\alpha} = \frac{1}{\lambda_s} \boldsymbol{s}_0 \cdot \boldsymbol{A}^\alpha s_{0\alpha} = \frac{1}{\lambda_s} \boldsymbol{s}_0 \cdot \boldsymbol{s}_0 = \frac{1}{\lambda_s} \tag{2.24}$$

where $\nu_{0\alpha} = \boldsymbol{\nu}_0 \cdot \boldsymbol{A}_\alpha$ and $s_{0\alpha} = \boldsymbol{s}_0 \cdot \boldsymbol{A}_\alpha$.

2. Similarly, from

$$\boldsymbol{\nu} \cdot \boldsymbol{a}^\alpha = \boldsymbol{\nu} \cdot \boldsymbol{F}^{-T} \cdot \boldsymbol{A}^\alpha = \left(\boldsymbol{F}^{-1} \cdot \boldsymbol{\nu}\right) \cdot \boldsymbol{A}^\alpha$$

it is found that

$$\boldsymbol{\nu} \cdot \boldsymbol{a}^\alpha \nu_{0\alpha} = \boldsymbol{\nu}_0 \cdot \boldsymbol{F}^{-1} \cdot \boldsymbol{\nu} \qquad \text{and} \qquad \boldsymbol{\nu} \cdot \boldsymbol{a}^\alpha s_{0\alpha} = \boldsymbol{s}_0 \cdot \boldsymbol{F}^{-1} \cdot \boldsymbol{\nu} \tag{2.25}$$

Note that in the reference state ($\boldsymbol{s} = \boldsymbol{s}_0$ and $\boldsymbol{\nu} = \boldsymbol{\nu}_0$):

$$\boldsymbol{s} \cdot \boldsymbol{a}^\alpha \nu_{0\alpha} = 0 \quad \text{and} \quad \boldsymbol{s} \cdot \boldsymbol{a}^\alpha s_{0\alpha} = 1$$
$$\boldsymbol{\nu} \cdot \boldsymbol{a}^\alpha \nu_{0\alpha} = 1 \quad \text{and} \quad \boldsymbol{\nu} \cdot \boldsymbol{a}^\alpha s_{0\alpha} = 0$$

2.2.5 Virtual power of the inflating pressure

The panel is inflated with air at a prescribed pressure p which exerts a follower force on the inner surface S_p of the panel in the current configuration. Let S_{0p}, the surface in the reference configuration corresponding to S_p, be partitioned into three parts S_{0p}^{sup}, S_{0p}^{inf} and S_{0p}^{edge} as shown in Fig. 2.8:

- S_{0p}^{sup} and S_{0p}^{inf} are the lower side of the upper membrane and the upper side of the lower membrane, respectively.
- S_{0p}^{edge} is the inner side of the lateral membrane.

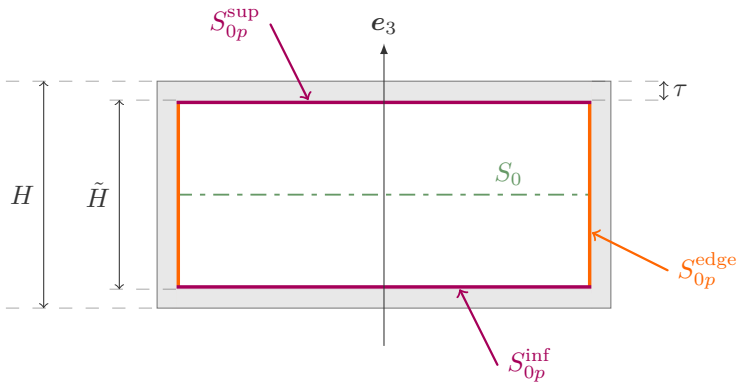

Figure 2.8: Definition of the surfaces on which the pressure is exerted.

The reference surfaces S_{0p}^{sup}, S_{0p}^{inf}, S_{0p}^{edge} become S_p^{sup}, S_p^{inf} and S_p^{edge}, respectively, in the current configuration. The distance between S_{0p}^{sup} and S_{0p}^{inf} is constant and equals $\tilde{H} = H - 2\tau$. The virtual power of the internal prescribed pressure p is

$$\mathcal{P}_p^* = \int_{S_p} p\boldsymbol{n} \cdot \boldsymbol{u}^*(\mathrm{Q})\, \mathrm{d}S$$

where $\boldsymbol{n}$ is the outward normal vector to the membrane, Fig. 2.9.

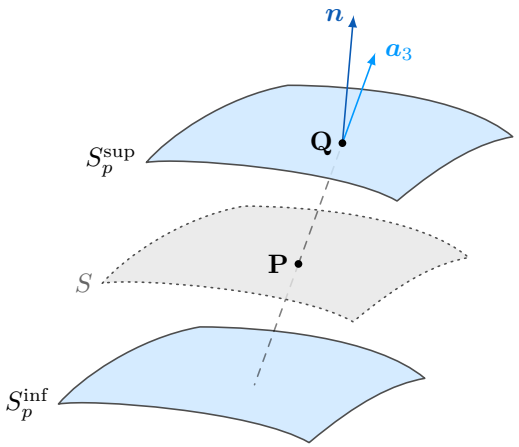

Figure 2.9: The surfaces S_p^{sup} and S_p^{inf} and the outward normal vector $\boldsymbol{n}$ at point Q on S_p^{sup}.

The virtual power of pressure forces is split into two terms, the integral $\mathcal{P}^*_{p\to S_p^{\text{sup}}\cup S_p^{\text{inf}}}$ over the upper and lower surfaces and the integral $\mathcal{P}^*_{p\to S_p^{\text{edge}}}$ over the lateral walls:

$$\mathcal{P}^*_p = \mathcal{P}^*_{p\to S_p^{\text{sup}}\cup S_p^{\text{inf}}} + \mathcal{P}^*_{p\to S_p^{\text{edge}}}$$

Pressure over the upper and lower faces

Let us first consider the virtual power of the pressure exerted on the upper surface:

$$\mathcal{P}^*_{p\to S_p^{\text{sup}}} = \int_{S_p^{\text{sup}}} p\boldsymbol{n}\cdot\boldsymbol{u}^*(\mathrm{Q})\,\mathrm{d}S \tag{2.26}$$

Similarly to the mid-surface S, the upper surface S_p^{sup} is parametrized by (ξ^1,ξ^2):

$$\begin{array}{ccc} S_\xi & \longrightarrow & S_p^{\text{sup}} \\ (\xi^1,\xi^2) & \mapsto & \mathrm{Q}(\xi^1,\xi^2,t) = \mathrm{P}(\xi^1,\xi^2,t) + \dfrac{\tilde{H}}{2}\boldsymbol{a}_3(\xi^1,\xi^2,t) \end{array}$$

The above expression involves the height $\boxed{\tilde{H} = H - 2\tau}$ over which the pressure is exerted on the lateral walls, rather than the total height H of the panel. The distinction between $\tilde{H}$ and H will prove to have a noticeable impact on the numerical results.

The natural vectors at a point Q on the upper surface S_p^{sup} are

$$\forall\alpha\in\{1,2\},\quad \boldsymbol{g}_\alpha = \frac{\partial\mathrm{Q}}{\partial\xi^\alpha} = \boldsymbol{a}_\alpha + \frac{\tilde{H}}{2}\boldsymbol{a}_{3,\alpha} \tag{2.27}$$

Since the surface element in Relation (2.26) is $\boldsymbol{n}\,\mathrm{d}S = \boldsymbol{g}_1\times\boldsymbol{g}_2\,\mathrm{d}\xi^1\,\mathrm{d}\xi^2$, the virtual power of the pressure on the upper surface writes

$$\mathcal{P}^*_{p\to S_p^{\text{sup}}} = p\int_{S_\xi}\boldsymbol{U}^*(\mathrm{Q}_0)\cdot(\boldsymbol{g}_1\times\boldsymbol{g}_2)\,\mathrm{d}\xi^1\,\mathrm{d}\xi^2$$

Moreover, Relation (2.10) leads to $\boldsymbol{U}^*(\mathrm{Q}_0) = \boldsymbol{U}^* + \boldsymbol{\omega}^*\times\dfrac{\tilde{H}}{2}\boldsymbol{a}_3$ so that Relation (2.27) becomes

$$\boldsymbol{g}_1\times\boldsymbol{g}_2 = \boldsymbol{a}_1\times\boldsymbol{a}_2 + \frac{\tilde{H}}{2}(\boldsymbol{a}_1\times\boldsymbol{a}_{3,2} + \boldsymbol{a}_{3,1}\times\boldsymbol{a}_2) + \frac{\tilde{H}^2}{4}\boldsymbol{a}_{3,1}\times\boldsymbol{a}_{3,2}$$

Since $\|\boldsymbol{a}_3\| = 1$, the virtual power of pressure forces acting upon the upper surface is finally

$$\begin{aligned}\mathcal{P}^*_{p\to S_p^{\text{sup}}} = p\int_{S_\xi}\Bigg\{&\boldsymbol{U}^*\cdot(\boldsymbol{a}_1\times\boldsymbol{a}_2) + \boldsymbol{U}^*\cdot\frac{\tilde{H}}{2}(\boldsymbol{a}_1\times\boldsymbol{a}_{3,2}+\boldsymbol{a}_{3,1}\times\boldsymbol{a}_2) + \boldsymbol{U}^*\cdot\frac{\tilde{H}^2}{4}\boldsymbol{a}_{3,1}\times\boldsymbol{a}_{3,2}\\ &+\boldsymbol{\omega}^*\cdot\frac{\tilde{H}}{2}\boldsymbol{a}_3\times(\boldsymbol{a}_1\times\boldsymbol{a}_2) + \boldsymbol{\omega}^*\cdot\frac{\tilde{H}^2}{4}\boldsymbol{a}_3\times(\boldsymbol{a}_1\times\boldsymbol{a}_{3,2}+\boldsymbol{a}_{3,1}\times\boldsymbol{a}_2)\Bigg\}\,\mathrm{d}\xi^1\,\mathrm{d}\xi^2\end{aligned} \tag{2.28}$$

The same procedure is applied to the lower face S_p^{inf}, with

$$\forall\alpha\in\{1,2\},\quad \boldsymbol{g}_\alpha = \frac{\partial\mathrm{Q}}{\partial\xi^\alpha} = \boldsymbol{a}_\alpha - \frac{\tilde{H}}{2}\boldsymbol{a}_{3,\alpha}$$

and the surface element $\boldsymbol{n}\,\mathrm{d}S = -\boldsymbol{g}_1\times\boldsymbol{g}_2\,\mathrm{d}\xi^1\,\mathrm{d}\xi^2$. The negative sign indicates that the normal to the lower

membrane faces downwards. Hence

$$\mathcal{P}^*_{p\to S_p^{\text{inf}}} = -p\int_{S_\xi}\Big\{\boldsymbol{U}^*\cdot(\boldsymbol{a}_1\times\boldsymbol{a}_2) - \boldsymbol{U}^*\cdot\frac{\tilde{H}}{2}(\boldsymbol{a}_1\times\boldsymbol{a}_{3,2}+\boldsymbol{a}_{3,1}\times\boldsymbol{a}_2) + \boldsymbol{U}^*\cdot\frac{\tilde{H}^2}{4}\boldsymbol{a}_{3,1}\times\boldsymbol{a}_{3,2} \\ -\boldsymbol{\omega}^*\cdot\frac{\tilde{H}}{2}\boldsymbol{a}_3\times(\boldsymbol{a}_1\times\boldsymbol{a}_2) + \boldsymbol{\omega}^*\cdot\frac{\tilde{H}^2}{4}\boldsymbol{a}_3\times(\boldsymbol{a}_1\times\boldsymbol{a}_{3,2}+\boldsymbol{a}_{3,1}\times\boldsymbol{a}_2)\Big\}\,\mathrm{d}\xi^1\,\mathrm{d}\xi^2 \tag{2.29}$$

By summing Relation (2.28) and Relation (2.29), the virtual power of pressure forces acting on the upper and lower surfaces of the panel can be expressed as an integral over the reference mid-surface S_0:

$$\boxed{\mathcal{P}^*_{p\to S_p^{\text{sup}}\cup S_p^{\text{inf}}} = \int_{S_0}\frac{p\tilde{H}}{\sqrt{A}}(\boldsymbol{a}_1\times\boldsymbol{a}_{3,2}+\boldsymbol{a}_{3,1}\times\boldsymbol{a}_2)\cdot\boldsymbol{U}^*\,\mathrm{d}S_0 + \int_{S_0}\frac{p\tilde{H}}{\sqrt{A}}\big[\boldsymbol{a}_3\times(\boldsymbol{a}_1\times\boldsymbol{a}_2)\big]\cdot\boldsymbol{\omega}^*\,\mathrm{d}S_0} \tag{2.30}$$

Pressure over the lateral wall

The internal pressure also acts on the lateral wall S_p^{edge}. The following parametrization is introduced to define the border of the mid-surfaces S_0 and S (Fig. 2.10):

$$\begin{array}{ccccc} \Lambda & \longrightarrow & \partial S_0 & \longrightarrow & \partial S \\ \lambda & \mapsto & \mathrm{P}_0(\lambda) & \mapsto & \mathrm{P}(\lambda)=\mathrm{P}_0(\lambda)+\boldsymbol{U}(\mathrm{P}_0,t) \end{array}$$

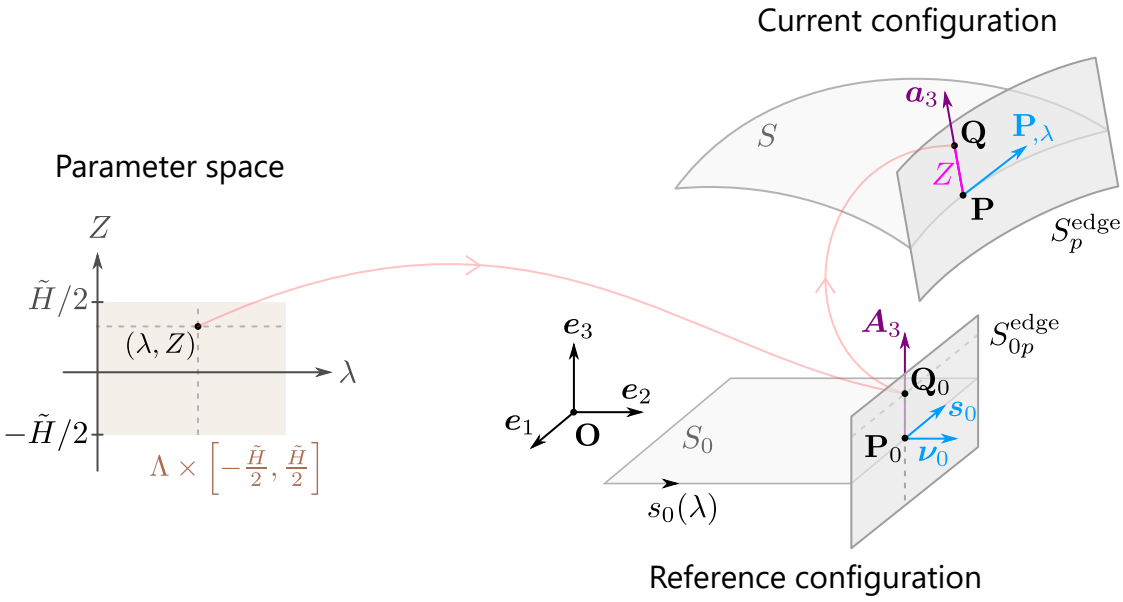

Figure 2.10: Parametrization of the border in the reference and current configurations. The red lines represent the transformations from the parameter space to the reference configuration and from the reference configuration to the current one.

The following parametrization defines the edge of the plate:

$$\begin{array}{ccc} \Lambda\times\left[-\frac{\tilde{H}}{2},\frac{\tilde{H}}{2}\right] & \longrightarrow & S_p^{\text{edge}} \\ (\lambda, Z) & \mapsto & \mathrm{Q}(\lambda,Z)=\mathrm{P}(\lambda)+Z\boldsymbol{a}_3(\lambda) \end{array} \tag{2.31}$$

In writing this, it is assumed that the material segments of the edges remain straight (Fig. 2.10), thus

ignoring the bulge that may form along the edge of the panel after inflation. The virtual power of the pressure on the lateral wall is recast in terms of parameters (λ, Z) as

$$\mathcal{P}^*_{p\to S_p^{\text{edge}}} = \int_{S_p^{\text{edge}}} p\boldsymbol{n}\cdot\boldsymbol{u}^*(\mathrm{Q})\,\mathrm{d}S = \int_{\Lambda\times\left[-\frac{\tilde{H}}{2},\frac{\tilde{H}}{2}\right]} \boldsymbol{U}^*(\mathrm{Q}_0)\cdot(\mathrm{Q}_{,\lambda}\times\mathrm{Q}_{,Z})\,\mathrm{d}\lambda\,\mathrm{d}Z \tag{2.32}$$

On account of the parametrization (2.31) of the border, the cross product $\mathrm{Q}_{,\lambda}\times\mathrm{Q}_{,Z}$ is

$$\mathrm{Q}_{,\lambda}\times\mathrm{Q}_{,Z} = \mathrm{P}_{,\lambda}\times\boldsymbol{a}_3 + Z\boldsymbol{a}_{3,\lambda}\times\boldsymbol{a}_3$$

Given the expression of the virtual velocity field, $\boldsymbol{U}^*(\mathrm{Q}_0) = \boldsymbol{U}^* + \boldsymbol{\omega}^*\times Z\boldsymbol{a}_3$, the integrand in Relation (2.32) becomes

$$\boldsymbol{U}^*(\mathrm{Q}_0)\cdot(\mathrm{Q}_{,\lambda}\times\mathrm{Q}_{,Z}) = \boldsymbol{U}^*\cdot\left(\mathrm{P}_{,\lambda}\times\boldsymbol{a}_3 + Z\boldsymbol{a}_{3,\lambda}\times\boldsymbol{a}_3\right) + \boldsymbol{\omega}^*\cdot\left[Z\boldsymbol{a}_3\times(\mathrm{P}_{,\lambda}\times\boldsymbol{a}_3 + Z\boldsymbol{a}_{3,\lambda}\times\boldsymbol{a}_3)\right]$$

In the right-hand side, the virtual quantities $\boldsymbol{U}^*$ and $\boldsymbol{\omega}^*$ are functions of point $\mathrm{P}_0 \in S_0$ only. The terms $\mathrm{P}_{,\lambda}$, $\boldsymbol{a}_3$ and $\boldsymbol{a}_{3,\lambda}$ depend solely on λ. Integrating over Z gives the virtual power of the pressure forces on the lateral wall of the panel:

$$\boxed{\mathcal{P}^*_{p\to S_p^{\text{edge}}} = p\tilde{H}\int_\Lambda \boldsymbol{U}^*\cdot(\mathrm{P}_{,\lambda}\times\boldsymbol{a}_3)\,\mathrm{d}\lambda + \frac{p\tilde{H}^3}{12}\int_\Lambda \boldsymbol{\omega}^*\cdot\boldsymbol{a}_{3,\lambda}\,\mathrm{d}\lambda} \tag{2.33}$$

The total virtual power of the pressure forces $\mathcal{P}^*_p$ is simply the sum of (2.30) and (2.33).

Prescribed inflation pressure

In practice, the majority of inflatable structures are first pressurized using a fixed amount of gas and then sealed to make them airtight. When the deformations of the panel increase or reduce the interior volume, it causes a change in internal pressure. Taking into account the pressure variations due to volume changes would require utilizing a state law governing the internal gas and solving a fluid-structure interaction problem. This difficult issue, possibly intractable by purely analytical means, is beyond the scope of our work. Throughout the foregoing, we have assumed that the inflating pressure p is prescribed, meaning that is independent of the interior volume of the inflatable panel, even in finite deformations of the panel.

Equivalence of the pressure-volume work or virtual power of pressure forces approaches

The principle of virtual power used in our work involves the pressure acting on the current configuration, thus it also takes into account – although indirectly – the change of the interior volume. Integrating the thermodynamic pressure-volume work over the volume or integrating the pressure forces over the internal surface is essentially the same thing: indeed, McComb [10] has considered the change in volume inside of the panel, and this reasoning has lead him to the same pressure terms in his governing equations as in our linearized equations of motions presented in Chapter 3.

2.2.6 Virtual power of inertial forces

The virtual power of the inertial quantity in Eq. (2.9) is

$$\mathcal{P}^*_{\text{accel}} = \int_{\Omega_0} \rho\ddot{\boldsymbol{U}}(\mathrm{Q}_0,t)\cdot\boldsymbol{U}^*(\mathrm{Q}_0)\,\mathrm{d}\Omega_0$$

where ρ is the density of the membrane measured in the *reference state*[1] and $\ddot{\boldsymbol{U}}(\mathrm{Q}_0,t)$ is the acceleration at point Q_0. Furthermore, since the membranes are very thin, the density ρ can be assumed uniform through the thickness. The above integral can be transformed into

$$\mathcal{P}^*_{\text{accel}} = \int_{S_0} \rho \left(\ddot{\boldsymbol{U}} \cdot \boldsymbol{U}^* \int_T \mathrm{d}Z + \ddot{\boldsymbol{a}}_3 \cdot \boldsymbol{U}^* \int_T Z \,\mathrm{d}Z \right.$$
$$\left. + (\boldsymbol{a}_3 \times \ddot{\boldsymbol{U}}) \cdot \boldsymbol{\omega}^* \int_T Z \,\mathrm{d}Z + (\boldsymbol{a}_3 \times \ddot{\boldsymbol{a}}_3) \cdot \boldsymbol{\omega}^* \int_T Z^2 \,\mathrm{d}Z \right) \mathrm{d}S_0$$

where $\ddot{\boldsymbol{a}}_3$ is the second derivative of the director vector $\boldsymbol{a}_3(\mathrm{P}_0,t)$ with respect to time. The integrals carried out over interval T (defined in (2.1)) are

$$\int_T \mathrm{d}Z = 2\tau \qquad \int_T Z \,\mathrm{d}Z = 0 \qquad \int_T Z^2 \,\mathrm{d}Z = \frac{H^3 - (H-2\tau)^3}{12} = \frac{\tilde{\tau} H^2}{2} \tag{2.34}$$

where use has been made of the notation $\boxed{\tilde{\tau} = \left(1 - \frac{2\tau}{H} + \frac{4\tau^2}{3H^2}\right)\tau}$. The virtual power of inertial forces thus becomes

$$\boxed{\mathcal{P}^*_{\text{accel}} = \int_{S_0} \left(2\tau\rho \ddot{\boldsymbol{U}} \cdot \boldsymbol{U}^* + \frac{\rho \tilde{\tau} H^2}{2} (\boldsymbol{a}_3 \times \ddot{\boldsymbol{a}}_3) \cdot \boldsymbol{\omega}^* \right) \mathrm{d}S_0} \tag{2.35}$$

Remark 2.4. In writing (2.34), only the upper and lower membranes have been considered. The expression (2.35) therefore does not contain the contribution of the lateral membrane. This approximation is justified since the mass of the lateral membrane is small compared to that of the upper and lower membranes. In the previous theories of inflatable beams, the same approximation was made by discarding the contribution of the closing cap sections of the beam.

2.2.7 System of nonlinear equations of motion

The final expression of the principle of virtual power (2.9) is obtained by summing the expressions (2.14), (2.22), (2.30), (2.33), and (2.35). For the sake of clarity, let us state the resulting governing equations before proving them.

- The **equations of motion** for the inflatable panel are: $\forall t$, $\forall \mathrm{P}_0 \in S_0$,

$$\boxed{\frac{1}{\sqrt{A}} \left(\sqrt{A} \boldsymbol{R}^\alpha \right)_{,\alpha} + \boldsymbol{q} + \frac{p\tilde{H}}{\sqrt{A}} (\boldsymbol{a}_{3,1} \times \boldsymbol{a}_2 + \boldsymbol{a}_1 \times \boldsymbol{a}_{3,2}) = 2\tau\rho \ddot{\boldsymbol{U}}} \tag{2.36a}$$

$$\boxed{\frac{1}{\sqrt{A}} \left(\sqrt{A} \boldsymbol{a}_3 \times \boldsymbol{L}^\alpha \right)_{,\alpha} + \boldsymbol{a}_\alpha \times \boldsymbol{R}^\alpha + \frac{p\tilde{H}}{\sqrt{A}} \boldsymbol{a}_3 \times (\boldsymbol{a}_1 \times \boldsymbol{a}_2) = \frac{\rho \tilde{\tau} H^2}{2} \boldsymbol{a}_3 \times \ddot{\boldsymbol{a}}_3} \tag{2.36b}$$

The first equation corresponds to the linear momentum balance and the second to the angular momentum balance.

- The **boundary conditions** are
  - force boundary conditions: $\forall t, \forall \mathrm{P}_0 \in \partial S_0$,

$$\boxed{\boldsymbol{R}^\alpha \nu_{0\alpha} - p\tilde{H} \mathrm{P}_{,s_0} \times \boldsymbol{a}_3 = \boldsymbol{q}'} \tag{2.37}$$

[1] Again, the density of the membrane in the reference state should be denoted ρ_0, but we neglect their change of volume because they are thin, letting us write $\rho = \rho_0$.

- moment boundary conditions: $\forall t$, $\forall \mathrm{P}_0 \in \partial S_0$,

$$\boxed{\boldsymbol{L}^{\beta}\nu_{0\beta}\cdot\boldsymbol{a}^{\alpha}\nu_{0\alpha}-\frac{p\tilde{H}^3}{12}(\boldsymbol{a}_{3,s_0}\times\boldsymbol{a}_3)\cdot\boldsymbol{a}^{\alpha}\nu_{0\alpha}=\|\boldsymbol{a}^3\|\Gamma^s\boldsymbol{\nu}\cdot\boldsymbol{a}^{\alpha}\nu_{0\alpha}} \tag{2.38a}$$

$$\boxed{\boldsymbol{L}^{\beta}\nu_{0\beta}\cdot\boldsymbol{a}^{\alpha}s_{0\alpha}-\frac{p\tilde{H}^3}{12}(\boldsymbol{a}_{3,s_0}\times\boldsymbol{a}_3)\cdot\boldsymbol{a}^{\alpha}s_{0\alpha}=\|\boldsymbol{a}^3\|\left(\Gamma^s\boldsymbol{\nu}\cdot\boldsymbol{a}^{\alpha}s_{0\alpha}-\Gamma^{\nu}\boldsymbol{s}\cdot\boldsymbol{a}^{\alpha}s_{0\alpha}\right)} \tag{2.38b}$$

Proof.

Since the principle of virtual power (2.9) holds for arbitrary $\boldsymbol{U}^*$ and $\boldsymbol{\omega}^*$, it leads to Eq. (2.36a) and the following equation: $\forall t$, $\forall \mathrm{P}_0 \in S_0$,

$$\boldsymbol{a}_3\times\frac{1}{\sqrt{A}}\left(\sqrt{A}\boldsymbol{L}^{\alpha}\right)_{,\alpha}-\boldsymbol{a}_3\times\boldsymbol{S}+\frac{p\tilde{H}}{\sqrt{A}}\boldsymbol{a}_3\times(\boldsymbol{a}_1\times\boldsymbol{a}_2)=\frac{\rho\tilde{\tau}H^2}{2}\boldsymbol{a}_3\times\ddot{\boldsymbol{a}}_3$$

By calculating $\boldsymbol{a}_{\alpha}\times\boldsymbol{R}^{\alpha}$, $\boldsymbol{a}_{3,\alpha}\times\boldsymbol{L}^{\alpha}$ and $\boldsymbol{a}_3\times\boldsymbol{S}$ from expressions (2.16), one can easily verify that the following equality holds:

$$\boldsymbol{a}_{\alpha}\times\boldsymbol{R}^{\alpha}+\boldsymbol{a}_{3,\alpha}\times\boldsymbol{L}^{\alpha}+\boldsymbol{a}_3\times\boldsymbol{S}=\boldsymbol{0}$$

Furthermore, it can also be shown that

$$\boldsymbol{a}_3\times\frac{1}{\sqrt{A}}\left(\sqrt{A}\boldsymbol{L}^{\alpha}\right)_{,\alpha}=\frac{1}{\sqrt{A}}\left(\sqrt{A}\boldsymbol{a}_3\times\boldsymbol{L}^{\alpha}\right)_{,\alpha}-\boldsymbol{a}_{3,\alpha}\times\boldsymbol{L}^{\alpha}$$

Combining the two previous equations yields Eq. (2.36b). The principle of virtual power (2.9) also yields the two following boundary conditions written on edge ∂S_0: the first one is Eq. (2.37) and the second is

$$\forall t,\forall \mathrm{P}_0\in\partial S_0,\quad \boldsymbol{a}_3\times\boldsymbol{L}^{\alpha}\nu_{0\alpha}-\frac{p\tilde{H}^3}{12}\boldsymbol{a}_{3,s_0}-\boldsymbol{\Gamma}=\boldsymbol{0} \tag{2.39}$$

On account of the following properties:

$$\forall\boldsymbol{v}\in\mathbb{R}^3,\ \boldsymbol{a}_3\times\boldsymbol{v}=\boldsymbol{0}\quad\Leftrightarrow\quad\forall\alpha\in\{1,2\},\ \boldsymbol{v}\cdot\boldsymbol{a}^{\alpha}=0\quad\Leftrightarrow\quad\begin{cases}\boldsymbol{v}\cdot\boldsymbol{a}^{\alpha}\nu_{0\alpha}=0\\ \boldsymbol{v}\cdot\boldsymbol{a}^{\alpha}s_{0\alpha}=0\end{cases} \tag{2.40}$$

Relation (2.39) then gives (2.38).

Surface loads equivalent to the 3D pressure distribution

The terms with a factor $\frac{p\tilde{H}}{\sqrt{A}}$ in Eq. (2.38) arise solely from pressurization. It seemed interesting to calculate these vector fields for simple deformed configurations of the panel. Doing so confirmed that these terms behave like surface forces and surface couples on the middle-plane which are equivalent to the 3D distribution of pressure follower forces pushing the membranes from the inside.

Let us place ourselves in a simple case where the displacements fields depend solely on the x coordinate, thus allowing to observe only the side of the panel. As a result, the inflatable panel is assimilated to a beam (Fig. 2.11), from which it is easier to make observations that generalize to the 3D case. As long as all the material segments remain parallel, the vector field $\boldsymbol{a}_3$ is uniform and the term $\boldsymbol{a}_{3,1}\times\boldsymbol{a}_2+\boldsymbol{a}_1\times\boldsymbol{a}_{3,2}$ is always zero in the equilibrium of forces (2.36a). Therefore, this term only activates when $\boldsymbol{a}_3$ is not constant over space, which reflects the fact that the top or bottom membrane is more stretched than the other, creating an imbalance in the pressure forces pushing them. Let us consider a case where the panel is bent with negative

curvature, such that the area is larger on the upper membrane than on the lower one (Fig. 2.11a). Therefore, the pressurized gas pushes the upper surface more than it repels the bottom one, and so a net upward force is created, resulting in an equivalent vertical surface force on the mid-surface (in green).

Besides, the term $\boldsymbol{a}_3 \times (\boldsymbol{a}_1 \times \boldsymbol{a}_2)$ in the angular momentum balance (2.36b) will only activate when the fiber orientation $\boldsymbol{a}_3$ deviates from the normal to the middle-plane whose direction is given by $\boldsymbol{a}_1 \times \boldsymbol{a}_2$, as can be seen in Fig. 2.11b. Fig. 2.11c shows a superposition of both surface forces and surface couples caused by a deformed state that combines stretching of the top membrane and misalignment between the material segments and the normal to the mid-surface.

As a conclusion, the pressurization is equivalent to a surface load that pushes the middle-plane of the panel in the direction that amplifies bending and a surface couple which tends to align the material segments with the normals of the mid-surface.

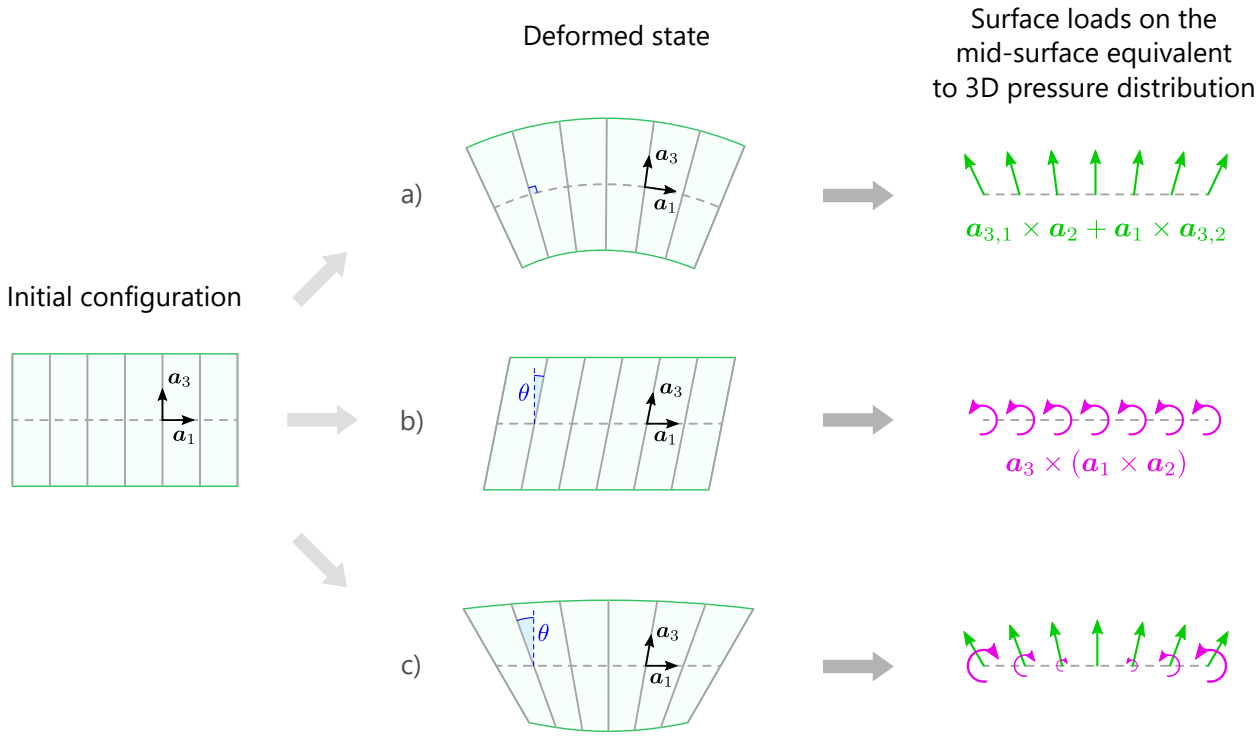

Figure 2.11: Deformed panels and the equivalent surface pressure loads on the middle-plane.

2.3 Determination of reference quantities (geometry after inflation)

The theory presented here was built by assuming that the reference (inflated) configuration is known. In practice however, only the natural (deflated) configuration is known precisely, since the dimensions and the material properties of the panel are measured while it is being made, before it is assembled and pressurized. Upon inflation, the geometry and the material coefficients will change due to the elasticity of the yarns (from $H_\varnothing$ to H) and the membranes ($L_\varnothing$ to L) as well as material nonlinearities ($E_\varnothing$, $\nu_\varnothing$ and $\rho_\varnothing$ to E, ν and ρ respectively). In this dissertation we only deal with the elasticity of the structure and not the material nonlinearities. Furthermore, the reduction of the membrane's thickness (from "$\tau_\varnothing$" to τ) is assumed to be negligible.

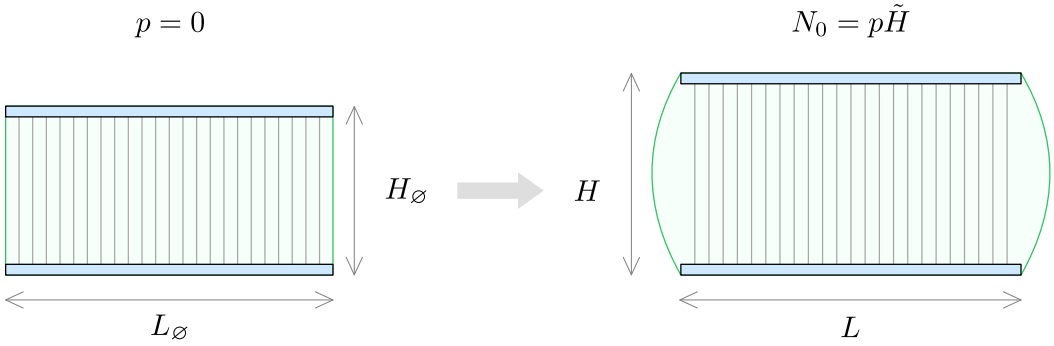

Figure 2.12: Geometry of the panel before and after inflation.

A characteristic length L (that is, R for a disk or a and b for a rectangle) and the height H must be derived from their initial values for any inflation pressure p. Obtaining (L, H) from $(L_\varnothing, H_\varnothing)$ is a preliminary calculation which should be carried out beforehand using infinitesimal strain theory. The inflated dimensions of the panel can be estimated by assuming that the increase in total height is entirely due to the elongation of the drop-stitch yarns (discarding the bulge on the edge of the panel), because the tensile stiffness of the lateral wall is small compared to the combined stiffness of all the drop cords inside the panel.

2.3.1 Change of height

The yarn density d is the number of yarns per meter squared. The vertical forces equilibrium condition of all the drop-stitch strings writes

$$p\pi R^2 = dN_y \pi R^2 \quad \Rightarrow \quad N_y = \frac{p}{d}$$

where N_y is the force in a single drop-stitch yarn. For small elongations:

$$N_y = E_y S_y \frac{\Delta H_\varnothing}{H_\varnothing} = \frac{p}{d}$$

hence

$$\Delta H_\varnothing = H_\varnothing \frac{p}{dE_y S_y}$$

finally,

$$\boxed{H = H_\varnothing \left(1 + \frac{p}{dE_y S_y}\right)} \tag{2.41}$$

In our work, we have set the average axial stiffness of a yarn $E_y S_y$ to 100 N and the yarn density d to 30,000 per square meter.

2.3.2 Change of length for a rectangular panel

From the force equilibrium condition for half of the rectangular panel,

$$\mathrm{Mat}(\boldsymbol{\sigma}; \boldsymbol{e}_x \boldsymbol{e}_y) = \frac{p\tilde{H}_\varnothing}{2\tau} \begin{bmatrix} 1 & 0 \\ 0 & 1 \end{bmatrix} \tag{2.42}$$

where $\tilde{H}_\varnothing = H_\varnothing - 2\tau$. Knowing the pre-stress resultant $\boldsymbol{N}_0 = p\tilde{H}_\varnothing \boldsymbol{I}^P$ (where $\boldsymbol{I}^P = \boldsymbol{e}_\alpha \otimes \boldsymbol{e}_\alpha$ is the identity tensor restricted to plane $\boldsymbol{e}_1\boldsymbol{e}_2$), an inflated dimension L can be deduced from its initial value $L_\varnothing$ using

infinitesimal strain theory. From Hooke's law in 3D:

$$\boldsymbol{\varepsilon} = \frac{1+\nu}{E}\boldsymbol{\sigma} - \frac{\nu}{E}(\mathrm{Tr}\,\boldsymbol{\sigma})\boldsymbol{I}^P \tag{2.43}$$

$$\mathrm{Mat}(\boldsymbol{\varepsilon};\boldsymbol{e}_x\boldsymbol{e}_y) = \begin{bmatrix} \frac{1-\nu}{E}\frac{p\tilde{H}_\varnothing}{2\tau} & 0 \\ 0 & \frac{1-\nu}{E}\frac{p\tilde{H}_\varnothing}{2\tau} \end{bmatrix} \tag{2.44}$$

For the elongation along x:

$$\varepsilon_{xx} = \frac{L-L_\varnothing}{L_\varnothing} = \frac{1-\nu}{E}\frac{p\tilde{H}_\varnothing}{2\tau} \tag{2.45}$$

$$\boxed{L = L_\varnothing\left(1+\frac{1-\nu}{E}\frac{p\tilde{H}_\varnothing}{2\tau}\right)} \tag{2.46}$$

The result is the same along y.

2.3.3 Change of radius for a circular panel

The initial geometry of a circular panel is described by the natural radius $R_\varnothing$ and the natural height $H_\varnothing$. Considering the upper or lower membrane, in polar coordinates, the local equilibrium of forces is

$$\frac{\partial\sigma_r}{\partial r} + \frac{1}{r}(\sigma_r - \sigma_\theta) = 0 \tag{2.47}$$

and Hooke's law gives

$$\sigma_r = \frac{E}{1-\nu^2}\left(\frac{\partial u}{\partial r} + \nu\frac{u}{r}\right) \qquad \text{and} \qquad \sigma_\theta = \frac{E}{1-\nu^2}\left(\frac{u}{r} + \nu\frac{\partial u}{\partial r}\right) \tag{2.48}$$

Assuming an axisymmetric problem $u = u(r)$, Relation (2.47) becomes

$$\frac{\mathrm{d}^2u}{\mathrm{d}r^2} + \frac{1}{r}\frac{\mathrm{d}u}{\mathrm{d}r} - \frac{u}{r^2} = 0 \quad \Leftrightarrow \quad \frac{\mathrm{d}}{\mathrm{d}r}\left(\frac{1}{r}\frac{\mathrm{d}}{\mathrm{d}r}(ru)\right) = 0 \tag{2.49}$$

hence

$$\frac{\mathrm{d}}{\mathrm{d}r}(ru) = Br \quad \Rightarrow \quad ru = B\frac{r^2}{2} + C \quad \Rightarrow \quad u(r) = Br + \frac{C}{r} \tag{2.50}$$

where B and C are constants of integration. The symmetry imposes $u(r=0) = 0$, which is finite. Thus $C = 0$ and $u(r) = Br$. Going back to Relation (2.48), we have

$$\sigma_\theta = \frac{E}{1-\nu^2}(B + \nu B) = \frac{EB}{1-\nu} \tag{2.51}$$

Neglecting the rounded panel edge, the force equilibrium condition for a half-disk yields

$$\sigma_\theta \times 2R\tau \times 2 = 2R \times \tilde{H}_\varnothing \times p \tag{2.52}$$

hence $\sigma_\theta = \dfrac{p\tilde{H}_\varnothing}{2\tau}$. Finally, Relation (2.51) writes

$$\frac{EB}{1-\nu} = \frac{p\tilde{H}_\varnothing}{2\tau} \quad \Rightarrow \quad B = \frac{1-\nu}{E}\frac{p\tilde{H}_\varnothing}{2\tau} \tag{2.53}$$

$$\boxed{R = R_{\varnothing}\left(1 + \frac{1-\nu}{E}\frac{p\tilde{H}_{\varnothing}}{2\tau}\right)} \tag{2.54}$$

which is the same expression as (2.46). Some numerical results are given in Table 2.2.

$R_{\varnothing}$ (m)	$H_{\varnothing}$ (cm)	p (kPa)	R (m)	H (cm)
1.5	10	30	1.504	10.10
		50	1.507	10.17
		70	1.510	10.23
		90	1.513	10.30
	20	30	1.509	20.20
		50	1.515	20.33
		70	1.521	20.47
		90	1.527	20.60

Table 2.2: Radii and heights of the inflated panel before and after inflation ($E = 0.59$ GPa).

Chapter 3

Linearized theory of inflatable panels

The equations of motion (2.36)–(2.38), where the internal forces $\boldsymbol{R}^{\alpha}$ and $\boldsymbol{L}^{\alpha}$ are functions of the stress resultants $N^{\alpha\beta}$, $M^{\alpha\beta}$, $M^{(2)\alpha\beta}$, Q^{β} and $Q^{(1)\beta}$ via Relations (2.15) and (2.16), are nonlinear equations in terms of the displacements $\boldsymbol{U}$ and $\boldsymbol{a}_3$. In the sequel, we assume that the inflatable panel undergoes small displacements and rotations and we shall derive the linearized equations from the above-found nonlinear equations.

It should be emphasized that one has to formulate the problem in the nonlinear framework as done in the previous sections, before proceeding to the linearization. On the contrary, if the equations were obtained directly from the linear context assuming small strains, the essential terms pertaining to the inflation pressure, which is a follower load, would be missing.

3.1 Linearization assumptions – Small displacements and rotations

The linearization will be carried out around the *pre-stressed reference configuration*, under the following assumptions:

1. The mid-surface displacements $\boldsymbol{U} \equiv \boldsymbol{x} - \boldsymbol{X}$ and its derivatives with respect to the spatial coordinates and time t are assumed to be infinitesimal of the *first order*.

2. The fiber rotation vector $\boldsymbol{\psi} \equiv \boldsymbol{a}_3 - \boldsymbol{e}_3$ is assumed to be infinitesimal of the *first order*. Its derivatives with respect to the spatial coordinates and time t are also small of the first order.

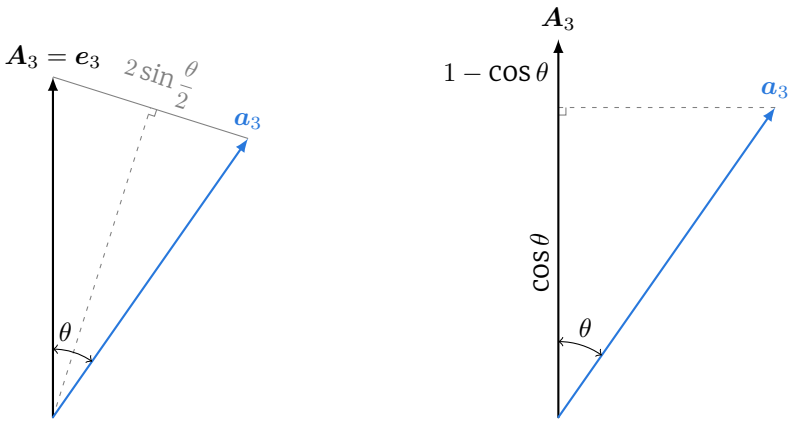

Figure 3.1: The fiber rotates by a small angle θ in the deformed configuration.

The linearized equations will be obtained by discarding infinitesimals of the second order and higher. Let the angle between the unit vectors $\boldsymbol{e}_3$ and $\boldsymbol{a}_3$ be θ, Fig. 3.1. Since $\|\boldsymbol{\psi}\| = 2\sin\frac{\theta}{2}$, assuming that $\boldsymbol{\psi}$ is small of the first order amounts to assuming that angle θ is small. Moreover, since $\boldsymbol{\psi}\cdot\boldsymbol{e}_3 = 1-\cos\theta = 2\sin^2\dfrac{\theta}{2}$, the out-of-plane component ψ_3 of $\boldsymbol{\psi}$ is of second order and can be neglected.

3.2 Linearization of the nonlinear equations

3.2.1 Current basis vectors

Local basis on the mid-surface

Calculations can be made simpler by temporarily setting the curvilinear coordinates (ξ^1,ξ^2) to be equal to the Cartesian coordinates (X,Y), meaning that $(\boldsymbol{A}_1,\boldsymbol{A}_2,\boldsymbol{e}_3) = (\boldsymbol{e}_1,\boldsymbol{e}_2,\boldsymbol{e}_3)$. Once the linearization is achieved, we will go back to component-free notations, which are independent of any particular coordinate system. The components of $\boldsymbol{U}$ are

$$\boldsymbol{U} = \boldsymbol{U}^P + W\boldsymbol{e}_3 = U_1\boldsymbol{e}_1 + U_2\boldsymbol{e}_2 + W\boldsymbol{e}_3$$

where the notation $\bullet^P$ is used to indicate in-plane quantities, meaning that $\boldsymbol{U}^P = U_\alpha\boldsymbol{e}_\alpha$ is the projection of the vector $\boldsymbol{U}$ onto the plane $\boldsymbol{e}_1\boldsymbol{e}_2$. Thus, the natural covariant basis vectors in Eq. (2.4) can be written as

$$\boldsymbol{a}_\alpha = \boldsymbol{e}_\alpha + \boldsymbol{U}^P_{,\alpha} + W_{,\alpha}\boldsymbol{e}_3$$

The contravariant basis must also be linearized. Using the definitions:

$$\boldsymbol{a}_\alpha = \boldsymbol{A}_\alpha + \boldsymbol{U}_{,\alpha}$$
$$\boldsymbol{a}_3 = \boldsymbol{e}_3 + \boldsymbol{\psi}$$

the matrix representation of the metric tensor writes

$$[a_{..}] = \begin{bmatrix} 1+2U_{1,1} & U_{1,2}+U_{2,1} & \psi_1+W_{,1} \\ & 1+2U_{2,2} & \psi_2+W_{,2} \\ \text{(SYM)} & & 1 \end{bmatrix}$$

which can be inverted to find

$$[a^{\cdot\cdot}] = [a_{..}]^{-1} = \begin{bmatrix} 1-2U_{1,1} & -(U_{1,2}+U_{2,1}) & -(\psi_1+W_{,1}) \\ & 1-2U_{2,2} & -(\psi_2+W_{,2}) \\ \text{(SYM)} & & 1 \end{bmatrix}$$

and from $\boldsymbol{a}^i = a^{ij}\boldsymbol{a}_j$, finally:

$$\boldsymbol{a}^\alpha = \boldsymbol{e}_\alpha - U_{\alpha,\mu}\boldsymbol{e}_\mu - \psi_\alpha\boldsymbol{e}_3 = \boldsymbol{e}_\alpha - \operatorname{grad}U_\alpha - \psi_\alpha\boldsymbol{e}_3$$

$$\boldsymbol{a}^3 = \boldsymbol{e}_3 - W_{,\mu}\boldsymbol{e}_\mu = \boldsymbol{e}_3 - \operatorname{grad}W$$

which implies $\|\boldsymbol{a}^3\| = 1$.

Local basis on the edge

In this paragraph, the Relations (2.24) and (2.25) pertaining to the projection of the local basis vectors on the edge are linearized. Indeed, they play an important role in the boundary conditions.

1. First, $\boldsymbol{s}\cdot\boldsymbol{a}^{\alpha}s_{0\alpha}=\dfrac{1}{\lambda_s}=\dfrac{1}{\sqrt{1+2E_{ss}}}$. The linearized relative elongation E_{ss} is computed as follows:

$$\begin{aligned}E_{ss}&=\boldsymbol{s}_0\cdot\boldsymbol{E}\cdot\boldsymbol{s}_0\\E_{ss}&\approx\boldsymbol{s}_0\cdot\mathrm{SYM}\,\mathbf{grad}\boldsymbol{U}\cdot\boldsymbol{s}_0\\E_{ss}&=\boldsymbol{s}_0\cdot\mathbf{grad}\,\boldsymbol{U}\cdot\boldsymbol{s}_0\end{aligned}$$

   In the last expression, $\mathbf{grad}\,\boldsymbol{U}$ may be replaced with $\mathbf{grad}\,\boldsymbol{U}^P$ given that

$$\boldsymbol{U}=\boldsymbol{U}^P+W\boldsymbol{e}_3\quad\Rightarrow\quad\mathbf{grad}\,\boldsymbol{U}=\mathbf{grad}\,\boldsymbol{U}^P+\mathbf{grad}\,W\otimes\boldsymbol{e}_3\quad\Rightarrow\quad\boldsymbol{s}_0\cdot\mathbf{grad}\,\boldsymbol{U}\cdot\boldsymbol{s}_0=\boldsymbol{s}_0\cdot\mathbf{grad}\,\boldsymbol{U}^P\cdot\boldsymbol{s}_0$$

   hence

$$\begin{aligned}\lambda_s&=\sqrt{1+2E_{ss}}\\\lambda_s&\approx1+E_{ss}\\\lambda_s&=1+\boldsymbol{s}_0\cdot\mathbf{grad}\,\boldsymbol{U}^P\cdot\boldsymbol{s}_0\end{aligned}$$

   Therefore, the linearized expression of $\boldsymbol{s}\cdot\boldsymbol{a}^{\alpha}s_{0\alpha}=\dfrac{1}{\lambda_s}$ is

$$\frac{1}{\lambda_s}=1-\boldsymbol{s}_0\cdot\mathbf{grad}\,\boldsymbol{U}^P\cdot\boldsymbol{s}_0 \tag{3.1}$$

2. Then, $\boldsymbol{\nu}\cdot\boldsymbol{a}^{\alpha}\nu_{0\alpha}=\boldsymbol{\nu}_0\cdot\boldsymbol{F}^{-1}_{|\mathrm{Q}_0=\mathrm{P}_0}\cdot\boldsymbol{\nu}$ and $\boldsymbol{\nu}\cdot\boldsymbol{a}^{\alpha}s_{0\alpha}=\boldsymbol{s}_0\cdot\boldsymbol{F}^{-1}_{|\mathrm{Q}_0=\mathrm{P}_0}\cdot\boldsymbol{\nu}$. The normal vector to the edge $\boldsymbol{\nu}$ can be expressed in the form of a cross product:

$$\boldsymbol{\nu}=\boldsymbol{s}\times\frac{\boldsymbol{a}^3}{\|\boldsymbol{a}^3\|}$$

   Combining this expression with $\boldsymbol{a}^3=\boldsymbol{e}_3-\mathbf{grad}\,W$ and $\boldsymbol{s}=\dfrac{1}{\lambda_s}\boldsymbol{F}\cdot\boldsymbol{s}_0$ (where $\boldsymbol{F}=\boldsymbol{I}+\mathbf{grad}\,\boldsymbol{U}$), one gets

$$\boldsymbol{\nu}=\frac{1}{\lambda_s}\Big[\boldsymbol{\nu}_0-\boldsymbol{s}_0\times\mathbf{grad}\,W+(\mathbf{grad}\,\boldsymbol{U}\cdot\boldsymbol{s}_0)\times\boldsymbol{e}_3\Big]$$

   Moreover, for small deformations, $\boldsymbol{F}^{-1}_{|\mathrm{Q}_0=\mathrm{P}_0}\approx\boldsymbol{I}-\mathbf{grad}\,\boldsymbol{U}-\boldsymbol{\psi}\otimes\boldsymbol{e}_3$. Thus

$$\boldsymbol{F}^{-1}_{|\mathrm{Q}_0=\mathrm{P}_0}\cdot\boldsymbol{\nu}=\frac{1}{\lambda_s}\Big[\boldsymbol{\nu}_0-\boldsymbol{s}_0\times\mathbf{grad}\,W+(\mathbf{grad}\,\boldsymbol{U}\cdot\boldsymbol{s}_0)\times\boldsymbol{e}_3-\mathbf{grad}\,\boldsymbol{U}\cdot\boldsymbol{\nu}_0\Big]$$

   Recalling that $\mathbf{grad}\,W\perp\boldsymbol{e}_3$:

$$\begin{aligned}\boldsymbol{\nu}_0\cdot\boldsymbol{F}^{-1}_{|\mathrm{Q}_0=\mathrm{P}_0}\cdot\boldsymbol{\nu}&=\frac{1}{\lambda_s}\Big[1+\boldsymbol{s}_0\cdot\mathbf{grad}\,\boldsymbol{U}\cdot\boldsymbol{s}_0-\boldsymbol{\nu}_0\cdot\mathbf{grad}\,\boldsymbol{U}\cdot\boldsymbol{\nu}_0\Big]\\\boldsymbol{s}_0\cdot\boldsymbol{F}^{-1}_{|\mathrm{Q}_0=\mathrm{P}_0}\cdot\boldsymbol{\nu}&=-\frac{1}{\lambda_s}\Big[\boldsymbol{\nu}_0\cdot\mathbf{grad}\,\boldsymbol{U}\cdot\boldsymbol{s}_0+\boldsymbol{s}_0\cdot\mathbf{grad}\,\boldsymbol{U}\cdot\boldsymbol{\nu}_0\Big]\\&=-\frac{2}{\lambda_s}\boldsymbol{s}_0\cdot\mathrm{SYM}\,\mathbf{grad}\boldsymbol{U}\cdot\boldsymbol{\nu}_0\end{aligned}$$

   As explained previously, $\mathbf{grad}\,\boldsymbol{U}$ can be replaced with $\mathbf{grad}\,\boldsymbol{U}^P$. Finally, we conclude by substituting the linearized expression of $1/\lambda_s$ from Relation (3.1) into the above ones.

Therefore, the linearized expressions are:

$$\begin{aligned}
\boldsymbol{s}\cdot\boldsymbol{a}^{\alpha}s_{0\alpha} &= 1-\boldsymbol{s}_0\cdot\operatorname{grad}\boldsymbol{U}^P\cdot\boldsymbol{s}_0\\
\boldsymbol{\nu}\cdot\boldsymbol{a}^{\alpha}\nu_{0\alpha} &= 1-\boldsymbol{\nu}_0\cdot\operatorname{grad}\boldsymbol{U}^P\cdot\boldsymbol{\nu}_0\\
\boldsymbol{\nu}\cdot\boldsymbol{a}^{\alpha}s_{0\alpha} &= -2\boldsymbol{s}_0\cdot\operatorname{SYM}\operatorname{grad}\boldsymbol{U}^P\cdot\boldsymbol{\nu}_0
\end{aligned} \tag{3.2}$$

3.2.2 Strain tensor

The Green strain components in Relation (2.8) can be rewritten in terms of $\boldsymbol{U}^P$ and $\boldsymbol{\psi}$. The same trick as the previous section is applied – that is, going through Cartesian coordinates as an intermediate to index-free notations. Starting with the components of the first tensor coefficient $\boldsymbol{E}^{(0)}$:

$$\begin{aligned}
E^{(0)}_{\alpha\beta} &= \frac{1}{2}\left(a_{\alpha\beta}-A_{\alpha\beta}\right)\\
&= \frac{1}{2}\left(\boldsymbol{e}_\alpha\cdot\boldsymbol{U}_{,\beta}+\boldsymbol{U}_{,\alpha}\cdot\boldsymbol{e}_\beta\right)
\end{aligned}$$

$$\boxed{\boldsymbol{E}^{(0)}=\frac{1}{2}\left(\operatorname{grad}\boldsymbol{U}^{(1)}+\operatorname{grad}^{\mathsf{T}}\boldsymbol{U}^{(1)}\right)}$$

Then,

$$\begin{aligned}
E^{(1)}_{\alpha\beta} &= \frac{1}{2}\Big(\boldsymbol{e}_\alpha\cdot\left(\boldsymbol{a}_{3,\beta}-\boldsymbol{e}_{3,\beta}\right)+\boldsymbol{e}_\beta\cdot\left(\boldsymbol{a}_{3,\alpha}-\boldsymbol{e}_{3,\alpha}\right)+\boldsymbol{U}_{,\alpha}\cdot\boldsymbol{a}_{3,\beta}+\boldsymbol{U}_{,\beta}\cdot\boldsymbol{a}_{3,\alpha}\Big)\\
&= \frac{1}{2}\Big(\boldsymbol{e}_\alpha\cdot\left(\boldsymbol{a}_3-\boldsymbol{e}_3\right)_{,\beta}+\boldsymbol{e}_\beta\cdot\left(\boldsymbol{a}_3-\boldsymbol{e}_3\right)_{,\alpha}+\underbrace{\boldsymbol{U}_{,\alpha}\cdot\left(\boldsymbol{a}_3-\boldsymbol{e}_3\right)_{,\beta}}_{\text{second order}}+\underbrace{\boldsymbol{U}_{,\beta}\cdot\left(\boldsymbol{a}_3-\boldsymbol{e}_3\right)_{,\alpha}}_{\text{second order}}\Big)\\
&= \frac{1}{2}\Big(\boldsymbol{e}_\alpha\cdot\left(\boldsymbol{a}_3-\boldsymbol{e}_3\right)_{,\beta}+\boldsymbol{e}_\beta\cdot\left(\boldsymbol{a}_3-\boldsymbol{e}_3\right)_{,\alpha}\Big)
\end{aligned}$$

thus

$$\boxed{\boldsymbol{E}^{(1)}=\frac{1}{2}\left(\operatorname{grad}\left(\boldsymbol{a}_3-\boldsymbol{e}_3\right)+\operatorname{grad}^{\mathsf{T}}\left(\boldsymbol{a}_3-\boldsymbol{e}_3\right)\right)}$$

And for the last tensor coefficient,

$$\begin{aligned}
E^{(2)}_{\alpha\beta} &= \frac{1}{2}\Big(\boldsymbol{a}_{3,\alpha}\cdot\boldsymbol{a}_{3,\beta}-\cancel{\boldsymbol{e}_{3,\alpha}\cdot\boldsymbol{e}_{3,\beta}}\Big)\\
&= \frac{1}{2}\Big(\underbrace{\left(\boldsymbol{a}_3-\boldsymbol{e}_3\right)_{,\alpha}}_{\text{first order}}\cdot\underbrace{\left(\boldsymbol{a}_3-\boldsymbol{e}_3\right)_{,\beta}}_{\text{first order}}\Big)\\
&= 0
\end{aligned}$$

and so

$$\boxed{\boldsymbol{E}^{(2)}=\boldsymbol{0}}$$

As for the shear strain:

$$\begin{aligned}
E_{\alpha 3} &= \frac{1}{2}\big(\boldsymbol{e}_\alpha \cdot \boldsymbol{a}_3 + \boldsymbol{U}_{,\alpha} \cdot \boldsymbol{a}_3\big) \\
&= \frac{1}{2}\Big(\boldsymbol{e}_\alpha \cdot \boldsymbol{a}_3 + \boldsymbol{U}_{,\alpha} \cdot \boldsymbol{a}_3 - \boldsymbol{U}_{,\alpha} \cdot \boldsymbol{e}_3 + \underbrace{\boldsymbol{U}_{,\alpha} \cdot \boldsymbol{e}_3}_{=(\boldsymbol{U}\cdot\boldsymbol{e}_3)_{,\alpha}}\Big) \\
&= \frac{1}{2}\Big(\boldsymbol{e}_\alpha \cdot \boldsymbol{a}_3 + \underbrace{\boldsymbol{U}_{,\alpha} \cdot \big(\boldsymbol{a}_3 - \boldsymbol{e}_3\big)}_{\text{second order}} + \big(\underbrace{\boldsymbol{U} \cdot \boldsymbol{e}_3}_{W}\big)_{,\alpha}\Big) \\
E_{\alpha 3} &= \frac{1}{2}\big(\boldsymbol{e}_\alpha \cdot \boldsymbol{a}_3 + W_{,\alpha}\big)
\end{aligned}$$

Moreover, since $\boldsymbol{e}_\alpha$ is orthogonal to $\boldsymbol{e}_3$,

$$\begin{aligned}
E_{\alpha 3} &= \frac{1}{2}\Big(\boldsymbol{e}_\alpha \cdot (\boldsymbol{a}_3 - \boldsymbol{e}_3) + W_{,\alpha}\Big) \\
&= \frac{1}{2}(\boldsymbol{e}_\alpha \cdot \boldsymbol{\psi} + W_{,\alpha})
\end{aligned}$$

To conclude, discarding terms of order 2 and above in the Green strain tensor expressions leads to

$$\begin{aligned}
\boldsymbol{E}^{(0)} &= \frac{1}{2}\left(\mathrm{grad}\,\boldsymbol{U}^P + \mathrm{grad}^{\mathsf{T}}\,\boldsymbol{U}^P\right) &&= \mathrm{SYM}\,\mathrm{grad}\boldsymbol{U}^P \\
\boldsymbol{E}^{(1)} &= \frac{1}{2}\left(\mathrm{grad}\,\boldsymbol{\psi} + \mathrm{grad}^{\mathsf{T}}\,\boldsymbol{\psi}\right) &&= \mathrm{SYM}\,\mathrm{grad}\boldsymbol{\psi} \\
\boldsymbol{E}^{(2)} &= \boldsymbol{0} \\
E_{\alpha 3} &= \frac{1}{2}(\psi_\alpha + W_{,\alpha})
\end{aligned} \tag{3.3}$$

where the symbol SYM designates the symmetric part of a tensor.

3.2.3 Stress resultants and internal forces – Material model

The response of the membrane material is assumed to be isotropic and based on a hyperelastic model. There exists a great variety of hyperelastic constitutive laws that take different forms and involve different material parameters. Fortunately enough, the common feature of the hyperelastic laws is that all of them reduce to the standard linear Saint Venant-Kirchhoff law within the context of small deformations. As a result, one has only to consider the Saint Venant-Kirchhoff law when carrying out the linearization of the governing equations:

$$\boldsymbol{\Sigma} = \boldsymbol{\Sigma}_0 + 2\mu\boldsymbol{E} + \lambda(\mathrm{Tr}\,\boldsymbol{E})\boldsymbol{I} \tag{3.4}$$

where $\boldsymbol{\Sigma}_0$ is the pre-stress tensor and λ, μ are the Lamé parameters. Furthermore, the membranes are assumed to be under plane stress in the current configuration, which means that, at any point in domain Ω,

$$\sigma^{13} = \sigma^{23} = \sigma^{33} = 0 \quad \Leftrightarrow \quad \Sigma^{13} = \Sigma^{23} = \Sigma^{33} = 0$$

The same assumption is made on the reference stress state: $\Sigma_0^{13} = \Sigma_0^{23} = \Sigma_0^{33} = 0$. The zero normal stress hypothesis $\Sigma^{33} = 0$ (or, equivalently, $\sigma^{33} = 0$) leads to the so-called *reduced constitutive law*:

$$\forall \alpha, \beta \in \{1, 2\}, \quad \Sigma^{\alpha\beta} = \Sigma_0^{\alpha\beta} + K^{\alpha\beta\delta\gamma} E_{\delta\gamma} \tag{3.5}$$

where

$$K^{\alpha\beta\delta\gamma} = \frac{E}{1-\nu^2}\left(\frac{1}{2}(1-\nu)\left(A^{\alpha\gamma}A^{\beta\delta} + A^{\alpha\delta}A^{\beta\gamma}\right) + \nu A^{\alpha\beta}A^{\gamma\delta}\right)$$

and E is the Young modulus, ν the Poisson's ratio. The pre-stress resultants induced by the internal pressure are calculated from Relation (2.15): $\forall \alpha, \beta \in \{1,2\}$,

$$\begin{aligned} N_0^{\alpha\beta} &= \int_T \Sigma_0^{\alpha\beta}\,\mathrm{d}Z &&= 2\tau\Sigma_0^{\alpha\beta} \\ M_0^{\alpha\beta} &= \int_T Z\Sigma_0^{\alpha\beta}\,\mathrm{d}Z &&= 0 \\ M_0^{(2)\alpha\beta} &= \int_T Z^2\Sigma_0^{\alpha\beta}\,\mathrm{d}Z &&= \frac{\tilde{\tau}H^2}{2}\Sigma_0^{\alpha\beta} \end{aligned} \tag{3.6}$$

The stress resultants defined in Relation (2.15) are evaluated by performing the integrations over interval T. Taking into account the reduced constitutive law (3.5) and Relation (3.3) gives the resultants written in component-free notations:

$$\begin{aligned} \boldsymbol{N} &= \boldsymbol{N}_0 + \frac{2E\tau}{1-\nu^2}\left((1-\nu)\mathrm{SYM}\,\mathrm{grad}\boldsymbol{U}^P + \nu(\,\mathrm{div}\,\boldsymbol{U}^P)\boldsymbol{I}^P\right) \\ \boldsymbol{M} &= \frac{E\tilde{\tau}H^2}{2(1-\nu^2)}\left((1-\nu)\mathrm{SYM}\,\mathrm{grad}\boldsymbol{\psi} + \nu(\,\mathrm{div}\,\boldsymbol{\psi})\boldsymbol{I}^P\right) \\ \boldsymbol{M}^{(2)} &= \boldsymbol{M}_0^{(2)} + \frac{E\tilde{\tau}H^2}{2(1-\nu^2)}\left((1-\nu)\mathrm{SYM}\,\mathrm{grad}\boldsymbol{U}^P + \nu(\,\mathrm{div}\,\boldsymbol{U}^P)\boldsymbol{I}^P\right) \\ \boldsymbol{Q} &= \boldsymbol{0} \\ \boldsymbol{Q}^{(1)} &= \boldsymbol{0} \end{aligned} \tag{3.7}$$

where $\boldsymbol{I}^P = \boldsymbol{e}_\alpha \otimes \boldsymbol{e}_\alpha$ is the identity tensor restricted to the plane $\boldsymbol{e}_1\boldsymbol{e}_2$. These relations are used to compute stresses after having found a solution to the problem. Substituting the linearized expressions of the stress resultants of Eq. (3.7) into Eq. (2.16) leads to

$$\boldsymbol{R}^\beta = N_0^{\alpha\beta}(\boldsymbol{e}_\alpha + \boldsymbol{U}_{,\alpha}) + \frac{2E\tau}{1-\nu^2}\left(\frac{1-\nu}{2}(U_{\beta,\alpha} + U_{\alpha,\beta}) + \nu\delta^{\alpha\beta}U_{\gamma,\gamma}\right)\boldsymbol{e}_\alpha \tag{3.8}$$

$$\boldsymbol{L}^\beta = \frac{E\tilde{\tau}H^2}{2(1-\nu^2)}\left(\frac{1-\nu}{2}(\psi_{\alpha,\beta} + \psi_{\beta,\alpha}) + \nu\delta^{\alpha\beta}\psi_{\gamma,\gamma}\right)\boldsymbol{e}_\alpha + M_0^{(2)\alpha\beta}\boldsymbol{\psi}_{,\alpha} \tag{3.9}$$

Remark 3.1. Note that the pre-stress bending moment of order two, $M_0^{(2)\alpha\beta}$, in the last equation has been obtained thanks to the correct linearization process described at the beginning of this section. It would not have been found if we had considered the linear framework from the start. It is analogous to the term pI_0/S_0 in previous works on inflatable beams [7].

Remark 3.2. The drop cords need not to be modeled: we assumed that they were stiff enough to guarantee a constant thickness of the panel.

3.2.4 External loads other than the internal pressure

The expressions of the external loads in Eq. (2.38) must also be linearized. From Relations (3.2), the right-hand sides of Eq. (2.38) then become

$$\|\boldsymbol{a}^3\|\Gamma^s\boldsymbol{\nu}\cdot\boldsymbol{a}^\alpha\nu_{0\alpha} = (1 - \boldsymbol{\nu}_0\cdot\mathrm{grad}\,\boldsymbol{U}^P\cdot\boldsymbol{\nu}_0)\Gamma^s$$

$$\|\boldsymbol{a}^3\|\left(\Gamma^s\boldsymbol{\nu}\cdot\boldsymbol{a}^\alpha s_{0\alpha}-\Gamma^\nu\boldsymbol{s}\cdot\boldsymbol{a}^\alpha s_{0\alpha}\right)=-\left(2\boldsymbol{s}_0\cdot\mathrm{SYM}\,\mathrm{grad}\boldsymbol{U}^P\cdot\boldsymbol{\nu}_0\right)\Gamma^s-\left(1-\boldsymbol{s}_0\cdot\mathrm{grad}\,\boldsymbol{U}^P\cdot\boldsymbol{s}_0\right)\Gamma^\nu$$

3.2.5 Internal pressure load

Taking into account the expressions of $\boldsymbol{a}_\alpha$ and $\boldsymbol{a}_3$, the pressure term in equation of motion (2.36a) becomes

$$\frac{p\tilde{H}}{\sqrt{A}}\left(\boldsymbol{a}_{3,1}\times\boldsymbol{a}_2+\boldsymbol{a}_1\times\boldsymbol{a}_{3,2}\right)=\frac{p\tilde{H}}{\sqrt{A}}\left(\boldsymbol{\psi}_{,1}\times\boldsymbol{e}_2+\boldsymbol{e}_1\times\boldsymbol{\psi}_{,2}\right)\tag{3.10}$$

Note that $\sqrt{A}=1$ because the basis is orthonormal. Projecting Relation (3.10) on $\boldsymbol{a}^\alpha$ yields

$$\forall\alpha\in\{1,2\},\quad\left(\boldsymbol{\psi}_{,1}\times\boldsymbol{e}_2+\boldsymbol{e}_1\times\boldsymbol{\psi}_{,2}\right)\cdot\boldsymbol{a}^\alpha=\boldsymbol{\psi}_{,1}\cdot(\boldsymbol{e}_2\times\boldsymbol{e}_\alpha)+(\boldsymbol{e}_\alpha\times\boldsymbol{e}_1)\cdot\boldsymbol{\psi}_{,2}=0$$

since $\boldsymbol{\psi}$ and its derivatives are perpendicular to $\boldsymbol{e}_3$. Then, projecting Eq. (3.10) on $\boldsymbol{a}^3$ yields

$$\begin{aligned}\left(\boldsymbol{\psi}_{,1}\times\boldsymbol{e}_2+\boldsymbol{e}_1\times\boldsymbol{\psi}_{,2}\right)\cdot\boldsymbol{a}^3&=\boldsymbol{\psi}_{,1}\cdot(\boldsymbol{e}_2\times\boldsymbol{e}_3)+(\boldsymbol{e}_3\times\boldsymbol{e}_1)\cdot\boldsymbol{\psi}_{,2}\\&=\boldsymbol{\psi}_{,1}\cdot\boldsymbol{e}_1+\boldsymbol{\psi}_{,2}\cdot\boldsymbol{e}_2=\psi_{1,1}+\psi_{2,2}=\mathrm{div}\,\boldsymbol{\psi}\end{aligned}$$

The pressure term in equation of motion (2.36b) becomes

$$\boldsymbol{a}_3\times\left(\boldsymbol{a}_1\times\boldsymbol{a}_2\right)=\boldsymbol{a}_3\times\left((\boldsymbol{e}_1+\boldsymbol{U}_{,1})\times(\boldsymbol{e}_2+\boldsymbol{U}_{,2})\right)$$

The second order terms are neglected, leaving only

$$\begin{aligned}\boldsymbol{a}_3\times\left(\boldsymbol{a}_1\times\boldsymbol{a}_2\right)&\approx\boldsymbol{\psi}\times\left(\boldsymbol{e}_1\times\boldsymbol{e}_2\right)+W_{,2}\boldsymbol{e}_1-W_{,1}\boldsymbol{e}_2\\&=\left(\boldsymbol{\psi}+W_{,1}\boldsymbol{e}_1+W_{,2}\boldsymbol{e}_2\right)\times\boldsymbol{e}_3=(\boldsymbol{\psi}+\mathrm{grad}\,W)\times\boldsymbol{e}_3\end{aligned}$$

Likewise, the pressure line force on the edge in boundary condition (2.37) writes

$$p\tilde{H}\mathrm{P}_{,s_0}\times\boldsymbol{a}_3\approx p\tilde{H}\left(\mathrm{P}_{0,s_0}\times\boldsymbol{\psi}+\boldsymbol{U}_{,s_0}\times\boldsymbol{e}_3\right)$$

The last term to be linearized is the pressure term in boundary conditions (2.38):

$$\frac{p\tilde{H}^3}{12}(\boldsymbol{a}_{3,s_0}\times\boldsymbol{a}_3)\cdot\boldsymbol{a}^\alpha\nu_{0\alpha}\approx\frac{p\tilde{H}^3}{12}\boldsymbol{\psi}_{,s_0}\cdot\boldsymbol{s}_0$$

3.2.6 Inertial quantities

The only fact worth noting for the inertial quantities is that the inertial term in the moment equation (2.36b) should be linearized as follows:

$$\frac{\rho\tilde{\tau}H^2}{2}\boldsymbol{a}_3\times\ddot{\boldsymbol{a}}_3=\frac{\rho\tilde{\tau}H^2}{2}\boldsymbol{a}_3\times\ddot{\boldsymbol{\psi}}$$

It is more convenient to keep $\boldsymbol{a}_3$ as is in the last right-hand side and not to replace it with $\boldsymbol{\psi}+\boldsymbol{e}_3$, since this enables one to more easily obtain the final expression of the moment equation (3.13) below.

3.3 Linearized equations of motion

The linearized equations of motion are obtained and written in component-free notations which are independent of the coordinate system.

Linearized equations of motion of inflatable panels

• The equilibrium conditions are:

- for the in-plane forces: $\forall t, \forall \mathrm{P}_0 \in S_0$,

$$\boxed{\boldsymbol{N}_0 : \operatorname{grad}\operatorname{grad}\boldsymbol{U}^P + \frac{E\tau}{1-\nu^2}\Big[(1-\nu)\boldsymbol{\Delta}\boldsymbol{U}^P + (1+\nu)\operatorname{grad}\operatorname{div}\boldsymbol{U}^P\Big] + \boldsymbol{q}\cdot\boldsymbol{a}^\alpha = 2\tau\rho\ddot{\boldsymbol{U}}^P} \tag{3.11}$$

- for the out-of-plane forces: $\forall t, \forall \mathrm{P}_0 \in S_0$,

$$\boxed{\boldsymbol{N}_0 : \operatorname{grad}\operatorname{grad} W + p\tilde{H}\operatorname{div}\boldsymbol{\psi} + \boldsymbol{q}\cdot\boldsymbol{a}^3 = 2\tau\rho\ddot{W}} \tag{3.12}$$

• The **moment equilibrium equations** are

$\forall t, \forall \mathrm{P}_0 \in S_0$,

$$\boxed{\begin{aligned}&\frac{D^*}{2}\Big[(1-\nu)\boldsymbol{\Delta}\boldsymbol{\psi} + (1+\nu)\operatorname{grad}\operatorname{div}\boldsymbol{\psi}\Big] + \operatorname{div}\Big(\operatorname{grad}\boldsymbol{\psi}\cdot\boldsymbol{M}_0^{(2)}\Big)\\ &- p\tilde{H}\left(\boldsymbol{\psi} + \operatorname{grad} W\right) = \frac{\rho\tilde{\tau}H^2}{2}\ddot{\boldsymbol{\psi}}\end{aligned}} \tag{3.13}$$

where $\boxed{D^* = \dfrac{E\tilde{\tau}H^2}{2(1-\nu^2)}}$.

• The two **force boundary conditions** are

- in-plane forces equilibrium: $\forall t, \forall \mathrm{P}_0 \in \partial S_0$,

$$\boxed{\frac{2E\tau}{1-\nu^2}\Big((1-\nu)\mathrm{SYM}\operatorname{grad}\boldsymbol{U}^P + \nu\big(\operatorname{div}\boldsymbol{U}^P\big)\boldsymbol{I}\Big)\cdot\boldsymbol{\nu}_0 + p\tilde{H}\big[\operatorname{grad}\boldsymbol{U}^P\cdot\boldsymbol{\nu}_0 + \boldsymbol{U}^P_{,s_0}\times\boldsymbol{e}_3\big] = \boldsymbol{q}'\cdot\boldsymbol{a}^\alpha} \tag{3.14}$$

- out-of-plane forces equilibrium: $\forall t, \forall \mathrm{P}_0 \in \partial S_0$,

$$\boxed{p\tilde{H}\left(\boldsymbol{\psi} + \operatorname{grad} W\right)\cdot\boldsymbol{\nu}_0 = \boldsymbol{q}\cdot\boldsymbol{a}^3} \tag{3.15}$$

• The two **moment boundary conditions** are

- equilibrium of moments normal to the border: $\forall t, \forall \mathrm{P}_0 \in \partial S_0$,

$$\boxed{\begin{aligned}&D^*\Big[(1-\nu)\boldsymbol{\nu}_0\cdot\mathrm{SYM}\operatorname{grad}\boldsymbol{\psi}\cdot\boldsymbol{\nu}_0 + \nu\operatorname{div}\boldsymbol{\psi}\Big] + \boldsymbol{\nu}_0\cdot\operatorname{grad}\boldsymbol{\psi}\cdot\boldsymbol{M}_0^{(2)}\cdot\boldsymbol{\nu}_0 + \frac{p\tilde{H}^3}{12}\boldsymbol{\psi}_{,s_0}\cdot\boldsymbol{s}_0\\ &= \left(1 - \boldsymbol{\nu}_0\cdot\operatorname{grad}\boldsymbol{U}^P\cdot\boldsymbol{\nu}_0\right)\Gamma^s\end{aligned}} \tag{3.16}$$

- equilibrium of moments tangent to the border: $\forall t, \forall \mathrm{P}_0 \in \partial S_0$,

$$\boxed{\begin{aligned}&D^*(1-\nu)\boldsymbol{s}_0\cdot\mathrm{SYM}\operatorname{grad}\boldsymbol{\psi}\cdot\boldsymbol{\nu}_0 + \boldsymbol{s}_0\cdot\operatorname{grad}\boldsymbol{\psi}\cdot\boldsymbol{M}_0^{(2)}\cdot\boldsymbol{\nu}_0 - \frac{p\tilde{H}^3}{12}\boldsymbol{\psi}_{,s_0}\cdot\boldsymbol{\nu}_0\\ &= -\left(2\boldsymbol{s}_0\cdot\mathrm{SYM}\operatorname{grad}\boldsymbol{U}^P\cdot\boldsymbol{\nu}_0\right)\Gamma^s - \left(1 - \boldsymbol{s}_0\cdot\operatorname{grad}\boldsymbol{U}^P\cdot\boldsymbol{s}_0\right)\Gamma^\nu\end{aligned}} \tag{3.17}$$

Proof.

The linear momentum equations (3.11) and (3.12) are obtained by substituting $\boldsymbol{R}^\alpha_{,\alpha}$ from Eq. (3.8) into

Eq. (2.36a). The equivalence (2.40) is applied to Eq. (2.36b) with the expression of $\boldsymbol{L}^{\beta}$ in Eq. (3.9) to produce the angular momentum equations (3.13). As for the boundary conditions, substituting Eq. (3.8) into Eq. (2.37) yields (3.14) and (3.15). Likewise, using Eq. (3.9) to rewrite Eq. (2.38) yields (3.16) and (3.17).

Common form of the pre-tension tensors

In Cartesian or cylindrical coordinates, it can be shown that the pre-stress tensor $\boldsymbol{\Sigma}_0$ is simply

$$\mathrm{Mat}(\boldsymbol{\Sigma}_0; \boldsymbol{e}_x\boldsymbol{e}_y\boldsymbol{e}_z) = \mathrm{Mat}(\boldsymbol{\Sigma}_0; \boldsymbol{e}_r\boldsymbol{e}_\theta\boldsymbol{e}_z) = \frac{p\tilde{H}}{2\tau}\begin{bmatrix}1&0&0\\0&1&0\\0&0&0\end{bmatrix}$$

Hence, the matrices of pre-tension $\boldsymbol{N}_0$ and pre-moment $\boldsymbol{M}_0^{(2)}$ after integrating over the thickness are

$$\mathrm{Mat}(\boldsymbol{N}_0; \boldsymbol{e}_x\boldsymbol{e}_y\boldsymbol{e}_z) = \mathrm{Mat}(\boldsymbol{N}_0; \boldsymbol{e}_r\boldsymbol{e}_\theta\boldsymbol{e}_z) = N_0\begin{bmatrix}1&0&0\\0&1&0\\0&0&0\end{bmatrix}$$

$$\mathrm{Mat}\left(\boldsymbol{M}_0^{(2)}; \boldsymbol{e}_x\boldsymbol{e}_y\boldsymbol{e}_z\right) = \mathrm{Mat}\left(\boldsymbol{M}_0^{(2)}; \boldsymbol{e}_r\boldsymbol{e}_\theta\boldsymbol{e}_z\right) = M_0^{(2)}\begin{bmatrix}1&0&0\\0&1&0\\0&0&0\end{bmatrix}$$

where $N_0 = p\tilde{H}$ and $M_0^{(2)} = \dfrac{pH^2\tilde{H}\tilde{\tau}}{4\tau}$. Note that the pre-stress moment of second order $M_0^{(2)}$ had been neglected in the literature on inflatable panel theories [10, 13]. Whenever $\boldsymbol{N}_0 = N_0\boldsymbol{I}^P = p\tilde{H}\boldsymbol{I}^P$ and $\boldsymbol{M}_0^{(2)} = M_0^{(2)}\boldsymbol{I}^P$, an alternative form of (3.12) and (3.13) is

$$p\tilde{H}(\Delta W + \operatorname{div}\boldsymbol{\psi}) + \boldsymbol{q}\cdot\boldsymbol{a}^3 = 2\tau\rho\ddot{W} \tag{3.18}$$

$$\left(D^*\frac{1-\nu}{2} + M_0^{(2)}\right)\Delta\boldsymbol{\psi} + D^*\frac{1+\nu}{2}\operatorname{grad}\operatorname{div}\boldsymbol{\psi} - p\tilde{H}(\boldsymbol{\psi} + \operatorname{grad} W) = \frac{\rho\tilde{\tau}H^2}{2}\ddot{\boldsymbol{\psi}} \tag{3.19}$$

Chapter 4

Application example in statics

Let us show how to solve the foregoing linearized equations for the static bending of a simply-supported circular inflatable panel subjected to a uniform vertical load. This problem admits an analytical solution as the geometry, the loading and the boundary conditions are simple.

4.1 Solution for the static bending of a circular inflatable panel

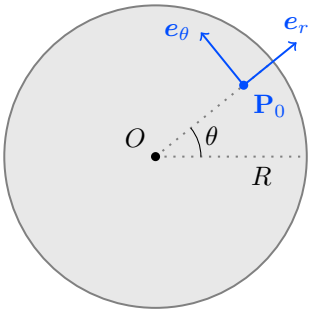

Figure 4.1: Geometry of the circular panel and local basis.

Let $\boldsymbol{q} = q\boldsymbol{e}_3$ denote the uniform, vertical dead load applied over the mid-surface S_0 and (r, θ, z) the cylindrical coordinates of any point of the panel (Fig. 4.1). Since the static bending problem is axisymmetric around the axis $(\mathrm{O}; \boldsymbol{e}_3)$, the unknown fields W and $\boldsymbol{\psi}$ are functions of the radial distance r only.

After discarding time-dependent terms, Eq. (3.12) and (3.13) become, in polar coordinates:

$$\frac{1}{r}\big(r(W_{,r} + \psi_r)\big)_{,r} = -\frac{q}{p\tilde{H}} \tag{4.1}$$

$$-K\left(\psi_{r,rr} + \frac{\psi_{r,r}}{r} - \frac{\psi_r}{r^2}\right) + p\tilde{H}(W_{,r} + \psi_r) = 0 \tag{4.2}$$

where $\boxed{K = D^* + M_0^{(2)} = \dfrac{E\tilde{\tau}H^2}{2(1-\nu^2)} + \dfrac{pH^2\tilde{H}\tilde{\tau}}{4\tau}} > 0$. The boundary condition are $W(R) = 0$ and Eq. (3.16) with $\Gamma^s = \Gamma^\theta = 0$:

$$K\psi_{r,r}(R) + K'\frac{\psi_r(R)}{R} = 0 \tag{4.3}$$

where $\boxed{K' = \nu D^* + \frac{p\tilde{H}^3}{12} = \frac{\nu E \tilde{\tau} H^2}{2(1-\nu^2)} + \frac{p\tilde{H}^3}{12}} > 0$. Integrating Relation (4.1) with respect to r gives

$$W_{,r} + \psi_r = -\frac{q}{p\tilde{H}}\left(\frac{r}{2} + \frac{C_1}{r}\right) \tag{4.4}$$

where C_1 is a constant of integration. Using Relation (4.2), one obtains a differential equation of unknown ψ_r, which is a Cauchy-Euler equation:

$$r^2\psi_{r,rr} + r\psi_{r,r} - \psi_r = -\frac{q}{K}\left(\frac{r^3}{2} + C_1 r\right) \tag{4.5}$$

With the change of variables $r = \exp x \Leftrightarrow x = \log r$ (with $r > 0$) and $z(x) = \psi_r(r) = \psi_r(\exp x)$, the associated homogeneous equation is

$$\frac{\mathrm{d}^2 z}{\mathrm{d}x^2} - z = 0$$

The solution is $z(x) = C_2 \exp(x) + C_3 \exp(-x)$ where C_2 and C_3 are constants of integration. Hence the solution to the homogeneous equation corresponding to Eq. (4.5):

$$\psi_r(r) = C_2 r + \frac{C_3}{r}$$

The method of variation of parameters is used to find the solution to Eq. (4.5). The following system of equations is obtained:

$$\begin{cases} r^2 C_2' + C_3' = 0 \\ r^2 C_2' - C_3' = -\frac{q}{K}\left(\frac{r^3}{2} + C_1 r\right) \end{cases} \Rightarrow \begin{cases} C_2 = -\frac{q}{2K}\left(\frac{r^2}{4} + C_1 \log r\right) + C_4 \\ C_3 = \frac{q}{2K}\left(\frac{r^4}{8} + C_1 \frac{r^2}{2}\right) + C_5 \end{cases}$$

where C_4 and C_5 are new constants of integration. Substituting C_2 and C_3 in the expression of ψ_r writes

$$\psi_r = \frac{q}{2K}\left(-\frac{r^3}{8} + C_1\frac{r}{2} - C_1 r \log r\right) + C_4 r + \frac{C_5}{r}$$

Given that the problem is axisymmetric, one must have $\lim_{r\to 0} \psi_r(r) = 0$, which implies $C_5 = 0$. The deflection W can then be derived from Relation (4.4):

$$W_{,r} = -\frac{q}{2K}\left(-\frac{r^3}{8} + C_1\frac{r}{2} - C_1 r \log r\right) - C_4 r - \frac{q}{p\tilde{H}}\left(\frac{r}{2} + \frac{C_1}{r}\right)$$

The constants of integration are deduced from the boundary conditions and physical considerations. It follows that:

$$\begin{cases} W(r) = q(R^2 - r^2)\left(\frac{1}{4p\tilde{H}} + \frac{1}{64K}\left(\frac{5K + K'}{K + K'}R^2 - r^2\right)\right) \\ \psi_r(r) = \frac{q}{16K} r \left(\frac{3K + K'}{K + K'}R^2 - r^2\right) \end{cases} \tag{4.6}$$

While the deflection W and the fiber rotation ψ depend linearly on the load q, they are intricate functions of pressure p via the ratio $1/4p\tilde{H}$ and the coefficients K and K'. Let us now plot the solution (4.6) using the geometric quantities $R_\varnothing$ and $H_\varnothing$ in the natural state, τ and the material properties E and ν from Table 5.1 and taking the external surface load $q = 100$ Pa. Fig. 4.2 shows the plots of the deflection W and the fiber rotation ψ_r for four different inflation pressures p and two panel heights $H_\varnothing$. As expected, the deflection

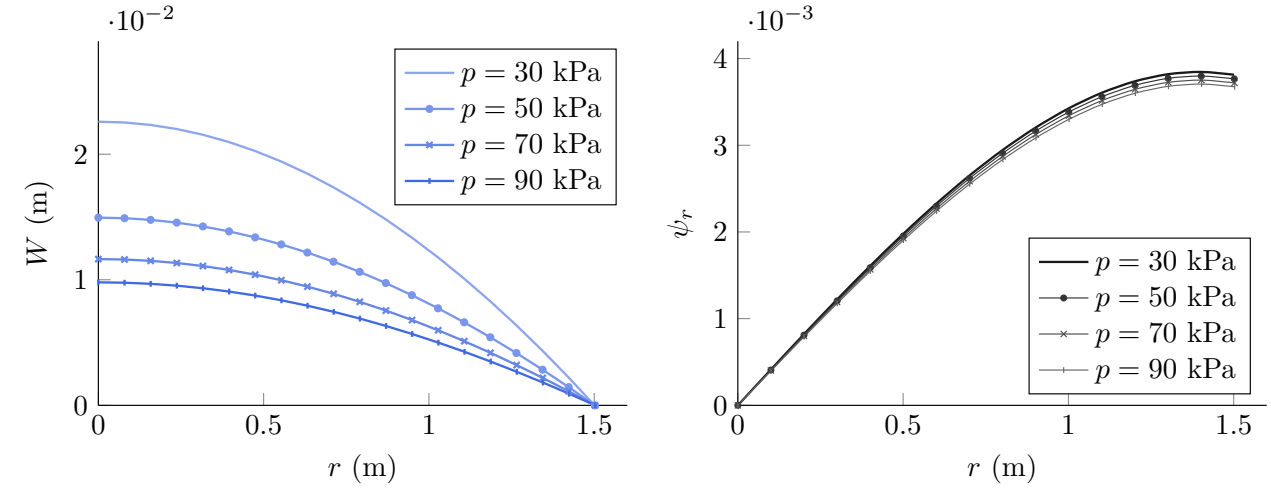

(a) $H_\varnothing = 10$ cm

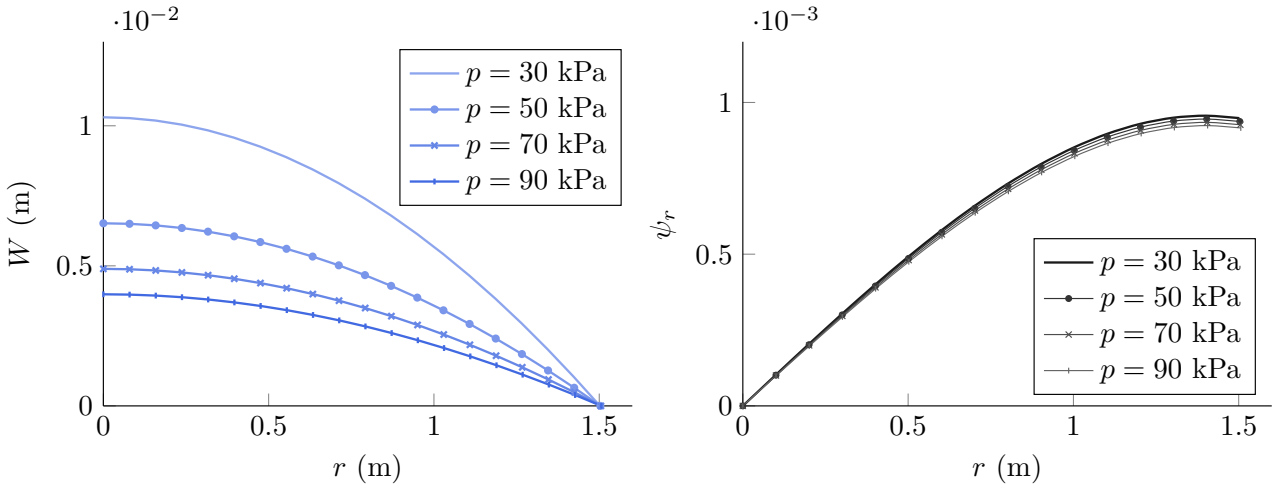

(b) $H_\varnothing = 20$ cm

Figure 4.2: Deflection W and fiber rotation ψ_r for a simply supported circular panel subjected to uniform vertical load $q = 100$ Pa for four different inflation pressures p ($R_\varnothing = 1.5$ m).

becomes lower as the pressure p increases, which reflects the stiffening phenomenon of inflatable panels, i.e. the increase in bending stiffness with pressurization. Also, the deflection decreases when the height H increases since the pre-stress $\boldsymbol{N}_0$ is proportional to $\tilde{H}$, creating additional structural stiffness. As regards the change of the fiber rotation ψ_r, it depends on the pressure p via coefficients K and K' and also via (R, H) given by Relations (2.41)–(2.54). However, the numerical computations show that the dependence of ψ_r on p is rather weak, see Fig. 4.2. The values of the rotation ψ_r are very small (here 10^{-3}), which means that the fibers remain practically vertical during the deformation process.

In order to show the sensitivity of the deflection W to the value of the membrane Young modulus E, use is made again of solution (4.6) to compute W with two values different by ± 0.8 GPa from $E = 2.5$ GPa, namely $E = 1.7$ GPa and $E = 3.3$ GPa. It is observed that W varies monotonically with E, so that two curves are enough to draw the envelope. Moreover, as one can see in Fig. 4.3, the larger the external load q is, the greater the influence of E on the deflection.

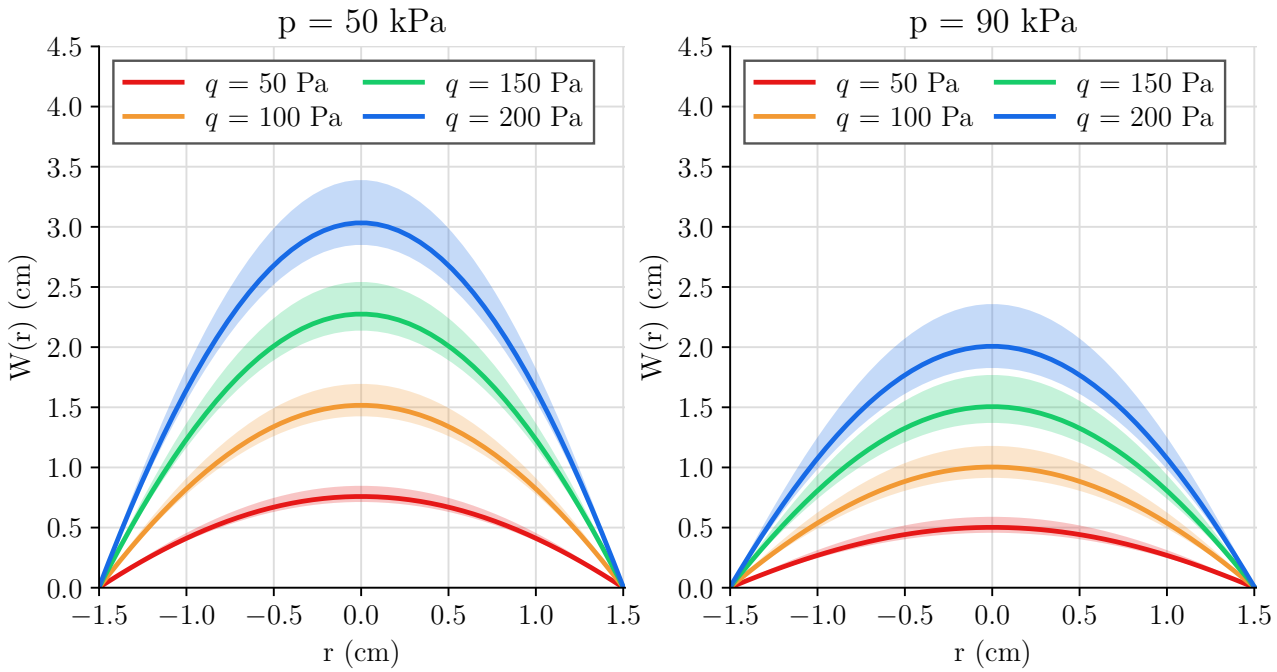

Figure 4.3: Sensitivity of the deflection to the membrane's Young modulus E for two inflation pressures and four external loads ($R_\varnothing = 1.5$ m, $H_\varnothing = 10$ cm, $E = 2.5$ GPa for the thick line).

4.2 Limit of validity of the solution (wrinkling load)

While fabric materials can withstand large tensile stresses, their stiffness when subjected to compressive stress is very low. Large deformations may cause the net stress to become zero or negative, giving rise to a localized buckling phenomenon, commonly named *wrinkling* (Fig. 4.4). Upon finding a solution, one must check that the stresses are positive everywhere in the membranes for the analytical solution to remain valid. The load for which the stress becomes zero is called the wrinkling load q_w. Since the determination of q_w is based on the linearized solution, it is only an estimate and cannot predict the actual onset of wrinkling for strongly nonlinear problems.

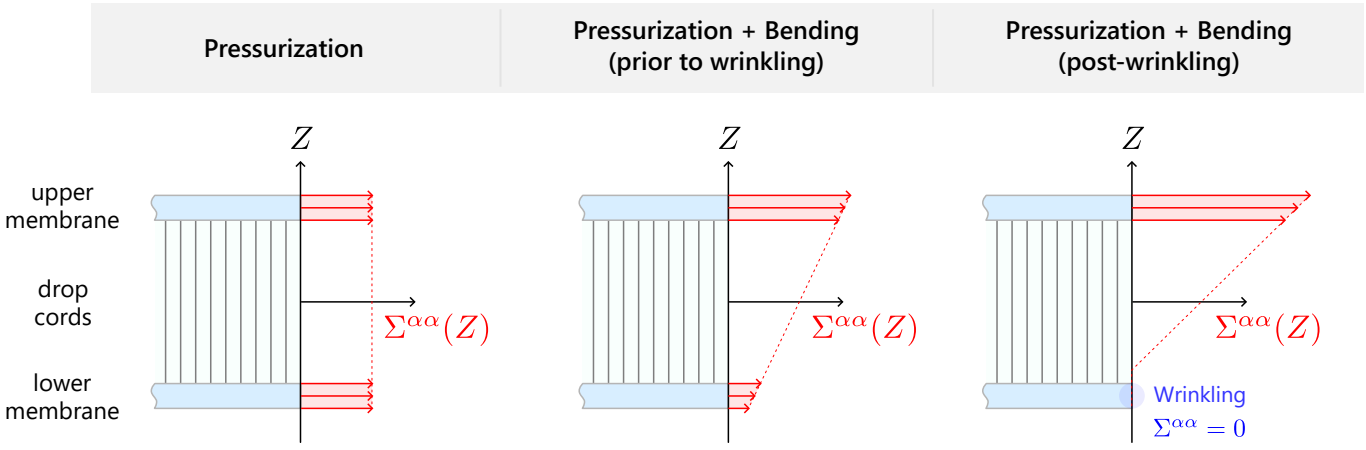

Figure 4.4: Stress profile in the panel before and after wrinkling.

Let us compute the strain tensors at every point of the panel. Combining the solution in Eq. (4.6) and

Relation Eq. (3.3) gives

$$\mathrm{Mat}(\boldsymbol{E};\boldsymbol{e}_r\boldsymbol{e}_\theta\boldsymbol{e}_3) = Z\begin{bmatrix}\psi_{r,r} & 0\\ 0 & \frac{\psi_r}{r}\end{bmatrix} = \frac{Zq}{16K}\begin{bmatrix}\frac{3K+K'}{K+K'}R^2-3r^2 & 0\\ 0 & \frac{3K+K'}{K+K'}R^2-r^2\end{bmatrix} \tag{4.7}$$

The reduced constitutive law (3.5) yields the principal stresses:

$$\Sigma^{rr} = \frac{p\tilde{H}}{2\tau} + \frac{EZq}{16K(1-\nu^2)}\left(\frac{3K+K'}{K+K'}R^2(1+\nu)-r^2(3+\nu)\right)$$
$$\Sigma^{\theta\theta} = \frac{p\tilde{H}}{2\tau} + \frac{EZq}{16K(1-\nu)}\left(\frac{3K+K'}{K+K'}R^2-r^2\right)$$

The principal stresses reach their maximum for $r=0$ and $Z=\pm H/2$ (depending on the sign of q). Cancelling either Σ^{rr} or $\Sigma^{\theta\theta}$ gives the same expression of the wrinkling load:

$$\boxed{q_w = \pm\frac{p\tilde{H}}{\tau H}\frac{16K(1-\nu)}{ER^2\frac{3K+K'}{K+K'}}} \tag{4.8}$$

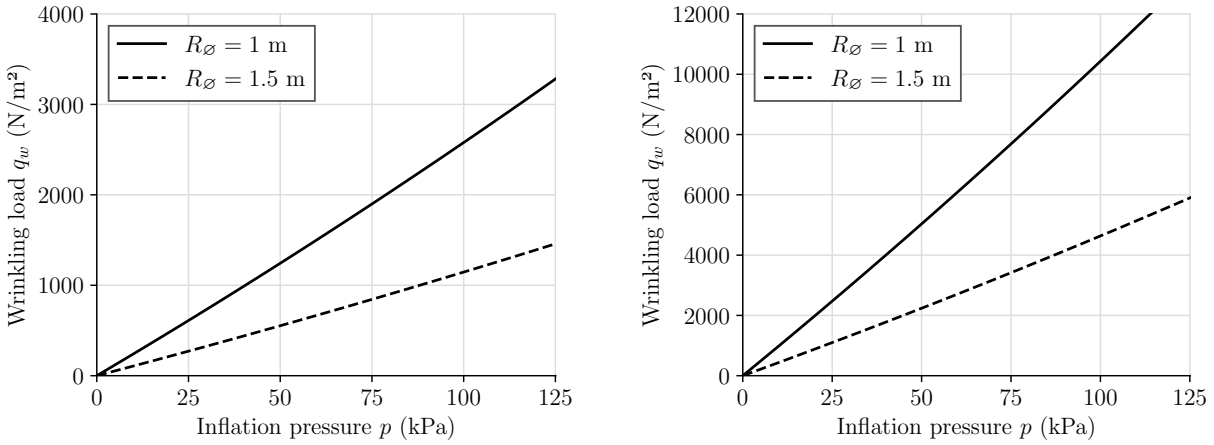

(a) Panel height $H_\varnothing = 10$ cm.

(b) Panel height $H_\varnothing = 20$ cm.

Figure 4.5: Wrinkling load of the bending solution for two different panel radii and heights (E=2.5 GPa).

For small pressures and small panel heights, Fig. 4.5 shows that the evolution of the wrinkling load is quasi-linear. Indeed, the coefficients K and K' are combinations of the membrane flexural rigidity and the pre-stress caused by inflation, which is very small compared to the first term: $K \approx \dfrac{E\tilde{\tau}H^2}{2(1-\nu^2)}$ and $K' \approx \nu K$. Furthermore, if $\tilde{\tau} \approx \tau$, $\tilde{H} = H - 2\tau \approx H$, $K \approx D^*$ and $K' \approx \nu D^*$, the equation (4.8) simplifies to

$$q_{\text{wrinkling}} \approx \pm\frac{8p}{3+\nu}\left(\frac{H}{R}\right)^2 \tag{4.9}$$

which no longer appears to depend on E, except through the inflated dimensions H and R.

Chapter 5

Finite element simulation of inflatable panels

After obtaining the linearized governing equations and having solved them for a circular panel, it is necessary to validate the theoretical deflection by comparing it to a reference solution of the fully nonlinear problem. By doing so, we can assess the range of applicability of our theory, before the loss of linearity becomes too important. Furthermore, the pre-dimensioning of the experimental setup relies on the values provided by the analytical model: the choice of loading type, measuring tools and the design of the supporting frame depend on the range of displacements that are expected to be observed. From a theoretical research perspective, being able to quickly iterate on the 3D finite element simulation also has the benefit of giving us a better intuition of the system's response and pointing out flaws in the analytical model that we were able to rectify. In this chapter, we present a three-dimensional, nonlinear finite element analysis of a circular inflatable panel and compare its outputs to the analytical results of Chapter 3.

The finite element simulation relies on the Surface Evolver program [34], an open source software originally intended for modelling liquid surfaces under constraints[1], which can be repurposed to the simulation of tensile membranes by implementing the appropriate strain energy density function for the material model. The mesh geometry, boundary conditions, material properties and loading increments are specified in a text file written in the Evolver scripting language. The software allows to simulate structures made of one-dimensional lines and two-dimensional facets undergoing finite strain and large displacements from minimization of potential energy. The gas used for inflation is taken into account exclusively through the pressure load it generates and does not constitute a heavy material medium, as justified by the static nature of the study.

5.1 Description of the numerical model

5.1.1 Nonlinearities

The simulation incorporates three kinds of nonlinearities: large displacements, follower pressure loads and slacking drop cords.

1. With large displacements, the current configuration will differ from the reference configuration, which

[1]The program was developed by Ken Brakke, Professor Emeritus from the Department of Mathematics and Computer Science of Susquehanna University. The simulations presented in this work were carried out using the last release version of the software from August 2013.

allows to precisely account for all the effects that are a function of the current geometry. It can also capture the formation of wrinkles, which was impossible with the simpler geometric description used in the theory.

2. The pressure forces will always act normal to the current mesh geometry. In the linearized theory, the current panel configuration (and therefore the orientation of the normals) is described by the vectors $\boldsymbol{U}$ and $\boldsymbol{\psi} = \boldsymbol{a}_3 - \boldsymbol{e}_3$ which were assumed small of the first order. The vertical component of $\boldsymbol{\psi}$ was also neglected at the beginning of the linearization process. Because small terms of the second order were neglected, some information about the normals was lost and the pressure-related terms which depend on it are incorrectly described when the displacements become large.

3. The kinematic assumptions of the theory remain valid as long as the drop cords are all taut. However, since the drop yarns cannot resist compression, they should loose their stiffness when they are not stretched. Therefore, we scan the drop cords at every iteration to cancel the stiffness of the bars whose current length is shorter than their original length. It should be noted, however, that this only occurred exceptionally throughout all of our simulations, and always at the panel's edge where the lateral wall would bring the membranes closer.

Another difference with the theory is that the lateral wall is modeled in the finite element simulation, while it was discarded in the theory.

5.1.2 Modeling membranes and drop cords

The 3D structure comprises three membranes (upper, lower and lateral) and drop cords that connect the upper and lower faces. The initial mesh is procedurally generated from a simple cylinder geometry which is then subdivided until convergence is reached at a total of 12,288 surface elements and 6,146 nodes (Fig. 5.1[2]). It is then scaled to have overall thickness $H_\varnothing$ and radius $R_\varnothing$. The membranes are discretized using 3-node pure membrane triangular elements and the yarns as 2-node bar elements connecting the upper and lower surfaces, Fig. 5.2. The behavior of the membranes is modeled by the Saint Venant–Kirchhoff law and the values of E, ν and τ are presented in Table 5.1.

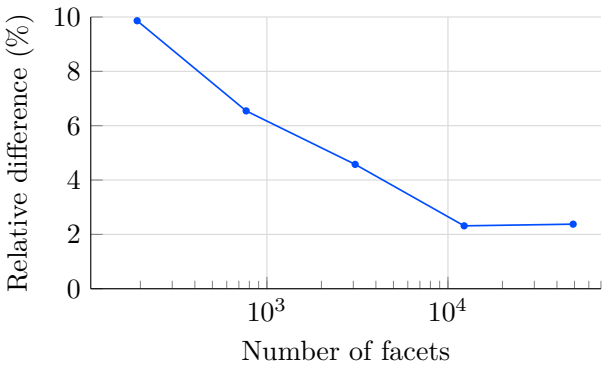

Figure 5.1: Convergence of the relative difference between the theoretical and numerical initial slopes as the number of surface elements in the mesh increases. ($H_\varnothing = 20$ cm, $R_\varnothing = 1$ m, $p = 50$ kPa)

Special care must be taken when modelling the drop cords, since modelling each of them individually

[2]The calculation of the relative difference on the slope will be explained in Section 5.2.4.

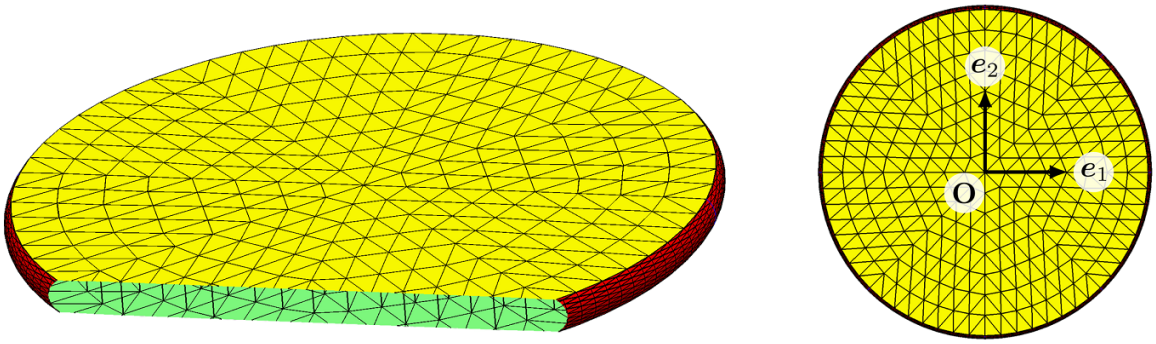

Figure 5.2: Cut-view and top view of the mesh used in the simulations in the reference configuration.

Parameter	Values
$E\tau$	389 N/mm
ν	0.25
τ	1 mm
ρ	1000 kg/m^3
$E_y S_y$	100 N
d	30,000 m^{-2}

Table 5.1: Material properties of the inflatable panel in the reference configuration.

would be unreasonably resource-consuming. The total potential energy in this case would be written as

$$\Pi_{\text{threads}} = \sum_{i=1}^{n_{\text{threads}}} \frac{1}{2} E_y S_y H_\varnothing \varepsilon_i^2$$

where the number of threads n_{threads} would be very large (around 300,000). Instead of doing this, bar elements are created to link each node of the upper membrane to the node facing it on the lower membrane (which is a mirror image of the upper one), and each bar needs to be assigned a stiffness representative of the yarns surrounding in reality. To this end, every node of the membranes is assigned a "neighboring area" which is the sum of the neighboring triangles' area divided by three (because all elements are triangles, so one third of their surface goes to each vertex), Fig. 5.3. Then, the bar elements will receive the axial stiffness of one thread, $E_y S_y$, multiplied by the estimated number of threads surrounding it, which is the average neighboring area of the bar's two nodes (denoted S_{avg}) multiplied by the thread density d. With mathematical notations:

$$\Pi_{\text{bar}}^i = d\, S_{\text{avg,i}} \times \frac{1}{2} E_y S_y H_\varnothing \varepsilon_i^2 \tag{5.1}$$

where n_{bars} the number of bar elements connecting the membranes (typically one thousand, much smaller than the true number of drop cords), $S_{\text{avg,i}}$ is the average neighboring surface around the i-th bar's nodes, and $\varepsilon_i = \frac{1}{2}\frac{H_i^2 - H_\varnothing^2}{H_\varnothing^2}$ is the Green strain in the i-th bar element. Note that this expression of the potential energy is only valid when the bar is stretched. If the Green strain in a bar becomes negative, then its axial stiffness should be cancelled, and reactivated as soon as the thread is taut again. That is:

$$\Pi_{\text{bar}}^i = d\, S_{\text{avg,i}} \times \frac{1}{2} E_y S_y H_\varnothing \big(\max(0, \varepsilon_i)\big)^2 \tag{5.2}$$

as a result, the total potential energy of all the threads is approximated by

$$\Pi_{\text{threads}} \approx \sum_{i=1}^{n_{\text{bars}}} \Pi_{\text{bar}}^{i} \tag{5.3}$$

The high rigidity of these bars can pose numerical challenges, making the simulation of inflatable panels a difficult task.

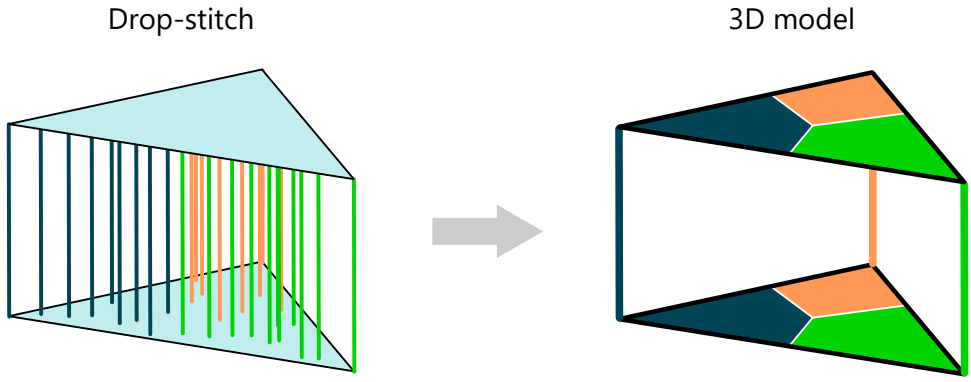

Figure 5.3: Drop-stitch fabric with drop yarns and 3D model with bar elements of equivalent stiffness. The "neighboring area" and the drop cords they account for are drawn in the same colors.

5.1.3 Boundary conditions, pressurization and external loads

Boundary conditions are applied so as to prevent rigid body motions: $U_x(X = 0) = 0$ and $U_y(Y = 0) = 0$. The internal pressure p will successively take four values: 30, 50, 70 and 90 kPa. After the panel is pressurized at the pressure p, the natural radius $R_\varnothing$ becomes R and the natural height $H_\varnothing$ increases to H; both reference dimensions R and H of the panel are used in the analytical equation (4.6) for comparison. Once the structure is inflated, a vertical dead load q is applied. Half of this external load is applied to the top membrane and the other half to the bottom membrane: this is because in theory the external loads are applied directly onto the plate's mid-surface, which is not materialized in the 3D mesh. Therefore, one has to decide how to divide the load on the upper and lower layers. For instance, one may put the entire load on the upper or lower layer, and each distribution has different consequences for the stresses in the membrane layers and the drop yarns. In our work, we did not study the influence of the load distribution type. Instead, we have arbitrarily decided to apply 50 % of the load on the upper layer and 50 % on the lower layer, as this minimizes the lever arm and thus undesirable surface couples.

5.1.4 Pressurization phase and loading phase

The simulation takes place in two stages: the pressurization phase and the loading phase Fig. 5.4. The problem that is considered is static, meaning that there is no time involved in the process. The finite element solutions are found by minimizing the total potential energy with respect to the current nodal positions, using the conjugate gradient method. The total potential energy is written as

$$\Pi = \Pi_{\text{membrane}} + \Pi_{\text{threads}} + \Pi_{\text{gas}}$$

where

$$\Pi_{\text{membrane}} = \int_{\Omega_0} \left(\frac{\lambda}{2} \big(\operatorname{Tr}(\boldsymbol{E}) \big)^2 + \mu \operatorname{Tr}(\boldsymbol{E}^2) \right) \mathrm{d}\Omega_0 \tag{5.4}$$

$$\Pi_{\text{threads}} = \frac{1}{2} E_y S_y H_{\varnothing} d \sum_{i=1}^{n_{\text{bars}}} \big(\max(0, \varepsilon_i) \big)^2 S_{\text{avg,i}} \tag{5.5}$$

$$\Pi_{\text{gas}} = pV \tag{5.6}$$

where λ, μ are the Lamé coefficients and $V = \operatorname{vol}(\Omega_0)$ is the volume inside the panel. Given the nonlinearity of the system, the loads cannot be applied all at once:

- first, the internal pressure is applied in 3 increments: 4% of the final inflation pressure (this first increment is especially long to compute), 30% and 100%;
- then, the external load is applied in 15 increments from 1 Pa to 3000 Pa: 1, 10, 30, 60, 100, 200, 300, 500, 700, 1000, 1300, 1600, 2000, 2500 and 3000 Pa.

At every load increment the program goes through dozens or hundreds of iterations, updating the position of the nodes until convergence is reached, that is, when the energy step size in the conjugate gradient method becomes smaller than a given threshold of 10^{-8} J.

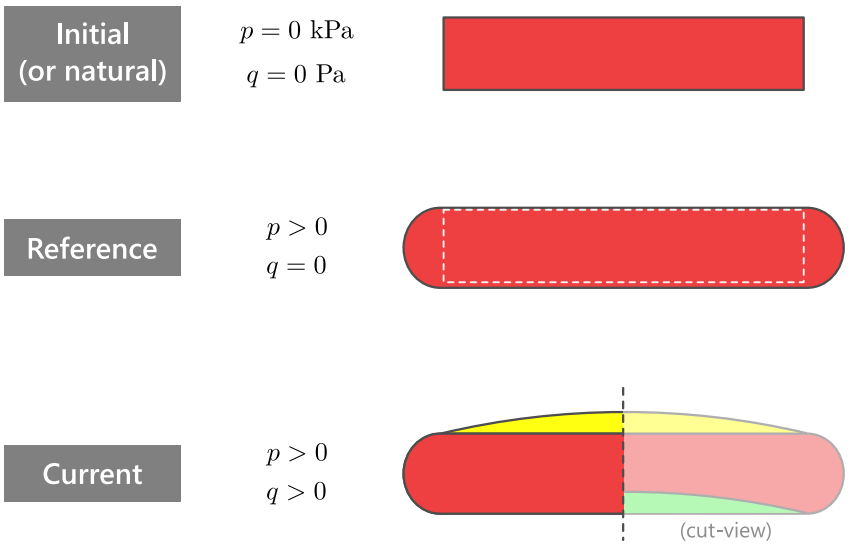

Figure 5.4: Configurations of the inflatable panel throughout the simulation.

5.1.5 Achieving convergence of very stiff systems

In some cases, convergence is hard to reach due to numerical instabilities. Sometimes the problem can be overcome simply by forcing the program to iterate one more step or by artificially displacing every node by a very small amount to escape from local minima, but this cannot be applied systematically or the iterative process also fails.

At first, the number of drop cords was set to be as high as it is in reality (40 000 per square meter). But in this case the iterative process would often come to a halt even when the increment step size was still relatively large. To overcome this, we had to decrease the density of the yarns to 30 000.

The lateral wall also hindered the resolution process, restricting the top and bottom membranes' expansion. This is partly due to the ill-conditioning of the mesh in this region (the triangular elements are very elongated). In order to get the simulation to match the theory assumption that the border simply doesn't exist, the elasticity modulus of the lateral was set to be 5 % of the stiffness of the membranes.

Overall, simulating stiff nonlinear systems is not straightforward because of numerical ill-conditioning and still requires some expertise and fine-tuning.

5.1.6 Code parametrization

In order to evaluate the analytical solution against finite element simulations, one must compare their predictions for a variety of geometries, materials and loads, and so the same program must be run several times with different inputs. To avoid editing the script manually each time, a simple code was written in the form of a Python notebook[3] to process every combination of parameters automatically. The Python notebook duplicates the original Evolver script, replaces the variable parameters with the desired values and saves each modified script as a separate file. The notebook then calls the Evolver program to run all the scripts which, in turn, write their outputs to individual text file for further post-processing in Python. This process is summarized in Fig. 5.5. Any number of variables can be parametrized in this way. We focused our attention on the initial geometry and inflation pressure, i.e. different combinations of $H_\varnothing$, $R_\varnothing$ and p.

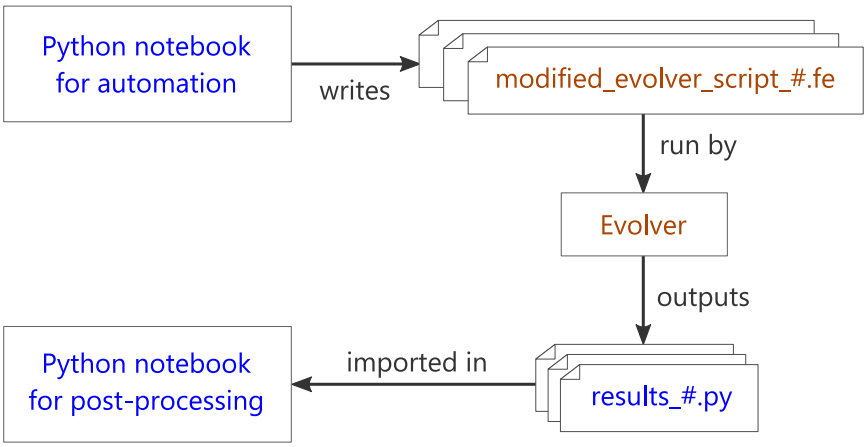

Figure 5.5: Batch processing workflow with Evolver.

5.1.7 Limitations

As was done in the theory, the behavior of the panel is studied at prescribed pressure, in other words, pressure variations due to volume changes are ignored. The code does not handle self-contact of the mesh, which means that the post-wrinkling response may not always be accurate. Since the mesh has to be procedurally generated from subdivisions of a cylinder, the finite elements on the lateral wall are much smaller than those on the membranes (see Fig. 5.2), and the junction between these regions with elements of very different sizes is unfavorable to convergence and should be addressed.

[3] In computer programming, a notebook is an interactive document where text, equations, code and code outputs can be displayed next to each other. They make it easier to interact with the code and present the results, especially when dealing with many tables or figures.

5.2 Finite element results

5.2.1 Load-displacement curves

Fig. 5.6 shows the maximal deflection $W(r=0)$ as a function of the external load q for two different geometries and two inflation pressures $p = 50$ kPa and $p = 90$ kPa. The analytical solution is only plotted for external load q less than the wrinkling load q_w defined by Relation (4.8). Recall that the linear elastic solution for the inflatable panel is valid as long as:

(i) the displacements and rotations are small (see Section 3.1)

(ii) the load q is less than the wrinkling load q_w given by (4.8)

Criterion (i) may be expressed in terms of ratio $W(r=0)/R_\varnothing$ and $\psi_r(r=0)$ for instance, say

$$\frac{W(r=0)}{R_\varnothing} < 3\% \quad \text{and} \quad \psi_r(r=0) < 1\%$$

The present results show that the higher the inflating pressure p and the membrane thickness $H_\varnothing$ are, the larger the range of validity of the solution – defined by the above-mentioned criteria (i) and (ii) – and the larger the external load q, or equivalently, the higher the bearing capacity of the panel. Furthermore, it can be seen in Fig. 5.6 that the criterion $W(r=0)/R_\varnothing < 3$ % may be violated before criterion $q < q_w$. In other words, one can go beyond the linear elastic range before reaching the wrinkling load.

5.2.2 Relative difference in terms of displacement

The analytical maximum deflection, denoted W_{theor}, and the maximum deflection given by the 3D finite element computations, denoted W_{FE}, are given in Table 5.2 for a uniform vertical load $q = 100$ Pa. The relative difference is defined as $(W_{\text{FE}} - W_{\text{theor}})/W_{\text{theor}}$. Across all 24 cases, the average absolute relative difference is 1.92 %. The comparison between W_{theor} and W_{FE} can be conducted in terms of the ratio $H_\varnothing/R_\varnothing$ and the external load q, respectively:

- Table 5.2 shows that, as expected, at a given pressure p, the smaller the ratio $H_\varnothing/R_\varnothing$ is, the better the panel analytical solution compares with the 3D finite element computations.
- For a given geometry and pressure p, the deflection varies with the external load q ranging from 0 to 3000 Pa as shown in Fig. 5.6. In the range where the load q is small enough for the linear solution to be valid, the analytical solution and the finite element results are found to be in fairly good agreement.

So far, all the numerical computations have been made with the membrane Young modulus $E = 2.5$ GPa. In order to show the sensitivity of the deflections to the value of E, we conduct a new series of computations taking now $E = 0.59$ GPa and the same values for all other quantities. This new value of E, significantly smaller than the previous one, is closer to the one measured with an inflatable panel that will be used in our experiments presented in Chapter 7. Table 5.3 displays the results corresponding to $E = 0.59$ GPa. These additional numerical values confirm that the inflated height H is insensitive to the membrane's Young modulus. Note also that the wrinkling load is rather insensitive to the change of elastic modulus, as it mostly depends on the geometry and load type. Here again, the values given by the inflatable panel theory agree quite well with those from the 3D finite element computations. Overall, the largest discrepancy between the theory and the finite element computations occurs at radius $R_\varnothing = 2$ m and height $H_\varnothing = 10$ cm, which is the geometry

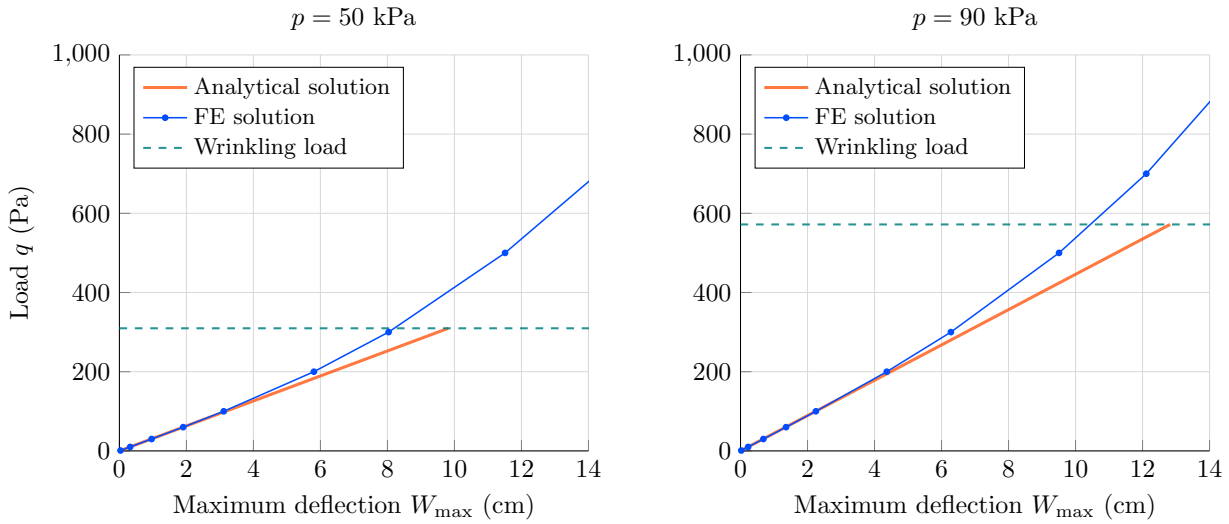

(a) $R_\varnothing = 2$ m, $H_\varnothing = 10$ cm

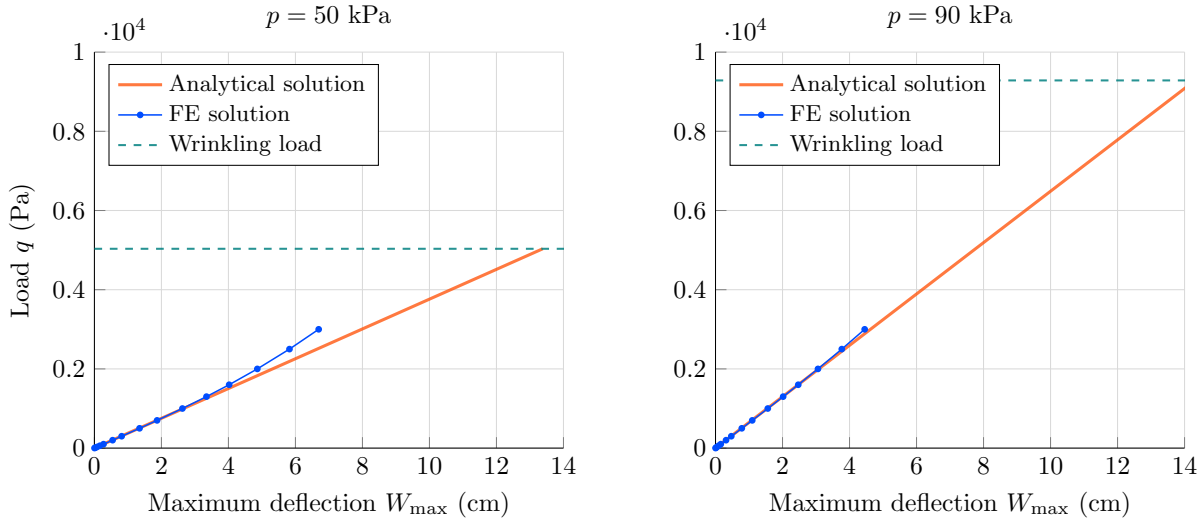

(b) $R_\varnothing = 1$ m, $H_\varnothing = 20$ cm

Figure 5.6: Linearized analytical load-deflection curves compared with the finite element results for two different geometries and inflation pressures. The analytical curves stop when the assumption of positive tensile stress is no longer valid ($q > q_w$) and the FE curve stops at the maximum applied load $q = 3000$ Pa. Parameters: $E = 2.5$ GPa, $\tau = 0.66$ mm $\nu = 0.25$.

corresponding to the lowest wrinkling load as can be seen in the last column of Table 5.3. For this geometry, the relative difference is negative, meaning that the analytical deflection is larger than the simulated one (which has additional geometric stiffness).

5.2.3 Some remarks on the exclusion of the membranes' thickness from the overall thickness

Two quantities were introduced as a result of excluding the membrane's thickness from the overall thickness of the panel: $\tilde{\tau}$ and $\tilde{H}$ introduced in Sections 2.2.6 and 2.2.5, respectively. When making the approximation $\tilde{\tau} \approx \tau$ the relative difference will generally not deteriorate unless the membranes are particularly thick or the panel is very thin. On the other hand, considering H instead of $\tilde{H} = H - 2\tau$ in (4.6) worsens the results as it increases the relative difference by up to 2 percentage points on every test case. This is mostly due to the fact

p (kPa)	$H_\varnothing$ (cm)	H (cm)	$R_\varnothing$ (m)	R (m)	W_{FE} (mm)	W_{theor} (mm)	Relative difference (%)	Wrinkling load q_w (Pa)
30	10	10.10	1.0	1.000	9.17	9.11	0.7	734
			1.5	1.501	22.10	22.59	-2.2	326
			2.0	2.001	42.39	45.35	-6.5	183
	20	20.20	1.0	0.999	4.49	4.33	3.7	2983
			1.5	1.501	10.49	10.29	2.0	1323
			2.0	2.002	19.86	19.59	1.4	743
50	10	10.17	1.0	1.001	5.79	5.72	1.2	1239
			1.5	1.502	14.98	14.94	0.3	551
			2.0	2.002	31.14	31.70	-1.8	310
	20	20.33	1.0	1.000	2.72	2.66	2.3	5034
			1.5	1.502	6.64	6.51	2.0	2232
			2.0	2.004	13.13	12.86	2.1	1255
70	10	10.23	1.0	1.001	4.32	4.27	1.2	1758
			1.5	1.502	11.76	11.64	1.0	781
			2.0	2.003	25.70	25.78	-0.3	439
	20	20.47	1.0	1.001	1.98	1.94	2.0	7134
			1.5	1.504	4.99	4.88	2.3	3164
			2.0	2.006	10.20	9.95	2.5	1778
90	10	10.30	1.0	1.002	3.50	3.46	1.4	2289
			1.5	1.503	9.92	9.79	1.3	1017
			2.0	2.004	22.51	22.43	0.4	572
	20	20.60	1.0	1.003	1.57	1.54	2.0	9285
			1.5	1.505	4.08	3.98	2.6	4119
			2.0	2.008	8.56	8.33	2.8	2315

Table 5.2: Analytical and 3D finite element results for a simply supported circular inflatable panel ($q = 100$ Pa, $E = 2.5$ GPa).

that $\tilde{H}$ is squared or cubed in several expressions, notably in the coefficients K and K'.

5.2.4 Initial stiffness calculation

The relative difference between the analytical and simulated deflections W_{theor}, W_{FE} is elementary and easy to compute directly using the raw data. However, a better criterion exists: from a theoretical perspective, the analytical and numerical models can only be compared while the deflection is small, in keeping with the linearization hypotheses. Therefore, the two models should agree on the initial stiffness of the structure, that is, $\left.\dfrac{\partial q}{\partial W}\right|_{W=0}$. The use of this criterion shows more consistent trends in the data that the simplistic deflection discrepancy criterion. The relative difference in slope is expressed by the following relationship:

$$\text{(relative difference on the slope)} = \frac{\text{(numerical slope)} - \text{(analytical slope)}}{\text{(analytical slope)}}$$

The numerical initial slope is obtained by performing a linear regression on the first three points of the simulated load-deflection curve (arbitrarily). The constant term in the regression is forced to zero, since the deflection is zero when no external loads are applied. This intercept-free linear model was selected among others because it did not assume an expression of the simulated curve (unlike quadratic, exponential, logarithmic or power models) and proved to be more accurate at describing the initial slope than interpolation methods (B-spline). One should observe that the computation of the slope is very sensitive to small variations in data: this comparison criterion is penalizing and the relative difference obtained must be analyzed

p (kPa)	$H_\varnothing$ (cm)	H (cm)	$R_\varnothing$ (m)	R (m)	W_{FE} (mm)	W_{theor} (mm)	Relative difference (%)	Wrinkling load q_w (Pa)
30	10	10.10	1.0	1.003	11.71	11.56	1.3	733
			1.5	1.504	34.49	34.92	-1.2	326
			2.0	2.006	76.85	84.24	-8.8	183
	20	20.20	1.0	1.005	5.12	4.98	2.8	2969
			1.5	1.508	13.87	13.44	3.1	1318
			2.0	2.011	30.23	29.46	2.6	741
50	10	10.17	1.0	1.005	8.35	8.16	2.2	1236
			1.5	1.507	27.33	27.20	0.5	549
			2.0	2.003	66.70	69.99	-4.7	309
	20	20.33	1.0	1.009	3.44	3.31	3.9	4996
			1.5	1.514	10.06	9.67	4.0	2218
			2.0	2.019	23.44	22.72	3.2	1247
70	10	10.23	1.0	1.007	6.87	6.69	2.6	1750
			1.5	1.510	24.04	23.83	0.9	778
			2.0	2.014	61.53	64.16	-4.1	437
	20	20.47	1.0	1.013	2.71	2.59	4.7	7062
			1.5	1.521	8.39	8.05	4.2	3137
			2.0	2.028	20.42	19.82	3.0	1764
90	10	10.30	1.0	1.009	6.03	5.87	2.8	2277
			1.5	1.513	22.08	21.90	0.8	1012
			2.0	2.018	58.20	60.56	-3.9	569
	20	20.60	1.0	1.018	2.31	2.19	5.3	9168
			1.5	1.527	7.44	7.14	4.2	4074
			2.0	2.036	18.62	18.20	2.3	2291

Table 5.3: Analytical and 3D finite element results for a simply supported circular inflatable panel with a smaller elastic modulus ($q = 100$ Pa, $E = 0.59$ GPa).

with regard to this severe criterion. The relative difference in displacement can be negative or positive for a same geometry depending on the pressure, which leads to believe that the theory can be unpredictably stiffer or softer than the FE simulation. This is misleading, because if one were to consider the relative difference in slope, it would be systematically positive and independent of the pressurization for a fixed geometry, Table 5.4. For $p = 30$ kPa, numerical instabilities made the convergence difficult to achieve and the relative difference are less consistent for this reason.

To summarize the results obtained in this chapter visually, the data from Tables 5.2 and 5.4 can be presented in a scatter plot to show that both the analytical and numerical approaches produce practically identical values, Fig. 5.7.

Relative difference on $W_{\max}$ (%)

$H_\varnothing$	$R_\varnothing$	Inflation pressure p (kPa) 30	50	70	90
10 cm	1 m	0.7	1.2	1.2	1.4
	1.5 m	-2.2	0.3	1.0	1.3
	2 m	-6.5	-1.8	-0.3	0.4
20 cm	1 m	3.7	2.3	2.0	2.0
	1.5 m	2.0	2.0	2.3	2.6
	2 m	1.4	2.1	2.5	2.8

Relative difference on $\partial q/\partial W|_{W=0}$ (%)

$H_\varnothing$	$R_\varnothing$	Inflation pressure p (kPa) 30	50	70	90
10 cm	1 m	2.0	1.4	1.4	1.4
	1.5 m	1.2	1.3	1.5	1.6
	2 m	0.4	1.0	1.3	1.4
20 cm	1 m	3.8	2.3	2.0	2.0
	1.5 m	2.4	2.1	2.3	2.6
	2 m	2.2	2.3	2.6	2.9

Table 5.4: Relative difference percentage on the maximum deflection (left) and slope (right) for various geometry and inflation pressures ($E = 2.5$ GPa, $\nu = 0.25$).

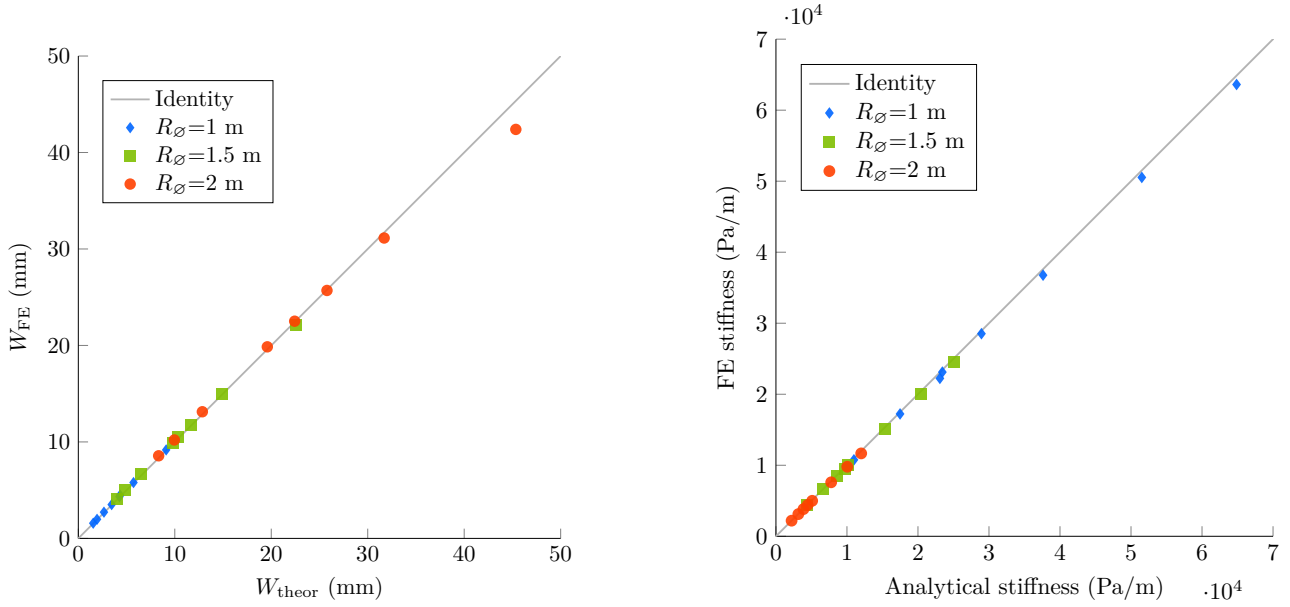

Figure 5.7: Comparison between the analytical and numerical maximum deflection at $q = 100$ Pa (left) and comparison between the analytical and numerical initial stiffnesses (right). The identity line represents perfect agreement between theory and simulation. ($E = 2.5$ GPa, $\nu = 0.25$)

Chapter 6

Vibrations of inflatable panels

In this chapter, the vibration of inflatable panels is considered. We will calculate the eigenfunctions and the eigenfrequencies (also called natural modes and natural frequencies) of rectangular and circular inflatable panels.

6.1 Hypotheses for the study of vibrations

- The amplitude of the vibrations is small enough for the response of the panel to remain linear.
- The dynamic material properties remain close to the statically measured ones.
- The pressure inside the panel is prescribed or does not vary significantly over time, such that it can be considered as constant through time and space.
- The inflatable panel is filled with a gas whose density is small compared to that of the membranes, such that its inertia does not affect the movement of the membranes. Modelling the fluid velocity and added mass of air on vibrating membranes is of current interest in research [82].
- The vibration of the drop cords is not considered.

6.2 Eigenvalue problem for inflatable panels

The linearized equations of motion for the inflatable panel are reminded here.

- **Equilibrium condition for out-of-plane forces.** $\forall t, \forall \mathrm{P}_0 \in S_0$,

$$\boxed{2\tau\rho\ddot{W} - \boldsymbol{N}_0 : \operatorname{grad}\operatorname{grad} W - p\tilde{H}\operatorname{div}\boldsymbol{\psi} = \boldsymbol{q}\cdot\boldsymbol{a}^3} \tag{6.1}$$

  where $\boldsymbol{N}_0$ is the membrane pre-stress tensor.

- **Moment equilibrium equations.** $\forall t, \forall \mathrm{P}_0 \in S_0$,

$$\boxed{\frac{\rho\tilde{\tau}H^2}{2}\ddot{\boldsymbol{\psi}} - \frac{D^*}{2}\Big[(1-\nu)\boldsymbol{\Delta}\boldsymbol{\psi} + (1+\nu)\operatorname{grad}\operatorname{div}\boldsymbol{\psi}\Big] - \operatorname{div}\Big(\operatorname{grad}\boldsymbol{\psi}\cdot\boldsymbol{M}_0^{(2)}\Big) + p\tilde{H}\left(\boldsymbol{\psi} + \operatorname{grad} W\right) = \boldsymbol{0}} \tag{6.2}$$

  where $\boldsymbol{M}_0^{(2)}$ is the second order moment pre-stress tensor.

These equations are of the form

$$\mathcal{M}_W \ddot{W} + \mathcal{L}_{WW} W + \mathcal{L}_{W\psi} \boldsymbol{\psi} = q_3$$
$$\mathcal{M}_\psi \ddot{\boldsymbol{\psi}} + \mathcal{L}_{\psi W} W + \mathcal{L}_{\psi\psi} \boldsymbol{\psi} = \mathbf{0}$$

where $\mathcal{M}_W$ and $\mathcal{M}_\psi$ are operators proportional to the identity operator $\mathbf{Id}$:

$$\mathcal{M}_W \equiv 2\tau\rho\,\mathbf{Id} \qquad \mathcal{M}_\psi \equiv \frac{\rho\tilde{\tau}H^2}{2}\,\mathbf{Id}$$

and $\mathcal{L}_{WW}$, $\mathcal{L}_{W\psi}$, $\mathcal{L}_{\psi W}$, $\mathcal{L}_{\psi\psi}$ are differential operators defined by

$$\mathcal{L}_{WW} \equiv -\boldsymbol{N}_0 : \mathbf{grad}\,\mathbf{grad} \qquad \mathcal{L}_{W\psi} \equiv -p\tilde{H}\,\mathbf{div}$$
$$\mathcal{L}_{\psi W} \equiv p\tilde{H}\,\mathbf{grad} \qquad \mathcal{L}_{\psi\psi} \equiv -\tfrac{D^*}{2}\left[(1-\nu)\boldsymbol{\Delta} + (1+\nu)\,\mathbf{grad}\,\mathbf{div}\right] - \mathbf{div}\left(\mathbf{grad}\cdot\boldsymbol{M}_0^{(2)}\right) + p\tilde{H}\mathbf{Id}$$

In condensed form:

$$\begin{bmatrix} \mathcal{M}_W & 0 \\ 0 & \mathcal{M}_\psi \end{bmatrix} \begin{Bmatrix} \ddot{W} \\ \ddot{\boldsymbol{\psi}} \end{Bmatrix} + \begin{bmatrix} \mathcal{L}_{WW} & \mathcal{L}_{W\psi} \\ \mathcal{L}_{\psi W} & \mathcal{L}_{\psi\psi} \end{bmatrix} \begin{Bmatrix} W \\ \boldsymbol{\psi} \end{Bmatrix} = \{f\} \quad \Leftrightarrow \quad \mathcal{M} \begin{Bmatrix} \ddot{W} \\ \ddot{\boldsymbol{\psi}} \end{Bmatrix} + \mathcal{L} \begin{Bmatrix} W \\ \boldsymbol{\psi} \end{Bmatrix} = \{f\}$$

Remark 6.1. The coefficient $p\tilde{H}$ replaces the shear stiffness term $\kappa^2 GH$ of the classical theory for solid plates. The term $-\boldsymbol{N}_0 : \mathbf{grad}\,\mathbf{grad}\,W = -N_0\,\mathbf{div}\,\mathbf{grad}\,W$ replaces $-\kappa^2 GH\Delta W$. Only the term $-\mathbf{div}\left(\mathbf{grad}\cdot\boldsymbol{M}_0^{(2)}\right)$ is completely new. It will be found to increase the flexural stiffness.

The **eigenvalue problem** consists in searching for the eigenvalues λ and the eigenfunctions (W, Ψ) verifying the following equations. Henceforth, W denotes the bending eigenfunction (which is independent of time t) instead of the vertical component of the displacement $\boldsymbol{U}$.

1. The eigenvalue equations

$$\begin{bmatrix} \mathcal{L}_{WW} & \mathcal{L}_{W\psi} \\ \mathcal{L}_{\psi W} & \mathcal{L}_{\psi\psi} \end{bmatrix} \begin{Bmatrix} W \\ \boldsymbol{\Psi} \end{Bmatrix} = \lambda \begin{bmatrix} \mathcal{M}_W & 0 \\ 0 & \mathcal{M}_\psi \end{bmatrix} \begin{Bmatrix} W \\ \boldsymbol{\Psi} \end{Bmatrix}$$

that is,

$$-\boldsymbol{N}_0 : \mathbf{grad}\,\mathbf{grad}\,W - p\tilde{H}\,\mathbf{div}\,\boldsymbol{\Psi} = 2\tau\rho\lambda W$$
$$-\frac{D^*}{2}\Big[(1-\nu)\boldsymbol{\Delta}\Psi + (1+\nu)\,\mathbf{grad}\,\mathbf{div}\,\boldsymbol{\Psi}\Big] - \mathbf{div}\left(\mathbf{grad}\,\boldsymbol{\Psi}\cdot\boldsymbol{M}_0^{(2)}\right) + p\tilde{H}\left(\boldsymbol{\Psi} + \mathbf{grad}\,W\right) = \lambda\frac{\rho\tilde{\tau}H^2}{2}\boldsymbol{\Psi}$$

Assuming $\boldsymbol{N}_0 = N_0\boldsymbol{I}^P = p\tilde{H}\boldsymbol{I}^P$ and $\boldsymbol{M}_0^{(2)} = M_0^{(2)}\boldsymbol{I}^P$, the eigenvalue problem can be rewritten as

$$\boxed{\Delta W + \lambda\frac{2\tau\rho}{p\tilde{H}}W + \mathbf{div}\,\boldsymbol{\Psi} = 0} \tag{6.3}$$

$$\boxed{\left(D^*\frac{1-\nu}{2} + M_0^{(2)}\right)\boldsymbol{\Delta}\boldsymbol{\Psi} + D^*\frac{1+\nu}{2}\,\mathbf{grad}\,\mathbf{div}\,\boldsymbol{\Psi} + \left(\lambda\frac{\rho\tilde{\tau}H^2}{2} - p\tilde{H}\right)\boldsymbol{\Psi} - p\tilde{H}\,\mathbf{grad}\,W = \mathbf{0}} \tag{6.4}$$

2. The boundary conditions without external actions, rewritten in terms of the eigenfunctions W, $\boldsymbol{\Psi}$.

   (a) On a clamped edge:

$$\boxed{W = 0} \qquad \text{and} \qquad \boxed{\boldsymbol{\Psi} = \mathbf{0}}$$

(b) On a simply-supported edge (soft type):

$$\boxed{W = 0}$$

And $\Gamma^s = \Gamma^\nu = 0$ imply

$$\boxed{D^*\left[(1-\nu)\boldsymbol{\nu}_0 \cdot \mathrm{SYM}\,\mathrm{grad}\,\boldsymbol{\Psi} \cdot \boldsymbol{\nu}_0 + \nu\,\mathrm{div}\,\boldsymbol{\Psi}\right] + \boldsymbol{\nu}_0 \cdot \mathrm{grad}\,\boldsymbol{\Psi} \cdot \boldsymbol{M}_0^{(2)} \cdot \boldsymbol{\nu}_0 + \frac{p\tilde{H}^3}{12}\boldsymbol{\Psi}_{,s_0} \cdot \boldsymbol{s}_0 = 0}$$

$$\boxed{D^*(1-\nu)\boldsymbol{s}_0 \cdot \mathrm{SYM}\,\mathrm{grad}\,\boldsymbol{\Psi} \cdot \boldsymbol{\nu}_0 + \boldsymbol{s}_0 \cdot \mathrm{grad}\,\boldsymbol{\Psi} \cdot \boldsymbol{M}_0^{(2)} \cdot \boldsymbol{\nu}_0 - \frac{p\tilde{H}^3}{12}\boldsymbol{\Psi}_{,s_0} \cdot \boldsymbol{\nu}_0 = 0}$$

(c) On a simply-supported edge (hard type):

$$\boxed{W = 0}$$

$$\boxed{D^*\left[(1-\nu)\boldsymbol{\nu}_0 \cdot \mathrm{SYM}\,\mathrm{grad}\,\boldsymbol{\Psi} \cdot \boldsymbol{\nu}_0 + \nu\,\mathrm{div}\,\boldsymbol{\Psi}\right] + \boldsymbol{\nu}_0 \cdot \mathrm{grad}\,\boldsymbol{\Psi} \cdot \boldsymbol{M}_0^{(2)} \cdot \boldsymbol{\nu}_0 + \frac{p\tilde{H}^3}{12}\boldsymbol{\Psi}_{,s_0} \cdot \boldsymbol{s}_0 = 0}$$

$$\boxed{\boldsymbol{\Psi} \cdot \boldsymbol{s}_0 = 0}$$

(d) On a free edge: $\boldsymbol{q} \cdot \boldsymbol{a}_3 = 0$ implies

$$\boxed{(\boldsymbol{\Psi} + \mathrm{grad}\,W) \cdot \boldsymbol{\nu}_0 = 0}$$

And $\Gamma^s = \Gamma^\nu = 0$ imply

$$\boxed{D^*\left[(1-\nu)\boldsymbol{\nu}_0 \cdot \mathrm{SYM}\,\mathrm{grad}\,\boldsymbol{\Psi} \cdot \boldsymbol{\nu}_0 + \nu\,\mathrm{div}\,\boldsymbol{\Psi}\right] + \boldsymbol{\nu}_0 \cdot \mathrm{grad}\,\boldsymbol{\Psi} \cdot \boldsymbol{M}_0^{(2)} \cdot \boldsymbol{\nu}_0 + \frac{p\tilde{H}^3}{12}\boldsymbol{\Psi}_{,s_0} \cdot \boldsymbol{s}_0 = 0}$$

$$\boxed{D^*(1-\nu)\boldsymbol{s}_0 \cdot \mathrm{SYM}\,\mathrm{grad}\,\boldsymbol{\Psi} \cdot \boldsymbol{\nu}_0 + \boldsymbol{s}_0 \cdot \mathrm{grad}\,\boldsymbol{\Psi} \cdot \boldsymbol{M}_0^{(2)} \cdot \boldsymbol{\nu}_0 - \frac{p\tilde{H}^3}{12}\boldsymbol{\Psi}_{,s_0} \cdot \boldsymbol{\nu}_0 = 0}$$

One can prove the following two results:

- The operators $\mathcal{M}$ and $\mathcal{L}$ are positive-definite, meaning that the eigenvalues λ are strictly positive, which justifies its interpretation as the square of the circular frequency $\lambda = \omega^2$.
- The operators $\mathcal{M}$ and $\mathcal{L}$ are symmetric, meaning that the eigenvectors $\begin{Bmatrix} W \\ \boldsymbol{\Psi} \end{Bmatrix}$ are $\mathcal{M}-$ and $\mathcal{L}-$orthogonal.

With these two conditions met, from the expansion theorem, any function that satisfies the boundary conditions can be written as an infinite sum of eigenfunctions:

$$\begin{Bmatrix} W \\ \boldsymbol{\psi} \end{Bmatrix} = \sum_{j=1}^{\infty} q_j(t) \begin{Bmatrix} W_j \\ \boldsymbol{\Psi}_j \end{Bmatrix}$$

where the coefficients $q_j(t)$ are unknown scalar functions of time to be determined.

6.3 Natural bending modes W

The local equations (6.3) and (6.4) are coupled. Without assuming a specific coordinate system, we will strive to separate the bending and shear problems as far as can be done. Taking the divergence of Eq. (6.4) yields

$$\left(D^* + M_0^{(2)}\right) \Delta \operatorname{div} \boldsymbol{\Psi} + \left(\lambda \frac{\rho \tilde{\tau} H^2}{2} - p\tilde{H}\right) \operatorname{div} \boldsymbol{\Psi} - p\tilde{H} \Delta W = 0 \tag{6.5}$$

thanks to the vector calculus identity $\operatorname{div} \boldsymbol{\Delta} \boldsymbol{\Psi} = \Delta \operatorname{div} \boldsymbol{\Psi}$. The divergence of $\boldsymbol{\Psi}$ can be expressed in terms of W with Eq. (6.3):

$$\operatorname{div} \boldsymbol{\Psi} = -\Delta W - \lambda \frac{2\tau\rho}{p\tilde{H}} W$$

and

$$\Delta \operatorname{div} \boldsymbol{\Psi} = -\Delta\Delta W - \lambda \frac{2\tau\rho}{p\tilde{H}} \Delta W$$

hence

$$\left(D^* + M_0^{(2)}\right) \left(-\Delta\Delta W - \lambda \frac{2\tau\rho}{p\tilde{H}} \Delta W\right) + \left(\lambda \frac{\rho \tilde{\tau} H^2}{2} - p\tilde{H}\right) \left(-\Delta W - \lambda \frac{2\tau\rho}{p\tilde{H}} W\right) - p\tilde{H} \Delta W = 0$$

$$\left(D^* + M_0^{(2)}\right) \Delta\Delta W + \left(\left(D^* + M_0^{(2)}\right) \lambda \frac{2\tau\rho}{p\tilde{H}} + \lambda \frac{\rho \tilde{\tau} H^2}{2} - p\tilde{H} + p\tilde{H}\right) \Delta W + \lambda \frac{2\tau\rho}{p\tilde{H}} \left(\lambda \frac{\rho \tilde{\tau} H^2}{2} - p\tilde{H}\right) W = 0$$

$$\Delta\Delta W + \underbrace{\left(\lambda \frac{2\tau\rho}{p\tilde{H}} + \frac{\lambda \rho \tilde{\tau} H^2}{2\left(D^* + M_0^{(2)}\right)}\right)}_{-S} \Delta W + \underbrace{\lambda \frac{2\tau\rho}{D^* + M_0^{(2)}} \left(\frac{\lambda \rho \tilde{\tau} H^2}{2p\tilde{H}} - 1\right)}_{P} W = 0$$

which is of the form

$$\Delta\Delta W - S\Delta W + PW = 0 \tag{6.6}$$

where

$$\begin{aligned} S &\equiv -\lambda \left(\frac{2\tau\rho}{p\tilde{H}} + \frac{\rho \tilde{\tau} H^2}{2\left(D^* + M_0^{(2)}\right)}\right) \quad (\text{in m}^{-2}) \\ P &\equiv \lambda \frac{2\tau\rho}{D^* + M_0^{(2)}} \left(\frac{\lambda \rho \tilde{\tau} H^2}{2p\tilde{H}} - 1\right) \quad (\text{in m}^{-4}) \end{aligned} \tag{6.7}$$

S is always negative: it is physically impossible to have $S > 0$. However, P can be positive or negative depending on λ. The quadratic equation associated to (6.6) is introduced:

$$r^4 - Sr^2 + P = 0 \tag{6.8}$$

Its discriminant is

$$S^2 - 4P = \left(\lambda \frac{2\tau\rho}{p\tilde{H}} + \frac{\lambda \rho \tilde{\tau} H^2}{2\left(D^* + M_0^{(2)}\right)}\right)^2 + 4\lambda \frac{2\tau\rho}{D^* + M_0^{(2)}} \left(\frac{\lambda \rho \tilde{\tau} H^2}{2p\tilde{H}} - 1\right) > 0 \tag{6.9}$$

and the two roots are

$$\boxed{\begin{aligned}\Omega_1^2 &\equiv \frac{1}{2}\left(S - \sqrt{S^2 - 4P}\right)\\ \Omega_2^2 &\equiv \frac{1}{2}\left(S + \sqrt{S^2 - 4P}\right)\end{aligned}} \tag{6.10}$$

The values of Ω_1^2 and Ω_2^2 are plotted in Fig. 6.1 along with Ω_3^2 which will be defined below in Eq. (6.16). Ω_2^2 vanishes when $P = 0$ at a specific λ denoted λ_c (c is for *cutoff* or *critical*). This value happens to be the ratio of shear stiffness over rotatory inertia:

$$\lambda_c = \omega_c^2 = p\tilde{H}\left(\frac{\rho\tilde{\tau}H^2}{2}\right)^{-1}$$

and $f_c = \omega_c/2\pi$ is the cutoff frequency (in Hz).

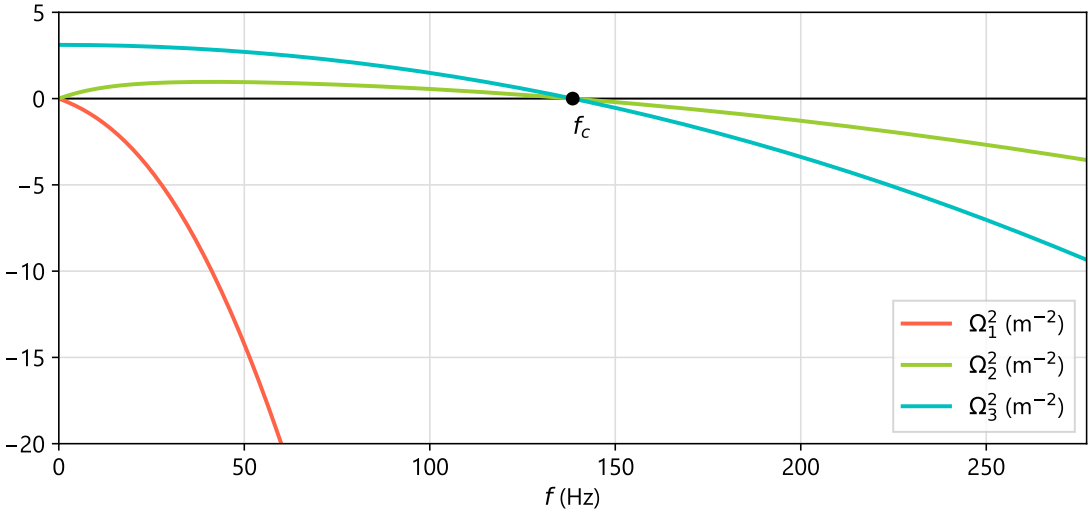

Figure 6.1: Dispersion relations ($E\tau = 389$ N/mm, $\nu = 0.25$, $\rho = 1000$ kg/m^3, $H_\varnothing = 20$ cm).

The differential equation (6.6) with unknown W is first rewritten as

$$\Delta\Delta W - S\Delta W + PW = 0 \Leftrightarrow (\Delta - \Omega_1^2)(\Delta - \Omega_2^2)W = 0$$

where Ω_1^2 and Ω_2^2 are the roots of the quadratic equation (6.8) given in Eq. (6.10). It is then solved in two steps by defining $W_1 \equiv (\Delta - \Omega_2^2)W$ which allows to restate the problem as

$$\left(\Delta - \Omega_1^2\right) W_1 = 0 \tag{6.11a}$$

$$\left(\Delta - \Omega_2^2\right) W = W_1 \tag{6.11b}$$

After the intermediate variable W_1 has been determined, the second equation (6.11b), which depends on W_1, must be solved. The complete solution W is the sum of:

- the general solution W_2 of the homogeneous equation $(\Delta - \Omega_2^2)W_2 = 0$,
- and a particular solution W^* of $(\Delta - \Omega_2^2)W^* = W_1$.

The homogeneous equation for W_2 is similar to Eq. (6.11a) for W_1 (which is known at this stage) and is therefore solved in a similar fashion, which will be detailed for a rectangular panel in Section 6.5.1. Let us

then look for a particular solution of the form $W^* = kW_1$, where k is a constant. As a result, $\Delta W^* = k\Delta W_1 = -k\Omega_1^2 W_1$. Substituting this expression into $(\Delta - \Omega_2^2)W^* = W_1$ yields

$$k = -\frac{1}{\Omega_1^2 + \Omega_2^2} \quad \Rightarrow \quad W^* = -\frac{1}{\Omega_1^2 + \Omega_2^2} W_1$$

Thus, one obtains

$$W = W_2 + W^* = W_2 - \frac{1}{\Omega_1^2 + \Omega_2^2} W_1$$

Insofar as W_1 is a solution of the homogeneous equation, so is any function proportional to W_1. Thus we can retract the multiplicative constant in front of W_1, which simplifies the above equation to

$$W = W_1 + W_2$$

We conclude from this demonstration that the eigenfunction W can be written as the sum of two solutions:

$$\boxed{W = W_1 + W_2} \qquad \text{where} \begin{cases} W_1 \text{ is solution of } & \boxed{(\Delta - \Omega_1^2)W_1 = 0} \\ W_2 \text{ is solution of } & \boxed{(\Delta - \Omega_2^2)W_2 = 0} \end{cases}$$

6.4 Natural shear modes $\boldsymbol{\Psi}$

Here we will show that $\boldsymbol{\Psi}$ can be written as a function of W_1, W_2 and a new potential that will be denoted as W_3, that will satisfy an equation of the same form as (6.11). Taking the gradient of Eq. (6.3):

$$\operatorname{grad}\Delta W + \lambda\frac{2\tau\rho}{p\tilde{H}}\operatorname{grad} W + \operatorname{grad}\operatorname{div}\boldsymbol{\Psi} = \mathbf{0} \tag{6.12}$$

hence $\operatorname{grad}\operatorname{div}\boldsymbol{\Psi} = -\operatorname{grad}\Delta W - \lambda\frac{2\tau\rho}{p\tilde{H}}\operatorname{grad} W$. Thus Eq. (6.4) becomes

$$\left(D^*\frac{1-\nu}{2} + M_0^{(2)}\right)\boldsymbol{\Delta}\boldsymbol{\Psi} + D^*\frac{1+\nu}{2}\left(-\operatorname{grad}\Delta W - \lambda\frac{2\tau\rho}{p\tilde{H}}\operatorname{grad} W\right) + \left(\lambda\frac{\rho\tilde{\tau}H^2}{2} - p\tilde{H}\right)\boldsymbol{\Psi} - p\tilde{H}\operatorname{grad} W = \mathbf{0} \tag{6.13}$$

$$\left(D^*\frac{1-\nu}{2} + M_0^{(2)}\right)\boldsymbol{\Delta}\boldsymbol{\Psi} + \left(\lambda\frac{\rho\tilde{\tau}H^2}{2} - p\tilde{H}\right)\boldsymbol{\Psi} = D^*\frac{1+\nu}{2}\operatorname{grad}\Delta W + \left(D^*\frac{1+\nu}{2}\lambda\frac{2\tau\rho}{p\tilde{H}} + p\tilde{H}\right)\operatorname{grad} W \tag{6.14}$$

As we have shown in the above, W is the sum of two functions W_1 and W_2 that satisfy the relations (6.11), which lets us write:

$$\begin{aligned}\operatorname{grad}\Delta W &= \operatorname{grad}\Delta(W_1 + W_2) \\ &= \operatorname{grad}\left(\Omega_1^2 W_1 + \Omega_2^2 W_2\right) \\ &= \Omega_1^2\operatorname{grad} W_1 + \Omega_2^2\operatorname{grad} W_2\end{aligned}$$

Hence

$$\boxed{\boldsymbol{\Delta}\boldsymbol{\Psi} - \Omega_3^2\boldsymbol{\Psi} = \frac{D^*\frac{1+\nu}{2}\left(\Omega_1^2 + \lambda\frac{2\tau\rho}{p\tilde{H}}\right) + p\tilde{H}}{D^*\frac{1-\nu}{2} + M_0^{(2)}}\operatorname{grad} W_1 + \frac{D^*\frac{1+\nu}{2}\left(\Omega_2^2 + \lambda\frac{2\tau\rho}{p\tilde{H}}\right) + p\tilde{H}}{D^*\frac{1-\nu}{2} + M_0^{(2)}}\operatorname{grad} W_2} \tag{6.15}$$

where

$$\boxed{\Omega_3^2 = \frac{p\tilde{H} - \lambda\dfrac{\rho\tilde{\tau}H^2}{2}}{D^*\dfrac{1-\nu}{2} + M_0^{(2)}}} \tag{6.16}$$

Remark 6.2. Note that we can also write Ω_3^2 as a function of the cutoff eigenvalue λ_c:

$$\Omega_3^2 = \frac{p\tilde{H}}{D^*\dfrac{1-\nu}{2} + M_0^{(2)}}\left(1 - \frac{\lambda}{\lambda_c}\right) \tag{6.17}$$

6.4.1 A particular solution for the natural shear modes

The form of Eq. (6.15) suggests that a particular solution could be a linear combination of the gradients of W_1 and W_2. This is coherent with the fact that in Love–Kirchhoff theory, the equivalent of $\boldsymbol{\Psi}$ would be $-\,\mathbf{grad}\,W$. From these observations, the solution is sought for in the following form:

$$\boxed{\boldsymbol{\Psi}^* = k_1\,\mathbf{grad}\,W_1 + k_2\,\mathbf{grad}\,W_2} \tag{6.18}$$

where the two scalar coefficients k_1, k_2 must be determined. The Laplacian of this candidate field is calculated using Eq. (6.11):

$$\begin{aligned}\boldsymbol{\Delta}\boldsymbol{\Psi}^* &= k_1\boldsymbol{\Delta}\,\mathbf{grad}\,W_1 + k_2\boldsymbol{\Delta}\,\mathbf{grad}\,W_2\\ &= k_1\,\mathbf{grad}\,\Delta W_1 + k_2\,\mathbf{grad}\,\Delta W_2\\ &= k_1\Omega_1^2\,\mathbf{grad}\,W_1 + k_2\Omega_2^2\,\mathbf{grad}\,W_2\end{aligned} \tag{6.19}$$

whence

$$\boldsymbol{\Delta}\boldsymbol{\Psi}^* - \Omega_3^2\boldsymbol{\Psi}^* = k_1\left(\Omega_1^2 - \Omega_3^2\right)\mathbf{grad}\,W_1 + k_2\left(\Omega_2^2 - \Omega_3^2\right)\mathbf{grad}\,W_2 \tag{6.20}$$

By equating this relation with Eq. (6.15):

$$k_1\left(\Omega_1^2 - \Omega_3^2\right) = \frac{D^*\dfrac{1+\nu}{2}\left(\Omega_1^2 + \lambda\dfrac{2\tau\rho}{p\tilde{H}}\right) + p\tilde{H}}{D^*\dfrac{1-\nu}{2} + M_0^{(2)}}$$

$$k_2\left(\Omega_2^2 - \Omega_3^2\right) = \frac{D^*\dfrac{1+\nu}{2}\left(\Omega_2^2 + \lambda\dfrac{2\tau\rho}{p\tilde{H}}\right) + p\tilde{H}}{D^*\dfrac{1-\nu}{2} + M_0^{(2)}}$$

$$\boxed{\begin{aligned}k_1 &= \frac{D^*\dfrac{1+\nu}{2}\left(\Omega_1^2 + \lambda\dfrac{2\tau\rho}{p\tilde{H}}\right) + p\tilde{H}}{\left(D^*\dfrac{1-\nu}{2} + M_0^{(2)}\right)\left(\Omega_1^2 - \Omega_3^2\right)}\\ k_2 &= \frac{D^*\dfrac{1+\nu}{2}\left(\Omega_2^2 + \lambda\dfrac{2\tau\rho}{p\tilde{H}}\right) + p\tilde{H}}{\left(D^*\dfrac{1-\nu}{2} + M_0^{(2)}\right)\left(\Omega_2^2 - \Omega_3^2\right)}\end{aligned}} \tag{6.21}$$

The values of k_1 and k_2 are plotted in Fig. 6.2. The coefficient k_1 is 1 for f = 0 Hz then quickly vanishes before the cutoff frequency. As for k_2, is starts at zero, goes to infinity from both sides of the cutoff frequency f_c, then converges to a positive value as f goes to infinity. These numbers are related to the σ_1, σ_2 of Section 6.6.2 by the relation $k_\alpha = \sigma_\alpha - 1$, and so the same observations are made.

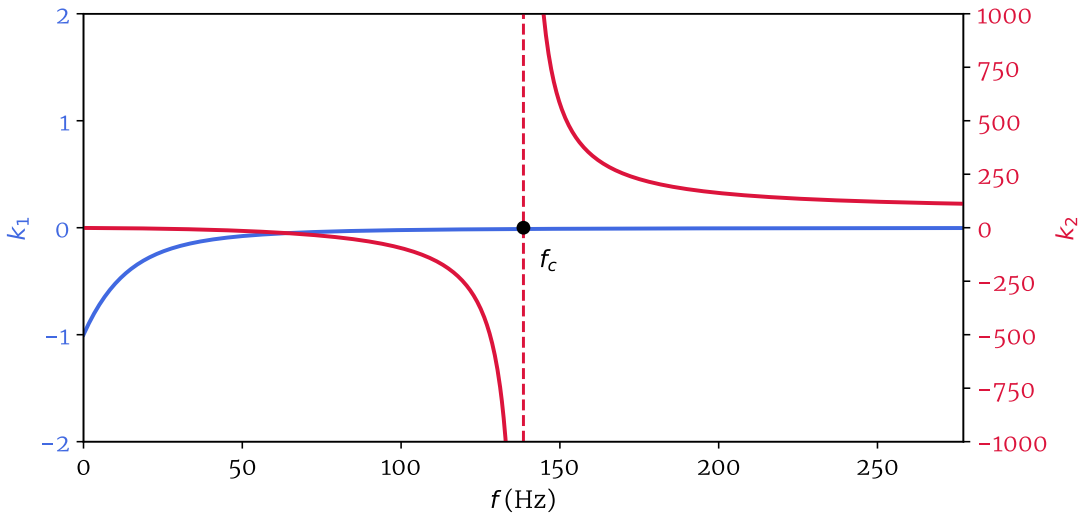

Figure 6.2: Values of the coefficients in the particular solution of the natural shear modes.

Remark 6.3. If the shear stiffness $p\tilde{H}$ becomes infinite and the rotatory inertia $\frac{\rho\tilde{\tau}H^2}{2}$ is suppressed, then both of the coefficients k_1, k_2 will equal -1, which corresponds to the Love–Kirchhoff kinematics $\boldsymbol{\Psi} = -\,\mathbf{grad}\, W$.

6.4.2 A solution to the homogeneous equation for natural shear modes

The homogeneous equation associated to Eq. (6.15) is

$$\boldsymbol{\Delta}\boldsymbol{\Psi}_0 - \Omega_3^2\boldsymbol{\Psi}_0 = \mathbf{0} \tag{6.22}$$

We will show that the unknown field $\boldsymbol{\Psi}_0$ is divergence free and thus it must derive from a potential W_3 for which we will provide a definition. Firstly, one must show that $\Delta\Delta \operatorname{div}\boldsymbol{\Psi} - S\Delta \operatorname{div}\boldsymbol{\Psi} + P \operatorname{div}\boldsymbol{\Psi} = 0$. By taking the Laplacian of Eq. (6.3):

$$\Delta\Delta W + \lambda\frac{2\tau\rho}{p\tilde{H}}\Delta W + \Delta \operatorname{div}\boldsymbol{\Psi} = 0 \tag{6.23}$$

and from the divergence of Eq. (6.4) that was previously calculated in Eq. (6.5):

$$\Delta W = \frac{D^* + M_0^{(2)}}{p\tilde{H}}\Delta \operatorname{div}\boldsymbol{\Psi} + \left(\lambda\frac{\rho\tilde{\tau}H^2}{2p\tilde{H}} - 1\right)\operatorname{div}\boldsymbol{\Psi} \tag{6.24}$$

The Laplacian of W from Eq. (6.24) is substituted into Eq. (6.23)

$$\frac{D^* + M_0^{(2)}}{p\tilde{H}}\Delta\Delta \operatorname{div}\boldsymbol{\Psi} + \left[\lambda\frac{\rho\tilde{\tau}H^2}{2p\tilde{H}} - 1 + \lambda\frac{2\tau\rho}{p\tilde{H}}\frac{D^* + M_0^{(2)}}{p\tilde{H}} + 1\right]\Delta \operatorname{div}\boldsymbol{\Psi} + \lambda\frac{2\tau\rho}{p\tilde{H}}\left(\lambda\frac{\rho\tilde{\tau}H^2}{2p\tilde{H}} - 1\right)\operatorname{div}\boldsymbol{\Psi} = 0$$

which is indeed

$$\Delta\Delta \operatorname{div}\boldsymbol{\Psi} - S\Delta \operatorname{div}\boldsymbol{\Psi} + P \operatorname{div}\boldsymbol{\Psi} = 0 \tag{6.25}$$

Now, the divergence of $\boldsymbol{\Psi}$ is expressed after replacing the unknown by the sum of the homogeneous solution $\boldsymbol{\Psi}_0$ and the particular solution $\boldsymbol{\Psi}^*$:

$$\operatorname{div}\boldsymbol{\Psi} = \operatorname{div}(\boldsymbol{\Psi}_0 + \boldsymbol{\Psi}^*) = \operatorname{div}\boldsymbol{\Psi}_0 + \operatorname{div}\boldsymbol{\Psi}^*$$

and Eq. (6.25) can be rewritten as:

$$\Delta\Delta \operatorname{div} \boldsymbol{\Psi}_0 - S\Delta \operatorname{div} \boldsymbol{\Psi}_0 + P \operatorname{div} \boldsymbol{\Psi}_0 + \Delta\Delta \operatorname{div} \boldsymbol{\Psi}^* - S\Delta \operatorname{div} \boldsymbol{\Psi}^* + P \operatorname{div} \boldsymbol{\Psi}^* = 0$$

the form of $\boldsymbol{\Psi}^*$ is known from Eq. (6.18), and therefore its divergence is

$$\begin{aligned} \operatorname{div} \boldsymbol{\Psi}^* &= k_1 \Delta W_1 + k_2 \Delta W_2 \\ &= k_1 \Omega_1^2 W_1 + k_2 \Omega_2^2 W_2 \end{aligned}$$

which is a linear combination of W_1 and W_2, meaning that it is also a solution of Eq. (6.6). Hence

$$\begin{aligned} \Delta\Delta \operatorname{div} \boldsymbol{\Psi}^* - S\Delta \operatorname{div} \boldsymbol{\Psi}^* + P \operatorname{div} \boldsymbol{\Psi}^* &= \Delta\Delta(k_1 \Omega_1^2 W_1 + k_2 \Omega_2^2 W_2) - S\Delta(k_1 \Omega_1^2 W_1 + k_2 \Omega_2^2 W_2) \\ &\quad + P(k_1 \Omega_1^2 W_1 + k_2 \Omega_2^2 W_2) \\ &= 0 \end{aligned}$$

which yields

$$\Delta\Delta \operatorname{div} \boldsymbol{\Psi}_0 - S\Delta \operatorname{div} \boldsymbol{\Psi}_0 + P \operatorname{div} \boldsymbol{\Psi}_0 = 0 \tag{6.26}$$

and from Eq. (6.22), we have $\Delta \operatorname{div} \boldsymbol{\Psi}_0 = \Omega_3^2 \operatorname{div} \boldsymbol{\Psi}_0$, which entails

$$\left(\Omega_3^4 - S\,\Omega_3^2 + P\right) \operatorname{div} \boldsymbol{\Psi}_0 = 0 \tag{6.27}$$

The expression between parentheses is the quadratic equation (6.8) whose roots are Ω_1^2 and Ω_2^2. We have shown earlier that Ω_1^2, Ω_2^2 and Ω_3^2 always take distinct values, except in the very special case where $P = 0 \Leftrightarrow \lambda = \lambda_c$, which causes $\Omega_2^2 = \Omega_3^2 = 0$ (as can be seen in Fig. 6.1). Therefore the expression in parentheses can never be zero and

$$\operatorname{div} \boldsymbol{\Psi}_0 = 0$$

unless the exciting frequency if the cutoff frequency ($\lambda = \lambda_c$).

We have proven that the homogeneous solution $\boldsymbol{\Psi}_0$ is **divergence free**, an important property that is applied immediately: by virtue of the fundamental theorem of vector calculus (also known as Helmholtz's theorem, illustrated in Fig. 6.3), any sufficiently smooth vector field can be written as the sum of a curl-free and a divergence-free vector fields, that is, there exist φ and $\boldsymbol{V}$ such that

$$\boldsymbol{\Psi}_0 = \operatorname{\mathbf{grad}} \varphi + \operatorname{\mathbf{curl}}(\boldsymbol{V})$$

In our case, the vector field $\boldsymbol{\Psi} = \begin{vmatrix} \Psi_1 \\ \Psi_2 \\ 0 \end{vmatrix}$ is two-dimensional, and so only one component of $\boldsymbol{V}$ is needed[1]:

$$\boldsymbol{\Psi}_0 = \operatorname{\mathbf{grad}} \varphi + \operatorname{\mathbf{curl}}(W_3 \boldsymbol{e}_3) \tag{6.28}$$

The last result to be established involves the definition of the potential W_3. The following conditions on φ and W_3 are *sufficient*, but not *necessary*. Doing so allows us to retrieve the expressions found in the literature available to us, which are often presented without further explanations. Two operations are applied to the above expression:

[1] In Cartesian coordinates: $\operatorname{\mathbf{curl}} \boldsymbol{\Psi} = \begin{vmatrix} 0 \\ 0 \\ \Psi_{y,x} - \Psi_{x,y} \end{vmatrix}$ and $\operatorname{\mathbf{curl}}(W_3 \boldsymbol{e}_3) = \begin{vmatrix} 0 \\ 0 \\ -W_{3,xx} - W_{3,yy} \end{vmatrix}$.

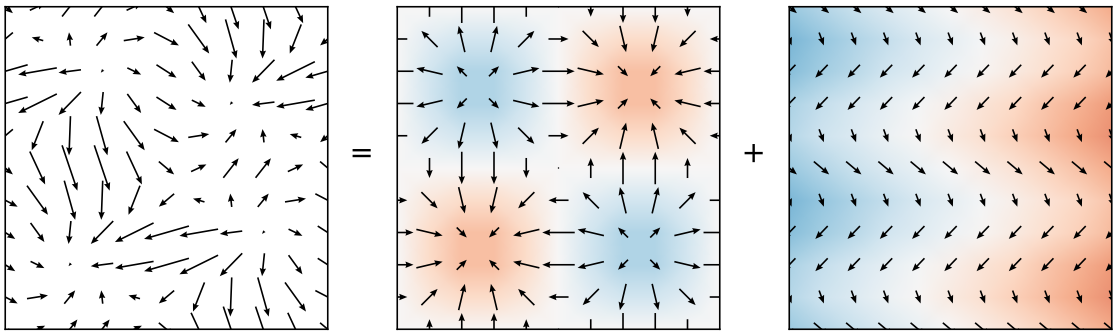

Figure 6.3: Illustration of the Helmholtz-Hodge theorem. Under the appropriate assumptions, a vector field can be decomposed as the sum of a gradient field and a divergence-free field. The scalar potentials φ and W_3 are shown in color.

- First, computing the divergence gives

$$\operatorname{div} \boldsymbol{\Psi}_0 = \Delta\varphi = 0$$

  We have shown previously that $\boldsymbol{\Psi}_0$ is divergence-free and so we will set $\varphi = 0$. This assertion seems restrictive since the scalar potential φ could be a harmonic function which satisfies the above Laplace's equation. The boundary conditions may forbid this possibility, but we have not been able to prove it rigorously within the time allotted to this research.

- Second, taking the curl of the Helmholtz decomposition (6.28) yields

$$\mathbf{curl}\, \boldsymbol{\Psi}_0 = \mathbf{curl}\, \mathbf{curl}(W_3 \boldsymbol{e}_3)$$

  Using the vector analysis identity $\mathbf{curl}\, \mathbf{curl}\, \boldsymbol{v} = \mathbf{grad} \operatorname{div} \boldsymbol{v} - \boldsymbol{\Delta v}$, this relation becomes

$$\mathbf{curl}\, \boldsymbol{\Psi}_0 = -\boldsymbol{\Delta}(W_3 \boldsymbol{e}_3)$$

  since W_3 is a 2D field that is independent of z. The curl of the homogeneous equation (6.22) writes

$$\mathbf{curl}(\boldsymbol{\Delta}\boldsymbol{\Psi}_0) - \Omega_3^2\, \mathbf{curl}(\boldsymbol{\Psi}_0) = \mathbf{0} \Leftrightarrow \boldsymbol{\Delta}\, \mathbf{curl}(\boldsymbol{\Psi}_0) - \Omega_3^2\, \mathbf{curl}(\boldsymbol{\Psi}_0) = \mathbf{0}$$

  and so

$$\boldsymbol{\Delta}\big(-\boldsymbol{\Delta}(W_3 \boldsymbol{e}_3)\big) + \Omega_3^2 \boldsymbol{\Delta}(W_3 \boldsymbol{e}_3) = \mathbf{0} \Leftrightarrow -\Delta\Delta W_3 \boldsymbol{e}_3 + \Omega_3^2 \Delta W_3 \boldsymbol{e}_3 = \mathbf{0}$$

  projected onto vector $\boldsymbol{e}_3$:

$$\Delta(\Delta W_3 - \Omega_3^2 W_3) = 0$$

  Again, we are restrictive by choosing to satisfy only $\Delta W_3 - \Omega_3^2 W_3 = 0$, hoping that the omitted solutions would not be permitted by boundary conditions anyway.

Finally, the homogeneous solution of Eq. (6.22) is

$$\boxed{\boldsymbol{\Psi}_0 = \mathbf{curl}(W_3 \boldsymbol{e}_3)} \tag{6.29}$$

where W_3 is defined by

$$\boxed{(\Delta - \Omega_3^2) W_3 = 0} \tag{6.30}$$

The natural modes of $\boldsymbol{\Psi}$ are obtained by summing the particular solution $\boldsymbol{\Psi}^*$ given by Eq. (6.18) and the homogeneous solution $\boldsymbol{\Psi}_0$ of Eq. (6.29).

$$\boxed{\boldsymbol{\Psi} = k_1 \,\mathbf{grad}\, W_1 + k_2 \,\mathbf{grad}\, W_2 + \mathbf{curl}(W_3 \boldsymbol{e}_3)} \tag{6.31}$$

where

$$\begin{aligned} (\Delta - \Omega_1^2) W_1 &= 0 \\ (\Delta - \Omega_2^2) W_2 &= 0 \\ (\Delta - \Omega_3^2) W_3 &= 0 \end{aligned} \tag{6.32}$$

6.5 Simply-supported rectangular inflatable panel

The three Helmholtz equations (6.32) will now be solved for a rectangular inflatable panel with four supported edges. Although Cartesian coordinates are easier to manipulate than polar coordinates, studying the free vibrations of rectangular plates is more challenging than circular plates. Indeed, the number of possibles expressions that are solution to the eigenvalue problem is bigger and each eigenmode should be examined one by one.

6.5.1 Natural shapes of rectangular inflatable panels

Figure 6.4: Geometry of the simply supported rectangular panel.

The rectangular panel has sides a and b along x and y and all its edges are simply-supported (SSSS), Fig. 6.4. In Cartesian coordinates, the unknown displacement components are

$$W = W(x, y, t) \qquad \boldsymbol{\psi} = \psi_x(x, y, t)\boldsymbol{e}_x + \psi_y(x, y, t)\boldsymbol{e}_y$$

and their corresponding eigenmodes are

$$W = W(x, y) \qquad \boldsymbol{\Psi} = \Psi_x(x, y)\boldsymbol{e}_x + \Psi_y(x, y)\boldsymbol{e}_y$$

The eigenmodes for $W = W_1 + W_2$ are determined by solving the two Helmholtz equations:

$$\begin{aligned} (\Delta - \Omega_1^2) W_1 &= 0 \\ (\Delta - \Omega_2^2) W_2 &= 0 \end{aligned}$$

1. The modified biharmonic equation (6.6) resembles the one commonly encountered in membrane vibration problems, which hints at the idea that it can be solved by separation of variables. Let us look for the solution W_1 as the product: $W_1 = X(x)Y(y)$. Substituting this expression into (6.11a) and dividing the result by $X(x)Y(y)$:

$$\underbrace{\frac{X_{,x^2}}{X}}_{\text{function of } x} + \underbrace{\frac{Y_{,y^2}}{Y}}_{\text{function of } y} - \Omega_1^2 = 0$$

The only possibility is for $\frac{X_{,x^2}}{X}$ and $\frac{Y_{,y^2}}{Y}$ to be constants. Thus, there are three options:

$$\begin{aligned}
&\frac{X_{,x^2}}{X} = +\alpha^2 \quad \text{and} \quad \frac{Y_{,y^2}}{Y} = +\beta^2 \quad \text{with} \quad +\alpha^2 + \beta^2 = \Omega_1^2 \\
\text{or} \quad &\frac{X_{,x^2}}{X} = -\alpha^2 \quad \text{and} \quad \frac{Y_{,y^2}}{Y} = +\beta^2 \quad \text{with} \quad -\alpha^2 + \beta^2 = \Omega_1^2 \\
\text{or} \quad &\frac{X_{,x^2}}{X} = +\alpha^2 \quad \text{and} \quad \frac{Y_{,y^2}}{Y} = -\beta^2 \quad \text{with} \quad +\alpha^2 - \beta^2 = \Omega_1^2
\end{aligned}$$

The case where $X_{,x^2}/X = -\alpha^2$ and $Y_{,y^2}/Y = -\beta^2$ is impossible since $-\alpha^2 - \beta^2 < 0$ and Ω_1^2 is always positive.

2. The second Helmholtz equation for W_2 is similar and is therefore solved in a similar fashion. Again, the solution W_2 is presumed to be a product of two functions: $W_2 = X(x)Y(y)$. The equation $(\Delta - \Omega_2^2)W_2 = 0$ then becomes

$$\underbrace{\frac{X_{,x^2}}{X}}_{\text{function of } x} + \underbrace{\frac{Y_{,y^2}}{Y}}_{\text{function of } y} - \Omega_2^2 = 0$$

which entails the following options:

$$\begin{aligned}
&\frac{X_{,x^2}}{X} = +\gamma^2 \quad \text{and} \quad \frac{Y_{,y^2}}{Y} = +\delta^2 \quad \text{with} \quad +\gamma^2 + \delta^2 = \Omega_2^2 \quad \text{(LF only)} \\
\text{or} \quad &\frac{X_{,x^2}}{X} = +\gamma^2 \quad \text{and} \quad \frac{Y_{,y^2}}{Y} = -\delta^2 \quad \text{with} \quad +\gamma^2 - \delta^2 = \Omega_2^2 \\
\text{or} \quad &\frac{X_{,x^2}}{X} = -\gamma^2 \quad \text{and} \quad \frac{Y_{,y^2}}{Y} = +\delta^2 \quad \text{with} \quad -\gamma^2 + \delta^2 = \Omega_2^2 \\
\text{or} \quad &\frac{X_{,x^2}}{X} = -\gamma^2 \quad \text{and} \quad \frac{Y_{,y^2}}{Y} = -\delta^2 \quad \text{with} \quad -\gamma^2 - \delta^2 = \Omega_2^2 \quad \text{(HF only)}
\end{aligned}$$

Note that the case $X_{,x^2}/X = +\gamma^2$ and $Y_{,y^2}/Y = +\delta^2$ may only happen in the low-frequency domain where Ω_2^2 is always positive, and the case $-\gamma^2 - \delta^2 = \Omega_2^2$ may only occur in the high-frequency domain where Ω_2^2 is always negative.

Hence, for a rectangular panel, the possible eigenmodes are expressed as

$$\boxed{W(x,y) = X_1(x)Y_1(y) + X_2(x)Y_2(y)} \tag{6.33}$$

where the products X_1Y_1 and X_2Y_2 can be

$$\boxed{\begin{aligned}
X_1(x)Y_1(y) &= (A_1 \sin\alpha x + A_2 \cos\alpha x)(A_3 \sin\beta y + A_4 \cos\beta y) \quad \text{with} \quad \alpha^2 + \beta^2 = \Omega_1^2 \\
\text{or} \quad &= (A_1 \sin\alpha x + A_2 \cos\alpha x)(A_3 \sinh\beta y + A_4 \cosh\beta y) \quad \text{with} \quad \alpha^2 - \beta^2 = \Omega_1^2 \\
\text{or} \quad &= (A_1 \sinh\alpha x + A_2 \cosh\alpha x)(A_3 \sin\beta y + A_4 \cos\beta y) \quad \text{with} \quad -\alpha^2 + \beta^2 = \Omega_1^2
\end{aligned}} \tag{6.34a}$$

and

$$\boxed{\begin{array}{lll} X_2(x)Y_2(y) &= (A_5\sinh\gamma x + A_6\cosh\gamma x)\,(A_7\sinh\delta y + A_8\cosh\delta y) & \text{with} \quad \gamma^2+\delta^2=\Omega_2^2 \\ \text{or} &= (A_5\sinh\gamma x + A_6\cosh\gamma x)\,(A_7\ \sin\delta y + A_8\ \cos\delta y) & \text{with} \quad \gamma^2-\delta^2=\Omega_2^2 \\ \text{or} &= (A_5\ \sin\gamma x + A_6\ \cos\gamma x)\,(A_7\sinh\delta y + A_8\cosh\delta y) & \text{with} \quad -\gamma^2+\delta^2=\Omega_2^2 \\ \text{or} &= (A_5\ \sin\gamma x + A_6\ \cos\gamma x)\,(A_7\ \sin\delta y + A_8\ \cos\delta y) & \text{with} \quad -\gamma^2-\delta^2=\Omega_2^2 \end{array}} \tag{6.34b}$$

where α, β, γ, δ are constants called the **wavenumbers** of the eigenmode. $A_1,\dots,A_8$ are other constants that determine the phase and amplitude of each stationary wave, and most of them will be determined when applying the boundary conditions. In a given frequency range (high or low), the three expressions for X_1Y_1 combine with the three possible expressions of X_2Y_2 to form nine expressions of W.

The potential W_3 is solution of $(\Delta-\Omega_3^2)W_3=0$ which has the same form as $(\Delta-\Omega_2^2)W_2=0$. Consequently, the solution W_3 has the same form as W_2 with Ω_3^2 instead of Ω_2^2.

$$\boxed{\begin{array}{lll} W_3(x,y) &= (C_1\sinh cx + C_2\cosh cx)\,(C_3\sinh dy + C_4\cosh dy) & \text{with} \quad c^2+d^2=\Omega_3^2 \\ \text{or} &= (C_1\sinh cx + C_2\cosh cx)\,(C_3\ \sin dy + C_4\ \cos dy) & \text{with} \quad c^2-d^2=\Omega_3^2 \\ \text{or} &= (C_1\ \sin cx + C_2\ \cos cx)\,(C_3\sinh dy + C_4\cosh dy) & \text{with} \quad -c^2+d^2=\Omega_3^2 \\ \text{or} &= (C_1\ \sin cx + C_2\ \cos cx)\,(C_3\ \sin dy + C_4\ \cos dy) & \text{with} \quad -c^2-d^2=\Omega_3^2 \end{array}} \tag{6.35}$$

In the following, to simplify the presentation of the solving process, we set the solution $W(x,y)=X_1(x)Y_1(y)+X_2(x)Y_2(y)$ to have only one of the above mentioned expressions:

$$W=(A_1\sin\alpha x+A_2\cos\alpha x)\,(A_3\sin\beta y+A_4\cos\beta y)+(A_5\sinh\gamma x+A_6\cosh\gamma x)\,(A_7\sinh\delta y+A_8\cosh\delta y)$$

where $\alpha^2+\beta^2=\Omega_1^2$ and $\gamma^2+\delta^2=\Omega_2^2$. Likewise, the potential W_3 in $\boldsymbol{\Psi}=k_1\,\mathbf{grad}\,W_1+k_2\,\mathbf{grad}\,W_2+\mathbf{curl}(W_3\boldsymbol{e}_3)$ is taken as

$$W_3(x,y)=(C_1\sinh cx+C_2\cosh cx)\,(C_3\sinh dy+C_4\cosh dy)$$

where $c^2+d^2=\Omega_3^2$. Hence the form of the eigenmode for $\boldsymbol{\Psi}$ is deduced from (6.31):

$$\begin{aligned} \Psi_x &= k_1X_{1,x}Y_1+k_2X_{2,x}Y_2+(C_1\sinh cx+C_2\cosh cx)(C_3\sinh dy+C_4\cosh dy) \\ \Psi_y &= k_1X_1Y_{1,y}+k_2X_2Y_{2,y}+(C_1\sinh cx+C_2\cosh cx)(C_3\sinh dy+C_4\cosh dy) \end{aligned} \tag{6.36}$$

The derivatives are computed as follows:

$$\Rightarrow \quad \begin{aligned} \Psi_{x,x} &= k_1X_{1,x^2}Y_1+k_2X_{2,x^2}Y_2+c(C_1\cosh cx+C_2\sinh cx)(C_3\sinh dy+C_4\cosh dy) \\ \Psi_{y,y} &= k_1X_1Y_{1,y^2}+k_2X_2Y_{2,y^2}+d(C_1\sinh cx+C_2\cosh cx)(C_3\cosh dy+C_4\sinh dy) \end{aligned}$$

$$\Rightarrow \quad \begin{aligned} \Psi_{x,x} &= -k_1\alpha^2X_1Y_1+k_2\gamma^2X_2Y_2+c(C_1\cosh cx+C_2\sinh cx)(C_3\sinh dy+C_4\cosh dy) \\ \Psi_{y,y} &= -k_1\beta^2X_1Y_1+k_2\delta^2X_2Y_2+d(C_1\sinh cx+C_2\cosh cx)(C_3\cosh dy+C_4\sinh dy) \end{aligned} \tag{6.37}$$

6.5.2 Boundary conditions

The boundary conditions on eigenmodes for a soft type simple-support given in Section 6.2 are now applied on the four edges of the panel. Considering first the boundary condition $W=0$ where at least one coordinate x or y is zero lets us cancel constants more rapidly. Starting on the bottom edge where $y=0$, the boundary

condition $W(x, y = 0, t) = 0$ is

$$X_1(x)Y_1(0) + X_2(x)Y_2(0) = 0$$

Since this relation holds for any $x \in [0, a]$,

$$\begin{cases} Y_1(0) = 0 \\ Y_2(0) = 0 \end{cases} \Rightarrow \begin{cases} A_3 \sin 0 & +A_4 \cos 0 & = 0 \\ A_7 \sinh 0 & +A_8 \cosh 0 & = 0 \end{cases} \Rightarrow \boxed{A_4 = A_8 = 0}$$

Similarly, the left border gives $\boxed{A_2 = A_6 = 0}$. Then, the right border gives

$$\begin{cases} X_1(a) = 0 \\ X_2(a) = 0 \end{cases} \Rightarrow \begin{array}{l} A_1 \sin(\alpha a) = 0 \\ A_5 \sinh(\gamma a) = 0 \end{array} \Rightarrow \begin{array}{llll} A_1 = 0 & \text{or} & \alpha a = m\pi, m \in \mathbb{N} \\ A_5 = 0 & \text{or} & \sinh(\gamma a) = 0 \Rightarrow \gamma = 0 \end{array}$$

If $A_5 = 0$ or $\gamma = 0$, in either way the term $A_5 \sinh(\gamma x)$ is zero. Finally, the top border gives

$$\begin{cases} Y_1(b) = 0 \\ Y_2(b) = 0 \end{cases} \Rightarrow \begin{array}{l} A_3 \sin(\beta b) = 0 \\ A_7 \sinh(\delta b) = 0 \end{array} \Rightarrow \begin{array}{llll} A_3 = 0 & \text{or} & \beta b = n\pi, n \in \mathbb{N} \\ A_7 = 0 & \text{or} & \sinh(\delta b) = 0 \Rightarrow \delta = 0 \end{array}$$

If $A_7 = 0$ or $\delta = 0$, in either way the term $A_7 \sinh(\delta x)$ is zero. Six constants have been cancelled by applying the first boundary condition: A_1, A_2, A_6, A_8, γ and δ, leaving only

$$W = A_1 A_3 \sin(\alpha x) \sin(\beta y)$$

The constants A_5 and A_7 disappear due to $\gamma = \delta = 0$. Cancelling either A_1 or A_3 leads to the trivial solution $W = 0$. The other solutions are obtained for $A_1 A_3 \neq 0$, which leads to $\alpha = \dfrac{m\pi}{a}$ and $\beta = \dfrac{n\pi}{b}$ as shown in the above.

The process of writing the boundary conditions for $\mathbf{\Psi}$ on all four edges is quite long as it is not possible to cancel any terms until the end, where one arrives at the conclusion that all coefficients C_i must vanish.

Finally, the boundary conditions are satisfied when $A_2 = A_4 = A_5 = A_6 = A_7 = A_8 = 0$ and $C_i = 0$. Therefore, the solution fields take the form

$$\boxed{\begin{aligned} W &= W_{mn} \sin(\alpha x) \sin(\beta y) \\ \Psi_x &= \Psi_{xmn} \cos(\alpha x) \sin(\beta y) \\ \Psi_y &= \Psi_{ymn} \sin(\alpha x) \cos(\beta y) \end{aligned}} \tag{6.38}$$

where $\alpha = \dfrac{m\pi}{a}$ and $\beta = \dfrac{n\pi}{b}$. The natural shapes are similar to the well-known ones for thin classical plates, Fig. 6.5. In the end, it appears that hyperbolic functions are not permitted by the SSSS boundary conditions, and that all the remaining terms in W stem from W_1 and not W_2, W_3. Note that in the high-frequency domain, other eigenmodes exist as the sum of two products of sine functions with different wavenumbers, and they should be addressed in future works.

6.5.3 Natural frequencies of rectangular inflatable panels

The classical method for finding the eigenfrequencies is to write the transcendent characteristic equation and look for its roots numerically. However, in the special case of simply-supported rectangular panels, there exists a simple method that yields analytical expressions of the natural frequencies. The reasoning in this section was inspired by Rakotomanana's book on the dynamics of elastic structures [78]. It takes advantage

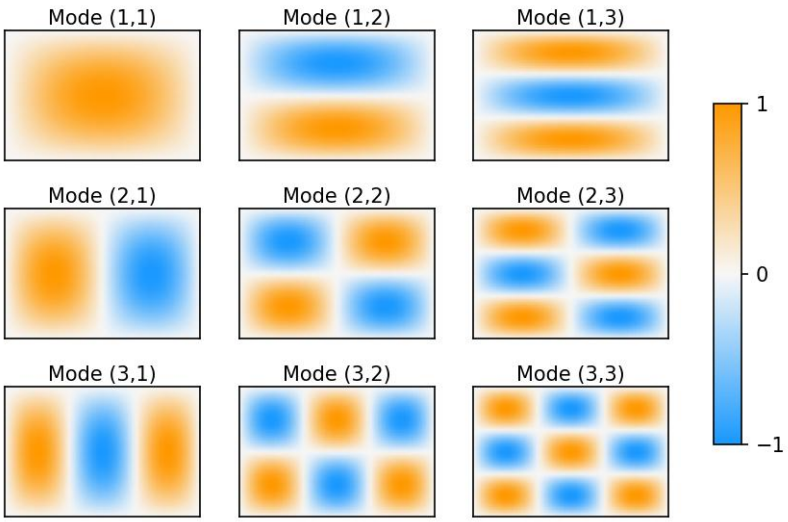

Figure 6.5: First flexural vibration modes (m, n) of a supported rectangular inflatable panel with $W_{mn} = 1$, $\Psi_{xmn} = \Psi_{ymn} = 1$.

of the sine and cosine functions' property of being proportional to their second derivatives, which allows them to be cancelled out from the equations of motion. Substituting the solution fields of Eq. (6.38) into the eigenvalue equations (6.3) and (6.4) yields the following 3 by 3 system:

$$\begin{bmatrix} \mathcal{P}_{11} - 2\tau\rho\omega^2 & \mathcal{P}_{12} & \mathcal{P}_{13} \\ \mathcal{P}_{12} & \mathcal{P}_{22} - \dfrac{\rho\tilde{\tau}H^2}{2}\omega^2 & \mathcal{P}_{23} \\ \mathcal{P}_{13} & \mathcal{P}_{23} & \mathcal{P}_{33} - \dfrac{\rho\tilde{\tau}H^2}{2}\omega^2 \end{bmatrix} \begin{pmatrix} W_{mn} \\ \Psi_{xmn} \\ \Psi_{ymn} \end{pmatrix} = \begin{pmatrix} 0 \\ 0 \\ 0 \end{pmatrix}$$

where

$$\begin{aligned} \mathcal{P}_{11} &\equiv p\tilde{H}(\alpha^2 + \beta^2) \\ \mathcal{P}_{22} &\equiv D^* \left(\alpha^2 + \frac{1-\nu}{2}\beta^2 \right) + M_0^{(2)}(\alpha^2 + \beta^2) + p\tilde{H} \\ \mathcal{P}_{33} &\equiv D^* \left(\frac{1-\nu}{2}\alpha^2 + \beta^2 \right) + M_0^{(2)}(\alpha^2 + \beta^2) + p\tilde{H} \\ \mathcal{P}_{12} &\equiv \mathcal{P}_{21} = p\tilde{H}\alpha \\ \mathcal{P}_{13} &\equiv \mathcal{P}_{31} = p\tilde{H}\beta \\ \mathcal{P}_{23} &\equiv \mathcal{P}_{32} = D^* \frac{1+\nu}{2}\alpha\beta \end{aligned}$$

where we recall that $D^* = \dfrac{E\tilde{\tau}H^2}{2(1-\nu^2)}$ and $M_0^{(2)} = \dfrac{p\tilde{H}\tilde{\tau}H^2}{4\tau}$. The first root from Cardan's method is

$$\boxed{\omega_0^2 = \frac{2}{\rho\tilde{\tau}H^2}\left[p\tilde{H} + \left(D^* \frac{1-\nu}{2} + M_0^{(2)} \right)(\alpha^2 + \beta^2) \right]} \tag{6.39}$$

Factorizing the determinant by this root unveils a quadratic equation in ω^2:

$$2\tau\rho \times \frac{\rho\tilde{\tau}H^2}{2}\omega^4 - \left[\frac{\rho\tilde{\tau}H^2}{2}p\tilde{H}\left(\alpha^2+\beta^2\right) + 2\tau\rho\left(p\tilde{H} + \left(D^* + M_0^{(2)}\right)\left(\alpha^2+\beta^2\right)\right)\right]\omega^2 + \left(D^* + M_0^{(2)}\right)p\tilde{H}\left(\alpha^2+\beta^2\right)^2 = 0$$

Note that $\alpha^2+\beta^2 = \Omega_1^2$. The two roots are

$$\boxed{\omega_\pm^2 = \frac{1}{2\rho^2H^2\tau\tilde{\tau}}\left[\frac{\rho\tilde{\tau}H^2}{2}p\tilde{H}\left(\alpha^2+\beta^2\right) + 2\tau\rho\left(p\tilde{H} + \left(D^* + M_0^{(2)}\right)\left(\alpha^2+\beta^2\right)\right) \pm \sqrt{\Delta}\right]} \tag{6.40}$$

where

$$\Delta \equiv \left[\frac{\rho\tilde{\tau}H^2}{2}p\tilde{H}\left(\alpha^2+\beta^2\right) + 2\tau\rho\left(p\tilde{H} + \left(D^* + M_0^{(2)}\right)\left(\alpha^2+\beta^2\right)\right)\right]^2 - 4\left(\rho^2H^2\tau\tilde{\tau}\right)\left(D^* + M_0^{(2)}\right)p\tilde{H}(\alpha^2+\beta^2)^2$$

Since the expressions of ω^2 from Eq. (6.39) and (6.40) are symmetric in m and n, when the panel is square ($a = b$), the modes that are simply a quarter turn rotation of another mode will have the same frequency: $f_{mn} = f_{nm}$. In Fig. 6.6 the three natural frequencies of a "classical" (not inflatable) plate are plotted and compared to Hashemi's results [33]. Interestingly, only the lowest of our previously calculated frequencies, ω_-, can be retrieved in his work. Although he does mention additional parameters denoted λ_1, λ_2 and λ_3, only λ_1 has non-zero values that may cancel the characteristic equation. While it is possible to compute the values of ω_0, ω_+ and ω_-, only values corresponding to ω_- are found in the literature. An explanation may be that the characteristic equation stems from applying the boundary conditions to the natural shapes: it can only be cancelled by eigenfrequencies that *satisfy the boundary conditions*. Thus it appears that ω_0 and ω_+ are eigenfrequencies that correspond to natural shapes which cannot exist in a plate with a simply-supported edge. An explanation is yet to be found as for why this approach produced two superfluous eigenfrequencies, even though the natural shape substituted into the local equilibrium took into account boundary conditions that forbade them. Following this discussion, we will focus exclusively on ω_- in the following.

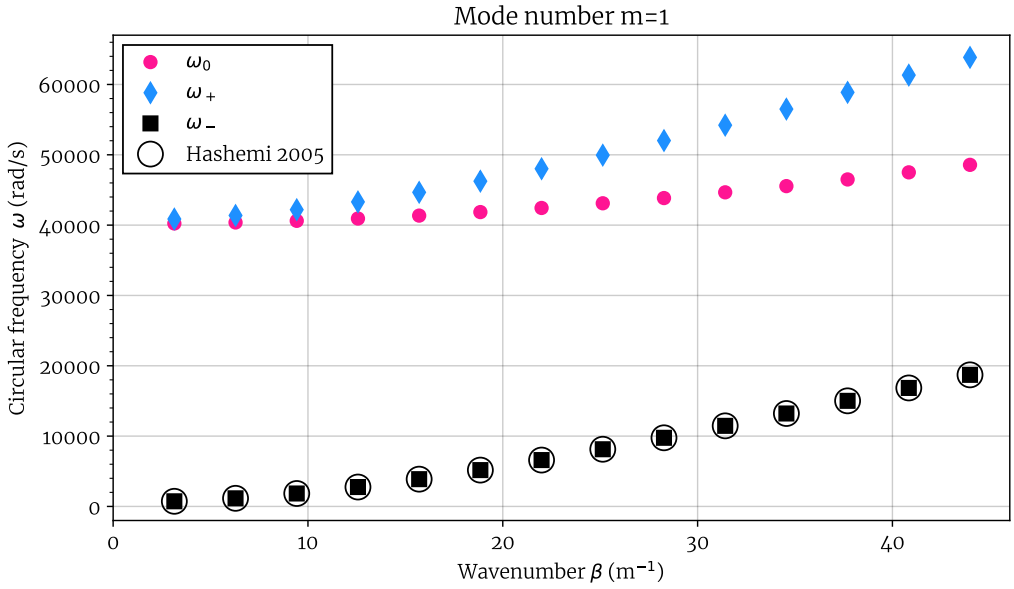

Figure 6.6: Eigenfrequencies of a simply-supported rectangular plate ($a = 0.5$ m, $b = 1$ m, $H_\varnothing = 5$ cm, $E = 2$ GPa, $\nu = 0.3$, $\rho = 2000$ kg/m³).

Returning to inflatable panels, the spectrum (the set of all the eigenfrequencies) is plotted against inflation pressure in Fig 6.7. As was the case with circular panels, they approximately follow a square root law of the inflation pressure p, especially as the resonance frequency becomes higher. A simplified model of the vibrations of rectangular membranes is proposed in the appendices, Section C.1.

6.6 Historical approach to solving the eigenvalue problem

Alternatively, the eigenvalue problem can be solved using the original method by Mindlin and Deresiewicz. The notations change but the main results remain identical to the ones that have been established in this chapter. Some additional observations will be discussed.

The Helmholtz-Hodge theorem in 2D assures that there exist two scalar fields φ and W_3 such that $\boldsymbol{\Psi} = \mathbf{grad}\,\varphi + \mathbf{curl}(W_3\mathbf{e}_z)$. In Cartesian coordinates, the components of the fiber orientation eigenmode $\boldsymbol{\Psi}$ derive from potentials φ, W_3:

$$\Psi_x = \frac{\partial \varphi}{\partial x} + \frac{\partial W_3}{\partial y}$$
$$\Psi_y = \frac{\partial \varphi}{\partial y} - \frac{\partial W_3}{\partial x}$$

If $\boldsymbol{\Psi}$ is expressed as a function of the potentials φ and W_3, then Eq. (6.3) becomes

$$\Delta(W + \varphi) + \omega^2 \frac{2\tau\rho}{p\tilde{H}} W = 0 \tag{6.41}$$

that is rewritten as

$$\Delta(W + \varphi) + V_s D_0^2 W = 0 \tag{6.42}$$

where $V_s = \dfrac{K}{p\tilde{H}}$ is the ratio of flexural stiffness over shear stiffness and $D_0^2 = \omega^2 \dfrac{2\tau\rho}{K}$ the frequency parameter

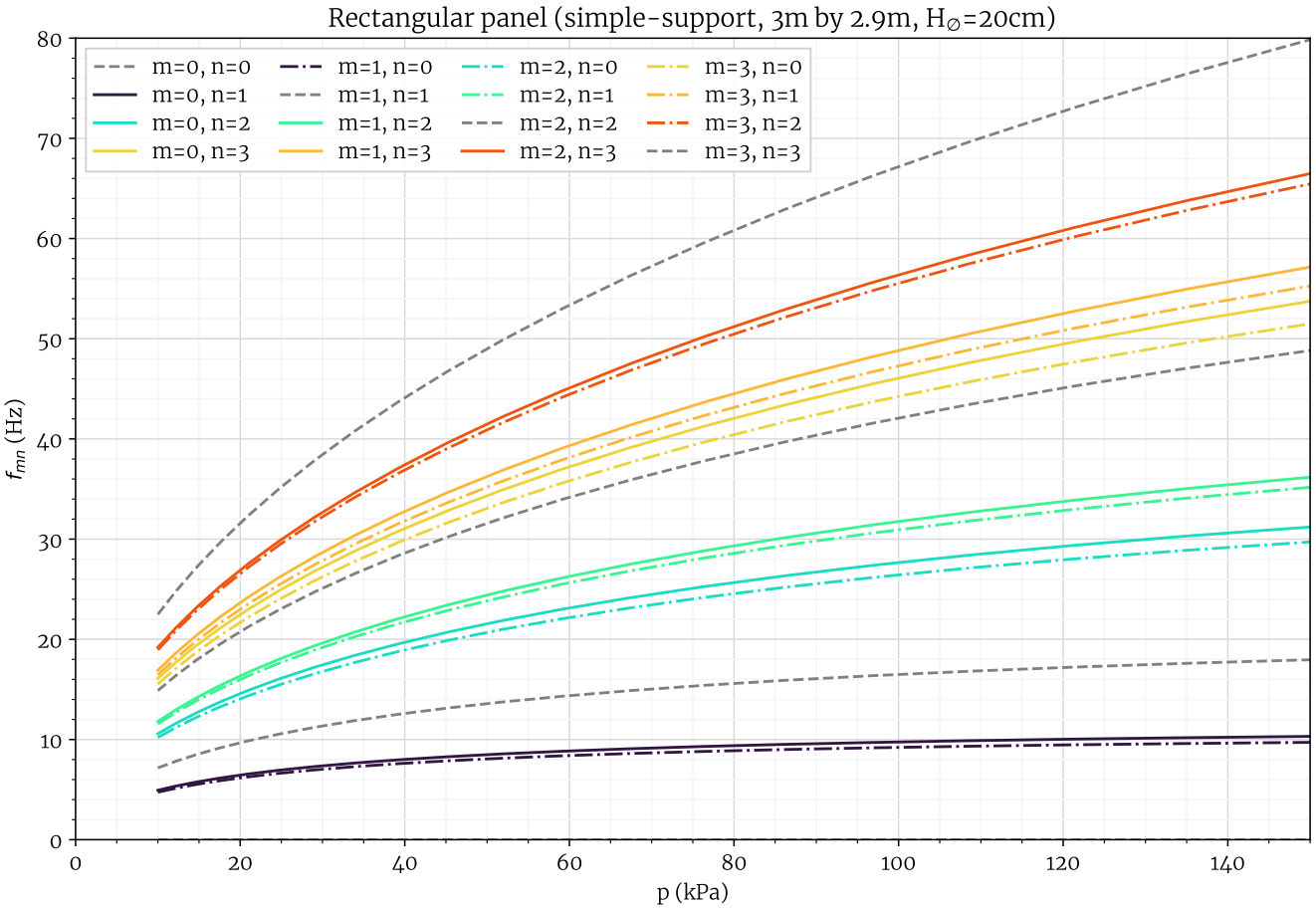

Figure 6.7: Natural frequencies of a simply-supported rectangular inflatable panel as a function of the inflation pressure ($E\tau = 390$ N/mm, $\nu = 0.25$, $\rho = 1000$ kg/m³).

(in m^{-2}). Recall that $K = D^* + M_0^{(2)}$. The moment equilibrium equation projected on the x axis writes

$$\frac{D^*}{2}\Big[(1-\nu)\Delta(\varphi_{,x}+W_{3,y})+(1+\nu)(\varphi_{,xxx}+W_{3,xxy}+\varphi_{,xyy}-W_{3,xxy})\Big] + M_0^{(2)}\Delta(\varphi_{,x}+W_{3,y}) - p\tilde{H}(\varphi_{,x}+W_{3,y}+W_{,x}) = -\omega^2\frac{\rho\tilde{\tau}H^2}{2}(\varphi_{,x}+W_{3,y})$$

$$\left(D^*+M_0^{(2)}\right)\Delta\varphi_{,x}+\left(D^*\frac{1-\nu}{2}+M_0^{(2)}\right)\Delta W_{3,y} - p\tilde{H}(\varphi_{,x}+W_{3,y}+W_{,x}) + \omega^2\frac{\rho\tilde{\tau}H^2}{2}(\varphi_{,x}+W_{3,y}) = 0$$

the terms are rearranged to separate those that affect φ and W from the ones that affect W_3:

$$\frac{\partial}{\partial x}\left[K\Delta\varphi+\left(\omega^2\frac{\rho\tilde{\tau}H^2}{2}-p\tilde{H}\right)\varphi-p\tilde{H}W\right]+\frac{\partial}{\partial y}\left[K_\nu\Delta W_3+\left(\omega^2\frac{\rho\tilde{\tau}H^2}{2}-p\tilde{H}\right)W_3\right]=0$$

where $K_\nu = D^*\dfrac{1-\nu}{2} + M_0^{(2)}$. The same reasoning is applied for the y component to produce the following system of two equations:

$$\frac{\partial}{\partial x}\left[\Delta\varphi+\left(V_iD_0^2-V_s^{-1}\right)\varphi-V_s^{-1}W\right]+\frac{K_\nu}{K}\frac{\partial}{\partial y}\left[\Delta W_3+\frac{K}{K_\nu}\left(V_iD_0^2-V_s^{-1}\right)W_3\right]=0 \tag{6.43a}$$

$$\frac{\partial}{\partial y}\left[\Delta\varphi+\left(V_iD_0^2-V_s^{-1}\right)\varphi-V_s^{-1}W\right]-\frac{K_\nu}{K}\frac{\partial}{\partial x}\left[\Delta W_3+\frac{K}{K_\nu}\left(V_iD_0^2-V_s^{-1}\right)W_3\right]=0 \tag{6.43b}$$

where $V_i = \frac{\frac{\rho\tilde{\tau}H^2}{2}}{2\tau\rho} = \frac{\tilde{\tau}H^2}{4\tau}$ is the ratio of rotatory inertia and flexural inertia. By differentiating (6.43a) with respect to x and (6.43b) with respect to y, the addition of the two resulting equations is the following Laplace equation

$$\Delta\Big(\Delta\varphi + \left(V_i D_0^2 - V_s^{-1}\right)\varphi - V_s^{-1}W\Big) = 0 \tag{6.44}$$

Next, differentiation with respect to y and x followed by subtraction of Equations (6.43) gives

$$\Delta\left(\Delta + \frac{K}{K_\nu}\left(V_i D_0^2 - V_s^{-1}\right)\right) W_3 = 0 \tag{6.45}$$

where we define

$$\boxed{D_3 \equiv \frac{K}{K_\nu}\left(V_i D_0^2 - V_s^{-1}\right)} \tag{6.46}$$

Note that Equation (6.45) can be solved independently from (6.44). From now on, the same reasoning applies in all coordinates systems. One can assume that the potential φ is proportional to the unknown transverse displacement W: by choosing $\varphi = (\sigma - 1)W$, Equation (6.45) implies

$$\Delta\big(W + (\sigma-1)W\big) + V_s D_0^2 W = 0 \quad \Rightarrow \quad \Delta W + \frac{V_s D_0^2}{\sigma} W = 0 \qquad , \sigma \neq 0$$

It is observed that the Laplacian of W must be proportional to W. Let us define D_W such that $\Delta W = -D_W W$. Equation (6.44) becomes

$$(\sigma-1)D_W^2 W - \left(V_i D_0^2 - V_s^{-1}\right)(\sigma-1)D_W W + V_s^{-1} D_W W = 0 \tag{6.47}$$

We introduced two constant parameters, σ and D_W, which must satisfy

$$D_W = \frac{V_s D_0^2}{\sigma} \tag{6.48a}$$

$$D_W = V_i D_0^2 - \frac{1}{V_s} - \frac{1}{V_s(\sigma-1)} \tag{6.48b}$$

Substituting the expression of σ from the first equation into the second yields

$$\left(\frac{V_s^2 D_0^2}{D_W} - V_s\right) V_i D_0^2 - \frac{V_s^2 D_0^2}{D_W} = V_s^2 D_0^2 - V_s D_W \tag{6.49}$$

multiplying by $-D_W/V_s$ and rearranging terms gives

$$D_W^2 - (V_i + V_s)D_0^2 D_W + V_i V_s D_0^4 - D_0^2 = 0$$

Two solutions for D_W exist, provided that

$$(V_i + V_s)^2 D_0^4 - 4V_i V_s D_0^4 + 4D_0^2 = D_0^4\left[(V_i - V_s)^2 + 4D_0^{-2}\right] > 0$$

then, the solutions are

$$\boxed{D_1, D_2 \equiv \frac{D_0^2}{2}\left(V_i + V_s \pm \sqrt{(V_i - V_s)^2 + 4D_0^{-2}}\right)} \tag{6.50}$$

The constant σ can then be deduced from $\sigma = \frac{V_s D_0^2}{D_W}$. Substituting D_1, D_2 from Equation (6.50) and using

the conjugate of the denominator:

$$\sigma = \frac{V_s D_0^2 \left[V_i + V_s \mp \sqrt{(V_i - V_s)^2 + 4D_0^{-2}} \right]}{\frac{1}{2} D_0^2 \left[(V_i + V_s)^2 - (V_i - V_s)^2 - 4D_0^{-2} \right]}$$

$$\boxed{\sigma_1 \equiv \frac{D_2}{V_i D_0^2 - V_s^{-1}}} \qquad \boxed{\sigma_2 \equiv \frac{D_1}{V_i D_0^2 - V_s^{-1}}} \tag{6.51}$$

From $\Delta W = -D_W W$ we deduced two possible values of D_W denoted as D_1 and D_2, which give rise to two possible solutions W_1 and W_2 for W. Ultimately, determining the natural modes of inflatable panels with the method of potentials comes down to solving three Helmholtz equations:

$$\boxed{\begin{aligned} (\Delta + D_1) W_1 &= 0 \\ (\Delta + D_2) W_2 &= 0 \\ (\Delta + D_3) W_3 &= 0 \end{aligned}} \tag{6.52}$$

The unknown fields W_1, W_2 and W_3 are called the **displacement potentials**. The plate-displacement components are computed with

$$\begin{aligned} W &= W_1 + W_2 \\ \Psi_x &= (\sigma_1 - 1) W_{1,x} + (\sigma_2 - 1) W_{2,x} + W_{3,y} \\ \Psi_y &= (\sigma_1 - 1) W_{1,y} + (\sigma_2 - 1) W_{2,y} - W_{3,x} \end{aligned} \tag{6.53}$$

Remark 6.4. When $V_i = 0$ (no rotatory inertia) and $V_s = 0$ (infinite shear stiffness), σ vanishes and $D_1 = -D_2 = D_0$, meaning that the equations reduce to those of Love–Kirchhoff theory:

$$(\Delta + D_0)(\Delta - D_0) W = 0$$

Note that D_1, D_2 and D_3 depend on the circular frequency ω through D_0. It is important to study the sign of D_2 and D_3 as a function of frequency, as this will change the solutions to Equations (6.52). The values of D_i are plotted against D_0 in Fig 6.8.

6.6.1 Cutoff frequency

The frequency for which D_2 and D_3 vanish is named **cutoff frequency** and it plays a crucial role in determining the natural shapes, since the sign of D_2 and D_3 changes when this special frequency is exceeded.

$$\begin{aligned} D_3 = 0 \Leftrightarrow D_0^2 &= \frac{1}{V_i V_s} \\ \Leftrightarrow \omega_c^2 \frac{2\tau\rho}{K} &= \frac{4\tau p \tilde{H}}{K \tilde{\tau} H^2} \\ \Leftrightarrow \omega_c^2 &= p\tilde{H} \left(\frac{\rho \tilde{\tau} H^2}{2} \right)^{-1} \end{aligned}$$

The cutoff frequency increases with the shear stiffness caused by pressurization and decreases with the rotatory inertia of the panel (when the membranes are thicker, heavier or farther apart).

Mode shape at the cutoff frequency

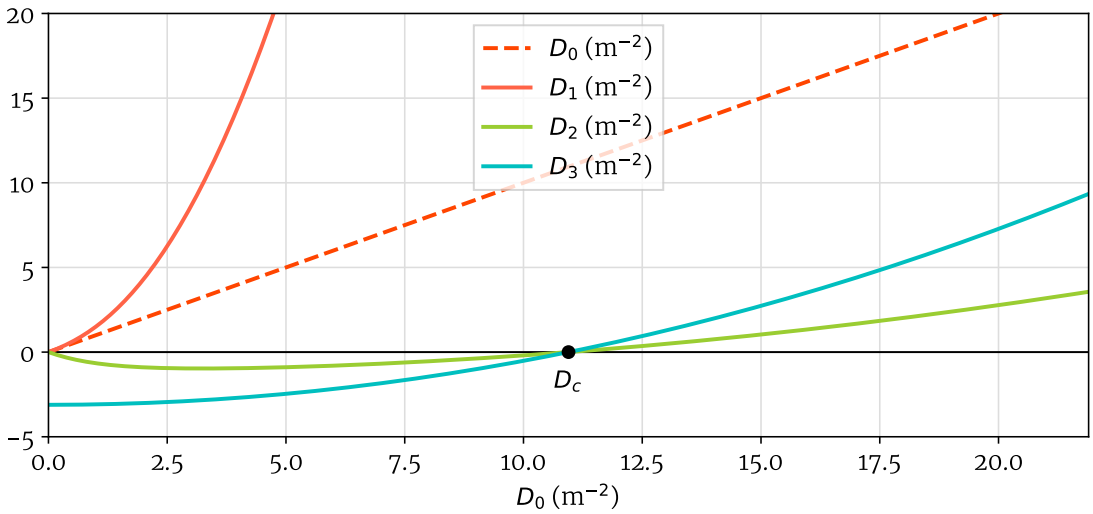

Figure 6.8: Dispersion relations for an inflatable panel ($E\tau = 389$ N/mm, $\nu = 0.25$, $\rho = 1000$ kg/m^3, $H_\varnothing = 20$ cm). D_c is the cutoff frequency parameter.

The last two equations of (6.52) reduce to Laplace equations that can be satisfied in Cartesian coordinates by a simple equation of the form $c_{11}xy + c_{10}x + c_{01}y + c_{00}$. This hints at the possibility of having a natural shape that contains an "offset by a plane" (if the boundary conditions allow it). However, σ_2 goes to infinity near the cutoff frequency (Fig. 6.9), such that the plate-displacement cannot be reconstructed: the equations at hand fail to describe what happens in this case. Chao and Pao [79] described a method to study flexural motions of plates at the cutoff frequency. They focused on the propagation of waves inside a plate and not on the eigenmode shape. To solve the vibration problem at the cutoff frequency, several notations need to be replaced to obtain a different set of equations. This very special case will not be investigated further in this dissertation as it seems unlikely to be observed in practice.

6.6.2 Contribution of the potentials to the natural shear modes

The contribution of W_1 and W_2 to Ψ_x and Ψ_y can be studied by examining the sign of σ_1 and σ_2 as a function of ω. Note that these two numbers are related to the k_1, k_2 of Section 6.4 by the relation $k_\alpha = \sigma_\alpha - 1$, and so the same observations are made. They are both zero when $\omega = 0$. Then, the first coefficient σ_1 rapidly converges to 1 before the cutoff frequency. In the low-frequency domain, σ_2 diverges to $-\infty$ as ω approaches ω_c from the left. In the high-frequency domain, it diverges to ∞ as ω approaches ω_c from the right and converges to $\frac{V_s}{V_i}$ at infinity. One may also compute the asymptotic values of σ_1 and σ_2 for very large frequencies. D_1 and D_2 both diverge to infinity with ω. From the definition of σ in Eq. (6.48a):

$$\sigma = \frac{V_s D_0^2}{D_W} = \frac{2V_s}{V_i + V_s \pm \sqrt{(V_i - V_s)^2 + \frac{4}{D_0^2}}} \tag{6.54}$$

Assuming $D_0^2 \longrightarrow \infty$ yields

$$\begin{aligned} \sigma_1 &= \frac{V_s D_0^2}{D_1} = \frac{2V_s}{V_i + V_s + |V_i - V_s|^2} \\ \sigma_2 &= \frac{V_s D_0^2}{D_2} = \frac{2V_s}{V_i + V_s - |V_i - V_s|^2} \end{aligned} \tag{6.55}$$

We need to determine whether V_i is smaller or larger than V_s. For an inflatable panel, $V_s/V_i = \frac{K}{p\tilde{H}}\frac{4\tau}{\tilde{\tau}H^2} \approx 4(D^* + M_0^{(2)})/(pH^3)$, which is numerically much larger than 1 with the geometric and material properties of our panels. Therefore:

$$\begin{aligned}\sigma_1 &= \frac{2V_s}{V_i + V_s - V_i + V_s} = 1\\ \sigma_2 &= \frac{2V_s}{V_i + V_s + V_i - V_s} = \frac{V_s}{V_i}\end{aligned} \tag{6.56}$$

Consequently, σ_2 is larger than σ_1 in the high-frequency domain. Since σ_1 converges to 1 before the cutoff frequency (as seen in Fig. 6.9), Equation (6.53) shows that W_1 will not contribute to the shear mode in the high-frequency domain: it only plays a role for very low frequencies.

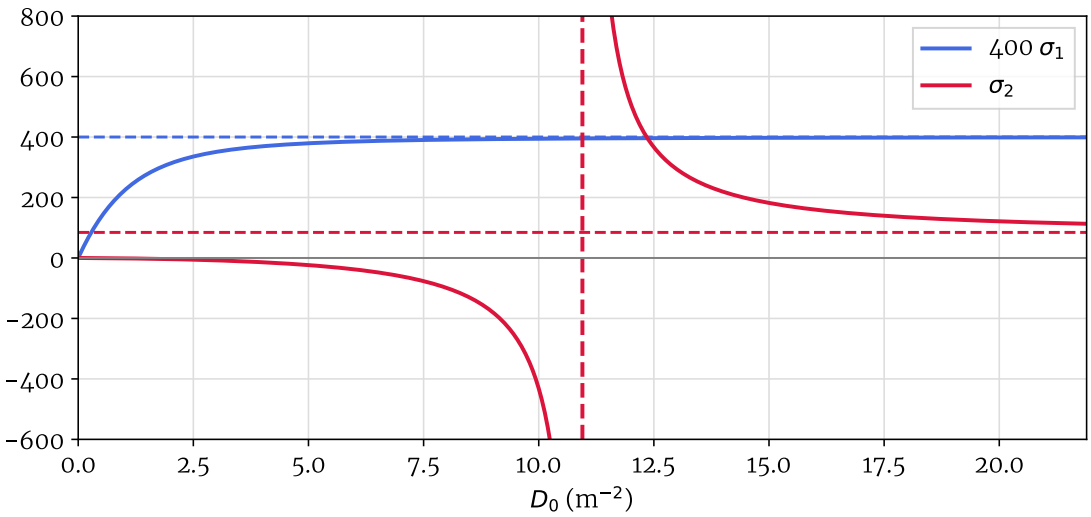

Figure 6.9: Graph of σ_1 and σ_2 and their asymptotic values in the frequency domain.

6.7 Vibrations of circular inflatable panels

The geometry and coordinate system of the circular panel is the same as for the static example, Fig. 4.1.

6.7.1 Natural shapes of circular inflatable panels

In polar coordinates, the Helmholtz-Hodge decomposition is written as:

$$\begin{aligned}\Psi_r &= \frac{\partial\varphi}{\partial r} + \frac{1}{r}\frac{\partial W_3}{\partial\theta}\\ \Psi_\theta &= \frac{1}{r}\frac{\partial\varphi}{\partial\theta} - \frac{\partial W_3}{\partial r}\end{aligned}$$

The plate-displacement components are computed with

$$\begin{aligned}W &= W_1 + W_2\\ \Psi_r &= (\sigma_1 - 1)W_{1,r} + (\sigma_2 - 1)W_{2,r} + \frac{W_{3,\theta}}{r}\\ \Psi_\theta &= (\sigma_1 - 1)\frac{W_{1,\theta}}{r} + (\sigma_2 - 1)\frac{W_{2,\theta}}{r} - W_{3,r}\end{aligned} \tag{6.57}$$

We will now solve the three Helmholtz equations (6.52). $\forall i \in \{1,2,3\}$,

$$\begin{aligned}(\Delta + D_i)W_i = 0 \Rightarrow W_{i,rr} + \frac{W_{i,r}}{r} + \frac{W_{i,\theta\theta}}{r^2} + D_i W_i = 0 \\ \Rightarrow r^2 W_{i,rr} + r W_{i,r} + W_{i,\theta\theta} + D_i r^2 W_i = 0\end{aligned}$$

The method of separation of variables is applied: assuming that the plate-displacements potentials can be written as $W_i(r,\theta) = f_i(r)\Theta_i(\theta)$, the previous equation may be written as

$$r^2 f_{i,rr}\Theta_i + r f_{i,r}\Theta_i + f_i \Theta_{i,\theta\theta} + D_i r^2 f_i \Theta_i = 0 \tag{6.58}$$

dividing by $f_i\Theta_i$ yields

$$\underbrace{\frac{r^2 f_{i,rr} + r f_{i,r}}{f_i} + D_i r^2}_{\text{function of } r \text{ only}} + \underbrace{\frac{\Theta_{i,\theta\theta}}{\Theta_i}}_{\text{function of } \theta \text{ only}} = 0 \tag{6.59}$$

Therefore, the two underbraced terms must be equal to a constant $\pm m^2 \in \mathbb{R}$. For the sake of clarity, we will anticipate the results of the integration to settle the sign of $\pm m^2$:

1. If $\dfrac{\Theta_{i,\theta\theta}}{\Theta_i} = m^2$, then Θ_i is the sum of hyperbolic sine and cosine functions, which are not periodic.
2. If $\dfrac{\Theta_{i,\theta\theta}}{\Theta_i} = -m^2$, then Θ_i is the sum of cosine and sine functions, which are periodic.

Only the second option is possible since the solution must be periodic with respect to θ. Hence

$$\Theta_{i,\theta\theta} = -m^2\Theta_i \quad \Rightarrow \quad \Theta_i(\theta) = C_i \cos(m\theta) + S_i \sin(m\theta)$$

Furthermore, in order to satisfy the periodicity condition $\Theta_i(r,\theta) = \Theta_i(r,\theta + 2\pi)$, one must have $m \in \mathbb{N}$. The constant integer m is called the **circumferential order** (or **angular wavenumber**) of the natural mode, since it dictates the number of sine wave cycles on the circumference of the disk. It corresponds to the number of nodal diameters.

$$r^2 f_{i,rr} + r f_{i,r} + D_i r^2 f_i = m^2 f_i \quad \Leftrightarrow \quad r^2 f_{i,rr} + r f_{i,r} + \left(D_i r^2 - m^2\right) f_i = 0 \tag{6.60}$$

If D_i is positive, then f_i is the solution of a Bessel equation of order m. However, both D_2 and D_3 are negative in the low-frequency range and positive in the high-frequency range. We define, $\forall i \in 2,3$,

$$\delta_i = \begin{cases} \sqrt{-D_i} & , \omega < \omega_c \\ \sqrt{D_i} & , \omega > \omega_c \end{cases}$$

and $\delta_1 = \sqrt{D_1}$. Let us anticipate the resolution by discussing the sign of D_2.

- When $\omega < \omega_c$ (low-frequency domain): $D_2 < 0$ will be replaced by $(j\delta_2)^2 = -\delta_2^2$, turning Eq. (6.60) into a modified Bessel equation (via the change of variable $r \leftarrow ir$, see Appendix A).
- When $\omega = \omega_c$ (cutoff frequency): Eq. (6.60) becomes a Cauchy-Euler equation with solutions of the form $f_i(r) = A_i \cosh(m\log(r)) + A_i' \sinh(m\log(r))$. The mode shape is independent of D_2 and D_3.
- When $\omega > \omega_c$ (high-frequency domain): in Eq. (6.60), D_2 and D_3 are replaced with δ_2^2 and δ_3^2 respectively (δ_2 and δ_3 are positive). It is therefore a classical Bessel equation.

Therefore, when $D_2, D_3 < 0$ (low-frequencies): $\forall i \in \{2,3\}$

$$W_i(r,\theta) = \left[A_i I_m(\delta_i r) + A_i' K_m(\delta_i r)\right]\left(C_i \cos(m\theta) + S_i \sin(m\theta)\right) \tag{6.61}$$

and when $D_2, D_3 > 0$ (high-frequencies): $\forall i \in \{2,3\}$

$$W_i(r,\theta) = \left[A_i J_m(\delta_i r) + A_i' Y_m(\delta_i r)\right]\left(C_i \cos(m\theta) + S_i \sin(m\theta)\right) \tag{6.62}$$

The linear combination of sine and cosine $\Theta_i(\theta) = C_i \cos(m\theta) + S_i \sin(m\theta)$ in Relations (6.61), (6.62) can also be rewritten as a phase-shifted sine function. A phase-shift in this angular-dependent factor simply means rotating the natural shape around the $(O, \boldsymbol{e}_3)$ axis. Eigenfrequencies are invariant under translation or rotation of their corresponding mode shape, and consequently the spectrum of the panel remains unchanged if the initial phase of $\Theta_i(\theta)$ vanishes. Therefore, as long as we are not concerned with the relative orientation of one natural shape to another, the discussion can be simplified by keeping only a cosine in W_1 and W_2 and a sine W_3, as was done in the literature [29, 31]. Leissa explains in his 1969 book [83] that for thin plates: *"If the boundary conditions possess symmetry with respect to one or more diameters of the circle, then the terms involving* $\sin\theta$ *are not needed"*. With this choice of potentials, Ψ_r and Ψ_θ will contain either sin or cos but not both, which makes them disappear easily when applying the boundary conditions that must hold for all θ. To simplify the following discussion where all the boundary conditions will be axisymmetric, we follow the same procedure and consider only one of the infinity of natural shapes that are identical up to a rotation.

The Bessel functions of the second kind Y_m and K_m have infinite limits at $r = 0$. This is not a problem for the potentials W_i, but the displacement W is required to be finite for physical reasons. If one were to keep these Bessel functions in W_i, the conclusion would be that all coefficients A_i' must vanish (except for the case of an annular panel). By anticipating this reasoning, the plate-displacement potentials are

$$\boxed{\begin{aligned} W_1 &= A_1 J_m(\delta_1 r)\cos(m\theta) \\ W_2 &= A_2 B_m(\delta_2 r)\cos(m\theta) \\ W_3 &= A_3 B_m(\delta_3 r)\sin(m\theta) \end{aligned}} \tag{6.63}$$

where $B_m = I_m$ in the low-frequency range and $B_m = J_m$ in the high-frequency range:

$$B_m = \begin{cases} I_m & \text{when } \omega < \omega_c \\ J_m & \text{when } \omega > \omega_c \end{cases} \tag{6.64}$$

Now, the plate-displacements components from (6.57) can be expressed in terms of these solutions:

$$\begin{aligned} W &= \left[A_1 J_m(\delta_1 r) + A_2 B_m(\delta_2 r)\right]\cos(m\theta) \\ \Psi_r &= \left[A_1(\sigma_1 - 1)\delta_1 J_m'(\delta_1 r) + A_2(\sigma_2 - 1)\delta_2 B_m'(\delta_2 r) + A_3 \frac{m}{r} B_m(\delta_3 r)\right]\cos(m\theta) \\ \Psi_\theta &= -\left[A_1(\sigma_1 - 1)\frac{m}{r} J_m(\delta_1 r) + A_2(\sigma_2 - 1)\frac{m}{r} B_m(\delta_2 r) + A_3 \delta_3 B_m'(\delta_3 r)\right]\sin(m\theta) \end{aligned} \tag{6.65}$$

Remark 6.5. When discarding the possible rotation of a natural shape around the central axis, the natural frequencies are still predicted correctly but the relative orientation of the eigenmodes cannot be captured. For instance, in the situation where the edge of the panel is pinned at one point, at least one nodal line of each mode should pass through this point in order to satisfy the boundary conditions, but the nodal diameters are generally not aligned with those of other modes. Therefore, when dealing with problems where the boundary conditions are not axisymmetric, it is necessary to work with the following sets of potentials. In the low

frequency range,

$$\begin{aligned} W_1 &= \left[A_m J_m(\delta_1 r) + B_m Y_m(\delta_1 r)\right]\cos(m\theta) + \left[a_m J_m(\delta_1 r) + b_m Y_m(\delta_1 r)\right]\sin(m\theta) \\ W_2 &= \left[C_m I_m(\delta_2 r) + D_m K_m(\delta_2 r)\right]\cos(m\theta) + \left[c_m I_m(\delta_2 r) + d_m K_m(\delta_2 r)\right]\sin(m\theta) \\ W_3 &= \left[E_m I_m(\delta_3 r) + F_m K_m(\delta_3 r)\right]\cos(m\theta) + \left[e_m I_m(\delta_3 r) + f_m K_m(\delta_3 r)\right]\sin(m\theta) \end{aligned} \tag{6.66}$$

and in the high frequency range:

$$\begin{aligned} W_1 &= \left[A_m J_m(\delta_1 r) + B_m Y_m(\delta_1 r)\right]\cos(m\theta) + \left[a_m J_m(\delta_1 r) + b_m Y_m(\delta_1 r)\right]\sin(m\theta) \\ W_2 &= \left[C_m J_m(\delta_2 r) + D_m Y_m(\delta_2 r)\right]\cos(m\theta) + \left[c_m J_m(\delta_2 r) + d_m Y_m(\delta_2 r)\right]\sin(m\theta) \\ W_3 &= \left[E_m J_m(\delta_3 r) + F_m Y_m(\delta_3 r)\right]\cos(m\theta) + \left[e_m J_m(\delta_3 r) + f_m Y_m(\delta_3 r)\right]\sin(m\theta) \end{aligned} \tag{6.67}$$

The numbers of unknown constants increases greatly.

6.7.2 Boundary conditions

The matrix system that represents the boundary conditions is

$$[C]\{A\} = \begin{bmatrix} C_{11} & C_{12} & C_{13} \\ C_{21} & C_{22} & C_{23} \\ C_{31} & C_{32} & C_{33} \end{bmatrix} \begin{pmatrix} A_1 \\ A_2 \\ A_3 \end{pmatrix} = \begin{pmatrix} 0 \\ 0 \\ 0 \end{pmatrix} \tag{6.68}$$

The coefficients C_{ij} must be chosen according to the boundary condition type.

- **Free edge** $\Gamma^r = \Gamma^\theta = 0, q_3 = 0$
- **Simply-supported edge (soft type)** $W = 0, \Gamma^r = \Gamma^\theta = 0$
- **Simply-supported edge (hard type)** $W = 0, \Gamma^r = \Psi_\theta = 0$
- **Clamped edge** $W = 0, \Psi_r = \Psi_\theta = 0$

Each boundary condition defines which set of 3 coefficients must be used to fill a line of the $[C]$ matrix. These coefficients are detailed here:

$\forall\theta, W(R,\theta) = 0$ implies

$$\begin{aligned} C_{i1} &= J_m(\delta_1 R) \\ C_{i2} &= B_m(\delta_2 R) \\ C_{i3} &= 0 \end{aligned} \tag{6.69}$$

$\forall\theta, \Psi_r(R,\theta) = 0$ implies

$$\begin{aligned} C_{i1} &= (\sigma_1 - 1)\delta_1 J'_m(\delta_1 R) \\ C_{i2} &= (\sigma_2 - 1)\delta_2 B'_m(\delta_2 R) \\ C_{i3} &= \frac{m}{R} B_m(\delta_3 R) \end{aligned} \tag{6.70}$$

$\forall\theta, \Psi_\theta(R,\theta) = 0$ implies

$$\begin{aligned} C_{i1} &= (\sigma_1 - 1)\frac{m}{R} J_m(\delta_1 R) \\ C_{i2} &= (\sigma_2 - 1)\frac{m}{R} B_m(\delta_2 R) \\ C_{i3} &= \delta_3 B'_m(\delta_3 R) \end{aligned} \tag{6.71}$$

The out-of-plane forces equilibrium boundary conditions (3.15) $q_3 = 0$ writes

$$\begin{aligned} C_{i1} &= \sigma_1 \delta_1 J'_m(\delta_1 R) \\ C_{i2} &= \sigma_2 \delta_2 B'_m(\delta_2 R) \\ C_{i3} &= \frac{m}{R} B_m(\delta_3 R) \end{aligned} \tag{6.72}$$

The moment equilibrium condition for moments tangent to the border (3.16) $\Gamma^\theta = 0$ gives

$$\begin{aligned} C_{i1} &= (\sigma_1 - 1)\left[K\delta_1^2 J''_m(\delta_1 R) + \frac{K'}{R}\delta_1 J'_m(\delta_1 R) - \frac{m^2 K'}{R^2} J_m(\delta_1 R)\right] \\ C_{i2} &= (\sigma_2 - 1)\left[K\delta_2^2 B''_m(\delta_2 R) + \frac{K'}{R}\delta_2 B'_m(\delta_2 R) - \frac{m^2 K'}{R^2} B_m(\delta_2 R)\right] \\ C_{i3} &= \frac{m}{R}(K - K')\left(\delta_3 B'_m(\delta_3 R) - \frac{1}{R} B_m(\delta_3 R)\right) \end{aligned} \tag{6.73}$$

where $K' \equiv D^*\nu + \dfrac{p\tilde{H}^3}{12}$.

The moment equilibrium condition for moments normal to the border (3.17) $\Gamma^r = 0$ gives

$$\begin{aligned} C_{i1} &= \frac{m}{R}(\sigma_1 - 1)\left(D^*(1-\nu) - \frac{p\tilde{H}^3}{12}\right)\left(\frac{1}{R} J_m(\delta_1 R) - \delta_1 J'_m(\delta_1 R)\right) \\ C_{i2} &= \frac{m}{R}(\sigma_2 - 1)\left(D^*(1-\nu) - \frac{p\tilde{H}^3}{12}\right)\left(\frac{1}{R} B_m(\delta_2 R) - \delta_2 B'_m(\delta_2 R)\right) \\ C_{i3} &= -D^*\frac{1-\nu}{2}\delta_3^2 B''_m(\delta_3 R) + \left(D^*\frac{1-\nu}{2} - \frac{p\tilde{H}^3}{12}\right)\left(\frac{\delta_3}{R} B'_m(\delta_3 R) - \frac{m^2}{R^2} B_m(\delta_3 R)\right) \end{aligned} \tag{6.74}$$

A nondimensional frequency parameter can be introduced, but unlike the case of classical plate theories, this parameter remains sensitive to the values of R, h, p, etc.

$$\Omega = \omega R^2 \sqrt{\frac{2\tau\rho}{D^* + M_0^{(2)}}} \tag{6.75}$$

If $\det([C]) \neq 0$, then the trivial solution $A_1 = A_2 = A_3 = 0$ is found. Therefore, $\det([C]) = 0$ is a necessary condition for resonance. The function $\det([C(\omega)])$ is called the **characteristic equation**, and its roots are related to the eigenfrequencies. This kind of equation is too complex to be solved manually. Next we present how to design a computer program to compute the characteristic equation and find its roots.

6.7.3 Natural frequencies of circular inflatable panels

The algorithm to find the natural frequencies is outlined here and summarized in Fig. 6.10. First, the circumferential mode number m is fixed. Then, we scan an interval $[\omega_{\min}, \omega_{\max}]$ by applying the following procedure to N values of ω within this interval. These two parameters (frequency range and number of samples) must be well-chosen by the user of the program. For each ω, each square of wavenumber D_i is computed using the dispersion relations (6.46) and (6.50). Depending on the sign of D_2 and D_3, a set of potentials is chosen. Then, the matrix of boundary conditions $[C]$ is formed. The determinant of this matrix as a function of ω is the characteristic equation and our goal is to determine its roots, which are the natural frequencies of the panel. To this end, a root-finding algorithm must be used, such as the Newton–Raphson method which is very fast and accurate. However, it must be initialized with an initial guess that is very close to an actual root.

Among all of the values of the characteristic equation that have been calculated for all the frequencies, we compare the sign of each evaluation to the next, which gives us the location of all changes of sign. Note that some changes of signs may not be detected if the evaluation points of the characteristic equation are too far from one another: it is crucial to have enough sample points to detect every sign changes. The value of ω just before the change of sign is used as the initial estimate for the optimization algorithm.

When a natural frequency is found, the coefficients of the $[C]$ matrix can be used to express A_2 and A_3 as a function of A_1, that is, to find the relative contribution of each potential to the final solution. Provided that $C_{12}C_{23} - C_{13}C_{22} \neq 0$:

$$\begin{aligned} A_2 &= -A_1 \frac{C_{11}C_{23} - C_{13}C_{21}}{C_{12}C_{23} - C_{13}C_{22}} \\ A_3 &= \quad A_1 \frac{C_{11}C_{22} - C_{12}C_{21}}{C_{12}C_{23} - C_{13}C_{22}} \end{aligned} \tag{6.76}$$

Once the process has been completed for a given circumferential mode m, we move on to the next one. The natural frequencies and relative amplitudes can then be stored in tables. We can also plot the evolution of the natural frequencies of each mode as a function of the inflation pressure in Fig. 6.11, 6.12 and 6.13 with $E\tau = 389$ N/mm, $\nu = 0.25$ and $\rho = 1000$ kg/m³. The values used in the numerical calculations are those determined when the structure is not in movement: the results could be improved by using dynamic material parameters, as they are assuredly different [12]. One may see that the frequencies of the simply-supported and clamped cases (Fig. 6.11 and 6.12) are almost identical. Indeed, since the fibers remain almost vertical in both cases, the deformation is very similar. A slight difference is observed for the lower modes at high inflation pressures.

It should come as no surprise that the frequencies vary as a square root of the pressure, as it is a general rule in vibrating systems that natural frequencies are the square root of the stiffness over the mass: $f \propto \sqrt{\frac{k}{m}}$, and in inflatable panels, the pressurization is responsible for the load-bearing capacity of the structure. The bending eigenmodes W for (soft) simple-support and free boundary conditions are shown in Fig. 6.14 and 6.15. The natural shapes for clamped boundary conditions are very similar to the simply-supported ones. Note that the position of the nodal circles and diameters are independent of material properties and inflation pressure.

The eigenfrequencies calculated by this theoretical approach are in agreement with those obtained by an approximate (pseudospectral) resolution method presented in Appendix B. As was done for the rectangular panel, a simplified "equivalent membrane" model is presented in Appendix C for faster estimation of the frequencies of an inflatable disk.

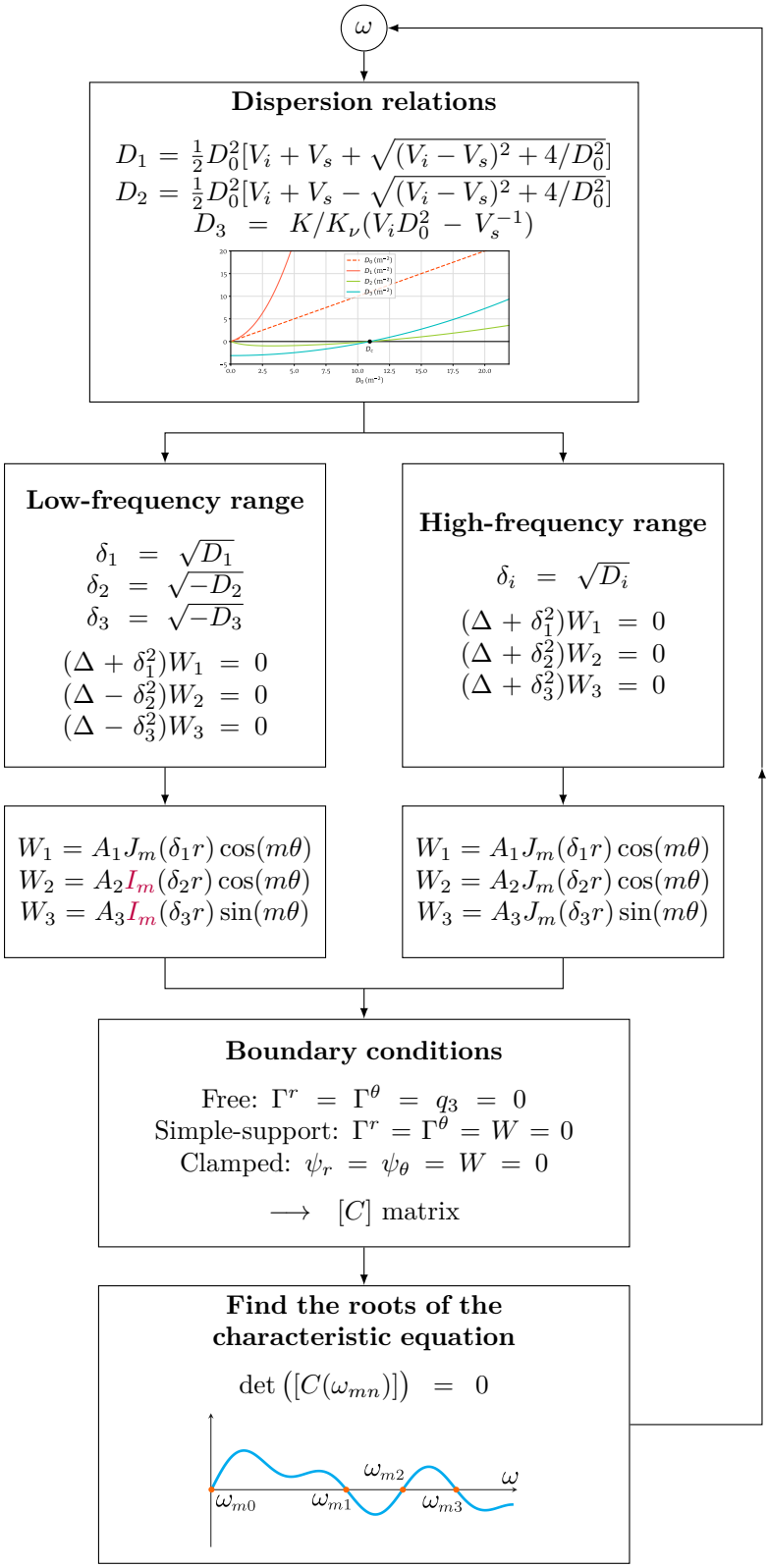

Figure 6.10: Algorithm for finding the natural frequencies of a circular inflatable panel (for a given m).

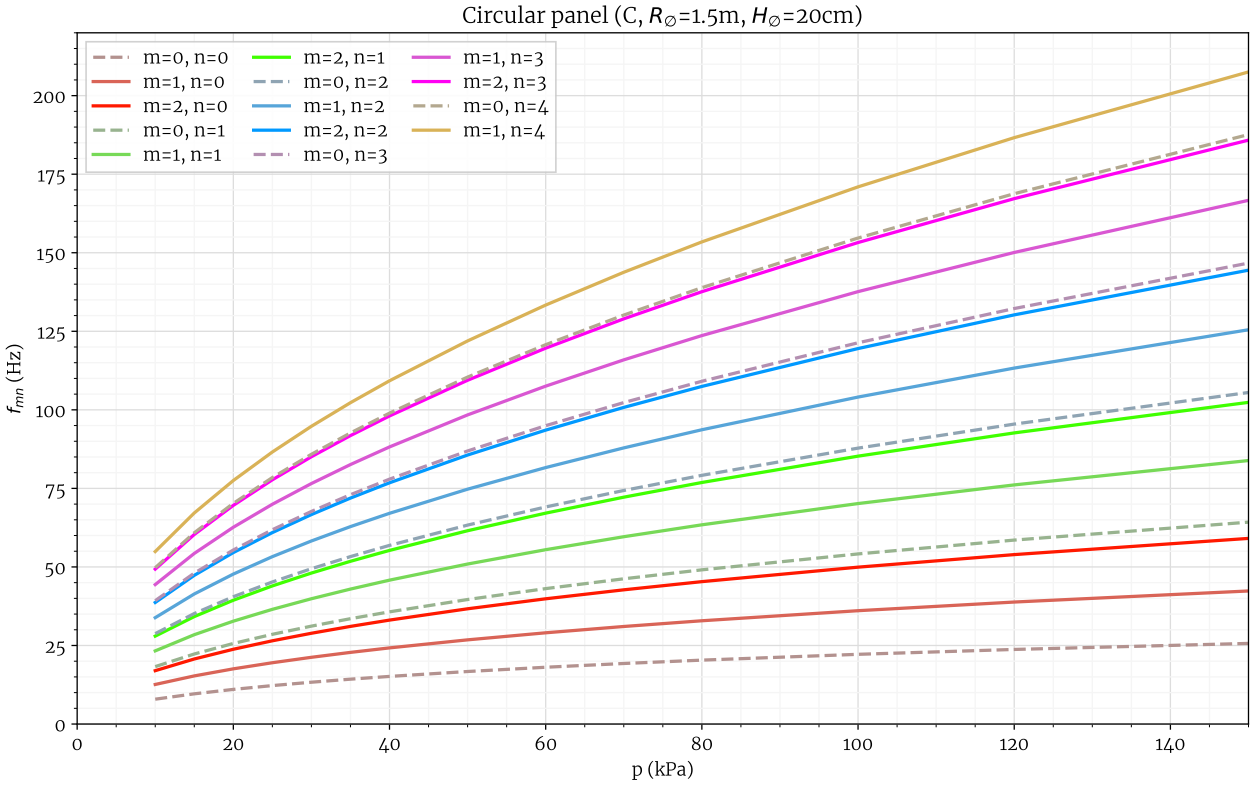

Figure 6.11: Natural frequencies of a clamped circular inflatable panel.

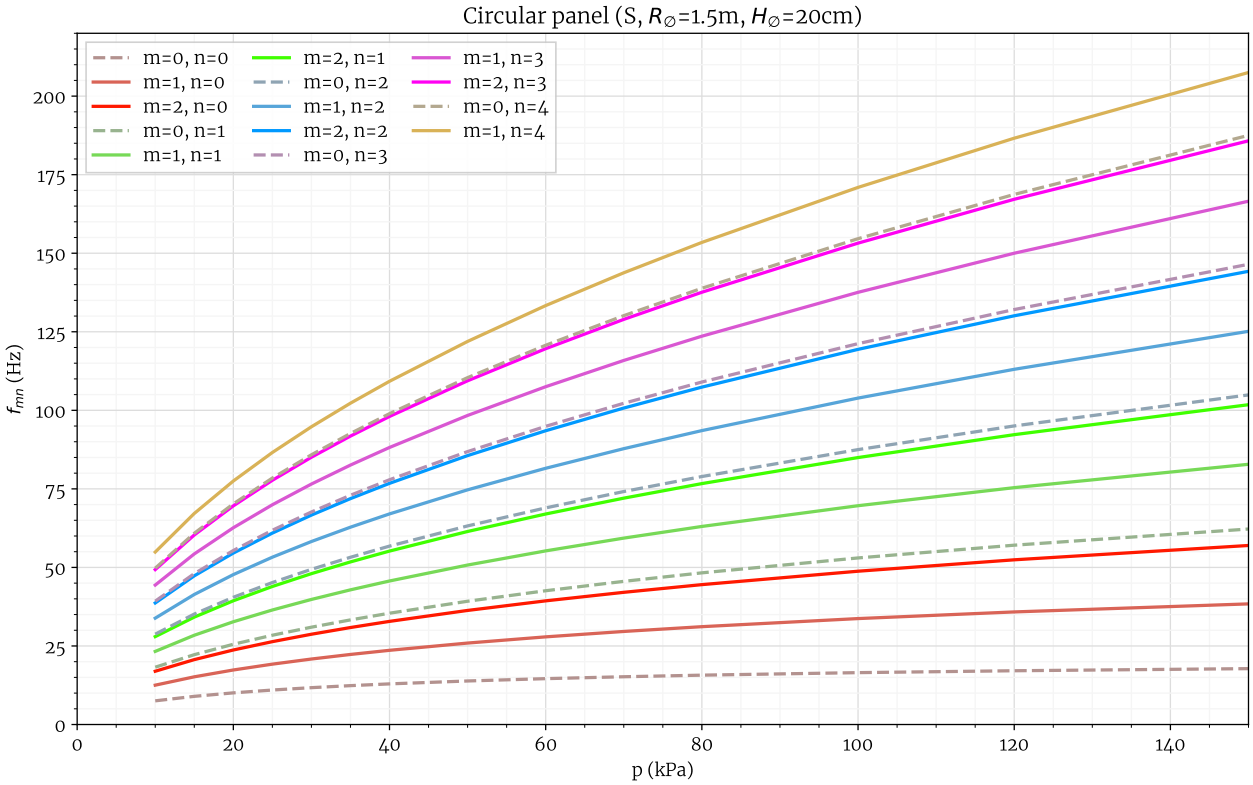

Figure 6.12: Natural frequencies of a circular inflatable panel on (soft) simple-support.

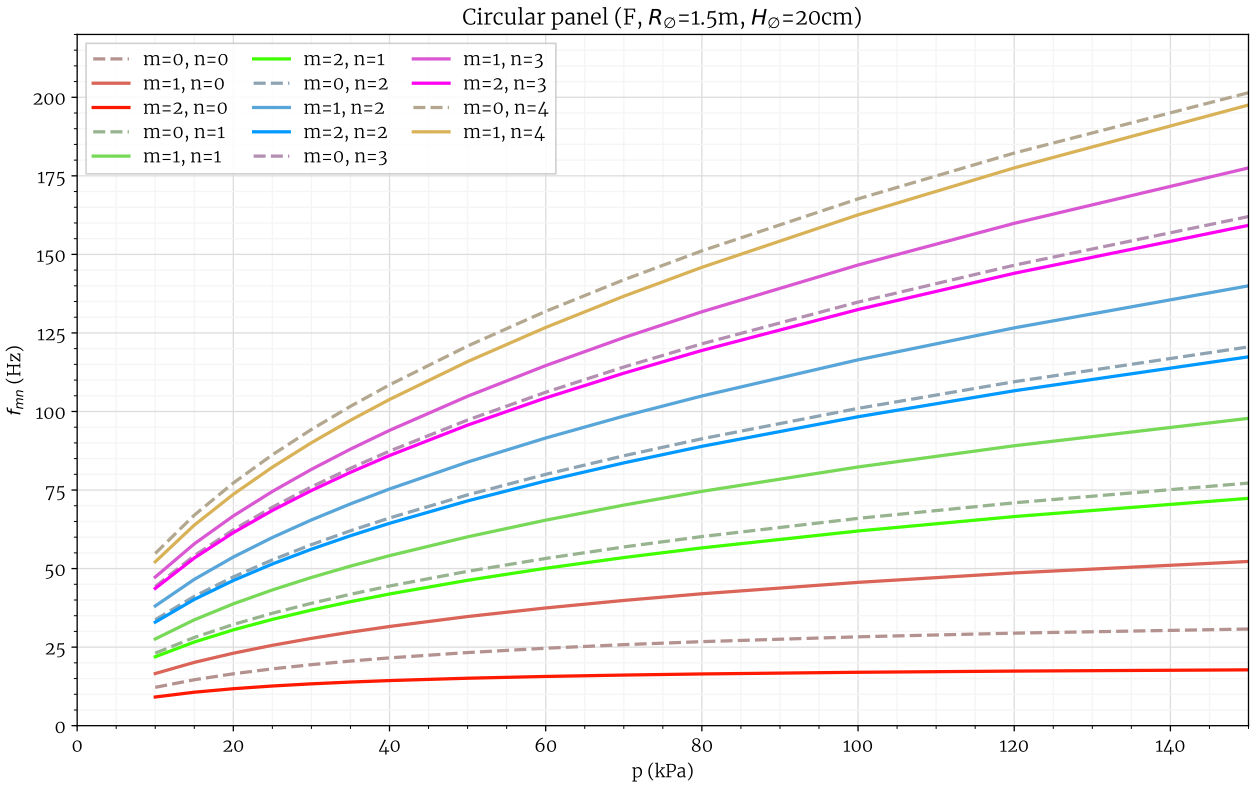

Figure 6.13: Natural frequencies of a free circular inflatable panel.

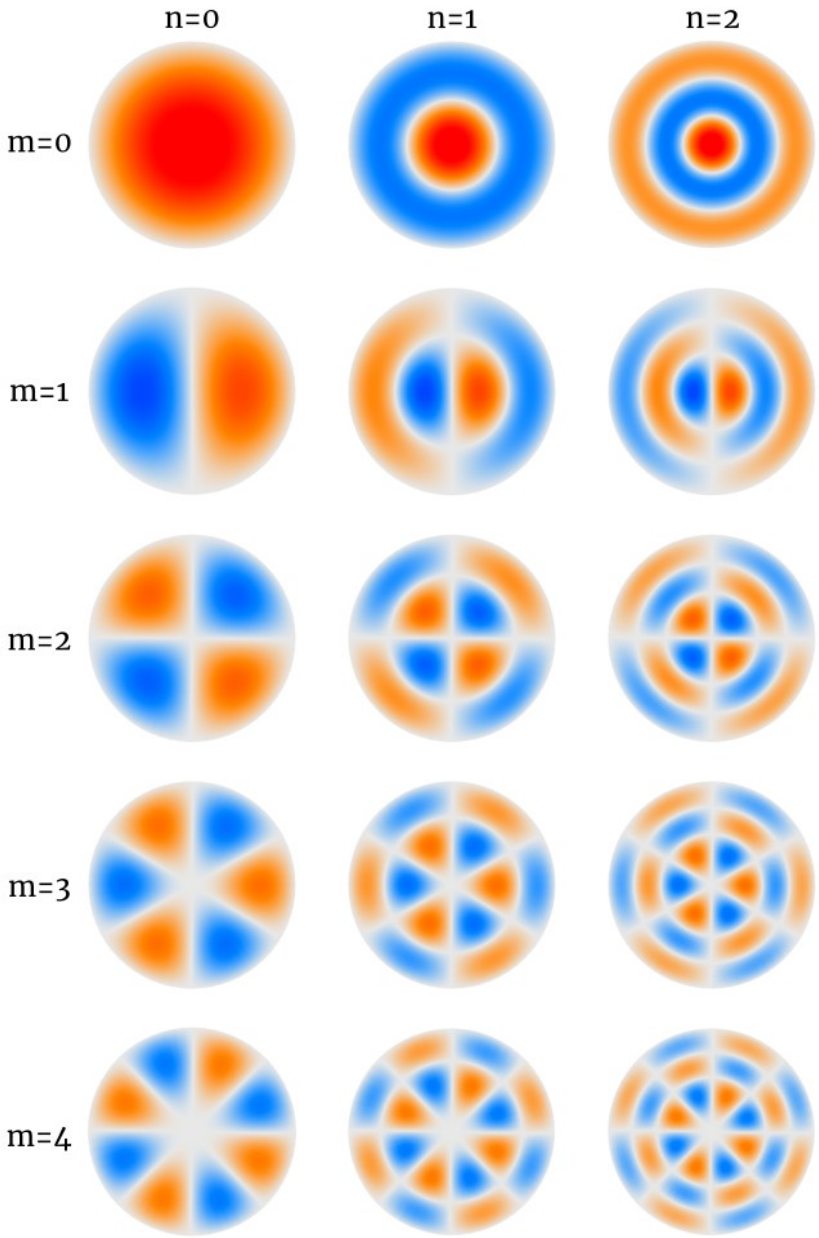

Figure 6.14: Natural bending modes of a circular inflatable panel on simple-support (soft type).

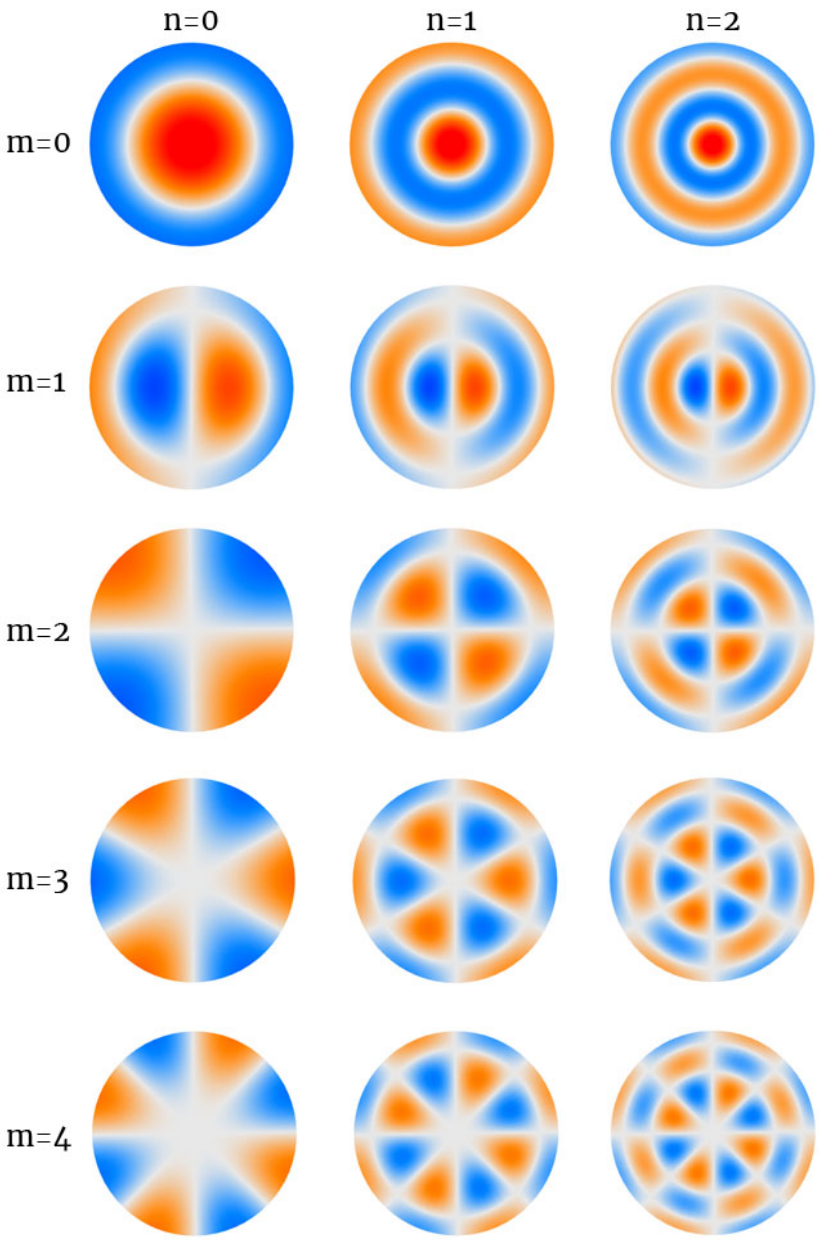

Figure 6.15: Natural bending modes of a free circular inflatable panel.

Chapter 7

Experimental validation

The axisymmetric deflection of a circular inflatable panel subjected to a uniform vertical load was determined in Chapter 4 and the natural frequencies of circular panels were calculated in Chapter 6. The analytical results were validated by comparing them to finite element simulations or approximated numerical solutions and it is now time to confront the theory to the experimental reality.

First, we determine the various material properties of the panel used in the analytical expressions and required for comparison with numerical results. Second, static bending testing of a circular panel subjected to a uniform vertical dead load is carried out for a variety of inflation pressure and external loads. Finally, we explore the possibility of determining the natural frequencies of inflatable panels from impact hammer tests.

7.1 Experimental determination of basic material properties of inflation panels

Two inflatable panels were acquired for the purpose of the experimental validation of our theory: they are both circular with a diameter of 3 m and have different heights (10 cm and 20 cm). They are made of woven PVC fabric and have total masses 21.6 kg and 23.8 kg (around 3200 g/m^2). The panels were bought from a company named Écocréation and assembled by gluing rolls of double wall fabric (with drop-stitch) together with a bonding strip that runs across the surface of the panel and sealed with a lateral wall. They were both perforated near the edge to insert a small tube through a glued valve to serve both as a pressure probe and air inlet.

7.1.1 Marking of a diameter on the inflatable panel

The deflection will be measured along a diameter of the panel, thus it must be accurately located. The center of the panel is located by wrapping a string around the perimeter and dividing its length by four, so that four equidistant points are placed on the circumference and marked using a pencil. The distance between two opposite marks was measured with a ruler to make sure that the diameter was correctly identified: the length between two opposite marks was the largest that could be measured compared to other points that were not perfectly symmetrical to the center of the panel, thus forming a diameter since these two points were as far apart as possible. The result was double-checked by verifying that the diameter was the hypotenuse of a triangle with its right angle on the perimeter, Fig. 7.1.

Figure 7.1: Geometric construction to mark two perpendicular diameters of a circular panel and mark its center.

7.1.2 Measurement of the membrane's thickness

The panel skins is a heterogeneous assembly of woven fabric, coating and stitched drop yarns, which makes the precise definition and measurement of its thickness challenging. The true thickness of each layer of material will change after pressurization and loading, and the drop cords will pull on the woven fabric. Nevertheless, a simple measurement of 8 folds of membranes scraps using a caliper gives a good estimation of the average initial thickness $\tau \approx 1\,\text{mm}$ ($\pm$ 6%). In this work, the thickness is assumed to be constant, so there is no reason to distinguish between the natural and inflated thicknesses ($\tau_\varnothing = \tau$).

7.1.3 Determination of membrane and drop cords densities

Since we know the mass of two different panels made from the same materials, it is possible to access the two unknown that are the densities of the membranes and the high strength threads. Technically, the drop cords are also part of the upper and lower membranes (they are intertwined) and account for a fraction of the fabric's weight, but the following calculation neglects the length of the drop thread material that runs inside the membranes, considering that the envelope is a continuous medium of area density σ_m (in kg/m^2) and the vertical part of the drop cords will have a line density ρ_{ly} (in kg/m). The masses of the 2 panels relate to their dimensions and the 2 unknown densities, thus forming a solvable system:

$$\begin{cases} m_1 = \sigma_m S_1 + \rho_{ly} l_{y1} \\ m_2 = \sigma_m S_2 + \rho_{ly} l_{y2} \end{cases} \tag{7.1}$$

where $S_1 = 2 \times \pi R^2 + 2\pi R \times H_1$ (resp. S_2) is the total surface of membranes of the panel with thickness $H_\varnothing = H_1 = 10\,\text{cm}$ (resp. $H_2 = 20\,\text{cm}$) and $l_{y1} = R^2 dH_1$ (resp. l_{y2}) is the total length of drop yarns of the first

panel (resp. second panel). The solution is simply:

$$\begin{aligned} \sigma_m &= \frac{m_1 l_{y2} - m_2 l_{y1}}{S_1 l_{y2} - S_2 l_{y1}} \approx 1.376\,\text{kg/m}^2 \\ \rho_{ly} &= \frac{S_1 m_2 - S_2 m_1}{S_1 l_{y2} - S_2 l_{y1}} \approx 4.12 \times 10^{-5}\,\text{kg/m} \end{aligned} \tag{7.2}$$

Using the value of σ_m, the homogenized density ρ of the membranes should be $\rho = \sigma_m/\tau$ where $\tau = 1$ mm, which is approximately $\rho = 1300$ kg/m³. Other more suitable units for the linear mass density of fibers are the tex (1 g/km) or the denier (1 g/9km): ρ_{ly} = 41.2 tex = 4.58 denier. It may be interesting to note that the total length of threads in the 10 cm thick panel is l_{y1} = 21 km, and the double for the twice as thick panel. The mass of drop threads is 0.87 kg and 1.75 kg respectively, which is 4% and 7% of the total mass of the panels.

7.1.4 Determination of the maximum inflation pressure

Before starting to design our experiments, knowing what the maximum inflation pressure should be was important for safety reasons. The panel may break in three ways: by tearing of the membranes, by tearing of the drop cords or by detachment of glued pieces of fabrics at their junction. Since manufacturing and gluing techniques are beyond the scope of this thesis, only the first two modes of failure are briefly discussed here.

Membranes' tensile strength

According to the manufacturer's specification sheet, the tensile strength of a single membrane R_m is 68/70 N/mm (warp/weft). Therefore, the maximum inflation pressure based on the resistance of the two membranes alone is calculated as

$$p_{\text{max}} = \frac{R_m}{2\tilde{H}}$$

And so the maximum inflation pressure would be around 1.7 bar for the 20 cm panel, which is consistent with the manufacturer's recommendations of not exceeding 0.8 bar (taking a safety coefficient of 2).

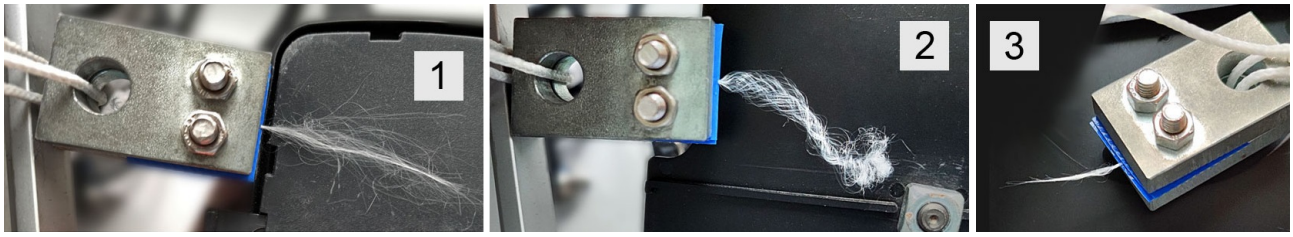

Figure 7.2: Broken drop-stitch cords after tensile tests.

Drop threads' tensile strength

We cut a few tension threads from a drop-stitch fabric sample and performed tensile tests. The cords' properties have a high variance as they are made of thin woven microfibers, but average properties can still be estimated. It took several attempts to improve the procedure, as the strings would get pinched and torn at the jaws, and so we ended up gluing them to small pieces of fabrics to increase the area of contact. Three strings broke at their center after being submitted to a tension force $N_{\text{break}} = 23$; 33 and 32 N, respectively (Fig. 7.2). The maximum inflation pressure is simply

$$p_{\text{max}} = N_{\text{break}} \times d$$

where d is the density of yarns, in our case

$$p_{\max} = 23\,\mathrm{N} \times 7600\,\mathrm{m}^{-2}$$

which is again 1.75 bar.

As a conclusion, even though these two calculations tend to show that the panel could withstand an inflation pressure of 1.6 bar, the strength of the glued junctions is uncertain and therefore we will not inflate the panels above 1 bar of pressure as recommended by the manufacturer. The failure mechanisms of inflatable panels are outside of the scope of this study, which is why we did not conduct further experiments: our main objective was to perform safe static bending experiments.

7.1.5 Determination of Young's modulus from inflation tests

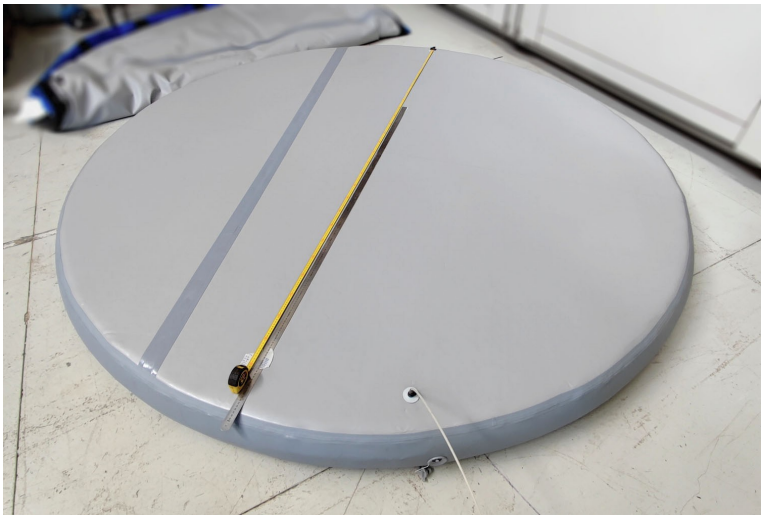

Figure 7.3: Measuring the elasticity modulus $E\tau$ of the 20 cm thick inflatable panel.

The effective fabric membrane modulus of elasticity is determined by measuring the increase of an initial length L_i along a diameter of the circular panel for several inflation pressures: the slope of the curve $\Delta L(p)$ can be used to retrieve $E\tau$ by using Relation (2.54) that relates the increase in radius to the inflation pressure.

$$\frac{L_f - L_i}{L_i} = \frac{1-\nu}{2E\tau} p \tilde{H}_{\varnothing}$$

where L_f is the measured length. Using experimental data, with the slope $m = \dfrac{\partial}{\partial p}\left(\dfrac{L_f - L_i}{L_i}\right)$ obtained from linear regression:

$$E\tau = \frac{1-\nu}{2m} \tilde{H}_{\varnothing}$$

The experiment was performed twice on the same day: once in the morning and once in the afternoon, using two different rulers to average the results and reduce imprecision (Fig. 7.4). After each change of the internal pressure p, the panel was lifted and lowered to allow free expansion of the panel and avoid friction with the floor. The manipulation was done over a short enough time period to avoid the effects of creep. The deduced moduli are presented in Table 7.1: their average is 393 N/mm, which is the value used in all calculations in this thesis unless mentioned otherwise.

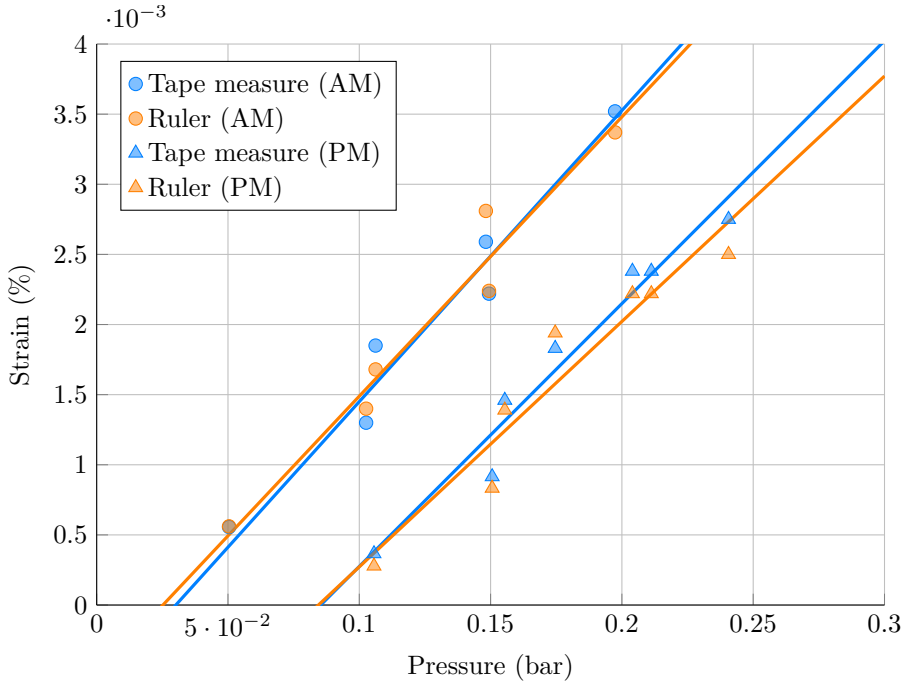

Figure 7.4: Strain $(L_f - L_i)/L_i$ VS inflation pressure for experimental determination of the panel's Young's modulus.

	Tape measure (N/mm)	Ruler (N/mm)
Test 1 (AM)	372	380
Test 2 (PM)	396	424

Table 7.1: Effective membrane modulus $E\tau$.

7.2 Experimental validation of the static bending solution

7.2.1 Experimental setup design

We thought about several ways to apply a uniform pressure load and realize the simple-support boundary condition, such as creating a ring of fabric to hold the panel's edge and suspend it to a larger metal ring. The load could be applied by covering the surface with wood blocks or carpets or sand, but none of these approaches seemed practical or close enough to the theoretical assumptions. One way to meet all of the requirements was to create a dome that could be mounted on top of the panels using duct tape. The dome shape is ideal since the forces at the equator are purely vertical: there are no in-plane forces, which corresponds to the definition of simple-support. Furthermore, with this envelope covering the panel, it becomes possible to create a pressure differential between the two sides of the inflatable panel, which counts as a uniform surface load. Only 200 Pascals (2 mbar) are needed to apply a force equivalent to a weight of 140 kg. First, we will see how the dome was constructed. Second, the experimental setup and measuring tools will be introduced. Then the results and their comparison with analytical predictions will be discussed.

Design and making of the dome

One way of drawing an approximate development of the sphere onto a plane is the gore method: by cutting a globe along several meridians, several pieces of fabric in the shape of an eye can be joined together by their longitude to form a sphere, and the greater the number of divisions, the smaller the distortion. The dome was

made from n = 16 cuts of fabric which divide sections of angle $\alpha = \dfrac{2\pi}{n}$. Let s denote the longitudinal distance along the meridian. For $s \in [0, R\pi/2]$,

$$\begin{aligned} z &= R\cos\left(\frac{s}{R}\right) \\ \rho(z) &= R\sqrt{1-\left(\frac{z}{R}\right)^2} \\ h(s) &= \alpha\,\rho\big(z(s)\big) \end{aligned} \tag{7.3}$$

The corresponding pattern is drawn in Fig. 7.5 and a cutting guide was created with a laser cutter[1] to speed up the fabrication process. The wooden template was outlined on the fabric with a marker before getting cut, Fig. 7.6.

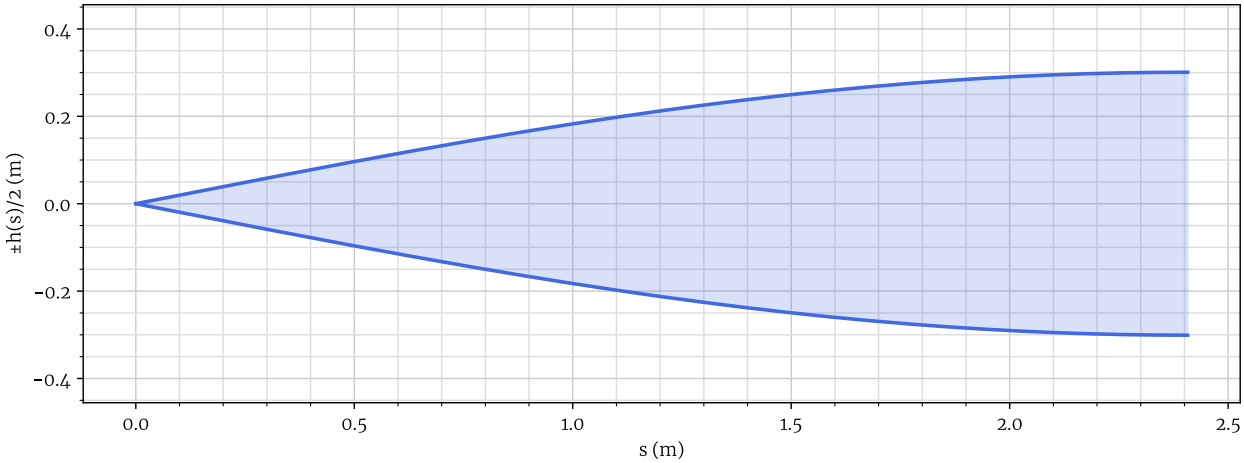

Figure 7.5: Half meridian section template for the dome ($R = 1.53$ m, $\alpha = 22.5°$, $n = 16$).

Figure 7.6: Marking of the outline of each meridian section using the wooden template.

We chose to experiment with the 10 cm panel first because the deflections are twice as large as the thicker panel for the same loading. Even after the dome was taped to the panel, the fabric could still be reused for the

[1]The fabric could not be put into the laser cutter directly because burning PVC releases toxic fumes of hydrochloric acid.

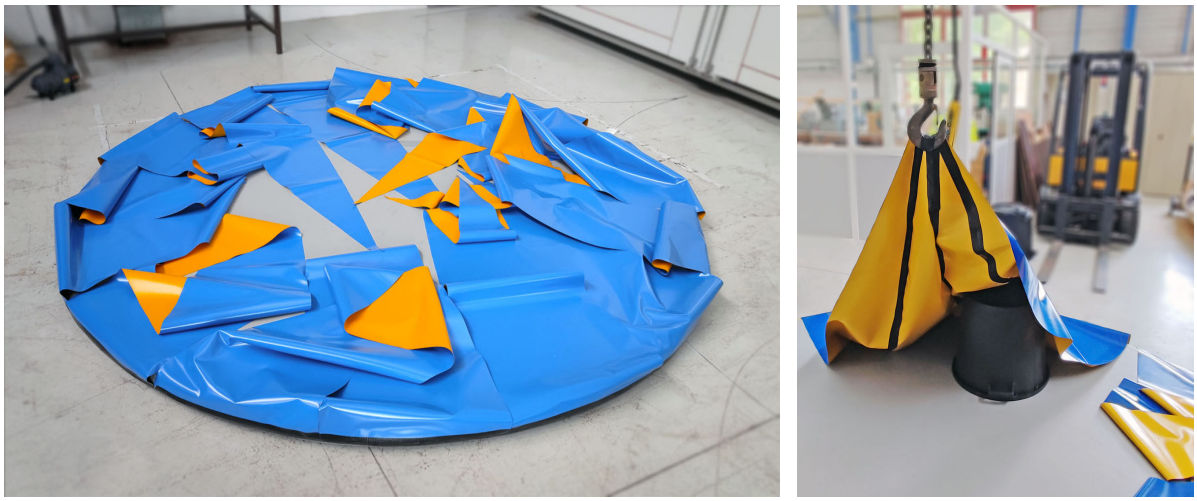

Figure 7.7: All sections are taped to the perimeter of the inflated panel and then to their neighbors.

Figure 7.8: (left) Inflated dome with continuous air supply. The airtightness is not achieved yet, since only one layer of adhesive tape was applied inside. (right) Deflated dome with two layers of adhesive tape (on the inside and the outside).

20 cm panel by peeling off the tape and cleaning the area with alcohol in order to tape it again.

Inflation pressure regulation

Although the panel is airtight when closed, the pressure measuring system requires a continuous supply of air to display the actual pressure inside. Furthermore, one assumption of our model is that the pressure always stays the same, and so it was precisely controlled to a prescribed value; although the section of the pressure inlet was too small to achieve uniform pressure everywhere in the panel instantaneously. The compressed air system of the workshop was plugged into a pressure limiter for safety and then redirected to a pressure regulation valve with a wheel, Fig. 7.10. Finally, the output was inserted into the inflatable panel and the pressure could be monitored in real time on a computer via a pressure gauge.

Loading pressure regulation

The surface load applied onto the panel results from the pressurization of air inside the dome. Continuous flowing air was provided by an electric fan with a power of 1.5 kW and a speed of 2800 RPM to counter air leakage through small gaps in the duct tape that holds the pieces of fabric together. The pressure was then measured with an inclined alcohol manometer: the angle from a horizontal plane was 32 deg which allowed for a resolution of 4.55 Pa (to the nearest reading inaccuracy). However, this tool is sensitive to temperature changes, which were important in July 2022. For the last measurement we had access to a low pressure digital

Figure 7.9: Inside of the inflated dome upon completion.

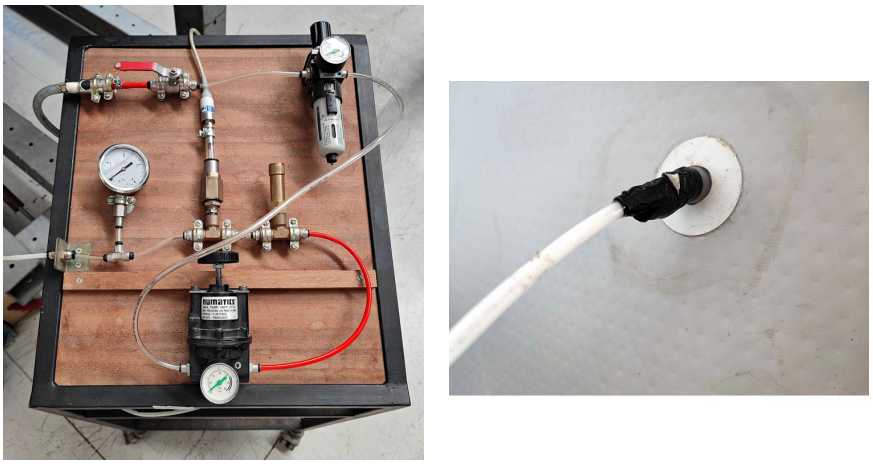

Figure 7.10: Pressure regulation panel and pressure inlet connected to the drop-stitch panel.

sensor which gave values in millimeters of water, achieving a resolution of 9.8 Pa (= 1 mmH2O).

Supporting structure

The panel was placed inside a square metal frame of sides 3 by 1 m (Fig. 7.11). The idea was to let the panel expand freely, which is why there are only three contact points: it stands on two rolls (Fig. 7.12) to support its own weight and was held upright by a tape between the dome and the metal frame to avoid falling over.

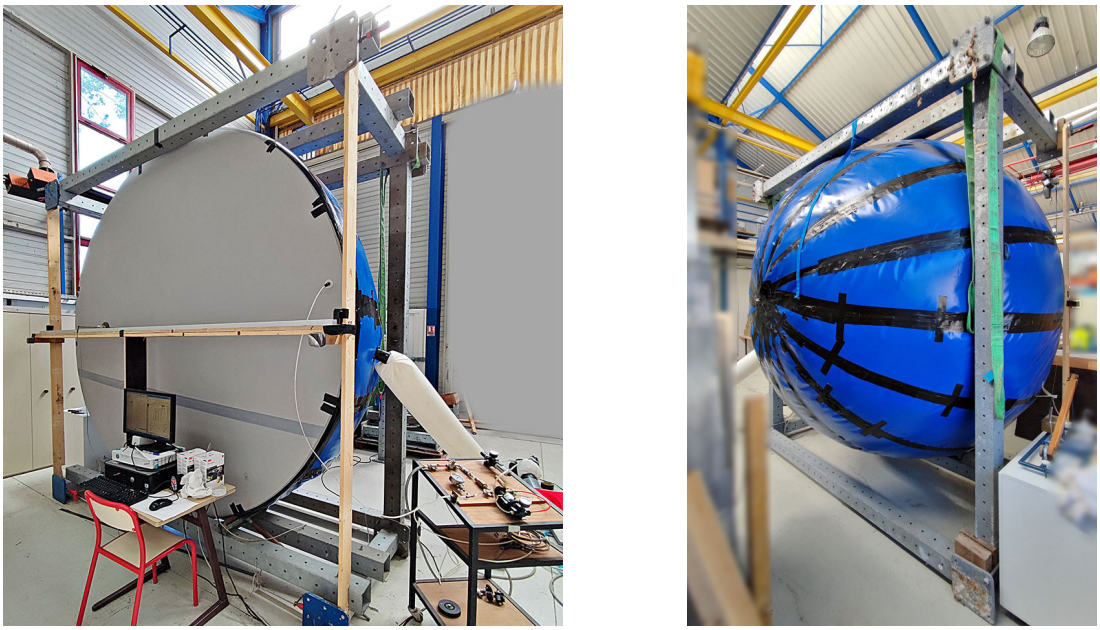

Figure 7.11: Front and back view of the experimental setup with the pressurized panel sitting upright on rollers, attached to the inflated dome and measurement rail aligned with a diameter.

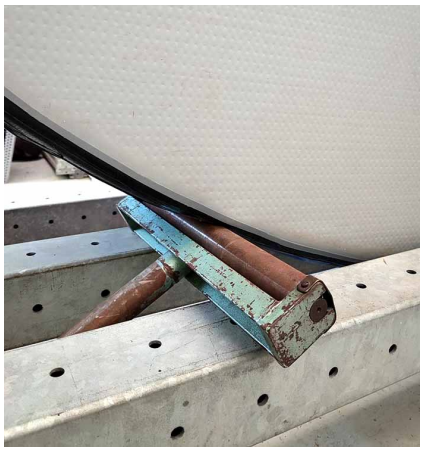

Figure 7.12: Roller used to hold the panel vertically. The linking forces applied to the panel are in-plane.

7.2.2 Deflection measurement

We wished to compare the deflection along the marked diameter of the panel as explained in the above. When the panel was placed upright, the rollers were moved closer or further apart to lift the diameter to the same height as a metal rail onto which the measuring tool could slide. The tool used for measuring the deflection is a Linear Variable Differential Transformer (LVDT) with resolution smaller than a hundredth of millimeter. First, the profile of the panel's top membrane is measured every 20 centimeters along a diameter parallel to

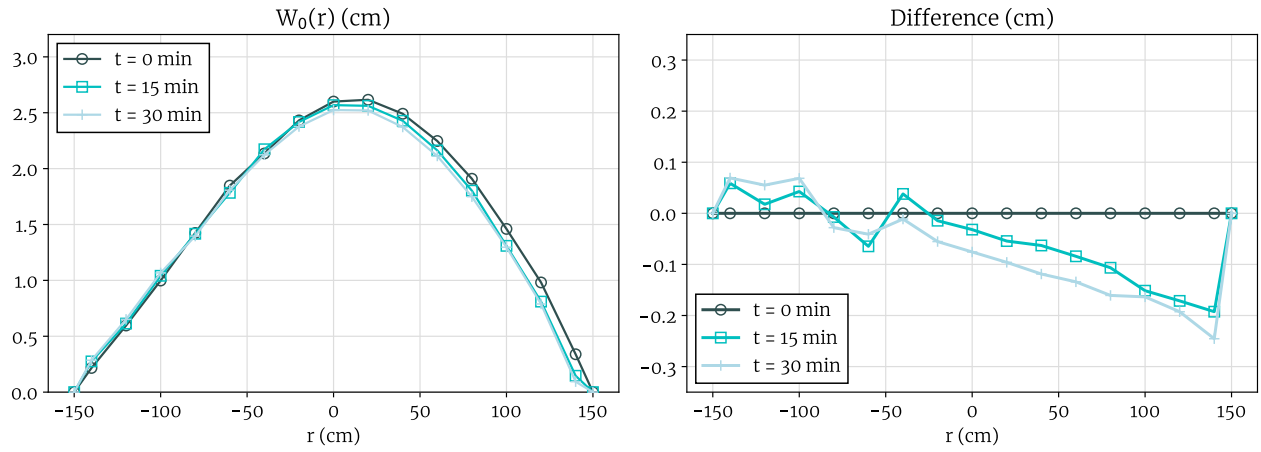

Figure 7.13: Initial deflection of the pressurized panel before any load is applied (left) and evolution over time (right) ($p = 0.2$ bar, $q = 0$ Pa).

the measuring rail when the dome is inflated but not pressurized (the differential pressure with the outside is zero but the dome almost has a spherical shape). Then, the dome is pressurized and the position of the panel's top membrane is measured again.

With this protocol, the post-processed deflection is sensitive to the positions of the leftmost and rightmost points, which were difficult to access since the diameter of the panel was similar to size of the frame, and columns hindered theses measurements.

Repeatability of the measurements and sagging

The deflection of the panel was measured three times over 30 minutes to observe the repeatability of the measuring protocol and the potential sagging of the panel, Fig. 7.13. There seems to be a slow evolution of the deflection over time, possibly due to its own weight or the weight of the deflated dome pulling on the circumference, causing the surface to bend. But it should be small enough not to interfere with the interpretation of the results: the drift is at most 5 mm per hour at the lowest inflation pressure (i.e. the lowest stiffness), and a series of measurement lasts less than 2 hours.

7.2.3 Experimental results

On every experiment day, the panel and the dome attached to it had to be mounted on the frame and dismantled for the night. The parameters were changed in the following order:

1. adjustment of the panel's pressurization (3 minutes)
2. then adjust the pressure load inside the dome (7 minutes)
3. then move the LVDT along the rail, touch the panel with the sliding rod and report the value into a spreadsheet (less than 2 minutes)

Fig. 7.14 shows the experimental results compared to the theory for three different pressurization levels: 20, 40, 60 kPa. For each inflation pressure, the same color palette is used (red, orange, green, blue) as the external load increases. Due to the experimental setup and the difficulty of stabilizing the external pressure applied onto the panel, the values of the loads q have a similar order of magnitude but they are not perfectly uniform for the three inflation pressures p. Overall, the experimental deflection points are close to the parabolic curves plotted from the analytical solution (4.6). As expected, the higher the inflation pressure

p, the smaller the deflection for a given external load q. The proportionality of the deflection with respect to the external load q is also confirmed experimentally. The average absolute relative difference between the theoretical and experimental maximum deflections is 11.7 %. However, this rather high value is found by taking the Poisson's ratio equal to 0.25 in the analytical expressions, which is chosen for the sake of consistency with the previous chapters. But the membranes were not tested to determine this quantity. If one were to lower this parameter down to 0.1, which is a realistic value [8], the average absolute relative difference drops to 5.7 % (Fig. 7.15). Therefore, a logical continuation is to measure the Poisson's ratio of the membranes.

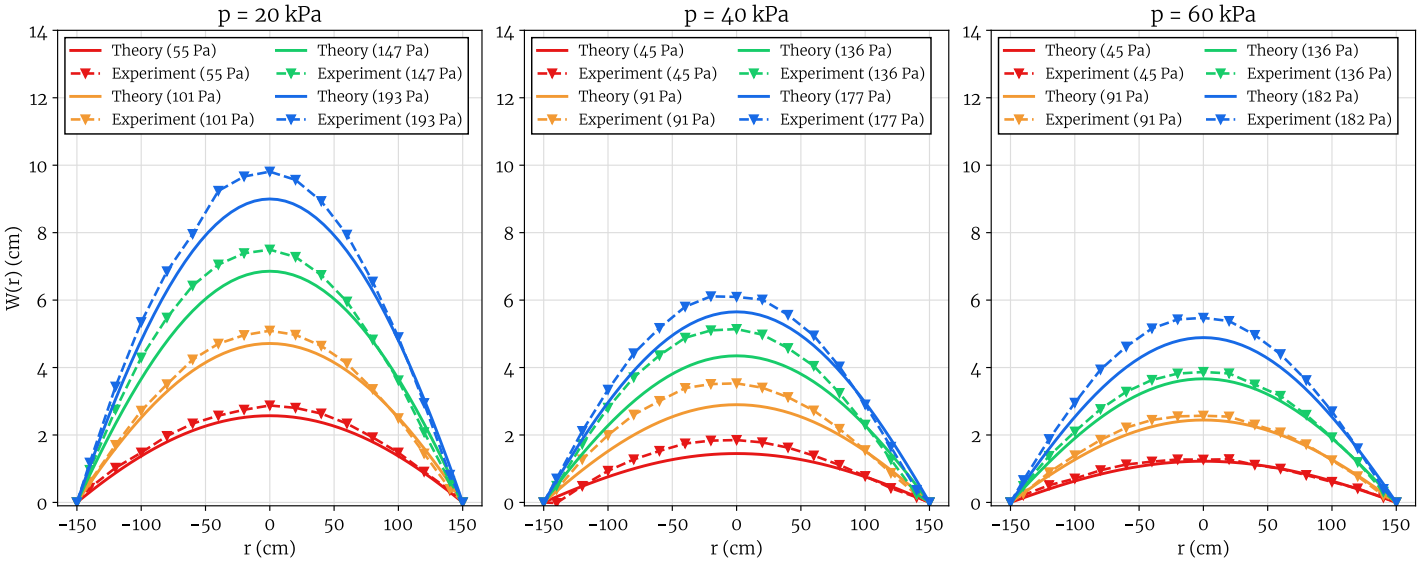

Figure 7.14: Experimental deflection profiles compared to the analytical solution (parameters: $R_{\varnothing} = 1.52$ m, $H_{\varnothing} = 10$ cm, $\nu = 0.25$, $E\tau = 390$ N/mm)

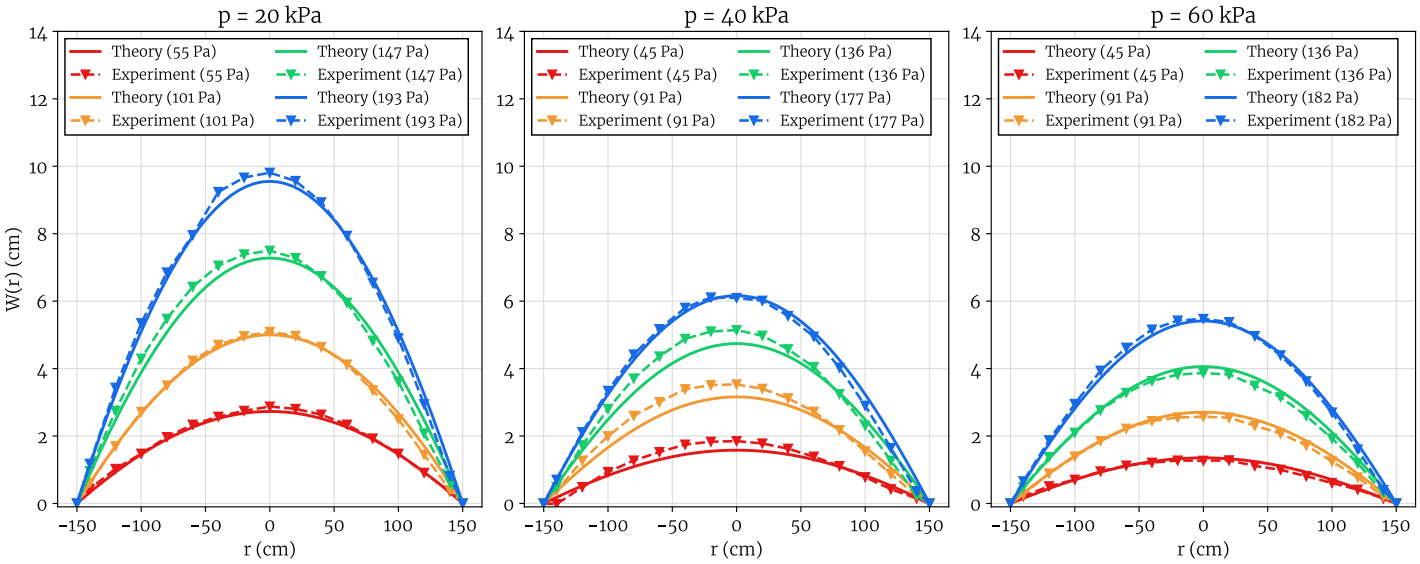

Figure 7.15: Experimental deflection profiles compared to the analytical solution with a smaller Poisson's ratio (parameters: $R_{\varnothing} = 1.52$ m, $H_{\varnothing} = 10$ cm, $\nu = 0.1$, $E\tau = 390$ N/mm)

7.2.4 Conclusion on static bending tests

We have successfully designed and performed experimental measurements on a large inflatable disk and measured its deflection under constant uniform pressure. The comparison with the analytical solution is satisfying, but could be greatly improved by measuring the Poisson's ratio. The protocol could be improved in some other ways. The dome could have benefited from a better manufacture, since the junctions could not withstand a loading pressure higher than 150 Pa: the dome came undone after several experiments, Fig. 7.16. Although a simple LVDT was well-suited for the measurements of this axisymmetric shape, it would be interesting to look into photogrammetry techniques to measure the out of plane components at every point of the panel. Such techniques have been applied successfully to inflatable structures [84].

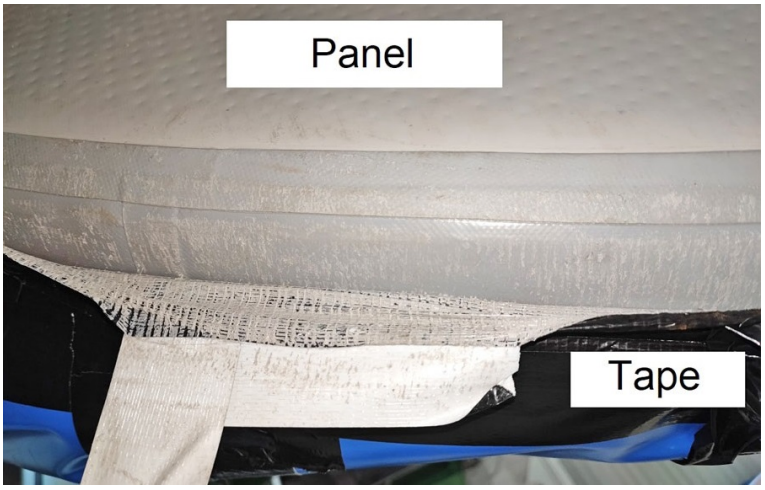

Figure 7.16: Dome coming unstuck from the panel after prolonged pressurization.

7.3 Modal analysis using an impact hammer

In this section, the natural frequencies of a circular inflatable panel with free edge will be measured experimentally in order to confirm the predictions made in Chapter 6. We had the opportunity to collaborate with engineers from Thales Group who lent us their testing material which comprises of accelerometers, a data acquisition unit (DAQ) and the associated software (Fig. 7.17). The idea behind hammer testing it to excite all the modes of vibration equally by applying a rectangular force pulse on the structure. This method of testing is generally applied to stiff structures, while inflatable structures are very soft: the results presented here are exploratory. The impact hammer is a heavy piece of metal with a rubber tip used to strike the structure. On one side of the panel, we positioned four triaxial accelerometers with the Z-direction normal to the surface. Each accelerometer must be registered along with its sensitivity (mV/g) in the acquisition software so that the conversion from voltage to acceleration is done correctly. The sampling frequency is set to be 10 times larger than the highest frequency of interest (100 Hz).

7.3.1 Preliminary checks

Modal analysis relies on the assumption that the modes are "well-formed" at the time of measurement. In stiff structures where the wave propagation is extremely fast, stationary waves appear after a fraction of second after multiple reflections on the boundaries of the structure. When performing the impact hammer experiments, we wondered if the system was maybe too soft for the waves to propagate and overlap enough

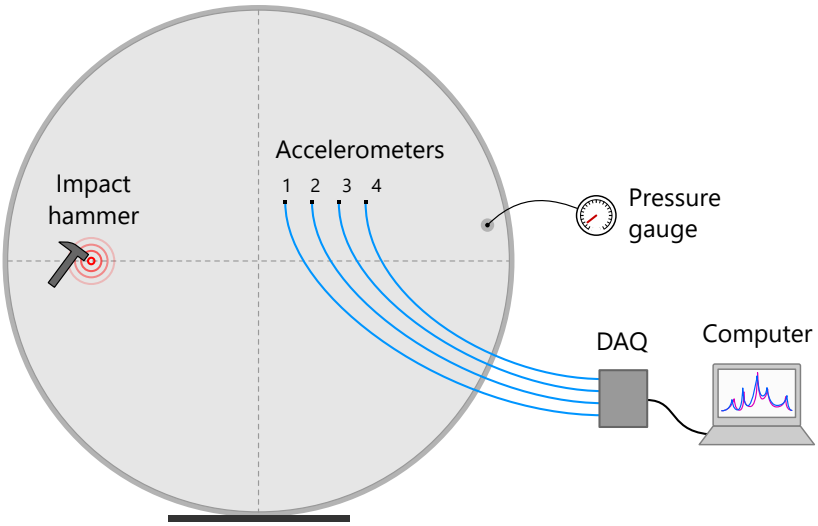

Figure 7.17: Impact hammer experiment on a circular panel (DAQ: Data AcQuisition unit).

times to form a mode before the energy dissipates due to damping. The speed of wave propagation in an isolated membrane is

$$c = \sqrt{\frac{p\tilde{H}}{2\tau\rho}}$$

For a 20 cm panel at the lowest tested inflation pressure (15 kPa), the wave velocity is 39 m/s, meaning that the wave can cross the panel 13 times within a second. This should be enough for a standing wave to form.

Before beginning the actual experiment, the background noise was recorded to make sure it wouldn't interfere with our measurements. Since the signal-to-noise ratio of the measured accelerations was very high, subtracting the background noise spectrum from the data seemed unnecessary.

7.3.2 Hammer test protocol

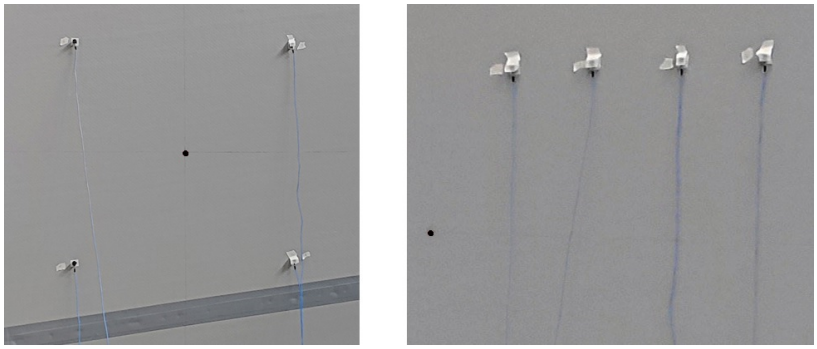

Figure 7.18: "Square" and "Aligned" positions of the sensors on the panel. The center is marked by a black dot.

After inflation, the valve is closed and the panel is held upright by two people. The experimenters took care to only put their hands on the edge of the panel without applying too much force. The pressure can still be measured continuously using a small hole linked to a pressure gauge. By placing the four sensors such that they form a square, they are symmetric with respect to the center, Fig. 7.18. In this configuration, the information given by the four sensors should be redundant (except for phase shifts, but we do not have

Test number	Sensors location	Pressure (kPa)	Impact position	Specificity
1	Square	20	Center	Half sampling frequency
2			Center	Hitting the back of the panel
3			Center	Baseline for 1–7
4			Center	Without hammer rubber tip
5			Center	Panel rotated 45° (sensors attached)
6			Right	1 hit with the hand on the right-hand side
7			Right	Hits on the right-hand side
8	Aligned	20	Center	
9		33.9	Center	
10		33.9	Right	
11		30	Center	
12		30	Center	Faster pace (1 hit per second)
13		30	Right	
14		30	Left	
15		25	Left	(discarded)
16		22.68	Left	
17		19	Left	
18		14.9	Left	
19		20.1	Left	

Table 7.2: Details of each vibration test.

access to this information). After this was confirmed and we had tested several hypotheses, we moved on to the second configuration with all the sensors aligned, which means that they have different radial and angular positions from the center, thus allowing to capture different observations. Since the vertical panel was touching the ground, we expected the nodal diameter (for modes where $m > 0$) to start from the contact point at the ground to the top of the panel, vertically. At first we hit the panel every 3 seconds, before testing a higher pace (1 hit per second). For recordings number 1 to 11, 10 hits were applied at the impact point with the hammer, whereas 20 hits were given for recordings 12 to 19. The spectra of tests #11 and #12 can be compared in Fig. 7.19. It can also be seen from Fig. 7.20 that hitting the panel faster makes the input spectrum noisier, less uniform. Thus, some spikes that appear in the output signals may not be due to resonance, but only to the way the panel was hit. This observation calls for further testing in future experiments.

7.3.3 Post-processing of the response spectra

The acceleration data from each test was collected into individual spreadsheet files that were then processed with a Python script. For each test, we have drawn the input spectrum (the frequencies excited by the hammer) and the output spectrum (the frequencies effectively observed in the panel's motion). The y-scale of the output spectrum is acceleration, originally measured in *g* (RMS). It was divided by the largest amplitude to make it easier to compare spectra with this "normalized" scale.

Fig. 7.21 presents the experimental spectra of tests #17 and #19. The predicted analytical frequencies are indicated by vertical lines with a label that specifies the mode using the values of m and n: for instance, "32" corresponds to the mode $(m = 3, n = 2)$. In theory, the spikes on the experimental spectra should be located at the frequencies indicated by those vertical lines. This is not the case with this exploratory batch of experiments. To us, it seems that the value of ρ is overestimated. It is computed from the membrane density via the relation $\rho = \sigma_m/\tau$, which is extremely sensitive to the membrane thickness τ (about 1 mm). Therefore,

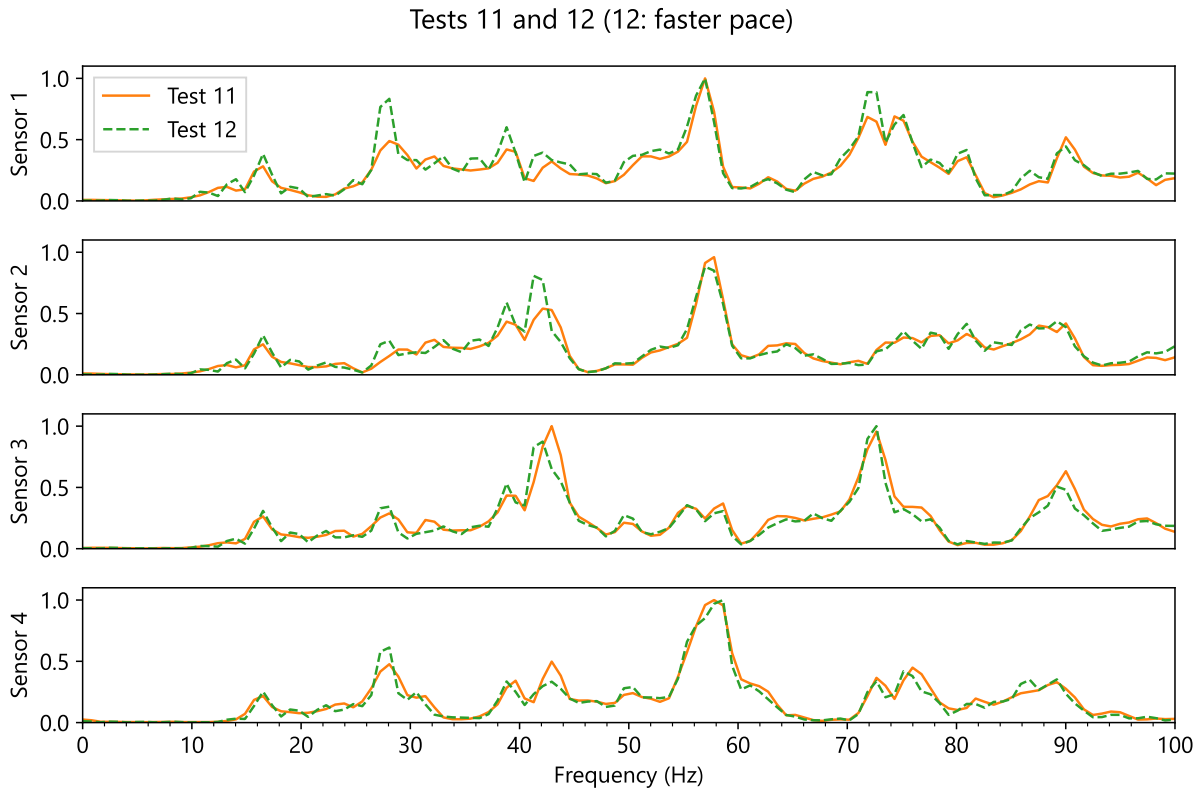

Figure 7.19: Increasing the pace of the impacts (from #11 to #12) does not affect the location of the resonance peaks.

one improvement track is to work on the determination of this thickness. One way to bring the theoretical result closer to the experimental results is to reduce the mass per unit area, as presented in Fig. 7.22 for a density $\rho = 1000$ kg/m³ where the first mode is in good agreement with the theory. It would make sense for the mode 00 to be absent in this graph, since the panel was struck on a nodal diameter of this mode. Further testing with different setups must be conducted in order to improve the identification of the eigenfrequencies of inflatable panels.

7.3.4 Improved placement of sensors and impact location

From these preliminary tests, we see that is difficult to observe all the modes in one test. To maximize the number of modes that can be excited and recorded at once, the impact and sensors locations should be placed at anti-nodes (where the amplitude of the mode is at maximum), as in Fig. 7.23 for instance. When drawing this figure, the orientation of each mode is taken such that a nodal point touches the ground.

7.4 Conclusion on impact hammer testing

We have applied impact hammer modal analysis to an inflatable panel, which has allowed for the identification of resonant frequencies at various inflation pressure levels. However, further investigation is necessary to match the theoretical prediction of Section 6.7.3, as the density of the membrane does not seem to be correctly identified. The dynamic material properties of the panel have not been determined, and so the static values of the constants are used in the calculations. This could be an important source of error, as these values can be differ greatly [12]. Another source of discrepancy is that the panels are not axisymmetric because of the

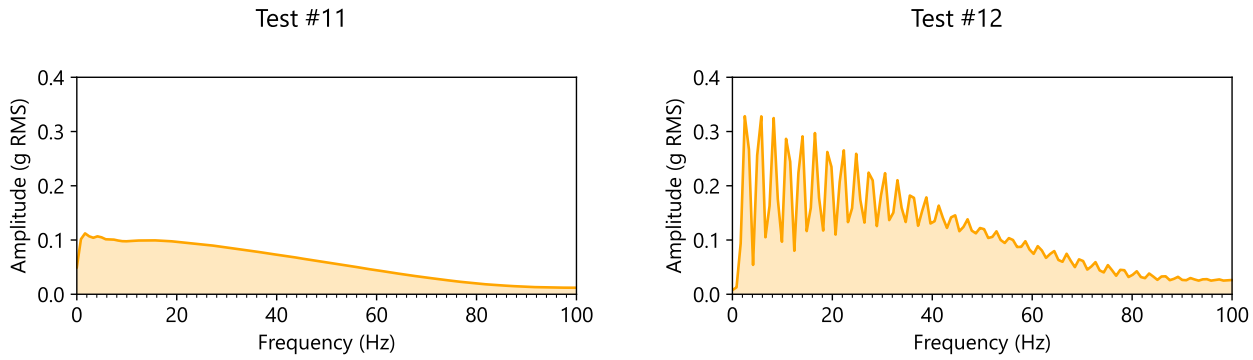

(a) Slow pace (test 11, T=3 s).

(b) Fast pace (test 12, T=1 s).

Figure 7.20: Spectra of the acceleration of the hammer at various paces.

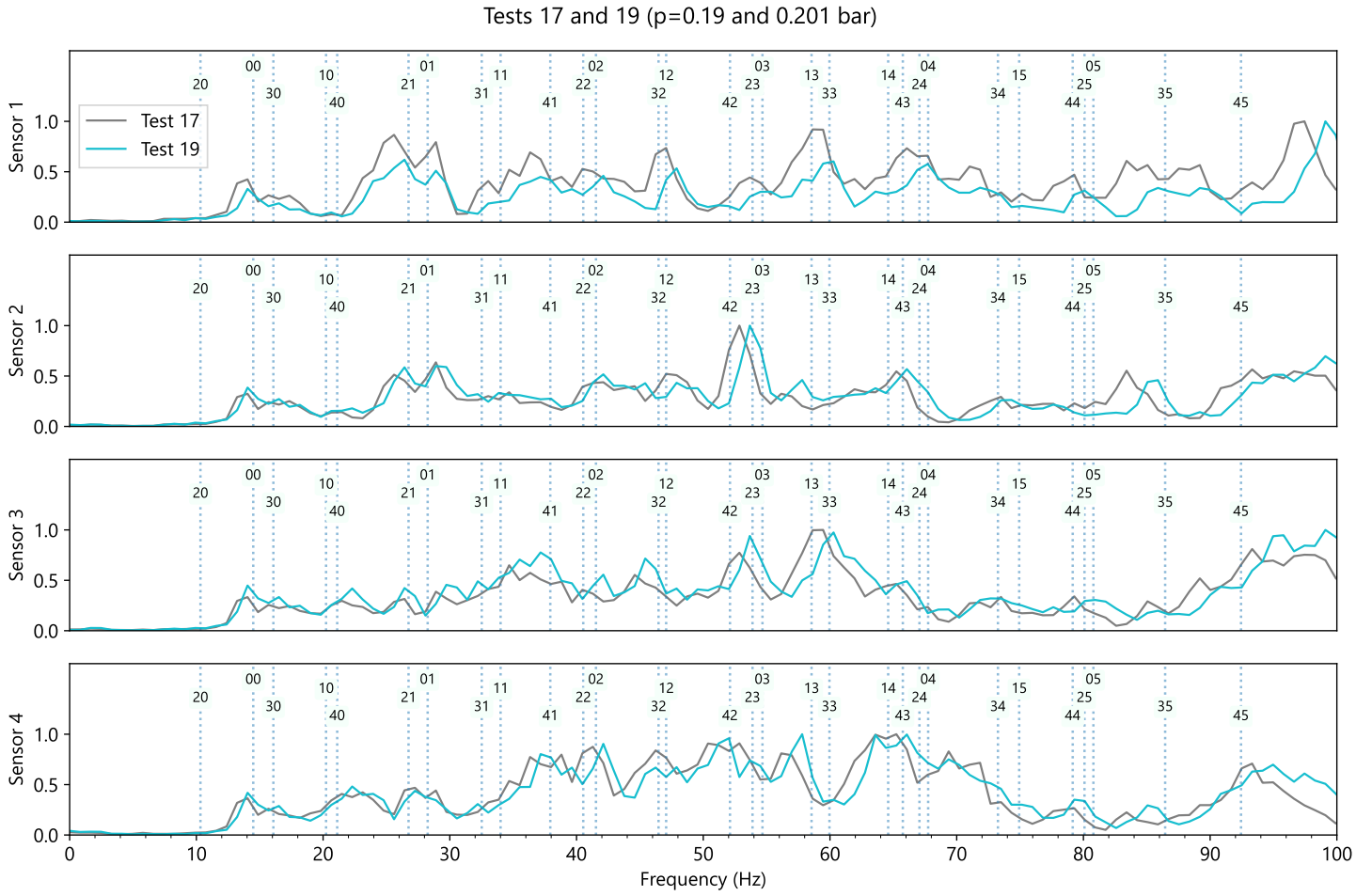

Figure 7.21: Experimental spectra for two different inflation pressures with analytically determined eigenfrequencies marked by vertical lines, with $\rho = 1300$ kg/m³. ($E\tau = 389$ N/mm, $\nu = 0.25$, $H_\varnothing = 20$ cm)

bonding strip that crosses the upper and lower sides of the panel. The main difficulty associated with impact testing is repeatability (care must be taken to always hit the panel with the same force and rhythm). Furthermore, sudden shocks may trigger nonlinearities in the system's response, and more generally the repeated impacts may damage the structure. Some of these challenges can be overcome by using a shaker instead of a hammer for modal excitation.

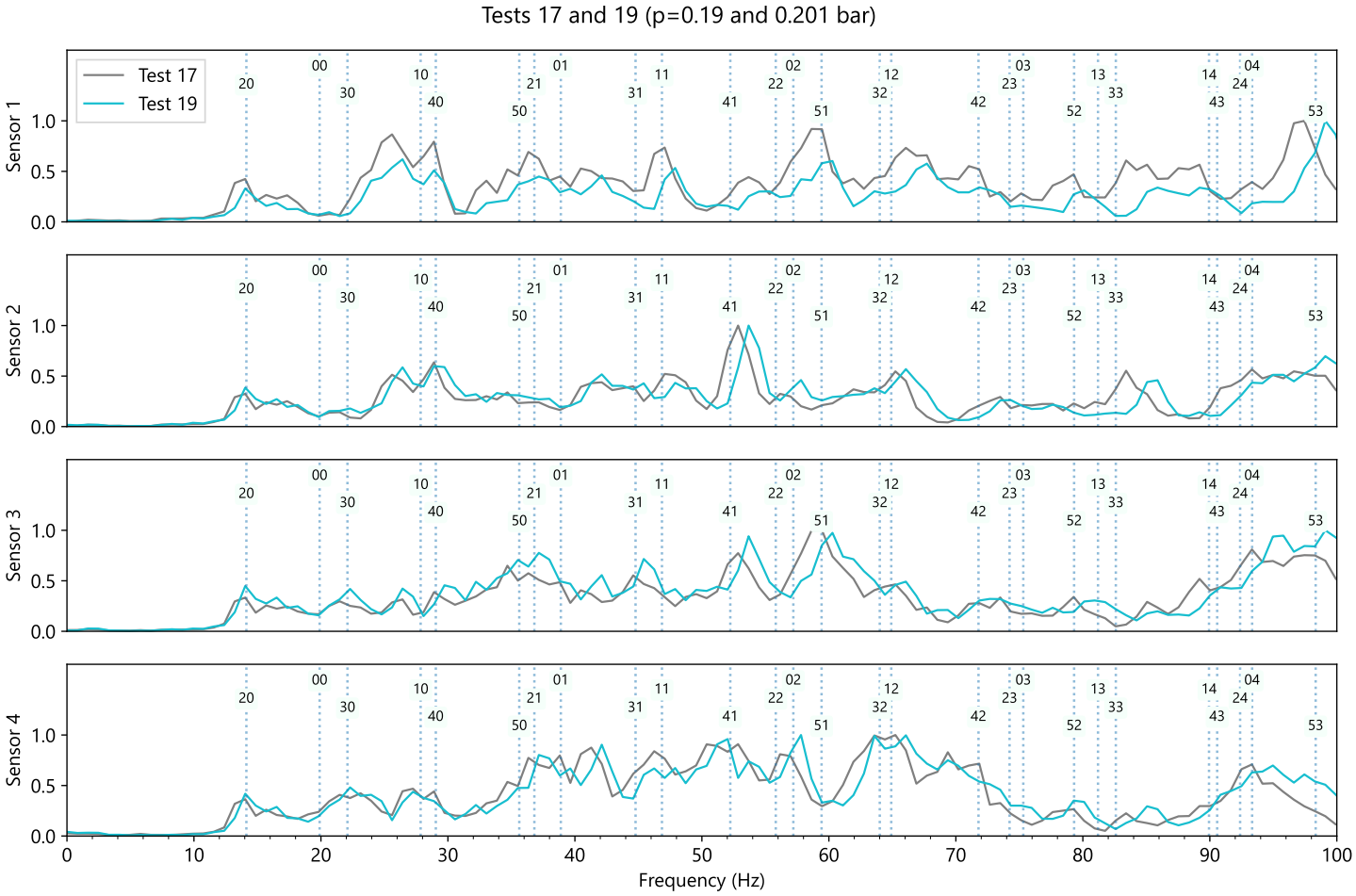

Figure 7.22: Experimental spectra for two different inflation pressures with analytically determined eigenfrequencies marked by vertical lines, with $\rho = 1000\,\mathrm{kg/m^3}$. ($E\tau = 389\,\mathrm{N/mm}$, $\nu = 0.25$, $H_\varnothing = 20\,\mathrm{cm}$)

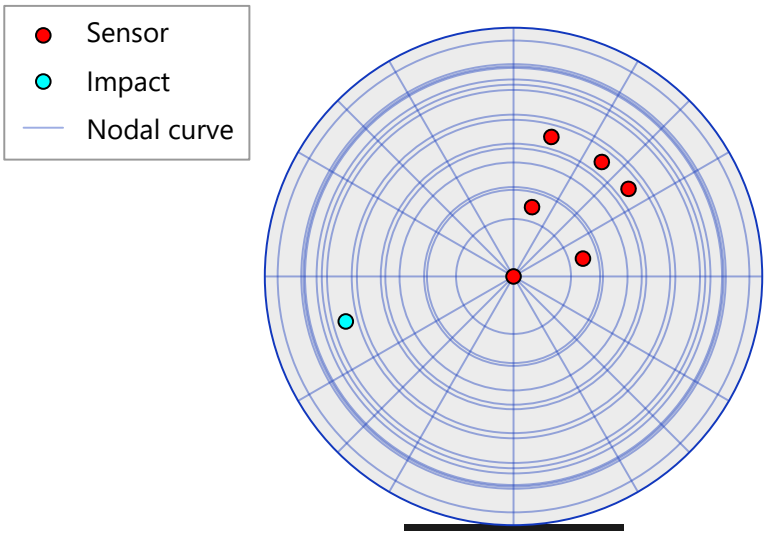

Figure 7.23: Improved sensors positions and impact point based on the nodal lines and diameters of all modes with $m \leq 2$, $n \leq 2$.

Conclusion and perspectives

The objective of this study was to investigate inflatable panels by three complementary approaches: analytical, numerical and experimental.

In Chapter 2, the analytical study has consisted in establishing the nonlinear equations of motion of inflatable panels using the principle of virtual power in large deformations. The nonlinear equations account for the effects of the internal pressure as well as shear effects through the Mindlin–Reissner kinematics.

In Chapter 3, the nonlinear governing equations were then linearized around the reference configuration to deal with the usual case where the displacements and rotations are small. The equations resemble those of the classical Mindlin–Reissner theory for solid plates with different stiffness terms due to internal pressure.

In Chapter 4, the linearized equations of motion were solved for the static bending problem of a simply-supported inflatable disk with uniformly distributed vertical load. The limit of validity of this solution in relation to the wrinkling of the membranes was established. The influence of the inflation pressure on the parabolic deflection profile was captured.

In Chapter 5, this solution was then confronted to a 3D nonlinear finite element simulation for a variety of geometries and inflation pressures and a very good agreement was found.

In Chapter 6, the dynamics of inflatable panels were also investigated. The eigenvalue problem was reduced to a system of Helmholtz equations which was solved to determine the eigenmodes and eigenfrequencies of inflatable disks and simply-supported rectangular panels. Two additional methods to determine the natural frequencies are proposed in the appendix: a numerical approximation method for axisymmetric eigenvalue problems (Appendix B) and the modal analysis of simplified membrane models (Appendix C).

Finally, in Chapter 7, the theoretical predictions were tested against experimental measurements performed on circular inflatable panels. A specific testing apparatus was built to handle the large disk and apply the simply-supported boundary conditions as well as a uniform transverse load to the panel. The static deflections are in agreement with the linear solution, although it could be improved by a better characterization of the materials. As for the experiments on dynamics, the dependence of the natural frequencies to the inflation pressure was observed but further work must be conducted to match the theory to the experimental data.

Perspectives

In addition to the results that have been established for the statics and dynamics of inflatable panels, many scientific challenges remain. Further research could be done in the following areas, starting with the most accessible ones:

- conduct further vibration analysis using modal exciters with a sine sweep as the input signal
- determine the inflated mechanical properties of the membranes from the values measured in the natural configuration
- study the post-wrinkling response of the panel, from the onset of wrinkling to bending collapse

- create a 2D nonlinear finite element for the numerical analysis of inflatable panels
- study the buckling of inflatable panels to anticipate their use as supporting structures

In the longer term, the following further studies could be considered, which go beyond the framework of this present work:

- include anisotropic behavior of the membranes, such as orthotropy
- perform reliability analysis to determine probabilities of failure
- explore new inflatable geometries (non-uniform diameter or thickness, with spaced or slanted cords)
- develop a theory of inflatable shells (with curved reference configuration)

Appendix

Appendix A

Bessel functions

Here we briefly define the Bessel functions and recall some of their useful properties that are used in Section 6.7.

A.1 Definition of the Bessel and modified Bessel functions

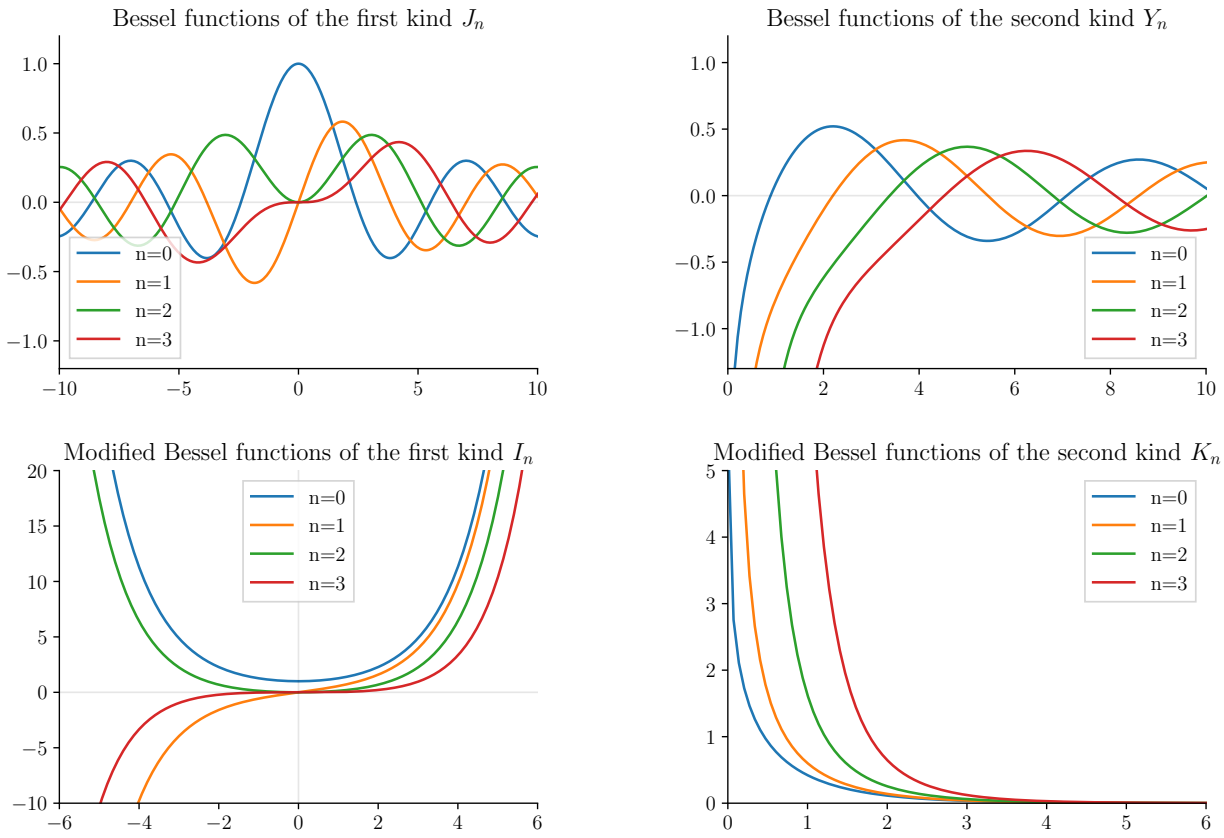

Figure A.1: Plots of the Bessel functions for real values ($n \in \mathbb{N}$).

The Bessel equation with unknown y is:

$$x^2y'' + xy' + (x^2 - n^2)y = 0$$

The solutions are J_n et Y_n for n integer (otherwise, for $n \in \mathbb{R}$ the solutions are J_n and J_{-n}). These functions have finite value near zero. The change of variable $x \leftarrow ix$ yields the modified Bessel equation:

$$(ix)^2 \frac{\partial^2 y}{\partial (ix)^2} + ix \frac{\partial y}{\partial ix} + \big((ix)^2 - n^2\big) y = 0$$

$$x^2 y'' + xy' - (x^2 + n^2) y = 0$$

which has solutions I_n and K_n (when n is an integer). Unlike the normal Bessel functions, I_n and K_n have an infinite limit near zero. A plot of some Bessel functions of small order is drawn in Fig. A.1.

The two kinds of Bessel and modified Bessel functions are related to one another:

$$I_n(x) = i^{-n} J_n(ix) \tag{A.1}$$

$$K_n(x) = \exp\left(i \frac{(n+1)\pi}{2}\right) \big[J_n(ix) + iY_n(ix)\big] \tag{A.2}$$

A.2 Properties of the Bessel and modified Bessel functions

Symmetries of the Bessel functions

Regarding the parity with respect to the variable x, both J_n and I_n are even when n is even, and odd when n is odd. There are also properties that resemble (anti-)symmetry with respect to the order n:

$$\begin{aligned} &\forall n \in \mathbb{Z}, \quad J_{-n} = (-1)^n J_n \\ &\forall n \in \mathbb{Z}, \quad I_n = I_{-n} \end{aligned} \tag{A.3}$$

The first equation is a consequences of the following relationships between the first and second kinds of Bessel functions:

$$J_{-n}(x) = J_n(x)\cos(\pi n) - Y_n(x)\sin(\pi n) \tag{A.4}$$

$$Y_{-n}(x) = Y_n(x)\cos(\pi n) + J_n(x)\sin(\pi n) \tag{A.5}$$

Recursive definitions

Bessel functions of different orders are related to one another: $\forall n \in \mathbb{Z}$,

$$J_{n+1} + J_{n-1} = \frac{2n}{x} J_n$$

$$I_{n-1}(x) - I_{n+1}(x) = \frac{2n}{x} I_n(x)$$

Recursive derivation

The first and second derivatives of J_n and I_n can be calculated in two manners.

1. First, using

$$J_{n+1} - J_{n-1} = -2J_n'$$

it is found that

$$J_n'(x) = \frac{1}{2}\big(J_{n-1}(x) - J_{n+1}(x)\big) \tag{A.6}$$

$$J_n''(x) = \frac{1}{4}\big(J_{n-2}(x) - 2J_n(x) + J_{n+2}(x)\big) \tag{A.7}$$

similarly

$$I_{n+1} + I_{n-1} = 2I_n'$$

$$I_n'(x) = \frac{1}{2}\big(I_{n-1}(x) + I_{n+1}(x)\big) \tag{A.8}$$

$$I_n''(x) = \frac{1}{4}\big(I_{n-2}(x) + 2I_n(x) + I_{n+2}(x)\big) \tag{A.9}$$

2. Second, using

$$J_n'(x) = \frac{n}{x}J_n(x) - J_{n+1}(x) \tag{A.10}$$

$$I_n'(x) = \frac{n}{x}I_n(x) + I_{n+1}(x) = -\frac{n}{x}I_n(x) + I_{n-1}(x) \tag{A.11}$$

it follows that

$$J_n''(x) = J_{n+2}(x) - \frac{2n+1}{x}J_{n+1}(x) + \frac{n(n-1)}{x^2}J_n(x) \tag{A.12}$$

$$I_n''(x) = I_{n+2}(x) + \frac{2n+1}{x}I_{n+1}(x) + \frac{n(n-1)}{x^2}I_n(x) \tag{A.13}$$

Hence $\frac{\mathrm{d}J_0}{\mathrm{d}x} = -J_1$ and $\frac{\mathrm{d}I_0}{\mathrm{d}x} = I_1 = I_{-1}$. Using the above formulas with $n < 1$ does not pose a problem given the symmetry and antisymmetry properties of the Bessel functions.

Appendix B

Vibration analysis of axisymmetric plates by a pseudospectral method

The eigenfrequencies obtained for circular plates in Section 6.7.3 can be compared to those produced by an approximate numerical solution of the eigenvalue problem in the axisymmetric case. We adapted a pseudospectral method presented by Lee and Schultz [85] for the eigenvalue analysis of axisymmetric Mindlin plates to the case of inflatable panels. They define a pseudospectral method as "a spectral method that performs a collocation process".

Derivation

After normalizing the coordinate variable $z = r/R$ and replacing the unknown fields W and Ψ_r with their polynomial expansion, a system of equations will be obtained by setting the residuals of the governing equations and the boundary conditions equal to zero at some collocation points. The solution fields W and Ψ_r are written as Chebyshev series:

$$\begin{aligned} W(z) &\approx \sum_{n=1}^{N+1} b_n T_{2n-2}(z) \\ \Psi_r(z) &\approx \sum_{n=1}^{N+1} a_n T_{2n-1}(z) \end{aligned} \tag{B.1}$$

where T_n is the Chebyshev polynomial of the first kind with degree n and the coefficients a_n, b_n are yet to be determined. One may choose N as large as one desires, but 35 is more than enough. Note that this expansion form takes advantage of the axisymmetry of the panel, as well as even and odd symmetries of Chebyshev polynomials. Then, the governing equations are "collocated" at the Chebyshev interpolation grid points z_i, which are

$$z_i = \cos\left(\frac{\pi(2i-1)}{4N}\right), \qquad i = 1, \ldots, N$$

Although the expansions in Eq. (B.1) contained $N+1$ terms, there are only N collocation points because the axisymmetry conditions at $z = 0$ are already satisfied. The eigenvalue problem and the boundary conditions are then written in matrix form and solved as described by Lee and Schultz [85]. This process is outlined below, but the reader is referred to the article for further details and explanations. The unknowns of the

problem, namely the coefficients in the polynomial expansion (B.1), are stored in vector form as

$$\{\mathrm{d}\} = \begin{Bmatrix} a_1 \\ \vdots \\ a_N \\ b_1 \\ \vdots \\ b_N \end{Bmatrix} \qquad \text{and} \qquad \{\mathrm{d}^\dagger\} = \begin{Bmatrix} a_{N+1} \\ b_{N+1} \end{Bmatrix}$$

which allows to write the eigenvalue problem in matrix form:

$$[\mathrm{H}]\{\mathrm{d}\} + \left[\mathrm{H}^\dagger\right]\left\{\mathrm{d}^\dagger\right\} = \omega^2\left([\mathrm{S}]\{\mathrm{d}\} + \left[\mathrm{S}^\dagger\right]\left\{\mathrm{d}^\dagger\right\}\right)$$

where the matrices $[\mathrm{H}]$, $\left[\mathrm{H}^\dagger\right]$ are related to stiffness terms and $[\mathrm{S}]$, $\left[\mathrm{S}^\dagger\right]$ are related to inertial terms. A dagger (†) is added when the matrix affects only the last coefficient of the expansion. The boundary conditions in matrix form are

$$[\mathrm{U}]\{\mathrm{d}\} + [\mathrm{V}]\left\{\mathrm{d}^\dagger\right\} = \{\mathrm{o}\}$$

where $[\mathrm{U}]$ and $[\mathrm{V}]$ are block diagonal matrices that describe the boundary conditions. The eigenfrequencies can be found in one step by incorporating the boundary conditions into the eigenvalue problem, which is achieved by eliminating $\{\mathrm{d}^\dagger\}$:

$$\left\{\mathrm{d}^\dagger\right\} = -[\mathrm{V}]^{-1}[\mathrm{U}]\{\mathrm{d}\}$$

The final result is the following generalized eigenvalue problem

$$\left([\mathrm{H}] - \left[\mathrm{H}^\dagger\right][\mathrm{V}]^{-1}[\mathrm{U}]\right)\{\mathrm{d}\} = \omega^2\left([\mathrm{S}] - \left[\mathrm{S}^\dagger\right][\mathrm{V}]^{-1}[\mathrm{U}]\right)\{\mathrm{d}\}$$

which is easy to implement and solve numerically.

Numerical results

The implementation of this algorithm was tested and it successfully retrieved the numerical results of several papers on classical plates [86, 87]. When applied to inflatable panels, both this numerical approach and the analytical results of Chapter 6 give the same natural frequencies to 4 digits of precision for the first 15 axisymmetric modes, and so the resulting values will not be listed here. This gives us confidence in the methodology used to solve the general vibration problem.

Although this approximate computation method is fast and reliable, it is restricted to the axisymmetric modes, and extending this method to the 2D polar case is beyond the scope of this thesis. We refer the reader to Fornberg's work on pseudospectral methods [88] for further exploration of this approach.

Appendix C

Simplified vibration models

Since the inertia and strain energy of the lateral wall is negligible compared to that of the upper and lower layers, the inflatable panel model is essentially a model of two membranes connected by stretched threads, and one may wonder how the spectrum of the panel compares to that of its two membranes. Guided by this physical intuition, we will compute the natural frequencies of membranes with the same tension force N_0 as the pressurized panel, and the thickness of this equivalent membrane will be chosen to match the inertia of the top and bottom membranes of the panel.

C.1 Natural frequencies of a tensed rectangular membrane

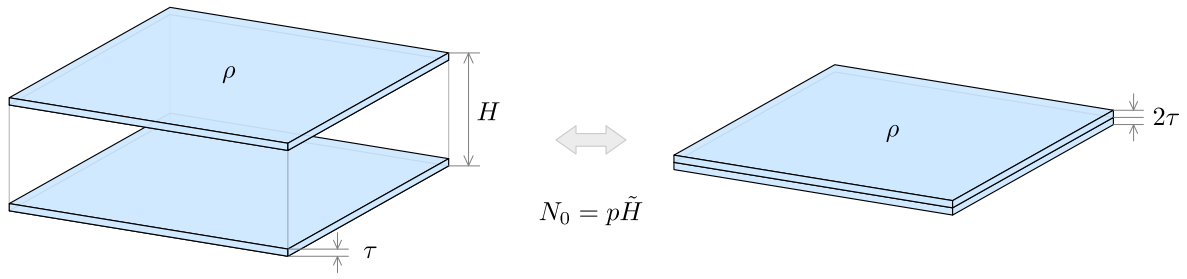

Figure C.1: Equivalent rectangular membrane for comparison with simply-supported inflatable panels.

The natural modes of a rectangular membrane of width a and length b with fixed boundary are, $\forall m, n \in \mathbb{N}$,

$$w_{mn}(x, y, t) = A_{mn} \sin(2\pi f_{mn} t) \sin\left(\frac{m\pi}{a} x\right) \sin\left(\frac{n\pi}{b} y\right) \tag{C.1}$$

where f_{mn} is the frequency of the mode. This shape is based on the assumption that the deflection w_{mn} equals zero on the whole boundary. Classically, the wave velocity is the square root of the ratio between the tension force and inertia:

$$c = \sqrt{\frac{\text{tension force}}{\text{inertia}}}$$

In our case the tension force is the pre-stress $N_0 = p\tilde{H}$ due to the inflation of the panel and the inertia comes

from the top and bottom membranes, which yields

$$c = \sqrt{\frac{p\tilde{H}}{2\tau\rho}} \tag{C.2}$$

This information makes it possible to represent the equivalent membrane (Fig. C.1). The natural frequencies of the membrane are known analytically from the relation

$$f_{mn} = \frac{c}{2}\sqrt{\left(\frac{m}{a}\right)^2 + \left(\frac{n}{b}\right)^2} \tag{C.3}$$

It turns out that this simplified model predicts natural frequencies that are close to the lowest predicted angular frequency ω_- of Eq. (6.40), as can be seen in Fig. C.2. This further reinforces our conviction that only ω_- holds physical significance for the SSSS boundary conditions, and that ω_0, ω_+ can be ignored. Note that $f_{00} = 0$ Hz since the mode $(m = 0, n = 0)$ corresponds to an absence of motion.

Remark C.1. The relative difference between the membrane equivalent and the complete method grows larger with inflation pressure, as seen with Table C.1 and Fig. C.2.

Inflation pressure p (kPa)	Frequency (Hz)		Relative difference
	Panel	Membrane	
30	12.56	14.16	+13%
50	15.15	18.26	+21%
70	16.88	21.57	+28%
90	18.14	24.42	+35%
100	18.65	25.73	+38%

Table C.1: Influence of the inflation pressure on the frequencies predicted by the inflatable panel theory and the membrane equivalent for the mode $(m = 1, n = 1)$. Parameters (prior to inflation): 3m by 2.5m by 20cm, $E\tau = 389$ N/mm, $\nu = 0.25$, $\rho = 1000$ kg/m^3.

Remark C.2. When either m or n equals zero, the mode is a shear-only vibration mode ($W = 0$ but $\boldsymbol{\psi} \neq \mathbf{0}$). Equation (C.1) clearly shows that such values of m and n do not give rise to any vibrations of the equivalent membrane, and yet, surprisingly, the frequencies predicted by (C.3) are not zero and still match the natural frequencies of the panel. Although it looks like an incorrect extension of the formula (C.3) to a case that should hold no physical significance, the numerical results still seem to be still realistic.

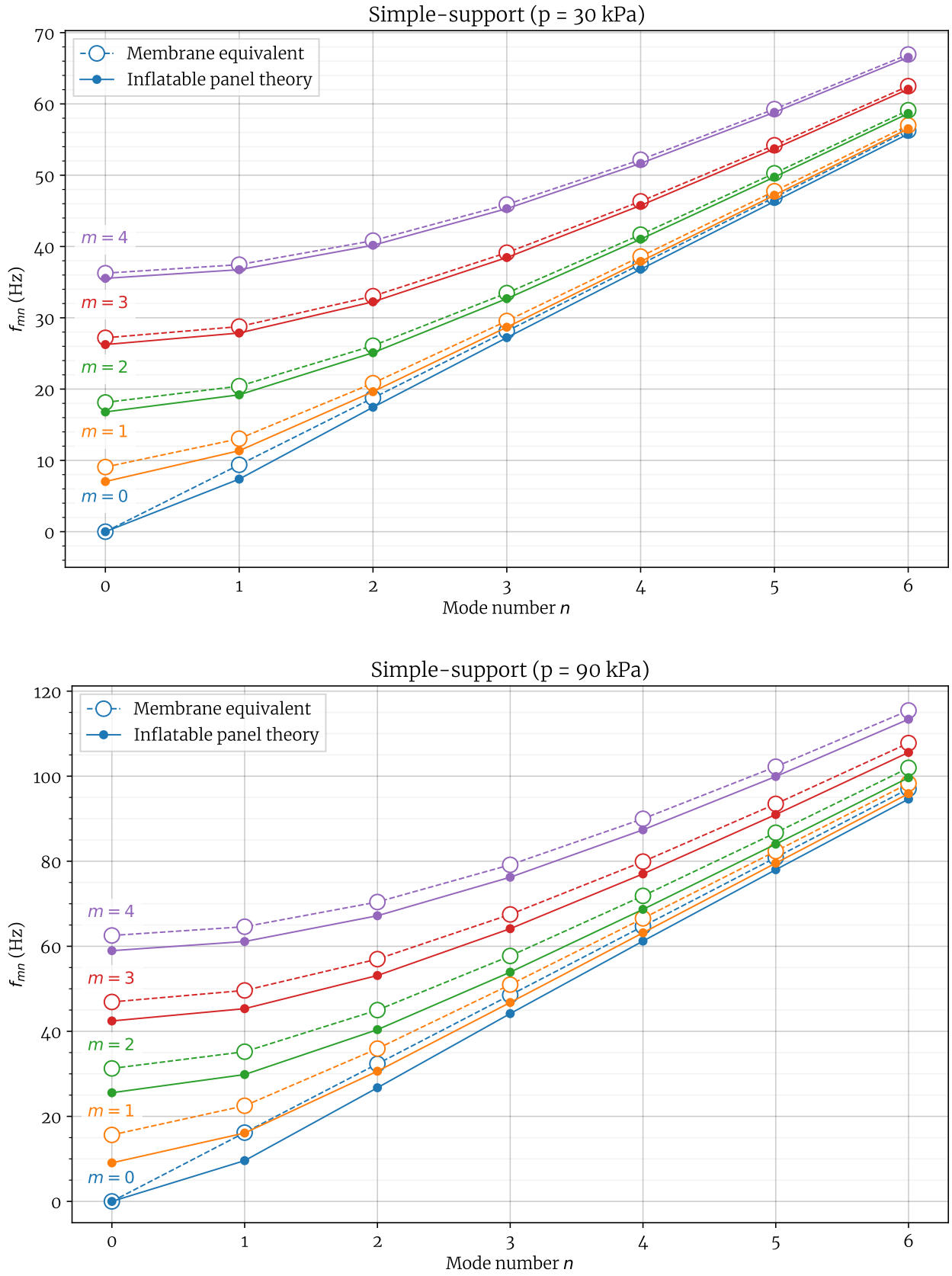

Figure C.2: Natural frequencies of a simply-supported rectangular inflatable panel (natural dimensions: 3m by 2.5m by 20cm) compared to those of an equivalent membrane for various modes and two inflation pressures. ($H_{\varnothing} = 20$ cm, $E\tau = 389$ N/mm, $\nu = 0.25$, $\rho = 1000$ kg/m^3)

C.2 Natural frequencies of a tensed circular membrane

The natural shapes of a circular membrane are well-known:

$$w_{mn}(r,\theta,t) = A_{mn}\cos(m\theta)J_m(\alpha_{mn}r)\cos(c\,\alpha_{mn}t) \tag{C.4}$$

where c is the speed of the wave propagation and α_{mn} are the wavenumber of the mode that must be determined for each m and n (the circumferential and radial mode numbers, respectively). The tension force in the membrane is the pre-stress $N_0 = p\tilde{H}$ of the panel, exactly like in the rectangular case, and so the speed of the wave propagation is again:

$$c = \sqrt{\frac{p\tilde{H}}{2\tau\rho}} \tag{C.5}$$

where $p\tilde{H}$ is the tension force due to the inflation pressure and $2\tau\rho$ the inertia of both membranes. This information makes it possible to represent the equivalent membrane (Fig. C.3). The stiffness and inertia of the rounded panel edges are again neglected since they have no direct equivalent in the membrane theory.

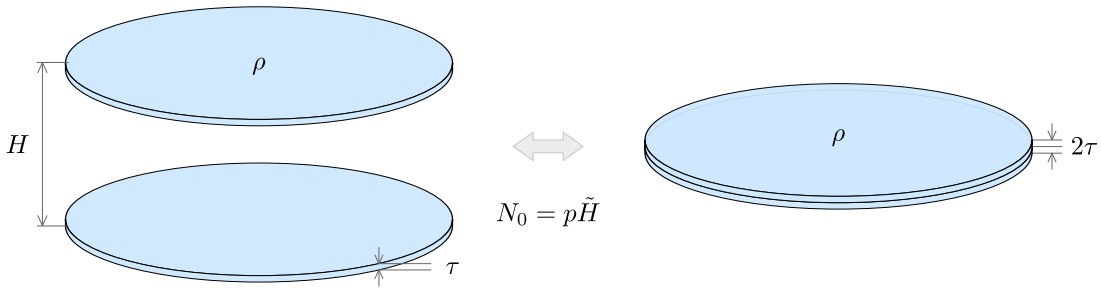

Figure C.3: Equivalent membrane for comparison with clamped or simply-supported inflatable disk.

The simplest boundary condition is to fix the edge of the membrane: $\forall t, \forall\theta,\ w_{mn}(r=R,\theta,t) = 0$ entails

$$J_m(\alpha_{mn}R) = 0$$

Therefore, if z_{mn} is the n-th zero of J_m, then $\alpha_{mn} = z_{mn}/R$ and the natural frequency is $f_{mn} = z_{mn}\dfrac{c}{2\pi R}$. The zeros of the Bessel function are easily accessible in the literature, see Table C.2.

n	$m=0$	$m=1$	$m=2$	$m=3$	$m=4$
0	2.405	3.832	5.136	6.380	7.588
1	5.520	7.016	8.417	9.761	11.065
2	8.654	10.173	11.620	13.015	14.373
3	11.792	13.324	14.796	16.223	17.616
4	14.931	16.471	17.960	19.409	20.827

Table C.2: First roots of the Bessel function J_m.

This calculation neglects the rounded panel edges and the drop yarns, and yet it gives a very good approximation of the natural frequencies of the clamped panel, as shown in Fig. C.4. The drawing of the equivalent membrane (Fig. C.3) suggests that this simpler model works best when the movement of the upper and lower membranes are identical, that is, when the fibers remain vertical ($\boldsymbol{\Psi} = \mathbf{0}$). As observed with the rectangular

panel, the relative difference between the natural frequencies of membrane equivalent and the panel theory grows larger with inflation pressure.

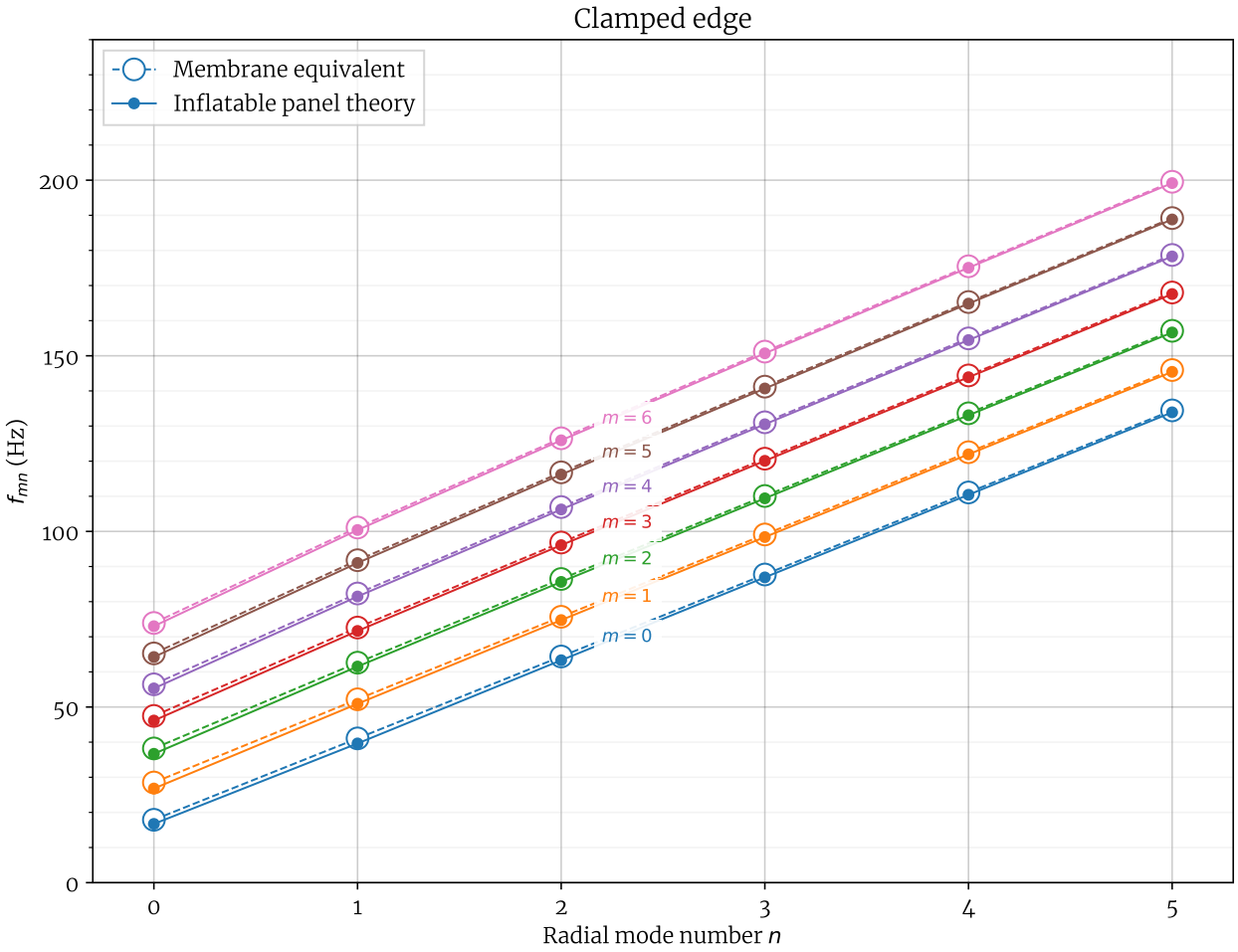

Figure C.4: Natural frequencies of a clamped inflatable panel compared to the simplified membrane model ($R_{\varnothing} = 1.5$ m, $H_{\varnothing} = 20$ cm, $p = 50$ kPa, $E\tau = 389$ N/mm, $\nu = 0.25$, $\rho = 1000$ kg/m³).

Bibliography

[1] R. L. Comer and Samuel Levy. Deflections of an inflated circular-cylindrical cantilever beam. *AIAA journal*, 1(7):1652–1655, 1963.

[2] J. P. H. Webber. Deflections of inflated cylindrical cantilever beams subjected to bending and torsion. *The Aeronautical Journal*, 86(858):306–312, 1982.

[3] J. A. Main, S. W. Peterson, and A. M. Strauss. Load-deflection behavior of space-based inflatable fabric beams. *Journal of Aerospace Engineering*, 7(2):225–238, 1994.

[4] W. B. Fichter. A theory for inflated thin-wall cylindrical beams. NASA Technical Note D-3466, NASA Scientific and technical publications, June 1966.

[5] Earl C. Steeves. A linear analysis of the deformation of pressure stabilized beams. NASA Technical Report 75-47-AMEL, US Army Natick Laboratories, January 1975.

[6] J.-C. Thomas and Christian Wielgosz. Deflections of highly inflated fabric tubes. *Thin-Walled Structures*, 42(7):1049–1066, 2004.

[7] Anh Le van and Christian Wielgosz. Bending and buckling of inflatable beams: some new theoretical results. *Thin-Walled Structures*, 43(8):1166–1187, 2005.

[8] Quang Tung Nguyen. *Contribution à l'étude du gonflage, de la flexion et du flambement de tubes membranaires orthotropes pressurisés*. PhD thesis, L'Université Nantes Angers Le Mans, France, 2013.

[9] Robert W. Leonard, George W. Brooks, and Harvey G. MacComb. Structural Considerations of Inflatable Reentry Vehicles. NASA Technical Note D-457, NASA, September 1960.

[10] Harvey G. McComb. A linear theory for inflatable plates of arbitrary shape. NASA Technical Note D-930, NASA, October 1961.

[11] Harvey G. Jr. McComb and Robert W. Leonard. Slanted Drop Cords in Inflatable Airmat Beams. *Journal of the Aerospace Sciences*, August 1961.

[12] W. J. Stroud. Experimental and Theoretical Deflections and Natural Frequencies of an Inflatable Fabric Plate. Technical Report D-931, NASA, October 1961.

[13] Charles Herbert Haight. Non-linear theory for airmat plates. Master's thesis, M.S. Univ. of Minnesota., 1962.

[14] Charles H. Haight. Large deflections of circular air-mat plates. *AIAA Journal*, 7(8):1630–1631, 1969.

[15] A. C. Kyser. A Contribution to the Theory of Pressure Stabilized Structures. Technical report, NASA, May 1963.

[16] Masaya KAWABATA and Kazuo ISHII. Effective stiffness evaluation of air-inflated dual membrane plates consist of drop cords and curved covers due to internal pressure. *Journal of Structural and Construction Engineering (Transactions of AIJ)*, 62(499):61–67, 1997. In Japanese.

[17] C. Wielgosz and J.-C. Thomas. Deflections of inflatable fabric panels at high pressure. *Thin-Walled Structures*, 40(6):523–536, 2002.

[18] Paul Cavallaro, Christopher Hart, and Ali Sadegh. Mechanics of air-inflated drop-stitch fabric panels subject to bending loads. In *ASME IMECE*, volume 9, November 2013.

[19] William G. Davids, Elisabeth Waugh, and Senthil Vel. Experimental and computational assessment of the bending behavior of inflatable drop-stitch fabric panels. *Thin-Walled Structures*, 167:108178, October 2021.

[20] William G. Davids and Hui Zhang. Beam finite element for nonlinear analysis of pressurized fabric beam-columns. *Engineering Structures*, 30(7):1969–1980, 2008.

[21] John William Leonard. *Behavior of Pressure-Stabilized Inflatable Shells of Revolution*. PhD thesis, University of Illinois, 1966.

[22] John W. Leonard. Inflatable Shells: Pressurization Phase. *Journal of the Engineering Mechanics Division*, 93(2):207–230, April 1967.

[23] John W. Leonard. Inflatable Shells: In-Service Phase. *Journal of the Engineering Mechanics Division*, 93(6):67–85, December 1967.

[24] John W. Leonard. Inflatable Shells: Nonsymmetric In-Service Loads. *Journal of the Engineering Mechanics Division*, 94(5):1231–1248, October 1968.

[25] Chin-Tsang Li and John W. Leonard. Finite Element Analysis of Inflatable Shells. *Journal of the Engineering Mechanics Division*, 99(3):495–514, June 1973.

[26] John W. Leonard. State-of-the-Art in Inflatable Shell Research. *Journal of the Engineering Mechanics Division*, 100(1):17–25, February 1974.

[27] R. D. Mindlin. Influence of rotatory inertia and shear on flexural motions of isotropic, elastic plates. *Journal of Applied Mechanics*, 18(1):31–38, 1951.

[28] H. Deresiewicz and R. D. Mindlin. Axially symmetric flexural vibrations of a circular disk. Technical report, Columbia University, December 1953.

[29] R. D. Mindlin and H. Deresiewicz. Thickness-shear and flexural vibrations of a circular disk. Technical report, Columbia University, December 1953.

[30] R. D. Mindlin, A. Schacknow, and H. Deresiewicz. Flexural Vibrations of Rectangular Plates. *Journal of Applied Mechanics*, 23(3):430–436, September 1956.

[31] T. Irie, G. Yamada, and S. Aomura. Natural Frequencies of Mindlin Circular Plates. *Journal of Applied Mechanics*, 47(3):652–655, September 1980.

[32] K. M. Liew, Y. Xiang, and S. Kitipornchai. Research on thick plate vibration: a literature survey. *Journal of Sound and Vibration*, 180(1):163–176, February 1995.

[33] Shahrokh Hosseini Hashemi and M. Arsanjani. Exact characteristic equations for some of classical boundary conditions of vibrating moderately thick rectangular plates. *International Journal of Solids and Structures*, 42(3-4):819–853, 2005.

[34] Kenneth A. Brakke. The Surface Evolver. *Experimental Mathematics*, 1(2):141–165, January 1992.

[35] Evi Corne, Marijke Mollaert, Natalie Stranghöner, Jörg Uhleman, Faruk Bilginoglu, Kai-Uwe Bletzinger, Heidrun Bögner-Balz, Nick Gibson, Peter Gosling, Rogier Houtman, Josep Llorens, Marc Malinowsky, Jean Marc Marion, Meike Nieger, Georgio Novati, Farid Sahnoune, Peter Siemens, Bernd Stimpfle, Vatyu Tanev, and Jean-Christophe Thomas. *SaP-Report: Prospect for European guidance for the Structural Design of Tensile Membrane Structures*. Science and Policy Report. Publications Office of the European Union, Luxembourg, 2016.

[36] Elliot W. Hawkes, Laura H. Blumenschein, Joseph D. Greer, and Allison M. Okamura. A soft robot that navigates its environment through growth. *Science Robotics*, July 2017.

[37] Nathan S. Usevitch, Zachary M. Hammond, Mac Schwager, Allison M. Okamura, Elliot W. Hawkes, and Sean Follmer. An untethered isoperimetric soft robot. *Science Robotics*, 5(40):eaaz0492, March 2020.

[38] Jung Chi, Ruy Pauletti, and Oliveira Pauletti. An outline of the evolution of pneumatic structures. September 2005.

[39] Tian-Wei Liu and Jiang-Bo Bai. Folding behaviour of a deployable composite cabin for space habitats - part 1: Experimental and numerical investigation. *Composite Structures*, 302:116244, December 2022.

[40] Suduo Xue, Fei Yan, and Guojun Sun. Deflation and collapse of air-supported membrane structures. *Thin-Walled Structures*, 169:108338, December 2021.

[41] Mélina Skouras, Bernhard Thomaszewski, Peter Kaufmann, Akash Garg, Bernd Bickel, Eitan Grinspun, and Markus Gross. Designing inflatable structures. *ACM Transactions on Graphics*, 33(4):63:1–63:10, July 2014.

[42] Constantin J. Monego. Air-supported tents for military use. Technical report, U.S. Army Natick Laboratories, July 1965.

[43] Glenn W. Quaint and Eldon C. Lown. Expandable Floating Bases. Technical report, Goodyear Aerospace Corporation, January 1972.

[44] Charles A. Rice and Michael L. Foust. Inflatable aquatic rescue board and method of rescue, 1974.

[45] J. D. Wood. The Flexure of a Uniformly Pressurized, Circular, Cylindrical Shell. *Journal of Applied Mechanics*, 25(4):453–458, December 1958.

[46] Eric Reissner. On Finite Bending of Pressurized Tubes. *Journal of Applied Mechanics*, 26(3):386–392, June 1959.

[47] John A. Main, Steven W. Peterson, and Alvin M. Strauss. Beam-type bending of space-based inflated membrane structures. *Journal of Aerospace Engineering*, 8(2):120–125, 1995.

[48] Earl C. Steeves. Behavior of pressure stabilized beams under load. Technical Report 75-82-AMEL, US Army Natick Laboratories, May 1975.

[49] Earl C. Steeves. Pressure stabilized beam finite element. Technical Report TR-79/002, US Army Natick Laboratories, December 1978.

[50] Earl C. Steeves. Optimum design of pressure stabilized beams. Technical Report TR-79/019, US Army Natick Laboratories, August 1979.

[51] Christian Wielgosz and Jean-Christophe Thomas. An inflatable fabric beam finite element. *Communications in Numerical Methods in Engineering*, 19(4):307–312, 2003.

[52] Jeffrey D. Suhey, Nam H. Kim, and Christopher Niezrecki. Numerical modeling and design of inflatable structures—application to open-ocean-aquaculture cages. *Aquacultural Engineering*, 33(4):285–303, October 2005.

[53] J.-C. Thomas, Z. Jiang, and C. Wielgosz. Continuous and Finite Element Methods for the Vibrations of Inflatable Beams. *International Journal of Space Structures*, 21(4):197–221, December 2006.

[54] Zhihong Jiang, Jean-Christophe Thomas, and Christian Wielgosz. Contribution à l'étude de la dynamique de poutres gonflables. In *8e Colloque national en calcul des structures*, Giens, France, May 2007. CSMA.

[55] Zhen Jiang. *Contribution à la dynamique des poutres gonflables*. PhD thesis, Université de Nantes, 2007. Thèse de doctorat dirigée par Wielgosz, Christian et Thomas, Jean-Christophe Sciences de l'ingénieur Nantes 2007.

[56] K. L. Apedo, S. Ronel, E. Jacquelin, M. Massenzio, and A. Bennani. Theoretical analysis of inflatable beams made from orthotropic fabric. *Thin-Walled Structures*, 47(12):1507–1522, December 2009.

[57] Thanh-Truong Nguyen, S. Ronel, M. Massenzio, K. L. Apedo, and E. Jacquelin. Analytical buckling analysis of an inflatable beam made of orthotropic technical textiles. *Thin-Walled Structures*, 51:186–200, 2012.

[58] Thanh-Truong Nguyen. *Numerical modeling and buckling analysis of inflatable structures*. PhD thesis, Université Lyon 1, 2012. Thèse de doctorat dirigée par Ronel, Sylvie et Massenzio, Michel Génie mécanique Lyon 1 2012.

[59] Thanh-Truong Nguyen, Sylvie Ronel, M. Massenzio, E. Jacquelin, K. L. Apedo, and Huan Phan-Dinh. Numerical buckling analysis of an inflatable beam made of orthotropic technical textiles. *Thin-Walled Structures*, 72:61–75, 2013.

[60] Jean-Christophe Thomas and Anh Le van. An exact solution for inflated orthotropic membrane tubes. *Thin-Walled Structures*, 67:116–120, June 2013.

[61] Quang-Tung Nguyen, Jean-Christophe Thomas, and Anh Le van. Inflation and bending of an orthotropic inflatable beam. *Thin-Walled Structures*, 88:129–144, 2015.

[62] Quang Tung Nguyen, Jean-Christophe Thomas, and Anh Le Van. An analytical solution for an inflated orthotropic membrane tube with an arbitrarily oriented orthotropy basis. *Engineering Structures*, 56:1080–1091, 2013.

[63] Alexis Bloch. *Expérimentation et modélisation du comportement des structures gonflables sous chargement aérodynamique aux états-limites*. PhD thesis, Université de Nantes, January 2016.

[64] Jean-Christophe Thomas and Alexis Bloch. Non Linear Behaviour of an Inflatable Beam and Limit States. *Procedia Engineering*, 155:398–406, January 2016.

[65] Jean-Christophe Thomas and Franck Schoefs. Reliability of inflatable bridge structures: challenge and first results for a new Eurocode Reliability of inflatable bridge structures: challenge and first results for a new Eurocode. In *40th IABSE Symposium*, September 2018.

[66] Edward D. Barker. Inflatable mattress, 1951.

[67] Summary: Engineering report of the development of a one-place inflatoplane. Technical Report AD-134 572, Goodyear Aircraft, 1957.

[68] Donald Dwidght Seath. *Vibration of an inflatable fabric wing model*. PhD thesis, Iowa State University of Science and Technology, 1963.

[69] L. M. Habip. A review: Recent work on inflatable structures. *International Journal of Mechanical Sciences*, 7(2):149–152, February 1965.

[70] Robert A. Dillman, Stephen J. Hughes, Richard J. Bodkin, David M. Bose, Joseph Del Corso, F. Neil Cheatwood, Stephen J. Hughes, Richard J. Bodkin, David M. Bose, Joseph Del Corso, and F. Neil Cheatwood. Flight Performance of the Inflatable Reentry Vehicle Experiment II. In *International Planetary Probe Workshop*, June 2010.

[71] Jie Wu, Quanyong Xu, Zhang Zhang, and Anping Hou. Aeroelastic characteristics of inflatable reentry vehicle in transonic and supersonic regions. *Computers & Fluids*, 237:105338, April 2022.

[72] Michael Smith. Mechanical response of polymer-fabric skin materials used in inflatable drop-stitch structures. Master's thesis, University of Rhode Island, January 2019.

[73] Alena Alich. Modeling, simulation and investigation of inflatable drop-stitch panels with finite element analysis. Master's thesis, University of Rhode Island, January 2019.

[74] Ryan Buglio. Characterization of drop-stitch constituent materials and inflated panel response. Master's thesis, University of Rhode Island, January 2020.

[75] Eric Reissner. The Effect of Transverse Shear Deformation on the Bending of Elastic Plates. *Journal of Applied Mechanics*, 12(2):A69–A77, March 1945.

[76] Eric Reissner. On bending of elastic plates. *Quarterly of Applied Mathematics*, 5(1):55–68, 1947.

[77] Raymond D. Mindlin. Thickness-Shear and Flexural Vibrations of Crystal Plates. *Journal of Applied Physics*, 22(3):316–323, March 1951.

[78] Lalaonirina R. Rakotomanana. *Éléments de dynamique des solides et structures déformables*. PPUR Presses polytechniques, June 2009.

[79] C. C. Chao and Yih-Hsing Pao. On the Flexural Motions of Plates at the Cut-Off Frequency. *Journal of Applied Mechanics*, 31(1):22–24, March 1964.

[80] K. M. Liew, Y. Xiang, S. Kitipornchai, and C. M. Wang. *Vibration of Mindlin Plates: Programming the p-Version Ritz Method*. Elsevier, Amsterdam ; New York, November 1998.

[81] Anh Le van. *Nonlinear Theory of Elastic Plates*. ISTE Press - Elsevier, 2017.

[82] Xiaofeng Wang, Yuqing Zhang, Siu-seong Law, Qingshan Yang, and Na Yang. Modeling of the added mass of air on ETFE cushions vibrating in still air. *Thin-Walled Structures*, 174:109170, May 2022.

[83] Arthur W. Leissa. *Vibration of Plates*. Scientific and Technical Information Division, NASA, 1969.

[84] Bing Zhao, Jianhui Hu, Wujun Chen, Jianwen Chen, Zhenyu Qiu, and Zhongliang Jing. Computational method for in-situ finite element modeling of inflatable membrane structures based on geometrical shape measurement using photogrammetry. *Computers & Structures*, 224:106105, November 2019.

[85] J. Lee and W. W. Schultz. Eigenvalue analysis of Timoshenko beams and axisymmetric Mindlin plates by the pseudospectral method. *Journal of Sound and Vibration*, 269(3):609–621, January 2004.

[86] Z. Celep. Free vibration of some circular plates of arbitrary thickness. *Journal of Sound and Vibration*, 70(3):379–388, June 1980.

[87] Beytullah Temel and Ahmad Reshad Noori. A unified solution for the vibration analysis of two-directional functionally graded axisymmetric Mindlin–Reissner plates with variable thickness. *International Journal of Mechanical Sciences*, 174:105471, May 2020.

[88] Bengt Fornberg. *A Practical Guide to Pseudospectral Methods*. Cambridge University Press, October 1998.

DOCTORAT BRETAGNE SCIENCES LOIRE POUR L'INGENIEUR

Nantes Université

Titre : Étude des panneaux membranaires pressurisés

Mots clés : panneau gonflable, statique, dynamique, plaque de Reissner-Mindlin, validation expérimentale

Résumé : Un panneau gonflable est une structure membranaire étanche remplie d'un gaz sous pression qui lui confère sa raideur et dont la planéité à l'état gonflé est assurée par des fils qui relient les membranes supérieure et inférieure. En assemblant des tubes et des panneaux pressurisés, il devient possible de créer des structures porteuses entièrement gonflables de formes complexes. Dans cette thèse, l'étude des panneaux membranaires pressurisés est menée de façon analytique, numérique et expérimentale. Les équations locales non linéaires sont déduites du principe des puissances virtuelles écrit en grandes transformations. Elles prennent en compte les effets de cisaillement grâce à la cinématique de Reissner-Mindlin ainsi que ceux de la pression de gonflage qui augmente la raideur globale. Ces équations sont ensuite linéarisées autour de la configuration de référence et résolues en statique dans le cas d'un disque simplement appuyé soumis à un chargement vertical uniforme. Cette solution est validée par comparaison à une simulation éléments finis 3D non linéaire. L'étude dynamique est menée par analyse modale : le problème aux valeurs propres se réduit à des équations de Helmholtz dont la résolution est donnée pour des panneaux rectangulaires appuyés ou circulaires. Enfin, les mesures issues d'essais de flexion statique avec un disque gonflable ont permis de valider la solution obtenue avec les équations linéarisées. L'évolution de la raideur en fonction de la pression interne est bien observée et correspond aux prédictions théoriques. Les résultats d'essais de vibration par marteau d'impact sont également présentés.

Title: Study of pressurized membrane panels

Keywords: inflatable panel, statics, dynamics, Mindlin-Reissner plate, experimental validation

Abstract: An inflatable panel is an airtight membrane structure filled with a pressurized gas that gives it its stiffness and whose flatness in the inflated state is ensured by drop cords that connect the upper and lower membranes. By assembling pressurized tubes and panels, it becomes possible to create fully inflatable load-bearing structures with complex shapes. In this thesis, the study of pressurized membrane panels is conducted analytically, numerically and experimentally. The nonlinear equations of motion are deduced from the principle of virtual power in large deformations. They take into account the shear effects through the Mindlin-Reissner kinematics, as well as the inflation pressure which increases the overall stiffness. These equations are then linearized around the reference configuration and solved in statics for a simply-supported disk subjected to a uniformly distributed vertical load. This solution is validated by comparison with a non-linear 3D finite element simulation. The study of dynamics is conducted through modal analysis: the eigenvalue problem is reduced to Helmholtz equations whose solutions are given for circular or simply-supported rectangular panels. Finally, the measurements from static bending tests with an inflatable disk were used to validate the solution obtained with the linearized equations. The increase in stiffness due to pressurization is observed and corresponds to the theoretical predictions. The results of vibration tests using an impact hammer are also presented.